Infrared Micro-tomography for the characterization of extra-terrestrial materials

Zelia Dionnet

NNT: 2018SACLS291

Thèse de doctorat

Infrared micro-tomography for the characterization of extra-terrestrial materials

Thèse de doctorat de l'Université Paris-Saclay
preparée à l'Université Paris-Sud

Ecole doctorale n°127 Astronomie et Astrophysique (A&A)
Spécialité de doctorat: Astronomie et Astrophysique

Thèse présentée et soutenue à Orsay, le 26 Septembre 2018, par

Zélia Dionnet

Composition du Jury :

Michael C. Martin Senior Staff Scientist, Lawrence Berkeley National Laboratory, Advanced Light Source Division	Rapporteur
Karine Demyk Directrice de Recherche, IRAP, Université de Toulouse	Rapportrice
Nathalie Carrasco Professeur, LATMOS, Université de Versailles Saint-Quentin	Présidente
Brigitte Zanda Maitre de Conférences, IMPMC, Muséum National d'Histoire Naturelle	Examinatrice
Akira Tsuchiyama Professeur, University of Kyoto, Division of Earth and Planetary Sciences	Examinateur
Alessandra Rotundi Professeur, Parthenope University of Naples	Examinatrice
Rosario Brunetto CR1, IAS, Université Paris Sud	Directeur de these
Ferenc Borondics Responsable de ligne SMIS, SOLEIL	Co-directeur de these

A mon père, qui m'a transmis très tôt son goût pour les sciences.
Cette aventure a aussi été la tienne.
A mon grand-père, un soutien indéfectible
et qui serait fière je l'espére de sa petite fille.

Acknowledgments

First, I would like to thanks all the people who have helped and supported me during these last three years. In particular, I am very grateful towards Rosario Brunetto and Ferenc Borondics who gave me the chance to work on this great project in a friendly environment. Ferenc, thanks for your precious advises and your optimism which help me to go through a lot of small troubles. Rosario, we spend a lot of times to discuss technical and scientific issues, but you are also here to listen to me, to advice me and to help me to become a researcher so thank you for your time, your patience and your implication during the three years.

I would like to thank all the members of my jury for their presence during my defense and for our fruitful discussions, and in particular I am grateful to: Mike Martins and Karine Demyk for having accepted to be rapportor of my manuscript; Nathalie Carrasco for being the president of my jury; Akira Tsuchiyama for his help with X-ray tomography, for providing data and for welcoming during my visit in Kyoto; Alessandra Rotundi for our discussion during the last summer and for her welcoming in Roma and finally Brigitte Zanda, who provided us one of the main samples of this thesis.

Cette thèse a été effectuée majoritairement au sein de l'équipe Astrochimie que je remercie chaleureusement pour leur accueil pendant ces trois ans. Merci à Alice Aléon, Zahia Djouadi et Donia Baklouti qui ont suivi mon travail et qui ont veillé au bon déroulement du projet. Leur aide et l'expertise qu'elles m'ont chacune apportées ont été très précieuses tant d'un point de vue professionnel que personnel. Alice tu as contribué pour beaucoup à la mise au point de la préparation des grains, et Zahia sans toi pour me guider en salle blanche, il m'aurait été bien difficile de travailler sur ces précieux petits grains. Merci à Obadias pour ton soutien et ta présence bienveillante. Cateline, cela a été un vrai plaisir de partager un bureau, nos états d'âmes et nos inquiétudes concernant nos manips respectives. Ton soutien m'a beaucoup aidée et permis de traverser plus sereinement la troisième année de thése.

J'ai passé une grosse partie de mon temps sur la ligne SMIS du synchrotron SOLEIL dont je remercie l'équipe pour son accueil. En particuler, merci à Christophe pour ses conseils et son aide pour les mesures. Stéphane, tu m'as beaucoup aidée pour mettre en place la tomo-

graphie et pour trouver des solutions concrètes qui ont rendu mes mesures en 3D possibles, pour cela merci.

Une autre aide précieuse durant cette thèse est venue de David Troadec qui s'est occupé de la préparation des échantillons.

J'ai ensuite eu la chance de pouvoir faire des mesures en tomographie X sur la ligne PSICHE du synchrotron SOLEIL. Merci à Andy King et à Eglantine Boulard de m'avoir transmis une partie de leurs connaissances dans ce domaine. Andy, merci pour ton accueil et ton aide lors de nos mesures, Eglantine, merci pour tes conseils qui m'ont permis d'obtenir ma premère reconstruction 3D dans l'infrarouge.

Cette thèse a aussi été l'occasion d'échanger avec de nombreux collègues que je remercie pour leur disponibilité et les échanges que nous avons eus : L. d'Hendecourt, E.Quirico, A. Rotundi et B. Zanda. Je remercie aussi A. Tsuchiyama, T. Nakamura, P. Beck and Y. Kebukawa d'avoir accepté de partager certaines de leurs données. Enfin, je remercie Francois Brisset pour son aide avec le miscroscope électronique ainsi que Donia Baklouti et Serge Della-Negra de m'avoir donné l'opportunité de travailler sur d'autres projets.

J'ai aussi eu l'occasion d'encadrer plusieurs stagiaires: Stéphano, Anne-Cécile et Nilly. Votre venue m'a permis de retrouver la magie et de réaliser mieux la chance que nous avons de pouvoir faire ce métier passionnant. Merci pour votre motivation, votre curiosité pour notre travail et pour tous les bons moments que nous avons partagés.

Ces trois ans auraient été trés différents sans le soutien de tous mes amis. Elise, Emmie, Anne, Marina et Karen vous avez toujours répondu présentes pour nos week ends et sorties qui m'ont permis de retrouver de l'énergie. Les discussions entre amis doctorants m'ont aussi permis de relativiser et de surmonter les difficultés que connait tout thésard: merci à Hélène, Mathilde, Etienne, Pierre, Lucie. Mention spéciale pour Pauline qui était à mes côtés il y a 6 ans lors de mes premières mesures sur des grains d'Hayabusa.

Sixtine, tu es comme une soeur pour moi, tu as été le témoin de tous les hauts et les bas

traversés depuis le lycée, et plus particulièrement durant ces trois années. Nous avons refait le monde à de nombreuses reprises et avec nos deux esprits rationnels, nous avons chassé les obstacles pour petit à petit construire les personnes que nous sommes aujourd'hui. Il nous reste plein de questions sans réponses mais heuresement encore toute une vie pour en trouver ensemble.

Raphaël, tu es l'homme que j'ai toujours révé d'avoir à mes cotés. Ton amour et la confiance que tu as placés en moi rendent ma vie plus douce avec toi. Tu m'as écoutée pleurer et douter, tu m'as encouragée quand pleine d'enthousiasme je relevai de nouveau défis, tu m'as suivie lors de mes conférences aux quatre coins du monde, tu as fais le bel effort de lire ma thèse, tu as même pensé au chocolat pour m'aider le jour J, bref tu étais sur tous les fronts. Merci pour tout et j'ai hâte de connaitre la suite de notre histoire.

Merci à tous les membres de ma famille pour leur soutien constant et la confiance qu'ils ont placé en moi dés le début. En particulier, je tiens à saluer mon grand père, parti avant la fin de cette aventure, qui a été un de mes plus grands supporter. Un immense merci à mes deux parents pour tout l'amour que j'ai recu. Maman, tu as toujours été là, prête à maudire la terre entière pour me protéger, et à corriger mes fautes d'orthographe. Papa, petite fille tu m'as transmis un très beau cadeau: ma passion pour la science. Quand j'ai grandi, tu t'es toujours impliqué dans mes études, n'hésitant pas à passer des heures sur d'obscurs problèmes (surement encore plus obscurs pour toi) de math durant mes années de prépa juste pour me donner le courage de les affronter. Tu as partagé et vécu toutes les étapes de ces 8 ans d'études si bien que cette belle victoire finale est aussi la tienne.

Merci à tous.

Contents

Chapter 1

Astrophysical context

Contents

1.1 Small bodies of the Solar System

The study of the origin and early evolution of our Solar System still has many points which need to be better understood. In particular, many open questions exist about the formation

of the extra-terrestrial organic matter, its potential interstellar heritage and its modification before and after the formation of the planetesimals.

The solar nebula is the result of the collapse of a molecular cloud under the effect of external perturbations, such as shock waves (Boss, 1995; Jones, 2004). When a portion of a molecular cloud reaches a critical size, mass, or density, it begins to collapse under its own gravity. During the collapse, as the cloud becomes denser, random gas motions initially present in the cloud average out in favor of the direction of the nebula's net angular momentum (Basri and Bertout, 1993). This rotation causes the cloud to flatten out and take the form of a disk. The initial collapse takes about 100,000 years. Fig. 1.1 presents the different stages of the formation of our Solar System. This first step corresponds to the panel (a).

Inside the disk, we can find the first elements of a Solar System. Near the star, where the temperature is very high (> 1400K), no complex molecules can be formed. In the region where the temperature reaches 1400 K, the refractory elements can condense and Calcium-Aluminum-rich Inclusions (CAIs) can form (Ebel and Grossman, 2000f; Lodders, 2003). These are the first solids formed in the disk. They are used as a reference to isotopically date other objects present in the Solar System (Rusell and al., 2006, Connelly et al., 2012). Further from the star, where the temperature is between 800 and 1400 K, magnesium-rich crystalline silicates as olivine and pyroxene, are formed (Lodders, 2003). Finally, beyond the ice line at about 5 Astronomical Units (AU), volatile elements can condensate, and we find water ice, methanol ice, methane ice, carbon dioxide ice, etc. This part of the disk is where bodies rich in gas and ice like comets or giant planet can form.

After the formation of the protoplanetary disk and the apparition of the star inside this disk (see Fig. 1.1(c)), our newly born Solar System is still filled with gas and dust (some of the dust may have retained an interstellar and/or and extrasolar heritage). The dust composing this disk can begin to aggregate (Weidenschilling, 1980 and 1995) and participate in the planetary formation. As a result of accretion, the smaller sized dust grains start to clump together because of the collisions due to the internal movement inside the disk, forming larger bodies. These larger bodies are called planetesimals, and we reach the stage (d) (Youdin, 2008). At some point the planetesimals become big enough so that they can attract other

small bodies because of their gravity. Some of these planetesimals form protoplanets and eventually the planets (see Fig. 1.1(d)). However, other planetesimals do not aggregate into planets or dwarf planets and remain in the form of small bodies.

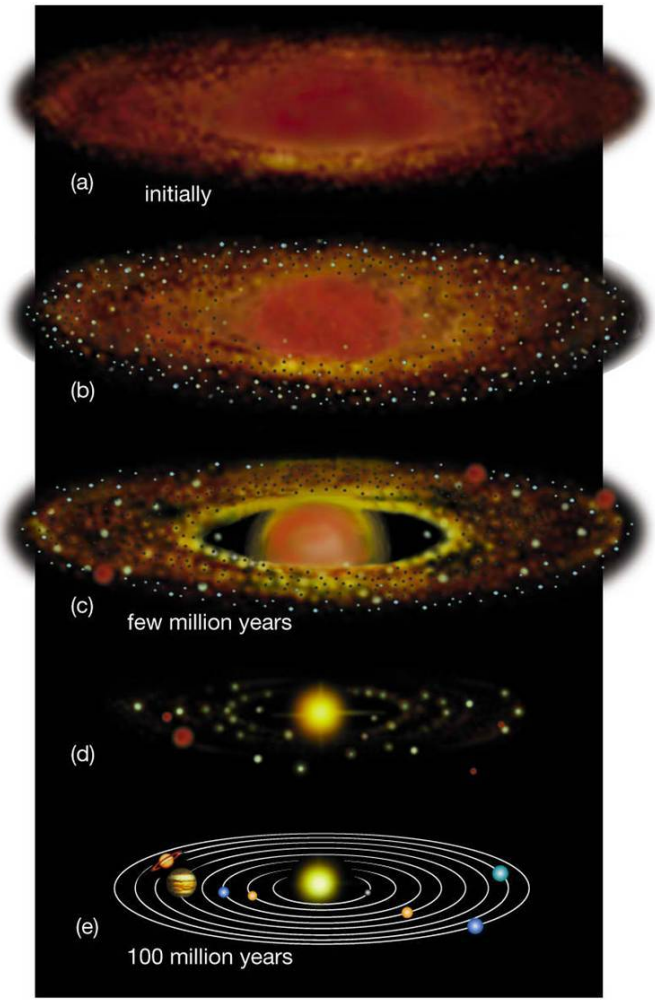

Figure 1.1: Schematic history of the beginning of our Solar System (from Chaisson et McMillan in Astronomy Today (1993)).

Some small bodies observed today in the Solar System are thus the relics of those early planetesimals. Unlike the planets, they did not undergo internal differentiation. Indeed, when a body has a diameter smaller than 20 km, differentiation is not efficient (Sramek et al., 2012). This means that the solid components of these bodies did not separate according to their density and they remained intimately mixed as they were during their formation. Thus, it is possible to study the composition and the processes that took place in the early Solar System by looking at these undifferentiated bodies. However other secondary processes,

such as collisions and thermal/aqueous alteration (see below), modified to some extent this primordial information.

All along the history of our young Solar System, before and after the planets were formed, many collisions between the planetesimals resulted in breaking up of some of these objects into smaller bodies. In the last decades, many progresses have been made in the understanding of the collisional evolution of small bodies, especially in the context of the orbital migration of the giant planets. It is currently accepted that at least two episodes of planetary migrations have significantly contributed to shaping the early Solar System, and in particular they have sculpted the distribution of small bodies (Bottke and al., 2002). These processes are modeled in the frame of the so-called Nice model (Morbidelli et al., 2005, 2007; Tsiganis et al., 2005) and Grand Tack model (Walsh et al., 2008). Even if the majority of asteroids observed today are fragments of older bodies (Bottke and al., 2002), their components can still be considered 'primitive' (as they did not undergo differentiation).

Finally, some of these undifferentiated bodies have reached (and still reach) the Earth all along its history in the form of meteorites and dust. The meteorites are rocks, coming from the interplanetary medium, which survived atmospheric entry and fell down on Earth. These rocks could come from asteroids, comets or even from others planets. It is fascinating to study these fragments of small bodies as some of them are the more primitive witnesses of the beginning of the time of accretion. Also, being available on Earth, they can be studied with the state-of-the-art laboratory techniques (see Chapter 2). There is a great diversity inside meteorites and here we will focus on the ones coming from undifferentiated bodies: the chondrites.

Undifferentiated meteorites: chondrites

This class of meteorites includes bodies which did not undergo differentiation. Their composition is very close to the one of the solar nebula (Sears and Dodd 1988). Inside meteorites, we can find small (few micrometers to centimeters) spherical mineral structures called chondrules. This characteristic is used to name this class of meteorites: chondrites. We can find three major types of meteorites inside the chondrites. The most common one is the ordinary chondrites (about 80 % of the falls). They come from asteroids rich in silicates. The second

type are the chondrites rich in enstatite, formed in very reductive conditions. And finally, we can also find carbonaceous chondrites, which contain carbon and are the more interesting for this study. We will now focus on this last class of meteorites.

Focus on carbonaceous chondrites

The carbonaceous chondrites are assembled by the intimate mix of three main components: the chondrules, the CAIs and the matrix. The chondrules are mainly composed of silicates such as olivine and pyroxene. Many scenarios have been conjectured to explain their formation (Hewins et al., 2005). One of these proposes that they were formed in the protoplanetary disk by crystallization of a liquid silicate (Lauretta et al., 2006). The CAIs are components made of refractory elements such as melilite, feldspaths, and oxides (Aleon et al. 2008). They formed at temperatures higher than 1400K in the protoplanetary disk, and they are the oldest witnesses of the beginnings of the Solar System. Finally, the matrix is the glue between all these components. It is a fine-grained (μm and sub-μm) assembly mainly composed of minerals, such as phyllosilicates, amorphous silicates, anhydrous silicates, carbonates, etc. (Rubin, 1996; Leroux et al., 2015), with inclusions of organic matter (Le Guillou et al., 2014; Vinogradoff et al., 2017; Remusat et al. 2005). Iron and nickel oxides, sulfides, and metals are also observed within the matrix.

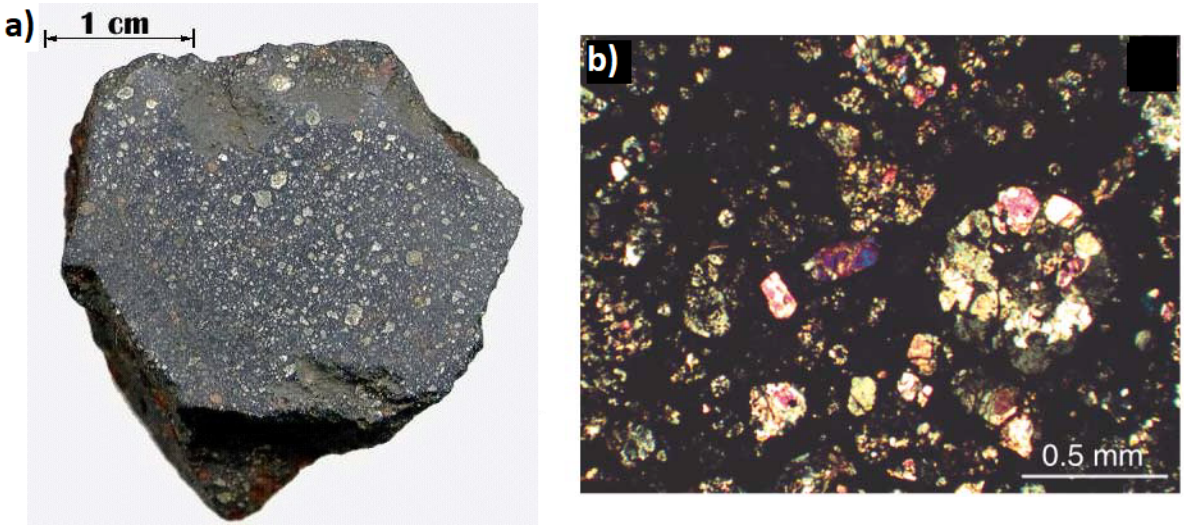

Figure 1.2: (a) A chunk of the Murchison meteorite. (Image from Northern Arizona University) (b) a thin section of the Dar al Gani 186 carbonaceous chondrite showing

spherical silicate chondrules surrounded by the matrix (from Sephton et al., 2002).

Inside this class of meteorites, we can distinguish several families. The second letter is given according to the most known sample inside the family: CI for Ivuna, CM for Murchison, CR for Renazzo, CO for Omans, CV for Vigarano and CK for Karoonda. The scope of the processes (metamorphism, aqueous alteration, see below) underwent on the parent bodies is a criterion to classify the meteorites inside the chondrite class (see Fig. 1.3). This classification is somewhat questioned within the community. For instance Sears et al. (1991) have shown that meteorites from the type 3 have undergone different degrees of both thermal metamorphism and aqueous alteration. In the matrix of primitive meteorites, these different phases are observed close to each other (e.g. amorphous and crystalline phases, minerals and carbonaceous materials, Leroux et al., 2015, and Le Guillou et al., 2014), with very different formation and evolution histories.

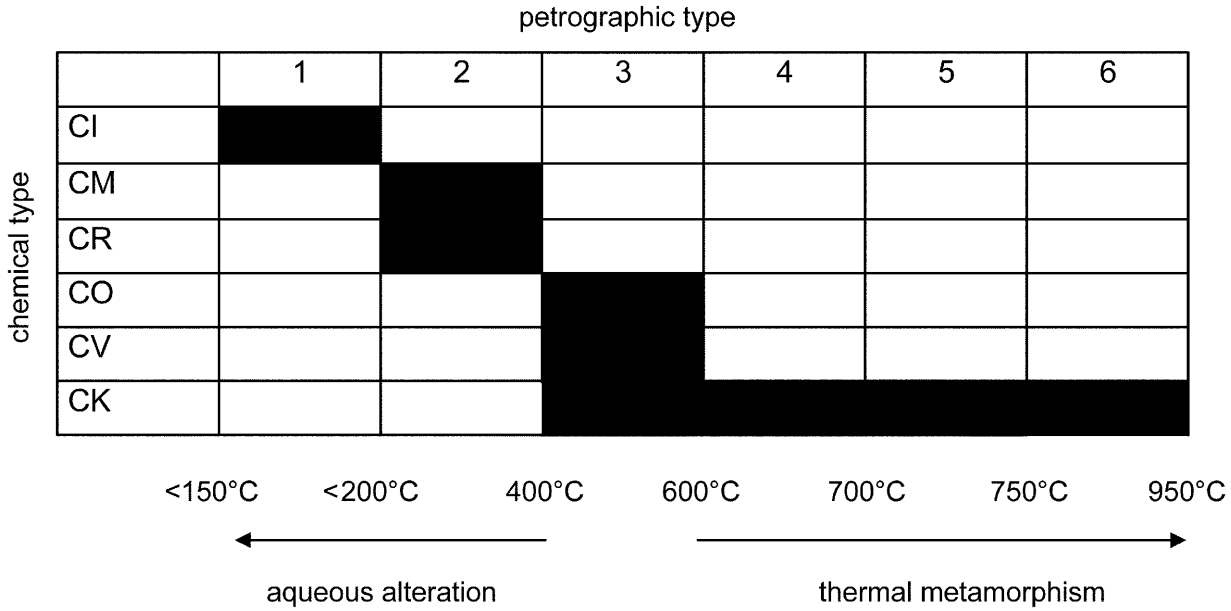

Figure 1.3: Classification of the meteorites according to a petrologic type (from Sephton et al. 2002).

The carbon inside the carbonaceous matrix represents only a few percents of the matrix (about 5 %s in mass) (Sephton et al., 2002; Gilmour, 2003; Pizzarello et al., 2006). As carbonaceous chondrites are considered as part of the most primitive extraterrestrial matter, their content in carbonaceous matter is particularly retaining attention and led to, these

last decades, different and extended analytical studies that showed a large chemical diversity and a great potential for prebiotic chemistry. To sum up, the carbonaceous content of these chondrites is generally divided into two families, the insoluble organic matter (IOM), and the soluble organic matter (SOM). This classification is related to the way the carbonaceous matter is extracted from the meteorites samples before analysis. The carbonaceous matter that is soluble into the acidic solution or in the solvent used forms the SOM, and the remaining insoluble one forms the IOM. Due to that physical-chemical separation, the IOM is composed of a cross-linked macromolecular organic matter, whereas, the SOM is composed of smaller entities completely soluble in the solvent used for extraction (generally water, but organic solvents were also used in some studies). Remusat et al. (2005) have proposed a schematic structure of the meteoritic organic matter made of aromatic rings connected by aliphatic chains (see Fig. 1.4).

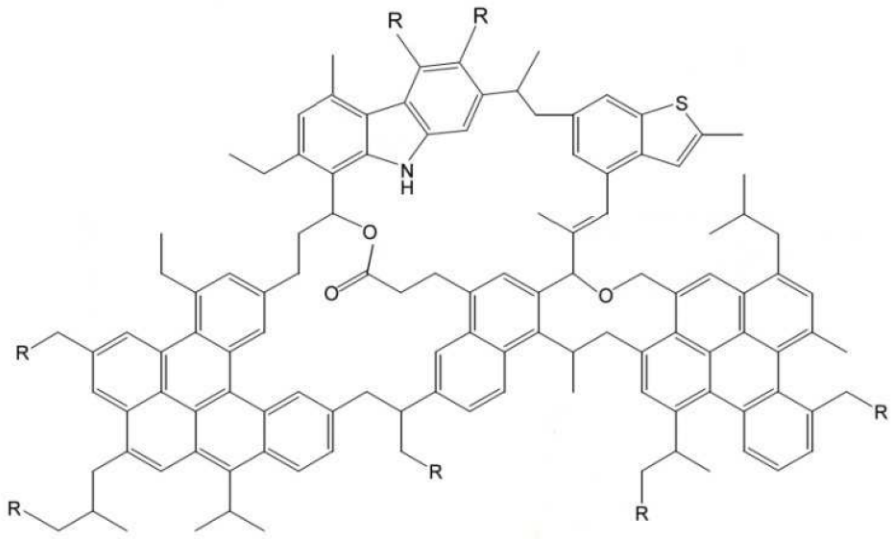

Figure 1.4: A model for the composition and structure of the organic matter inside carbonaceous meteorites according to Remusat et al. (2005).

1.2 Study of post-accretional processes

1.2.1 Heterogeneity inside extra-terrestrial materials: key of complex processes

As mentioned above, primitive extraterrestrial materials are characterized by large mineralogical and compositional heterogeneity at different scales: from nm to mm (Rietmeijer, 1998). This heterogeneity is the result of a complex set of pre- and post-accretional processes (Alexander et al., 2007). For instance, aqueous alteration (Brearley, 2006) and thermal metamorphism (Huss et al., 2006) can modify the matter inside the parent body. Carbonaceous chondrites and more specifically CM chondrites have accreted the primordial components of our Solar System. They have undergone different degrees of aqueous alteration (and low metamorphism) and the study of such primitive objects gives keys to understand the composition of primitive solid matter. Let's now briefly describe the two main post-accretional processes and their effect on the different components of the carbonaceous matrix.

1.2.2 Aqueous alteration

Aqueous alteration is a process undergone inside the parent bodies due to the circulation of water (e.g., Kerridge and Bunch, 1979; Zolensky and McSween, 1988). In his review, Brearley (2006) showed that for CI and CM chondrites, this process has mainly taken place on the parent bodies. Even if some chondrites may have undergone pre-accretional aqueous alteration, the result of it is not visible anymore as the much stronger post-accretional process has erased it (Brearley (2006)). The most severe manifestation of aqueous alteration on an extra-terrestrial material is the apparition of hydrated phyllosilicates (often serpentine or smectite, Leroux et al. 2015) which could be associated to sulfates, carbonates and oxides (e.g., Zolensky and McSween, 1988; Brearley and Jones, 1998). The mineralogical variations inside the different objects could be due to varying conditions of alteration (P, T, fO2, water/rock ratio, e.g. Zolensky and McSween, 1988).

Leroux et al. (2015) proposed the following scenario for describing the effects of aqueous alteration on silicates of the Paris CM primitive meteorite (Fig. 1.5; see Chapter 3 for a

description of the Paris meteorite). The unaltered material consisted of amorphous units, containing nano-inclusions of Fe-sulfides, separated from one another by porosity. The second step was the formation of fine grained silicates within the open spaces and at the edges of the amorphous units. Later, the amorphous phases were progressively replaced by fibrous texture which at the end became coarser and lead to the formation of phyllosilicates. Beck and al. (2014) showed that aqueous alteration also affects olivine which is progressively replaced by OH-bearing phases.

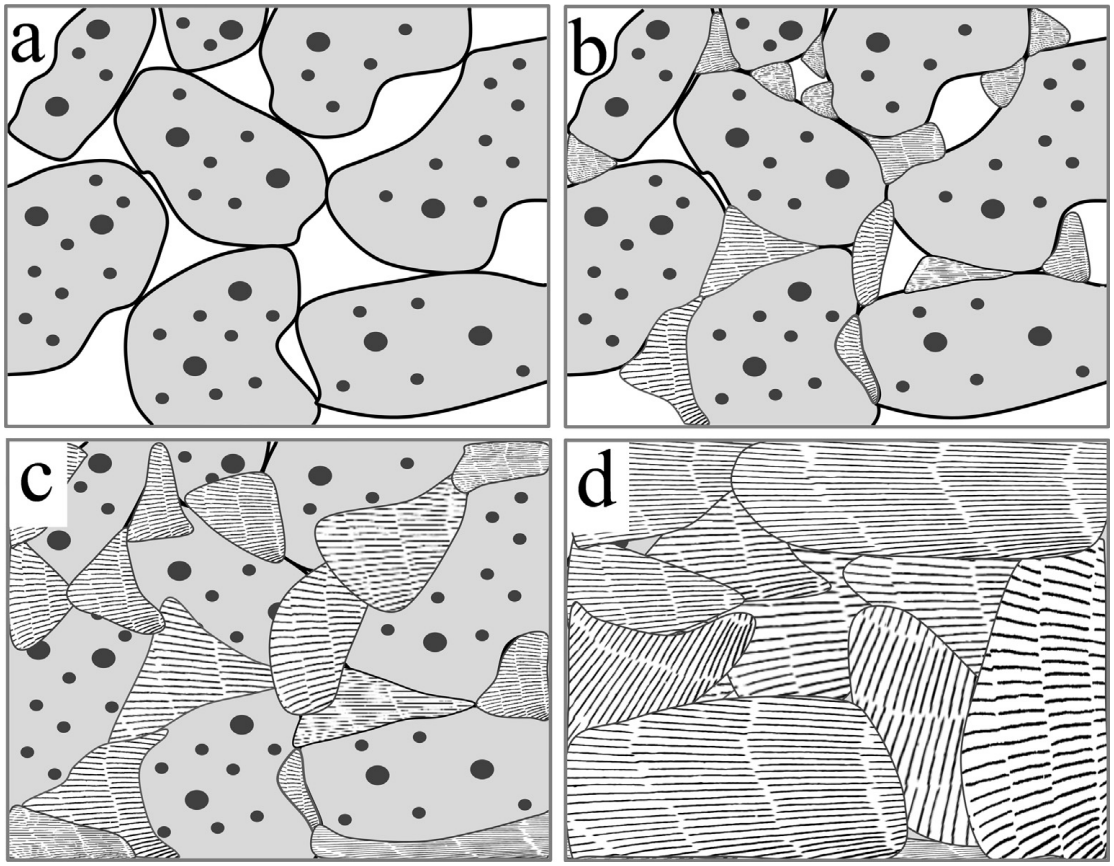

Figure 1.5: A possible scenario for the aqueous alteration on the Paris meteorite (from Leroux et al., 2015): from amorphous units separated from one another by porosity (a), to the formation of fine grains silicates (b) which progressively fill the porosity (c) to become coarser and less amorphous (d).

The effects of hydrothermal alteration on the organic matter are less clear: the evolution of carbon moieties with water is still a matter of debate (Le Guillou et al., 2014; Brearley, 2006). Infrared analyses bring information about hydration of the organic component: by

studying the FTIR spectra of IOM, Kebukawa et al. (2011) observed that the majority of the primitive IOM type 1 and 2 chondrites are characterized by low CH_2/CH_3 and high H/C ratios. At the opposite type 3.0 chondrites were characterized by a slightly higher CH_2/CH_3 ratio and a lower aliphatic C-H intensity. Moreover, they noticed lower abundance of aliphatic moieties and lower abundance of OH-bearing phase in more altered meteorites, suggesting this could be a signature of partial oxidation of aliphatic moieties during a mild parent body alteration. Orthous-Daunay et al., 2013 studied the variations of the IOM composition in meteorites showing different degrees of hydrothermal alteration. They concluded that the more altered is the meteorite, the higher is the CH_2/CH_3 ratio, and the more the IOM has an aromatization.

In this Ph.D. thesis, I contribute to the study of how composition and heterogeneity at small scale give information about the effects of aqueous alteration on minerals and organic matter on primitive meteorites.

1.2.3 Thermal metamorphism

Thermal metamorphism is the second post-accretional process which could change the composition and the structure of the matter inside asteroids. The main source of heating is the radioactive decay of heavy elements such as ^{26}Al or, in a less significant extent, ^{60}Fe (Scott and Krot, 2005). Shocks also bring kinetic energy which can be converted into thermal energy, but for the smaller asteroids (smaller than about 100 km), this source of heating is not efficient for global metamorphism (Keil et al., 1997). The major effect of thermal metamorphism is the progressive disappearance of chondrule's contours and their integration to the matrix (McSween et al., 1988) from a petrological type 3 to a petrological type 6. Concerning the organic matter, the main effect of the thermal methamorphism is the graphitization of the polyaromatic carbons (Bonal et al., 2005, 2006; Chaumard et al. 2013).

In this Ph.D. thesis, I study few particles coming from a CM meteorite (Chapters 3 and 7), which have undergone aqueous alteration but limited thermal metamorphism. Another part of my study deals with asteroidal particles (Chapter 6) which have undergone thermal metamorphism (between type 4 and 6).

1.3 Relationship between Organic Moieties and Minerals

Different groups observed the proximity of the organic and the mineral phases in many extraterrestrial samples (see Meourane et al,. 2013 for an example). It is interesting to consider the possible links between these two phases. For instance, did the minerals contribute to the formation of the organic moieties inside carbonaceous meteorites? As explained in Pizzarello and Shock (2010), the main processes responsible for the formation of organic molecules are Miller-Urey type (Miller et al., 1976) and Fisher-type reactions (Lancet et Anders, 1970). Both need dust as a catalyst. Furthermore, both mineral assemblages and organic matter underwent modifications during parent body aqueous alteration and thermal metamorphism. Thus, mineral phases may have played a key role in the history of organic matter and studying the relation between them is a crucial point. IR spectroscopy has the ability to detect both minerals and organics and thus it is a very useful tool to help answer some of these questions.

A few recent analyses addressed these questions by using in situ high spatial resolution imaging techniques like Transmission Electron Microscopy (TEM) (Le Guillou and Brearley, 2014) sometimes combined to electron energy loss spectroscopy (EELS) (Garvie and Buseck, 2007) or to XANES (X-ray Absorption Near Edge Structure) spectroscopy (Le Guillou et al., 2014) for a thorough characterization of the detected organic matter. All these studies essentially evidenced a spatial correlation between the organic matter and the phyllosilicates present in the meteorites matrix. More specifically, the organic matter of the Paris meteorite has been recently studied by Vinogradoff et al. (2017). By combining different techniques, they detected spatial and compositional heterogeneity of the organics in the matrix of Paris. They observed that organic grains are embedded within the silicate matrix and frequently in contact with nanosulfides.

1.4 Interest of Infrared measurements

The compositional heterogeneity of extraterrestrial materials has been investigated in the last decades with different techniques, such as scanning electron microscopy (SEM) coupled with energy dispersive spectroscopy (EDS), transmission electron microscopy (TEM), nano-scale secondary ion mass spectrometry (NanoSIMS), synchrotron-based X-ray techniques (XANES, STXM), micro-Raman spectroscopy, and infrared microspectroscopy and imaging (see Fig. 1.6 extracted from a recent review by Westphal et al., 2016).

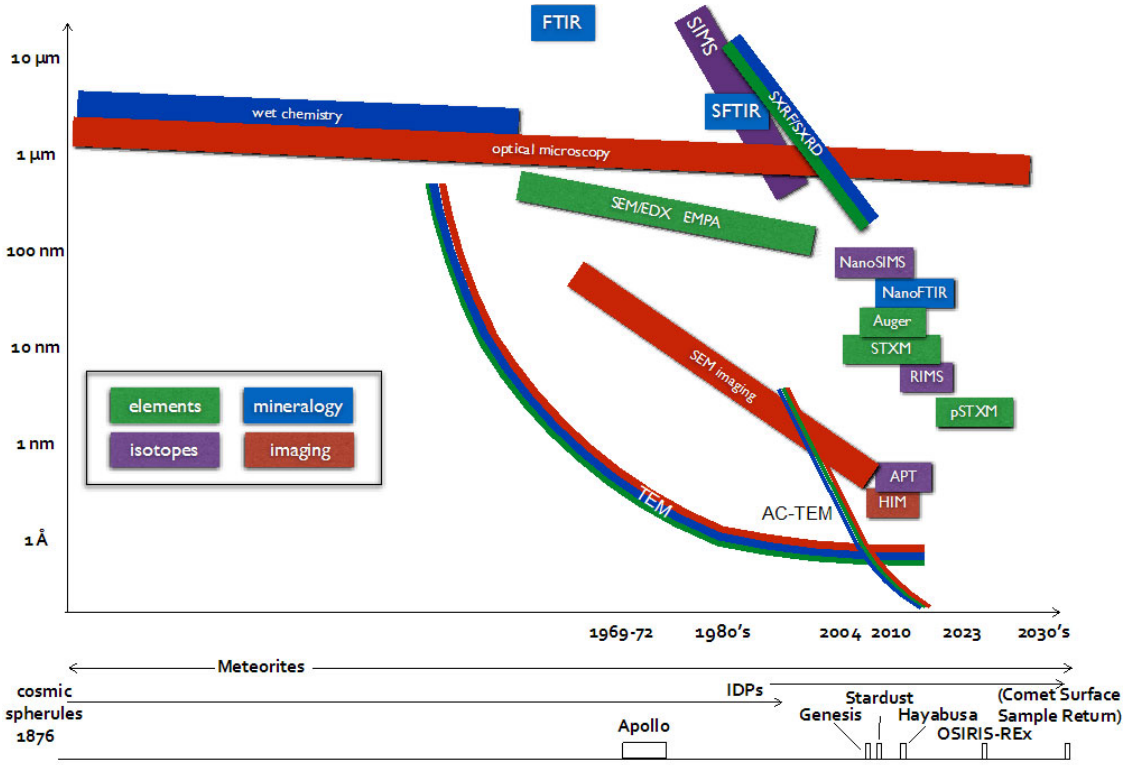

Figure 1.6: Illustration of the advances in spatial resolution of various microanalytical techniques and in parallel the progression of the sample return space missions (from Westphal et al., 2016).

Among these techniques, IR microspectroscopy is a powerful tool as it is non-destructive; able to characterize molecular vibrations and phonons, and in particular to detect both the mineral and the carbonaceous phases. It also allows hyperspectral imaging studies, useful to visualize the spatial distribution of different components, their assembly and thus to deduce

constraints about their formation and their evolution in the young Solar System. However, the analysis of different forms of extraterrestrial organic materials is challenging, because of their relatively low abundance with respect to other components (Le Guillou et al., 2014).

So far, IR microspectroscopy has been performed, at diffraction limited spatial resolution (2.5-15 μm in the mid-IR) using synchrotron radiation sources (e.g. Brunetto et al., 2011) or using Focal Plan Array (FPA) imager for rapid acquisition. FPA imaging systems allow high-throughput analysis of large samples with resolutions close to the diffraction limit, while synchrotron radiation microspectroscopy performed in confocal mode is better suited for obtaining information at the diffraction limit at specific locations.

The use of FPA matrix detectors on IR microspectroscopy (see Yesiltas et al., 2014 for an application to meteorites) has triggered the development of FTIR microtomography (Martin et al., 2013; Quaroni et al., 2015). With the possibility to perform IR 3D analysis without destroying the spatial structure of the samples, we will have a deeper comprehension of the spatial correlation between organics and minerals, and we could bring new constraints about the formation and evolution of organic matter in a mineral context. Analysis on 3D structure with X-ray analysis could bring complementary information on porosity or information about shape and fracture at a lower scale (Tsuchiyama et al., 2014; Consolmagno et al., 2008) This is why by coupling IR and X-ray tomography, we could give a first powerful physical and chemical description of precious samples without destroyed their spatial structure.

To study the link between these two phases thanks to spatial correlation, preserving the spatial structure is very important and IR 3D analyzes on intact grains will represent a huge step to answer these questions. During this Ph.D. thesis, I have implemented a new setup to perform IR micro-tomography of precious extraterrestrial grains. This setup opens a new window for the study of the spatial correlations in 3D, getting free of some degeneracy of 2D analyzes.

1.5 Comparing laboratory spectroscopy with observational data

Another strength of infrared spectroscopy is that the data obtained in the laboratory are also comparable to the astronomical observations of the interstellar medium (ISM) and the primitive Solar System's small bodies (asteroids, comets, TNOs) (Bradley et al., 1999; Brunetto et al., 2011; Merouane et al., 2012; Vernazza et al., 2015). Infrared hyperspectral imaging is also widely used in planetary science. Imaging remote sensing spectrometers have been developed in the last decades, and these instruments have been successfully used on-board different exploration missions across the Solar System (e.g., de Sanctis et al., 2017, for a recent example on dwarf planet Ceres). Developments of miniaturized IR hyperspectral imaging instruments for in situ exploration of planetary surfaces have achieved tens of microns spatial resolution (Pilorget and Bibring, 2013).

The problem of space weathering

However, a direct comparison between laboratory spectroscopic data and remote sensing observations of small Solar System bodies is not so obvious, and the link between asteroids observation and extraterrestrial samples collected on Earth is still a matter of debate. It is quite hard to obtain a precise correlation between the different classes of asteroids observed in space and the typology of meteorites fallen on Earth. Many biases may affect the arrival of meteorites and their sampling. Moreover, some energetic processes can modify the surface of an asteroid and have to be taken into account when we perform surface observations. This set of processes is called space weathering (Fig. 1.7) and it includes cosmic ion bombardment, irradiation by solar wind and bombardment by micrometeorites of the interplanetary medium. The effects of such processes on the spectra of weathered materials and on the composition of the surface of asteroids can be studied in the laboratory thanks to experiments reproducing this process on meteorites (Brunetto et al., 2007; Lantz et al., 2017, for simulation of solar wind, and Hiroi et al., 2006 for simulation of micrometeorites bombardment). In these experiments, the effects of energetic processes are typically studied by measuring the spectra on large areas (above 1 mm) of individual meteorites before and after ion or laser irradiation.

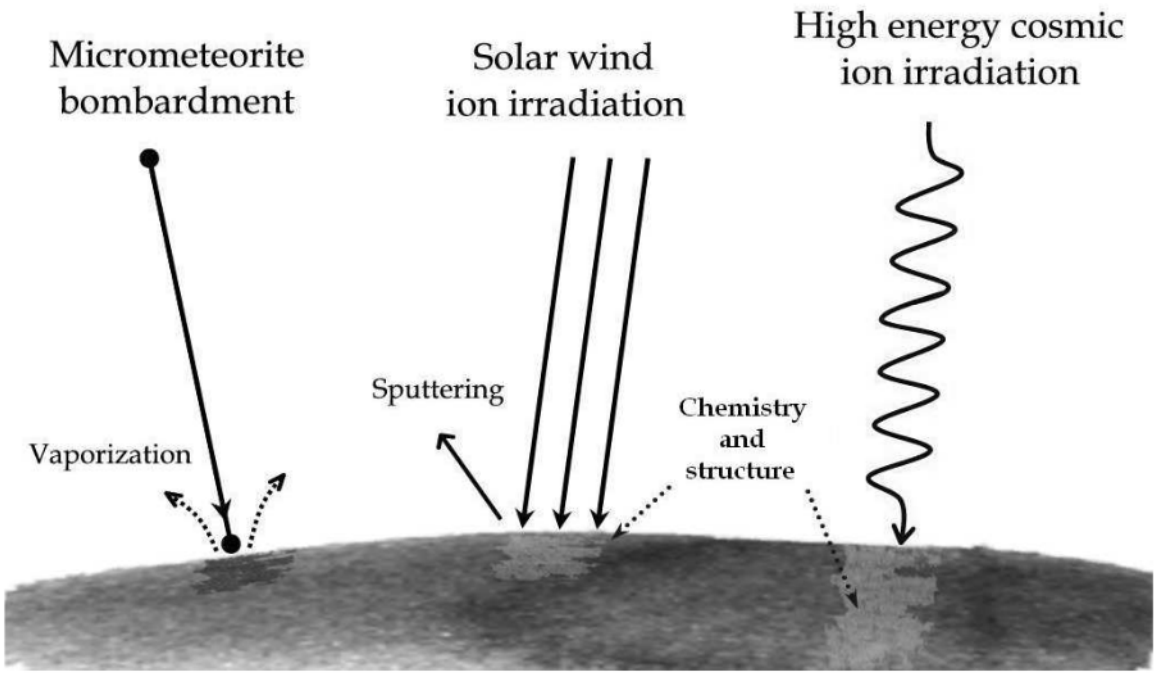

Figure 1.7: A schematic view of the space weathering processes (from Brunetto (2007)).

With the development of hyperspectral imaging analyses at the micron-scale, new information can be obtained to better understand the effects of energetic processing on individual microscopic grains. These new analyses can also be used to discriminate the spectral effects of the natural compositional heterogeneity of meteorites from those due to the specific response to space weathering of each component. Examples of analysis led during this Ph.D. thesis will be presented in Chapter 4.

To better constrain the link between asteroids and meteorites and understand the remote sensing observations of minor bodies' surfaces, the next step is to directly study asteroidal samples in the laboratory. This chance was offered for the first time by the Japanese Hayabusa mission as explained in the next section.

1.6 Study of asteroidal fragments in laboratory

The Hayabusa mission (JAXA) was the first one to collect and bring back an asteroidal sample to the Earth. Hayabusa-returned samples offer an excellent perspective for understanding the link between asteroids and samples available in the laboratory. A review on implications and main results of the mission was done by Tsuchiyama (2014) and I briefly summarize it below.

The mission visited the small (535 x 294 x 209 m) S-type asteroid Itokawa. Material coming from S-type asteroids are thought to be similar to ordinary chondrites. This class of meteorites is divided in three groups: H (high), L (low) and LL which are defined according to the quantity of iron they contain. Itokawa is probably similar to thermally metarmorphised LL5-6 chondrites as shown by ground-based observations (Binzel et al., 2001) and remote sensing images taken by the spacecraft itself (Abe et al., 2006). Moreover, Itokawa samples, examined after the return of the mission, allowed a direct validation of the link between S-type asteroids and ordinary chondrites.

Here I review the main steps of the mission and the sample collection and analysis procedure.

1.6.1 Presentation of the Hayabusa mission

May 9, 2003: The Hayabusa spacecraft was launched from the Earth

November 25, 2005: The Hayabusa spacecraft touched down on the surface of asteroid Itokawa. When the spacecraft touched the asteroid, some grains were thrown and sent to the collect room B (see Fig. 1.8). Then the lander bounced due to the low gravity of the asteroid and touched down the asteroid a second time. The rotational cylinder turned to block the entry of the room B and let the entry of the room A free. The second set of samples was then collected in the room A during the second touch down (Nakamura et al. 2011). In total, more than 2000 particles have been collected.

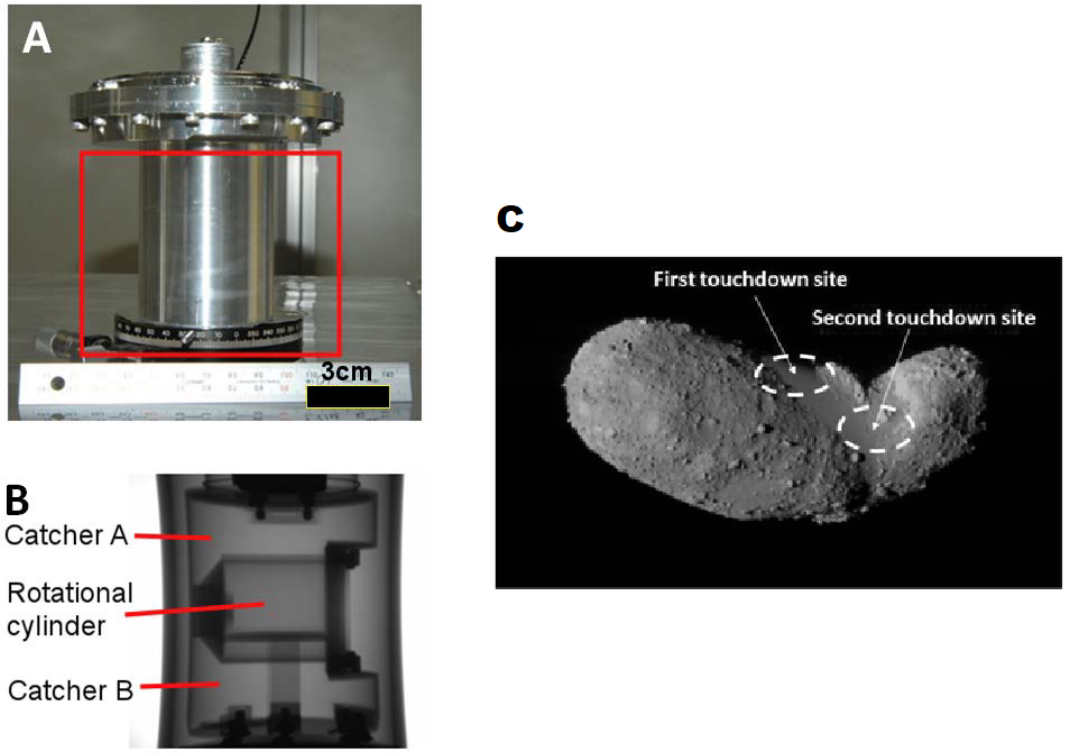

Figure 1.8: A and B: Photo and scheme of the collecting rooms on the spacecraft (from Nakamura et al., 2011). C: representation of the two touched down sites on Itokawa (modified from a JAXA image).

January 2007: The Hayabusa spacecraft departed asteroid Itokawa and begun its return trip to Earth 3 months later.

June 13, 2010: The Hayabusa spacecraft released its 40-centimeter-wide capsule before harmlessly burning up in Earth's atmosphere. The capsule parachute down in South Australia, where ground teams recovered it the following day.

Once the capsule was back on Earth, the preliminary analysis for characterization of the collection could start. Two methods were used to collect particles from the capsule (Nakamura et al. 2011): a first one consisted of sweeping the inner wall of room A with a Teflon Spatula and the second one was to collect particles that fell onto a silica glass plate after physically taping the catcher. Particles from 30-80 micrometers in size were collected by this second method and analyzed during the campaign of initial examination.

Sequence of analysis on the collected grains

A part of these particles was used to bring answers about asteroid surface processes and space weathering, and the rest was sequentially analyzed by progressively more and more destructive methods (see Fig. 1.9; Nakamura et al., 2011; and Tsuchiyama et al., 2013a).

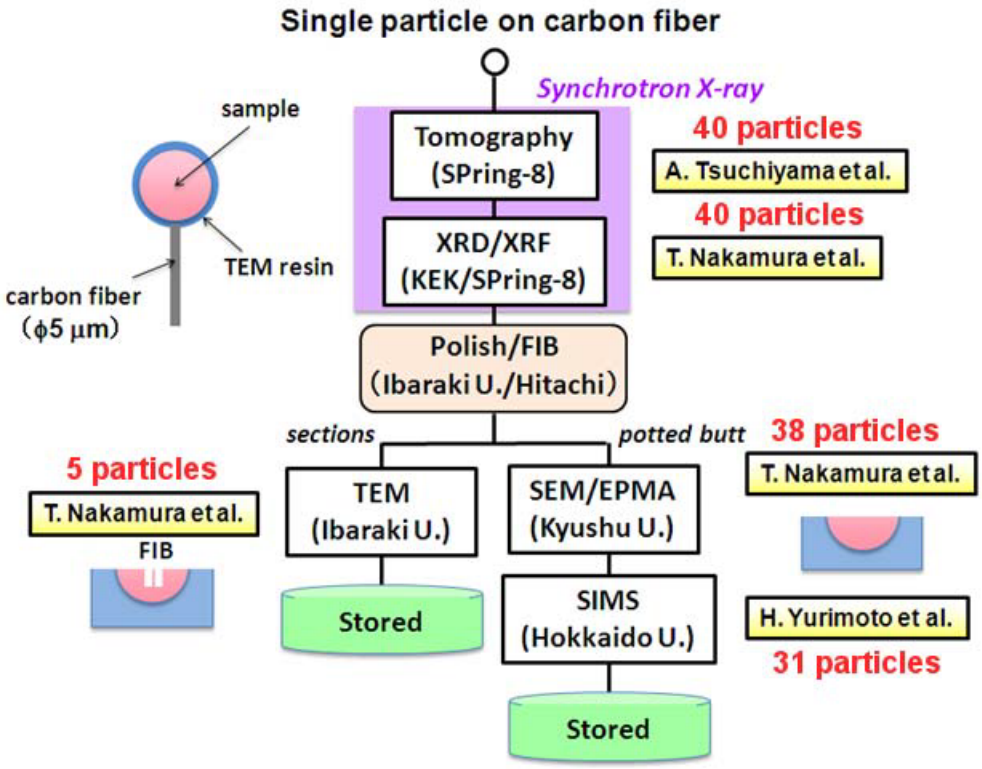

Figure 1.9: Protocol of analysis of the Hayabusa grains after the extraction (from Nakamura et al., 2011)

First dual energy X-rays micro-tomography with synchrotron was used to obtain three-dimensional structures of the samples (Tsuchiyama et al., 2011, 2013a). Examples of slices obtained by X-CT (X-rays Computed Tomography) tomography at 7 keV (see Chapters 5 and 6) are shown in Fig. 1.10. This image corresponds to the X-ray linear attenuation coefficient of the material, and the difference in contrast allows the identification of mineral phases. We can observe structural heterogeneity between samples. Grains RA-QD02-0038 (panel C) and RA-QD02-0042 (panel D) are monomineralic grains, grain RA-QD02-0031 (panel A) presents a higher diversity. Finally, grain RA-QD02-0048 (grain B) is made of fine silicate grains with more heterogeneous composition. This last grain is representative of 10 % of the

collected samples and the difference in the structure is a sign of lower thermal metamorphism.

Moreover, X-CT tomography brings information about physical properties such as structure and porosity. For Hayabusa grains, the porosity evaluated with X-CT tomography varies between 1 to 11 % with a mean at 1,4 % (Tsuchiyama et al., 2011). This value is lower than the one for LL chondrites: 8.2 +/− 5.5 % (Consolmagno et al., 2008). The difference can be explained by a size effect: most porosity in LL chondrites is in cracks between grains and these cracks are not represented in the study of single Hayabusa grains.

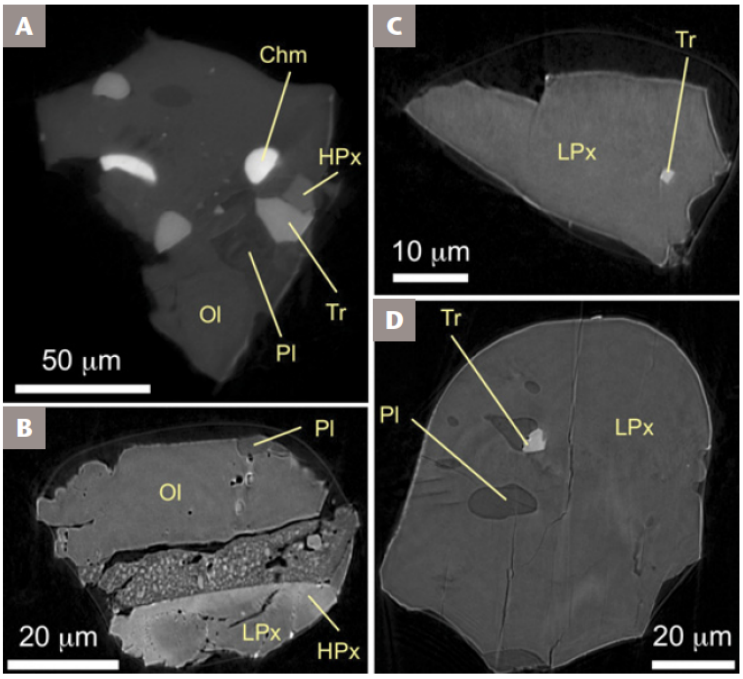

Figure 1.10: Examples of slices obtained by X-CT tomography at 7 keV of grain RA-QD02-0031 (panel A), grain RA-QD02-0048 (panel B), grain RA-QD02-0038 (panel C) and grain RA-QD02-0031(panel D) (from Tsuchiyama et al., 2014).

Then, X-ray diffraction (XRD) with a synchrotron beam (Nakamura et al., 2011) was led to identify mineral phases precisely. The diffraction peaks of X-ray beam are produced by constructive interferences of a monochromatic beam diffused at specific angles by the structure of the crystalline planes of a sample. The presence of peaks at given angles, as shown in Fig. 1.11, allows to characterize the crystalline structure of the matter and to determine its mineralogical composition. This technique is very sensitive to crystalline phases and enables detection of even minor phases (concentration above 1 %). The main drawback

of this method for the studies of extraterrestrial samples is that it cannot give any indication on amorphous phases. Moreover, the measurement spot (around 50 μm) is either similar or greater than the majorities of grains analyzed, so it gives a global indication about the mineral composition but no indication on spatial distribution of the different phases.

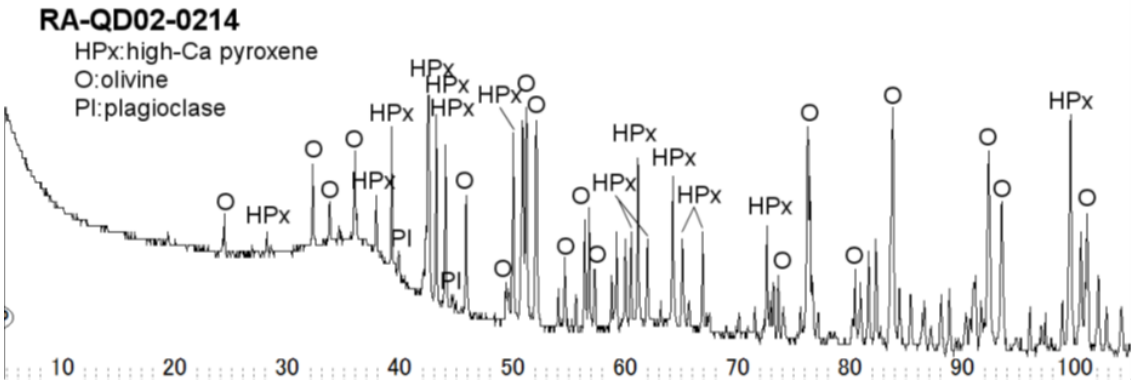

Figure 1.11: example of XRD data of grain RA-QD02-0214 with detection of Ca-rich pyroxene, plagioclase and olivine (kindly provided by T. Nakamura)

The three-dimensional distribution of the mineral phases coupled with precise identification of the minerals can provide critical information to select where a particle should be sectioned (by FIB for instance), to ensure that the most interesting slices are correctly selected for subsequent destructive analyses. X-CT and X-RD are then very complementary methods.

Main implications

The following table shows a list of the main minerals observed in Hayabusa grains and LL chondrites. The abundance of each mineral was obtained by X-CT tomography (Tsuchiyama et al., 2013a), and the chemical identification comes from Nakamura et al. (2011 and 2012). Overall, the abundance and chemical compositions of minerals are consistent with those measured on LL chondrites. The study of oxygen isotopic composition of pyroxene, olivine, and plagioclase performed by Yurimoto et al., (2011) confirmed the link between the Hayabusa samples and the LL chondrites. The small differences between these two populations could be explained by the few numbers of Itokawa grains analyzed and consequently by insufficient statistics.

Mineral	Abbreviation	Formula	Crystal system[a]	Mineral abundance (wt%)[b]		Chemical composition[c,d]	
				Itokawa	LL4-6	Itokawa	LL4-6
Olivine	Ol	$(Mg,Fe)_2SiO_4$	Orth	67.2	51.1±2.2	Fa28.6±1.1	Fa26–32
Low-Ca pyroxene	LPx	$(Mg,Fe)SiO_3$	Orth, Mono	18.1	21.1±2.0	Fs23.1±2.2 Wo1.8±1.7	Fs22–26
High-Ca pyroxene	HPx	$(Ca,Mg,Fe)SiO_3$	Mono	2.6	7.4±0.9	Fs8.9±1.6 Wo43.5±4.5	
Plagioclase	Pl	$(Na,Ca)Al(Al,Si)Si_2O_8$	Mono, Tri	8.5	9.7±0.8	Ab83.9±1.3 Or5.5±1.2	
Troilite	Tr	FeS	Hex	2.9	5.7±1.5		
Kamacite	Kam	α-(Fe,Ni)	Cub	0.0	3.5±2.0	3.8–4.2 wt% Ni 9.4–9.9 wt% Co	~5.0 wt% Ni 1.4–37 wt% Co
Taenite	Tae	γ-(Fe,Ni)	Cub	0.5		42–52 wt% Ni 2.0–2.5 wt% Co	
Chromite	Chm	$FeCr_2O_4$	Cub	0.1	1.6±0.1		
Apatite	Cp[i]	$Ca_5(PO_4)_3(F,Cl,OH)$	Hex	0.1			
Merrillite		$Ca_9NaMg(PO_4)_7$	Tri				

Figure 1.12: Minerals in Itokawa particles and in LL 5-6 chondrites: abundance and composition (from Tsuchiyama, 2014).

Moreover, particles show an almost homogeneous chemical composition, which indicates that these samples have been thermally annealed and are similar to LL5-6. The maximum temperature undergone by minerals containing both Ca-poor and Ca-rich pyroxene is about 800 degrees (Nakamura et al., 2011). Some of the grains, the 10 %s similar to the one shown in panel B of the Fig. 1.10, have undergone lower thermal alteration and are more similar to LL4.

Concerning organic matter, even if organic materials have been actively searched for (Kitajima et al., 2011; Naraoka et al., 2012), they have not been detected so far.

1.6.2 New sample return missions to carbonaceous asteroids

The possibility to perform non-destructive laboratory-based micro-FTIR hyperspectral imaging will be very important in the coming years. Sample return missions Hayabusa2 (JAXA) and OSIRIS-REx (NASA), will collect precious samples on primitive asteroids rich in carbonaceous materials (and probably in water) and will bring them back to Earth (in 2020

for Hayabusa 2 and 2023 for OSIRIS-REx) to be studied in the laboratory, combining various analytical techniques. The mains goals of these missions are to study primitive organic matter and to question the role of water and its effects on primitive materials. Finally, the study of both fine and coarse grains could bring answers about how the planets were created through the collision, destruction and combination of the planetesimals.

With the mission Hayabusa2, the JAXA plans to bring back samples smaller than the centimeter, made of both inorganic and organic matter and coming from both the surface and the sub-surface. They will try to collect between 10 and 1000 mg of extra-terrestrial materials. The grains collected will be very precious and a curation plan has been prepared very carefully by the JAXA. They will collect as much information as possible without contaminating or destroying the samples. As a non destructive technique, IR is interesting and the JAXA team plan to install an IR imager in the clean rooms which are going to serve for the curation of samples.

IR tomography on these grains can provide precious information about the organics and hydration inside the samples. In particular, the mineral context and the organic composition can be characterized simultaneously. In the sequence of analysis, micro-FTIR hyperspectral imaging can provide a first, powerful non-destructive characterization of whole fragments, to identify areas of interest and provide useful information before subsequent destructive analysis. Coupled with X-ray Tomography and XRD, physical and chemical characterization of precious grains can be obtained.

1.7 Presentation of this work

In this Ph.D. thesis, I explore the spatial relationships (both in 2D and in 3D) between the mineral and the organic parts on extraterrestrial materials thanks to the development of the FTIR hyperspectral imaging. More specifically, I implement a new micro-imaging setup to measure the FTIR micro-tomography of micrometric extraterrestrial samples. The goal is to contribute to a better knowledge of the relationship between minerals, water and organics, to better constrain the formation and the evolution of the organic matter during

post-accretional processes.

After a brief explanation about IR spectroscopy and description of our setup, I will detail in Chapter 3 the results of the analyses in 2D at the micron scale on two different fragments of the Paris meteorite (one of the most primitive carbonaceous chondrites), supported by Raman and SEM-EDS measurements. The first fragment is small (tens of microns) and crushed in a diamond compression cell. For this sample, the micro-FTIR analyses are performed in transmission with two setups, an imaging microscope with a matrix detector using a thermal source and a system using a single point detector coupled with the synchrotron source at the SOLEIL synchrotron facility (SMIS beamline).

We obtain the spatial distribution of chemical/mineralogical components. We confirm at a larger scale (10 μm) the presence of hydrated amorphous silicates observed at a smaller scale (1 μm). Based on the relative abundance of different minerals (hydrated amorphous silicate, olivine, diopside and serpentine) we propose a sequence of aqueous alteration. Considering the spatial correlation of minerals with organic matter, we discuss the effects of aqueous alteration on the organic matter in bulk. In particular, we detect an increase of the CH_2/CH_3 ratio in the altered zone and present the possible scenarios that lead to the observed chain length shortening/cracking of hydrocarbons.

The second fragment of the Paris meteorite studied here is a larger chip (mm-sized). A multi-analytical study on this fragment is currently coordinated by D. Baklouti (IAS) and S. Della Negra (IPNO). My contribution to this study was micro-FTIR mapping of the surface of the sample in reflexion geometry (comparable to remote sensing observations of asteroids) and the main results will be presented in the second part of Chapter 3.

As mentioned above, laboratory and remote sensing data are not always directly comparable, because asteroid surfaces are continuously modified by energetic processes, impeding us to decipher their composition from their spectra. These effects, widely studied for the Moon and bright asteroids, are still poorly known in the case of the dark, carbon-rich asteroids. In Chapter 4, I will show how micro-FTIR mapping can be used to study the space weathering effect in the heterogeneous matrix of carbonaceous chondrites, and in particular

I will show that the new laboratory results obtained at IAS suggest an original spectroscopic method to detect irradiated areas that may be used by missions visiting carbon-rich asteroids.

Finally, I will show my results on the implementation of a new 3D hyperspectral micro-tomography setup, to access structural information on intact samples thanks to the Focal Plane Array detector. We perform IR 3D hyperspectral micro-tomography at SMIS to reconstruct the sample at different wavelengths and to reconstruct the spatial distribution of the different components. This allows studying the 3D spatial correlation between the meteoritic organic and mineral phases at scales down to ≈ 3 μm. Moreover, X-rays tomography is also performed on the same particles, at the PSICHE beamline of the SOLEIL synchrotron, to obtain complementary information about the physical properties of the grains (shape, fractures, porosity). By combining X-ray and FTIR data, we obtain a physical-chemical description of precious grains in a non-destructive way. All the setup used to perform and combine IR and X-rays analyses will be presented in Chapter 5.

We confirm the feasibility of the new analytical technique on five precious grains brought back by the Hayabusa mission, kindly provided by the JAXA curator and previously analyzed in Japan by A. Tsuchiyama and T. Nakamura by X-CT and XRD. The results of the 3D analysis will be presented in Chapter 6.

Performing FTIR micro-tomography on extraterrestrial samples rich in organic matter is an essential step in view of the sample return of dust particles from carbonaceous asteroids Ryugu by the Hayabusa2 mission and Bennu by the OSIRIS-REx mission. In the sequence of analyses, micro-FTIR 3D spectral imaging coupled with X-rays tomography can provide a first, powerful non-destructive characterization of whole grains, to identify areas of interest and provide useful information before subsequent destructive analysis. To study the feasibility to perform IR tomography on carbonaceous material, we also present the first 3D infrared reconstruction of three fragments of the Paris meteorites combined to X-ray micro-tomography. The 3D study of these particles and the conclusion about the spatial relationship of their components will finally be presented in Chapter 7.

Conclusions and both experimental future improvements and scientific perspectives will

be summarized in Chapter 8.

Chapter 2

Infrared and Raman spectroscopy

Contents

During this Ph.D. thesis, I have used mainly infrared (IR) spectroscopy to analyze our samples. In this chapter, I am going to explain the principles of Fourier Transform infrared (FTIR) spectroscopy and how I processed the data. I will also show the principles of Raman spectroscopy, a tool complementary to FTIR.

2.1 FTIR spectroscopy principle

Infrared spectroscopy is a non destructive technique used in this study to identify the chemical components present in a sample.

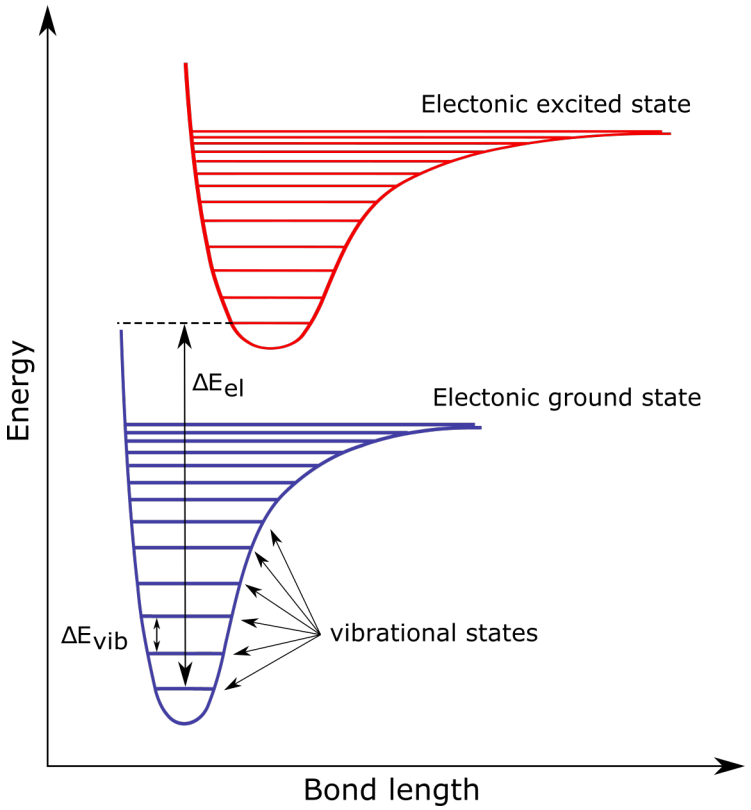

Figure 2.1: Energy level diagram.

A molecule is a set of atoms connecting through chemical bonds which can be modeled by quantum oscillators. The classical vibrational frequency for a diatomic molecules is given by :

$$\nu = \frac{1}{2\pi}\sqrt{K(\frac{1}{m_1} + \frac{1}{m_2})}, \tag{2.1}$$

with K the force constant of the bond and m_1 and m_2 the masses of the two atoms. In the model of the quantum mechanical harmonic oscillator (see Fig 2.1), the energy of the vibrational level n is given by :

$$E_{vib} = (n + \frac{1}{2})h\nu, \tag{2.2}$$

with ν the classical vibrational frequency.

If we send an electromagnetic wave onto a molecule, it can absorb the energy of the photon and reach an excited state (see Fig. 2.1). The quantity of energy needed to reach an excited level is specific to the nature of the transition, i.e. electronic, vibrational or

rotational, where $E_{el} > E_{vib}$. Vibrational transition energies fall into the infrared energy range. More specifically, the fundamental vibrational transitions of most organic molecules are characteristically in the mid infrared (MIR), between 2-15 μm. In reality, the energy of vibrational transitions is influenced by many factors that provide information of the sample (e.g. chemical composition, bond order, symmetry, chemical environment), while the intensity of the absorption provides information about the concentration or abundance of the respective vibration through the Lambert-Beer formula:

$$A = \epsilon \cdot c \cdot l, \tag{2.3}$$

where A represents absorbance, ϵ is the molar extinction coefficient, c is the concentration and l is the optical pathlength.

Most measurements in this work were done in the 2.5 μm $< \lambda <$ 11.8 μm wavelength range and I will use the wavenumber scale $[cm^{-1}]$ given by:

$$\nu = \frac{10000}{\lambda}, \tag{2.4}$$

corresponding to 4000-850 cm^{-1}. In this spectral range we can detect stretching and bending modes of the molecular bonds active in IR (i.e. those whose vibration implies a modification of the dipole moment).

FTIR measurements can be done in reflection and in transmission geometries. In case of reflection, only the near surface region of the sample would be analyzed, however, in our case we are interested by the internal composition and 3D structure of the samples the majority of measurements done during my Ph.D. thesis have been performed in transmission geometry.

For each sample, we measure the intensity of the light after passing thought of the sample and then the transmittance T is given by :

$$T = \frac{I}{I_0} \tag{2.5}$$

with I_0 as the intensity of the incident light and I as the intensity of the light transmitted through the sample. Then we can calculate the optical depth τ and the absorbance A with :

$$\tau = -\ln T \quad and \quad A = -\log T \tag{2.6}$$

For some specifics energy, we can detect absorption features in the spectra. Once we have identify the bonds responsible of the absorption band, thank to the literature, we can calculate the columns density N which represents the number of oscillators per cm^2, with Ax the band strength (d'Hendecourt and Allamandola, 1986) :

$$N = \frac{\int A d\nu}{Ax} \tag{2.7}$$

In the case of FTIR spectroscopy, we send a polychromatic light into a Michelson interferometer. The interferometer consists of three main elements: a fixed mirror, a moving mirror and a beamsplitter. The beamsplitter divides the incoming beam to two parts and sends it into each interferometer arm. The moving mirror creates a varying path difference between the two beams. Upon their return, the beams interfere and propagate towards a detector through the sample. In our case, the detector is either an MCT (Mercury-Cadmium Telluride) or a FPA (Focal Plane Array, a matrix of MCT detectors) cooled by liquid nitrogen. The signal is collected as the function of the optical pathlength difference between the fixed and moving mirrors (see Fig. 2.2) and produces the raw data, called interferogram. With a simple Fourier transformation one can obtain the infrared spectrum, hence the name FTIR spectroscopy.

In the case of FTIR microscopy, the light is sent through an infrared microscope focused by reflective objectives on the focal plane, where the sample is usually placed.

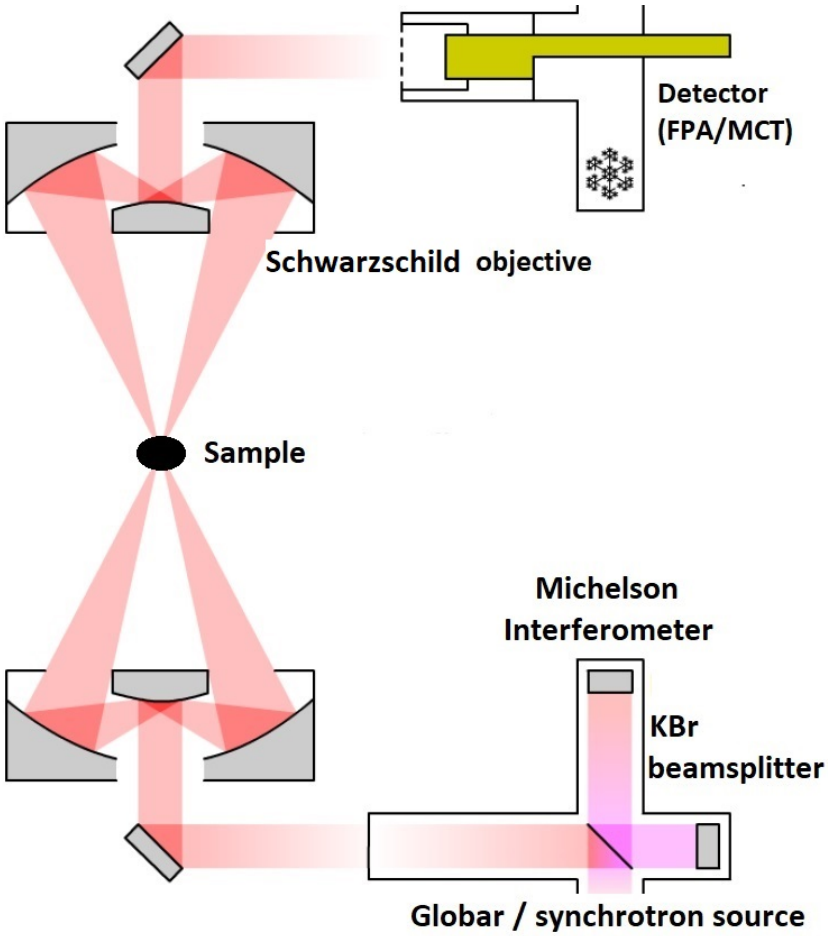

Figure 2.2: Scheme of a FTIR microscope (adapted from Orthous-Daunay, Ph.D. thesis).

Compared to a dispersive spectrometers, interferometry has the advantage of being quicker, because all the wavelengths are analyzed at the same time (Fellgett's advantage), higher throughput, since FT instruments don't use slits or pinholes (Jacquinot's advantage), better wavelength accuracy (Connes' advantage). Spectrometers are usually purged with dry nitrogen to remove contamination by water and carbon dioxide present in the atmosphere. Our instruments are not calibrated radiometrically, which implies that any measurement performed on a meteorite sample must be ratioed to a background (or reference) measurement on a standard or on the sample substrate. This allows to take into account the spectral response of the different elements (source, beamsplitter, mirrors, detector response, etc.) and to obtain the relative transmittance or reflectance of the sample.

When a sample is placed on top of a diamond window (see Chapter 3), the spectra are divided by a reference spectrum acquired on a clean area of the diamond window. In the case

of 3D preparations (sample attached to a needle), the reference spectra are acquired simply by removing the sample from the field of view, as no substrate window is used in this case. In the case of reflection measurements on thick samples (see second part of Chapter 3, and Chapter 4), a gold foil was used to collect the background.

The detection of small spatial features inside a sample is limited by the Rayleigh criteria and the spatial resolution d is given by the Abbe formula :

$$d = \frac{0.61 * \lambda}{N.A.} \tag{2.8}$$

with N.A. the numerical aperture of the objective. The user can choose others parameters as the spectral resolution and the number of spectra collected for each measurement. A high spectral resolution allows to detect small bands better but also requires more time.

2.2 Presentation of the FTIR setup at SMIS in SOLEIL

FTIR measurements in this work were done at the SMIS infrared spectromicroscopy in the SOLEIL synchrotron. SMIS provides a very bright source in the MIR spectral range exploiting synchrotron and edge radiation emission from the SOLEIL bend magnet. Due to its low divergence and small source size, synchrotron infrared radiation can be very efficiently focused and thus very high brightness beams can be realized. As shown in Fig. 2.3, by using the synchrotron radiation, it is possible to detect a much brighter signal than using conventional Globar sources, especially for small apertures. At SMIS, the synchrotron IR radiation can be injected into different microscopes and focused onto micrometer-sized samples.

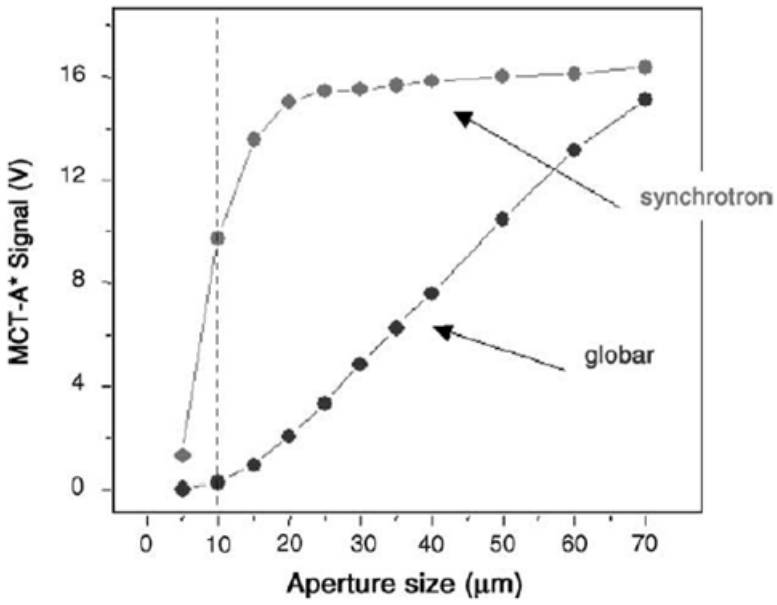

Figure 2.3: Comparison between the signal obtained with a Globar source and by using synchrotron radiation (from Miller et al., 2005).

In my thesis, I mainly used two setups available at SMIS, based on FTIR micro-spectroscopy. Below, I describe the different specifications used for each setup.

A first series of infrared raster maps (in transmission or reflection mode depending on the sample) were collected using a Thermo Scientific Continuum XL microscope equipped with a 32× objective (numerical aperture 0.65) coupled with a Nicolet 5700 FTIR spectrometer and illuminated by the synchrotron IR source. Typically, I used 6×6 μm^2 apertures, a spectral resolution of 4 cm^{-1} and a single-element MCT detector in the 650-4000 cm^{-1} spectral range (see Fig. 2.4).

Figure 2.4: Photo of the Continuum XL microscope with the MCT detector.

I also collected IR imaging data with an Agilent (model Cary 670/620) micro-spectrometer acquired by IAS and SOLEIL installed at the SMIS beamline in 2016. Typically (and especially for tomography), I used a 25× objective (numerical aperture 0.81) amplified by a high magnification system (providing additional magnification of 2.5×) placed in front of a 128x128 pixels FPA detector, and I obtained a projected pixel size of 0.66 μm^2 on the focal plane (see Fig. 2.5). The spatial resolution limited by diffraction for the whole investigated MIR spectral region.

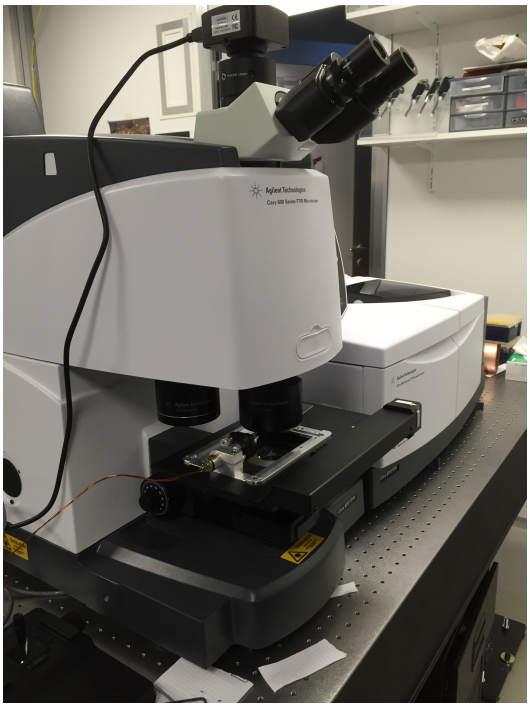

Figure 2.5: Photo of the Agilent FPA microscope.

In the case of the single element MCT detector, a point to point mapping is performed to cover a chosen area on the sample. Typical mapping measurements over an area of 80×80 μm^2 with 1024 scans per spectrum lasted about 200 minutes. In the case of FPA detector, the whole image of the FPA matrix is projected on the focal plane, providing field of views of 84×84 μm^2 using the above-mentioned optics and settings. All spectra are thus collected simultaneously without moving the X-Y stage of the microscope and we can directly image the sample with much shorter acquisition time (typically about 20 minutes for 1024 scans).

Using these two systems I have studied the localization and spatial correlation of the different components in the extraterrestrial samples.

2.3 Data analysis

In this section I describe some general procedures I used for data analysis in my thesis.

Given the high number of measured spectra, a point by point analysis would be extremely

time consuming. Therefore, we isolated spectra with meteoritical signature, eliminating all the points of the substrate or empty pixels around the sample for the subsequent analysis. The chemical and mineral components of the samples were thus detected by three methods:

1. A first inspection of the IR vibrational bands observed in the average spectrum of the whole sample revealed the main components. We then traced spectral maps revealing the distribution of the main components observed in the average spectrum such as amorphous silicate, carbonate, serpentine, aliphatic matter and hydrated phases. Several regions with different chemical compositions were determined from these maps.

2. Then, for each region found by the previous method, we identified smaller bands that are present in selected spectra of these regions.

3. Finally, for each spectra of the sample, we studied the spatial distribution of the minima of the spectral second derivative of the absorbance. This method allowed to easily remove the spectral continuum and to better detect minor components (for instance, we can better separate the contribution of aliphatic CH_2 and CH_3 stretching modes, and estimate their ratio, as shown in section 3.1).

Knowing the major and minor IR components present in our sample, for each spectrum we have extracted the abundance of each component. To do so, after subtracting the continuum, we calculated the area under the band of each component. Finally, the band strengths provided in the literature (Brunetto et al., 2011 and references therein) were used to deduce their column density (molecules/cm^2). We thus obtained spatial distributions of the main components abundances. For OH and CH bands, we normalized their areas to the silicate band area at about 1035 cm^{-1} (Matrajt et al., 2004), which can be used as a signature of the quantity of matter (Yesiltas et al., 2015).

We also studied the correlations by reporting the abundance of one component with respect to the abundance of another one for each spectrum. The dispersion of such a scatter plot indicated the correlation between the chosen components.

For most of the samples, we applied a PCA (Principal Components Analysis) denoising method to improve the spectral signal to noise ratio. In this method, we decomposed the signal in principal components and then we reconstructed the data keeping only the first 30 components with highest variance contribution to significantly reduce the noise (e.g Pedregosa et al., 2011). We can see the effect of the FPA denoising by comparing a spectrum before (blue) and after (red) the noise correction processing (see Fig. 2.6). This example is from a 2D spectral map of the Paris meteorite.

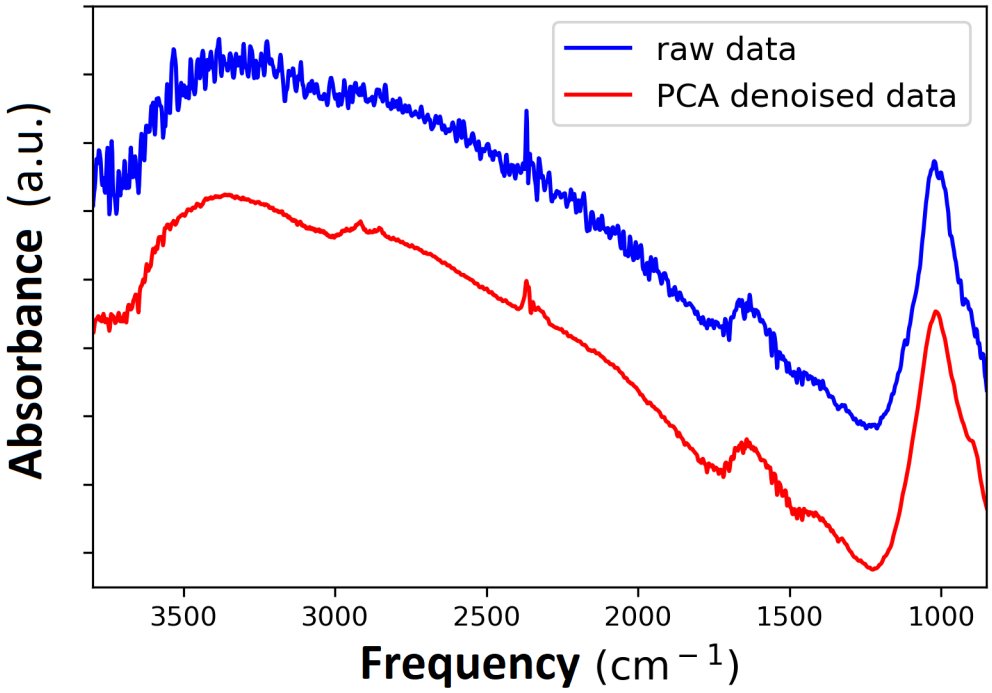

Figure 2.6: Comparison of spectra in transmission the same sample with (red) and without (blue) PCA denoising treatment.

2.4 Identification of the main IR bands of extraterrestrial samples

Infrared spectroscopy of extraterrestrial materials has been performed by many authors. An example taken from the literature of a typical spectrum of a meteorite sample is shown on Fig. 2.7. In my thesis, we mainly used band assignment from the articles of Matrajt et al.,

2005, Dartois et al., 2005 Salibusry et al., 1991 and Yesiltas et al., 2014 and 2015 to identify the different components present in our samples.

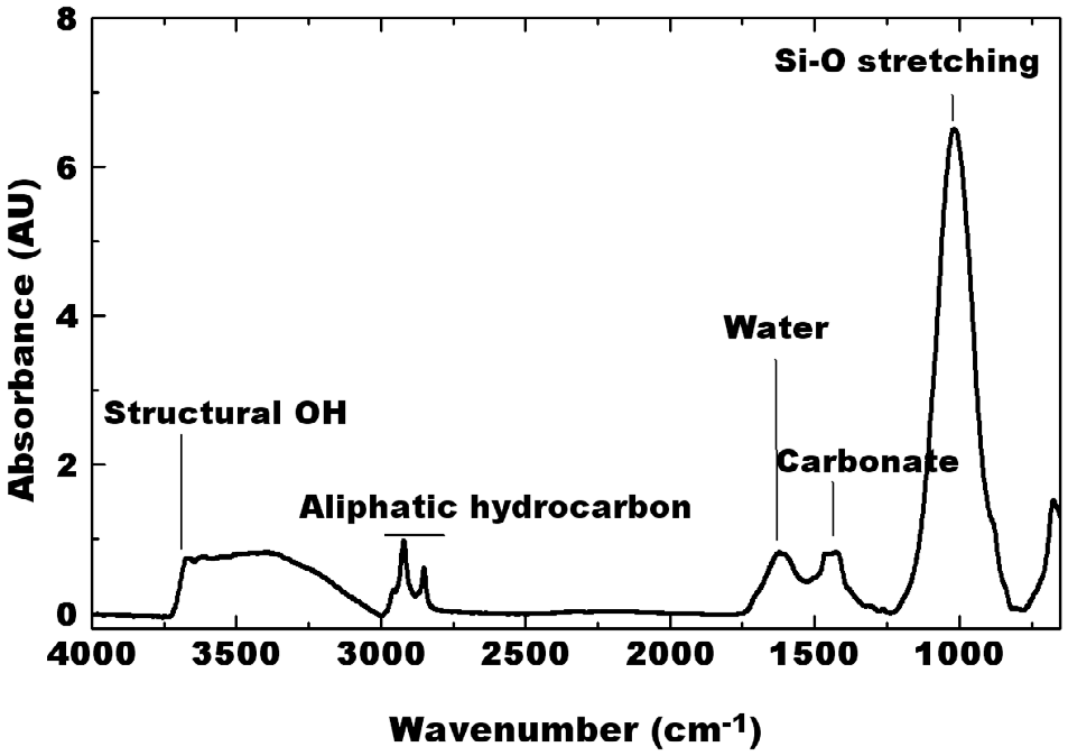

Figure 2.7: The spectrum of the Tagish Lake meteorite shows some features commonly observed the IR spectra of hydrated carbonaceous chondrites (from Matrajt et al., 2004).

With FTIR spectroscopy, we can characterize the aliphatic part of the organic matter. An interesting and significant signature is the one due to the C-H bond stretching region around 2900 cm^{-1}. We can distinguish two bands due to the CH_2 group, the symmetrical stretching at about 2855 cm^{-1} and the asymmetrical stretching at about 2930 cm^{-1}. We can easily observe the CH_2 bands in the spectra of samples which include long aliphatic chains: the longer the chain, the stronger the CH_2 band. The other two bands usually observed in this range are due to the vibration of the CH_3 functional group, located for instance at the end of the aliphatic chains. Again, we observe the symmetrical vibration at about 2865 cm^{-1} and the asymmetrical vibration at about 2960 cm^{-1}. A fifth, smaller band is sometimes observed, and usually attributed to a Fermi resonance around 2900 cm^{-1} . We are going to use a fit with 5 Gaussian profiles (Merouane et al., 2012, and references therein), to characterize and quantify the relative abundance of the aliphatic component (see Fig. 2.8).

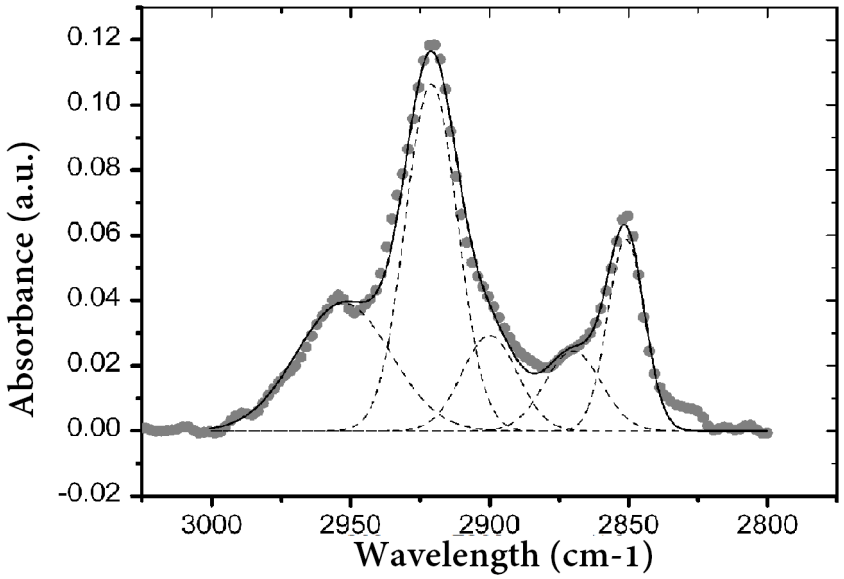

Figure 2.8: Example of aliphatic bands measured by FTIR on the Paris meteorite and of their spectral fit.

We can also observe the CH_2 and CH_3 bending at about 1413 cm^{-1} and 1326 cm^{-1}, respectively. Finally, the aromatic C=C bond have a signature around 1256 cm^{-1}, but these features are harder to see in the spectra of untreated meteorite fragments (i.e. without separation of the organics from the other components) and it is hard to perform a systematic study of them in our samples.

Concerning the mineral part, the main signature is usually the stretching of the Si-O band around 1000 cm^{-1}. The structure of this band gives indications about the structure of the silicate (see example in Beck et al., 2014). A broad band suggests amorphous silicates and in case we observe a structured band, we can concluded that the mineral part of our sample is at least partially crystalline. The precise positions of the peaks inside the spectral structure give specific identification on the nature and composition of the minerals.

Additionally, localized grains of other minerals are detectable in the IR spectra of meteoritic samples. For instance, carbonates and sulfates with signatures around 1410-1480 cm^{-1} for carbonates and 1150-1180 cm^{-1} for sulfates (these are often due to terrestrial alteration). Among other things, the exact position of the bands depends on the chemical nature of the cation.

2.5 Raman spectroscopy

2.5.1 Raman spectroscopy principle

While IR spectroscopy is an absorption technique, in the Raman effect one observes the inelastic scattering of a monochromatic photon. The energy diagram of the process is shown on Fig. 2.9. Briefly, monochromatic light, usually from a laser is sent on the sample and after a virtual excitation the system relaxes. Relaxation can end in the starting electronic and vibrational state $\Delta\nu = 0$ or with $\Delta\nu = \pm 1$ vibrational configuration. The majority of the backscattered light is at the same frequency (Rayleigh effect), but a small portion interacts with the sample and an energy loss/gain can be observed. The structure of the resulting spectrum depends on the vibrational energy levels of the studied material, hence Raman spectroscopy is also a vibrational spectroscopy technique, the electronic structure of the sample (resonant vs. non-resonant interactions) and potentially plasmonic or photonic field enhancement due to nanostructured samples or substrates. Comparing the energy of the scattered photon to the excitation frequency, we can talk about a Stokes, energy loss, or anti-Stokes process, energy gain (see Fig. 2.9).

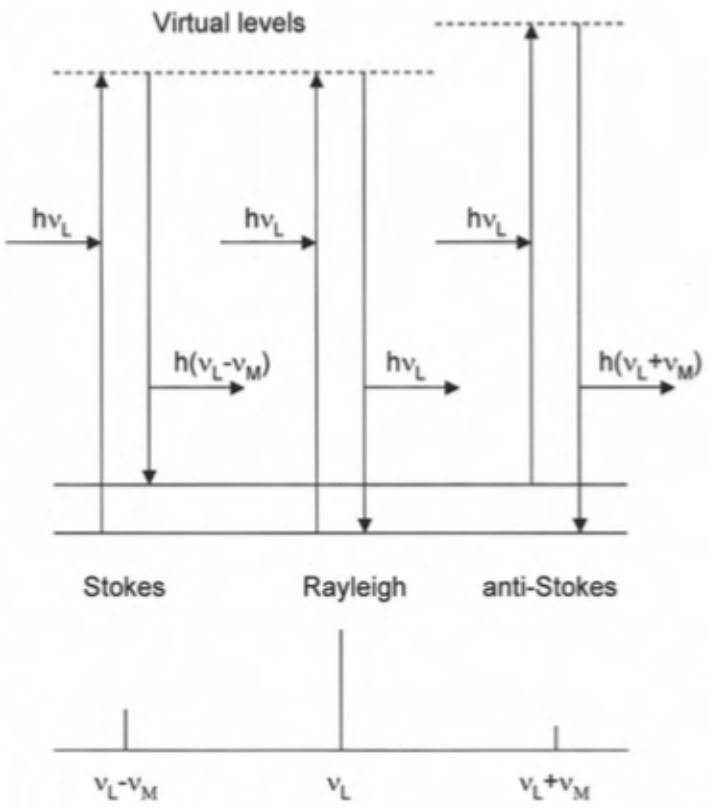

Figure 2.9: Principle of the Raman spectroscopy (from S. Wartewig in IR and Raman spectroscopy: Fundamental Processing) .

The Stokes and anti-Stokes spectra appear on the opposite sides of the laser excitation peak as shown on Fig. 2.10.

A vibration is active in Raman analysis only if it implies a change of polarizability. Moreover, if the virtual state corresponds to a real state, then there is a resonance with the initial state, and the signal of the band is very strong. We take advantage of this effect to easily observe the aromatic C=C band in the spectra of meteorites. Spatial resolution in Raman microscopy is usually higher than that of FTIR microscopy, because Raman is usually performed using a visible laser, i.e. shorter wavelength. Thus, we can obtain information below the micron scale, but unfortunately Raman only probes a shallow surface region of a sample and it is difficult to use it as a quantitative technique. FTIR and Raman spectroscopies are therefore highly complementary techniques.

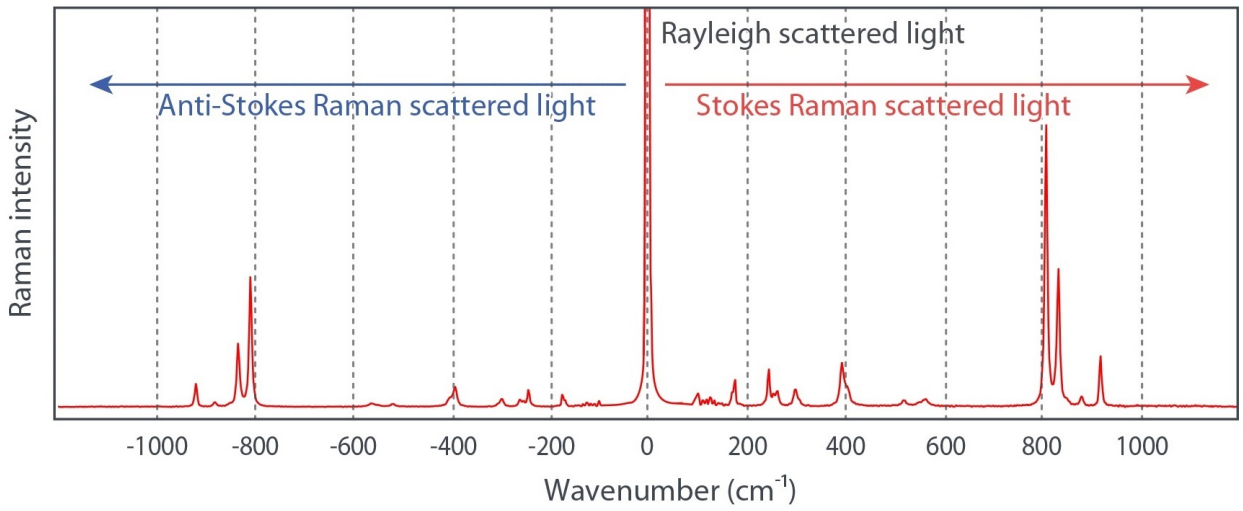

Figure 2.10: Stokes and anti-Stokes bands.

In this work, we performed Raman microscopy measurements to confirm the identification of some minerals of the meteorites and their accurate localization. We used a confocal Thermo Fischer DXR Raman microscope at SMIS. The laser excitation was at 532 nm and we used a power of 0.3 mW to avoid radiation damage. We used an Olympus UIS2 100X/0.90 NA LWD objective providing about 0.6 μm spot size.

2.5.2 Typical spectra of minerals and organics in meteorites

Organic characterization

For extraterrestrial samples, the stronger bands visible with Raman spectroscopy are those associated with different modes of the aromatic C=C bonds (Merouane et al., 2016, Rotundi et al., 2008, Busemann et al.,x 2007). Polyaromatic carbons show 5 bands in their Raman spectrum: the G band around 1580 cm^{-1} due to the vibration of an ordered graphitic matrix and 4 other bands D1, D2, D3 and D4 around 1350 cm^{-1}, 1620 cm^{-1}, 1500 cm^{-1} and 1200 cm^{-1}, due to different vibrations of a disordered polyaromatic matrix (Sadezky et al., 2005).

In the case of extraterrestrial samples, the structure of these carbonaceous materials is quite disordered, which induces a broadening of the bands, and we cannot separate all these modes: we usually detect a large G band (which is a mixture of the G, D2 and a part of D3

bands) and a large D band, which is a mixture of the rest of the D3 band and the bands D1 and D4 (Busemann et al., 2007, Rotundi et al., 2008). Fig. 2.11 presents a typical spectrum of the polyaromatic matter in meteorites. These very strong bands can mask the presence in the spectra of mineral signatures. The shape and position of these bands also give an indication about the structure of the matter and how crystalline/amorphous is the carbon skeleton.

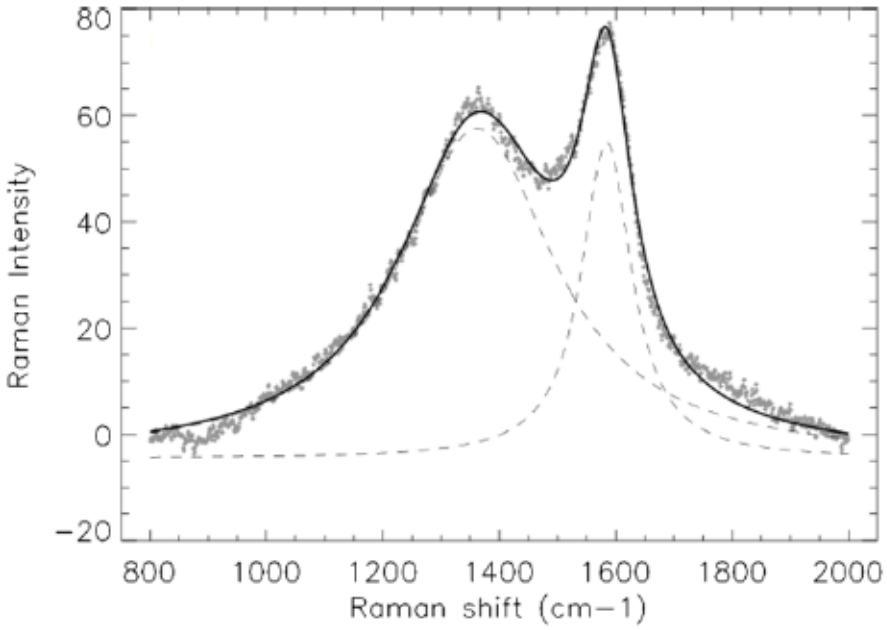

Figure 2.11: Typical D and G signatures of the aromatic organic moieties in the Raman spectrum of an Interplanetary Dust Particle (from Merouane et al., 2013).

The peak position and broadening of the Raman G-band are sensitive to ion irradiation, and therefore, are good indicators of irradiation processes (Busemann et al., 2007). They can be used to investigate a potential role of irradiation in determining the compositional and spatial heterogeneity of the aliphatics discussed above. Ion irradiation of carbonaceous materials in pure electronic (inelastic) energy loss regime induces little changes in the Raman spectra (Brunetto et al., 2009, Lantz et al., 2017), but it may strongly reduce the abundance of the aliphatic CHs (see Godard et al., 2011). A nuclear energy loss regime is necessary to produce a significant spectral modification of the G-band (Brunetto et al., 2009).

Inorganic characterization

Raman spectroscopy is also useful to detect silicates. The band position of a silicate mineral depends on the composition and on the abundance of different cations such as Ca, Fe, or Mg. Identifying bands at precise positions helps to identify mineral compositions and during this Ph.D., Raman measurements were done to confirm the identification and the localization of minerals inside our samples. We have for instance confirmed the presence of calcite, chrysotile, serpentine and olivine thanks to Raman analyzes.

2.6 Comparison of the three spectroscopy setups

One of the first major issues after the installation of the new imaging setup, was to characterize its response, especially diffraction. To do this we worked on a 2D sample which contained very localized and pure grains of carbonates. We analyzed these two grains with the two micro-FTIR systems described above and with the Raman microscope to characterize the effect of the diffraction.

With the Raman, we obtained the best spatial resolution of the three systems, since we use the shortest excitation wavelength (532 nm) and the highest numerical aperture (0.9).

In an infrared microscope such as those available at SMIS, the spatial resolution is given by the wavelength, the numerical aperture of the Schwarzschild objective and by the size of an adjustable aperture which is used to define the size of the infrared spot projected on the sample. Infrared microscopes are generally operated in a confocal arrangement with two apertures to eliminate diffraction caused by the first aperture and by inhomogeneity in the sample. The spatial resolution becomes further limited by the number of photons capable of passing through apertures hence the use of high brilliance sources such as synchrotron radiation sources or lasers. In theory, such systems may achieve spatial resolutions of the order of lambda.

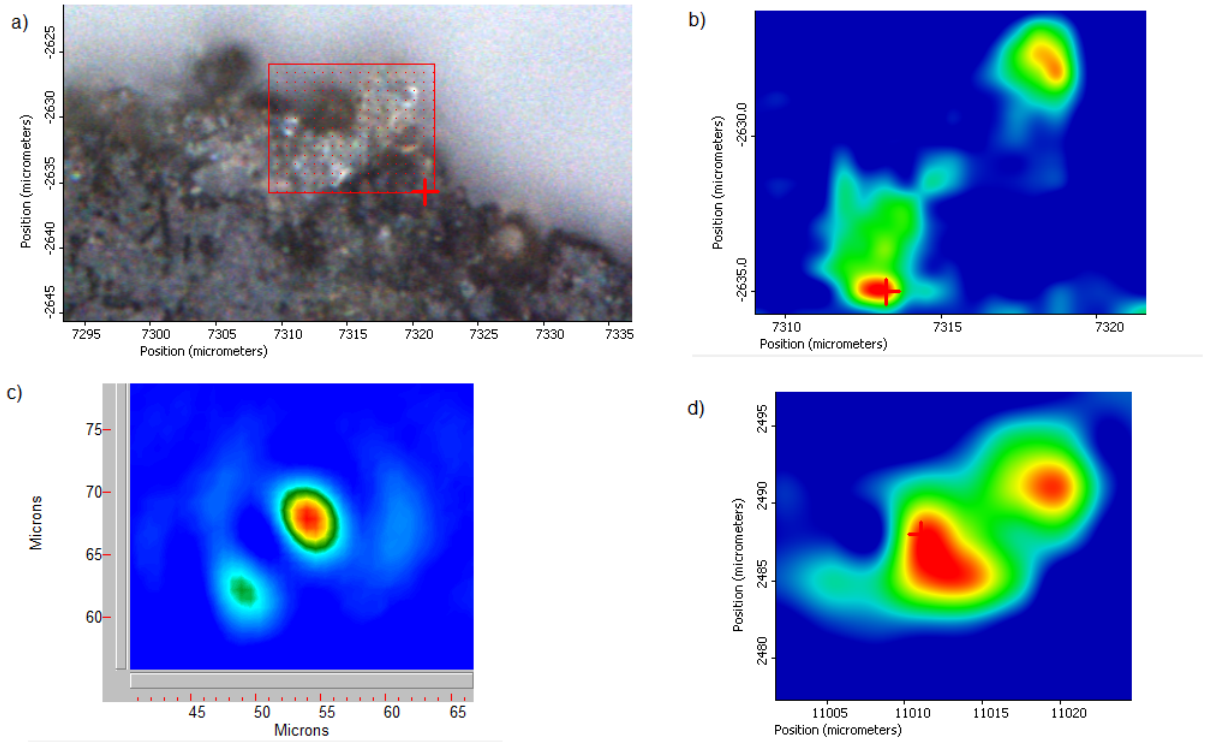

Figure 2.12: Comparison of two grains of carbonates observed with different setups: optical image (a) and maps of the same area obtained with (b) the Raman spectrometer, (c) the FPA, Globar source and (d) the single point MCT, SR source.

Comparing the chemical maps obtained with the three methods (see Fig. 2.12), we note that we can detect the two grains of carbonate with all three setups. The Raman analysis indicates that the lower grain is larger and more concentrated (Fig. 2.12 (b)), while with the synchrotron setup, the two grains appear to be almost the same size (Fig. 2.12 (d)). With the FPA, we can still observe the two grains but the upper one appears larger. It is due to the fact that this grain is located on the edge of our sample and is thus less affected by the diffraction from the surrounding silicate. Moreover, the ratio between the area under the carbonate band and the silicate one is higher in this spot in the case of the FPA setup than with the other setups.

The quality of a spectral image may be assessed by its contrast fidelity, and spatial resolution. As seen above, the infrared maps obtained on the Paris meteorite presented spatial distortions which were stronger with the FPA imaging for the small grains. In addition, the intensity of the absorption peaks were more affected with the apertureless system due to

contribution of the surrounding material through diffraction. For the larger C-H rich and C-H poor areas the FPA system gave an accurate evaluation of the C-H peak intensity.

In my Ph.D. thesis, the FPA imaging allowed us to quickly capture chemical maps of large areas of a sample and to detect the various chemical species present. However, for an accurate estimation of the concentration, the use of a synchrotron source coupled to a confocal system was more appropriate. The FPA imaging is a powerful tool for the study of samples presenting a strong chemical contrast such as meteorites which are assembly of grains of radically different chemical compositions.

Chapter 3

Analysis of fragments of Paris in 2D

Contents

In this section, we focus on the study on a primitive meteorite. Two fragments were analyzed in a 2D configuration. A first study was conducted in transmission on a micrometric fragment and the results presented here are the object of a paper: Dionnet, Z., Aleon-Toppani, A., Baklouti, D., Borondics, F., Brisset F., Djouadi, Z., Sandt, C. and Brunetto, R., 2018, Organic and mineralogic heterogeneity of the Paris meteorite followed by FTIR hyperspectral, MAPS, under press.

The first part of this chapter is entirely based on that publication.

A bigger (millimetre-sized) fragment was analyzed in the framework of a larger study involving several groups and techniques, and I have contributed to the analysis performing MIR spectral imaging of the sample. By studying both micrometric and millimetric fragments, we can investigate the effects of aqueous alteration at different scales.

The Paris meteorite is a CM carbonaceous chondrite exceptionally well preserved from terrestrial alteration (Bourot-Denise et al., 2010, Zanda et al., 2010, Hewins et al., 2014, Leroux et al., 2015), it contains peculiar inclusions of organic matter having IR signatures similar to those of some interstellar carbons (Merouane et al., 2012). The heterogeneity of the organic matter was also described in Vinogradoff et al., 2017, where they observed two types of organic matter: sub-micrometric individual organic particles and diffuse organic matter finely distributed in the matrix. The Paris meteorite has two lithologies, which have undergone different degrees of aqueous alteration: the less altered regions are rich in amorphous silicate with nano inclusions of iron and sulfide (type GEMS -glass with embedded metal and sulfides-). On the other hand, Leroux et al., (2015) described the matrix in the more altered regions as a mixture of amorphous material and Fe-rich poorly crystalline phyllosilicates containing less metal inclusions. The presence of amorphous silicates and metals inclusions in the two lithologies shows that Paris has remained quite pristine (Marocchi et al., 2014 and Hewins et al., 2014).

3.1 Study in transmission

We analyzed a small fragment from the matrix of the Paris meteorite. The sample was provided by B. Zanda of the MNHN (Muséum National d'Histoire Naturelle de Paris). Unfortunately, the information on the lithology it originated from was not recorded at the time of extraction.

The sample was crushed (see Fig. 3.1) in a diamond compression cell, which is transparent in the IR range (similarly to what is described by Brunetto et al., 2011). After crushing we obtained a sample of 50x40 μm^2 and 3.0 +/− 0.5 μm in thickness. During measurements the cell was opened and the sample was exposed to air.

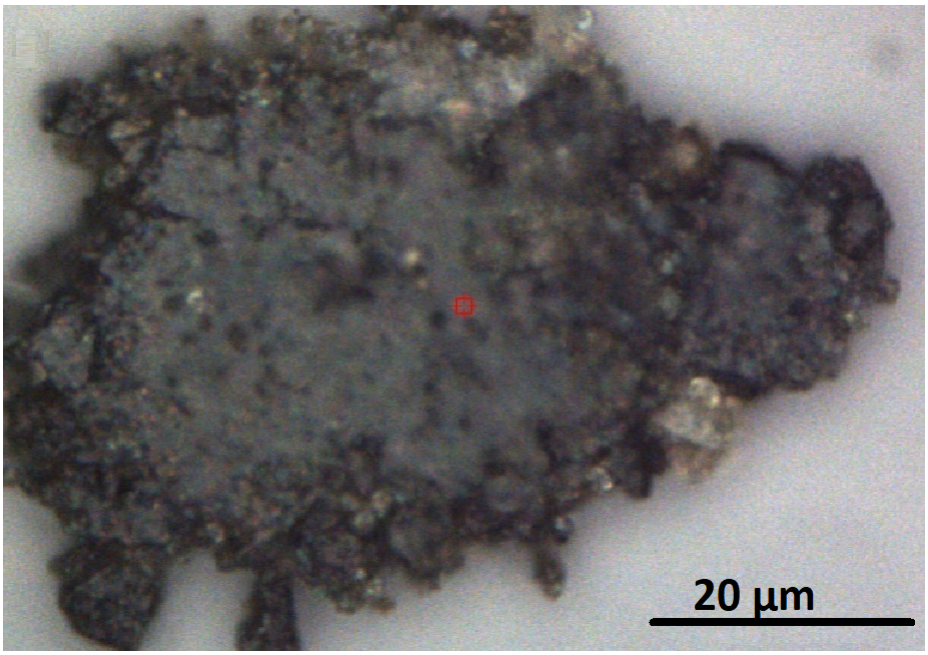

Figure 3.1: Optical image (obtained by reflectance) of the Paris fragment pressed in a diamond compression cell.

We used two apparatus based on IR microspectroscopy to obtain hyperspectral maps in transmission, combined with Raman measurements. The specifications used for each analytical technique are described in the previous Chapter. The spectral resolution was 4 cm^{-1} for all the measurements and the spatial resolution, depending on the wavelength is given by the Abbe's equation (Hackett et al., 2015). Table 3.1 gives the band strengths A used to deduce the column density N (molecules.cm^{-2}) thanks to the following formula: N = Area/A.

Finally, some analyses were also performed with SEM and we have mapped the 170 repartition of magnesium, silicon, calcium and iron. SEM acquisitions were done at 20 kV under 171 20 Pa nitrogen pressure on a Zeiss Supra 55 VP FEG fitted with an EDAX EDS analytical system.

Component	Band strength (x10^{-18} cm/group)
Silicate	200
Carbonate	100
OH bending	210
CH2 symmetric stretching	2.4
CH3 symmetric stretching	2
CH2 asymmetric stretching	8.4
CH3 asymmetric stretching	12.5

Table 3.1: Band strength for major IR bands measured according to Matrajt et al., (2005), Dartois et al., (2004), Jager et al., (1998) and Brunetto et al., (2011).

3.1.1 Results

In this section we first listed the components present in the sample, explored their spatial distribution and finally, we focused on results from few peculiar points useful for the discussion, such as the CH_2/CH_3 ratio or the spatial correlation between OH and CH stretching vibrations.

Average spectra and fragment composition

In Fig. 3.2, we reported the average spectra for the whole sample and the average of 10 spectra extracted from the three different regions of interest described below and measured with the FPA connected to the globar source.

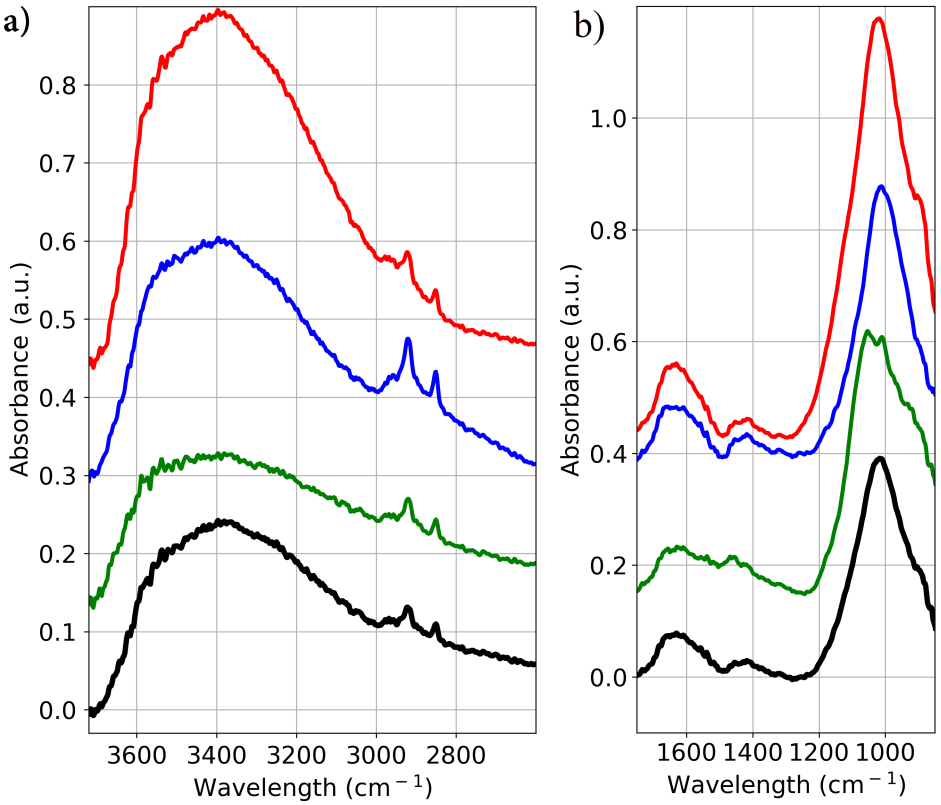

Figure 3.2: Spectra (a) between 2600 and 3720 cm^{-1} and (b) between 850 and 1250 cm^{-1} for different regions of the samples. We distinguished 3 different regions A, B and C, corresponding to different composition (see Fig. 3.3). From bottom to top: the average spectrum of the whole sample (black), an average of 10 spectra extracted from the serpentine-rich region (extracted from region B, green), from the region rich in aliphatic CH (region C, blue), and from the amorphous silicate and olivine rich region (region A, red). For clarity, all curves are spaced by 0.15 in the absorbance scale.

Position (cm^{-1})	Assignment
large band between 850-1140 with a maximum at 1035	Amorphous SiO stretching
880	Olivine SiO stretching (B3)
921	Diopside SiO stretching
960	Diopside/Serpentine SiO stretching
1014	Serpentine SiO stretching
1069	Diopside SiO stretching
1086	Diopside SiO stretching
1150-1180	Sulfate SO stretching
1256	CC Aromatic skeleton
1326	CH3 bending
1413	CH2 bending
1410-1480	Carbonate CO stretching
1633	OH bending
2854	CH2 symmetric stretching
2864	CH3 symmetric stretching
2926	CH2 asymmetric stretching
2958	CH3 asymmetric stretching
3000-3750	OH stretching
3660	OH stretching mode of the hydroxyl groups in hydrated silicates

Table 3.2: Peak positions of the spectral bands in the sample.

Our assignment is presented in Table 2 and is based on previous studies of meteorites or interstellar dust analogs (Matrajt et al., 2004; Dartois et al., 2005; Merouane et al., 2012; Yesiltas and Kebukawa 2016). The description of the corresponding modes is presented in these papers. The assignation of specific silicates is described below.

The main feature was the SiO silicate band around 1035 cm^{-1}, visible almost everywhere in our sample with variable intensities and structures. For the majority of the spectra and also for the average spectrum (see black spectrum in Fig. 3.2) we observed this feature as a broad peak, which is characteristic of a disordered structure, that is an amorphous structure

(Tamanai et al., 2009) or at least a poorly crystalline silicate. We assign this almost ubiquitous large band to an amorphous or poorly crystalline silicate dominating the Paris sample. Indeed, the shape of the observed band and the position of the maximum is very similar to the one observed by Demyk et al., 2017 which synthetized Mg and Fe-rich amorphous silicates (especially sample E1O containing 10 percents of iron). In that paper, the degree of amorphisation was confirmed by XRD diffraction and comparison with crystalline silicates was led (see also Copeaud et al., 2011 and Boudet et al., 2005). In Fig. 3.3, we compare the spectrum of synthesized amorphous silicate (pink dashed line) with the spectrum of the amorphous rich region observed in our sample (red solid line). A similar band was also observed in chondritic smooth IDPs with a hydrated amorphous silicate by Bradley (2003).

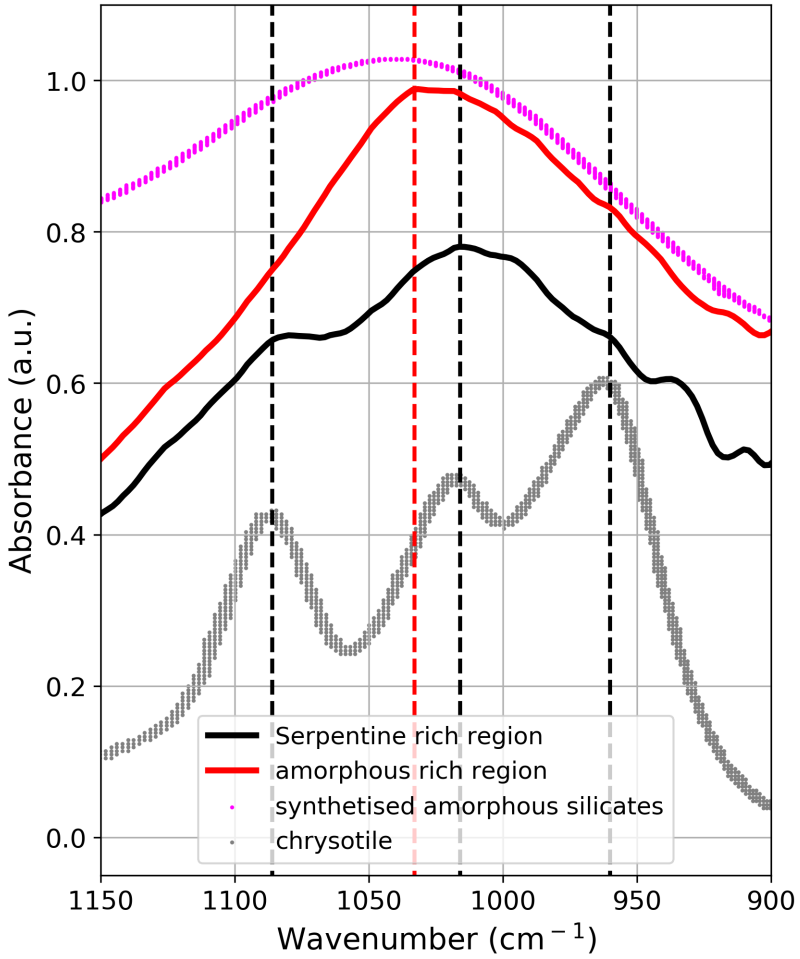

Figure 3.3: Spectrum from the amorphous region in red compared to amorphous spectrum from Demyk et al., 2017 in dashed pink and spectra from the serpentine region in black compared to the one from a pur serpentine in gray (Beck et al., 2014).

Moreover, we observed some differences in the shape and peak position of the SiO band for some specific locations in our sample: the maxima of the band can be shifted by few tens of wavenumbers, the full-width half-maximum varies by +/− 10 cm^{-1}, and in some spots of the sample a peculiar structure of the peak appears. We used the term 'amorphous silicate' loosely to refer to the spectra exhibiting a single broad SiO band (the structure could be poorly crystalline) and on the contrary the detection of small structures inside this band indicates the presence of more organized silicates contributing to the SiO feature (see Fig. 3.3). This structuration is indicative of the local presence of diopside, serpentine and olivine. We observed three bands at 1086 cm^{-1}, 1014 cm^{-1} and 960 cm^{-1} which can be assigned to serpentine (more specifically to chrysotile according to Salisbury et al., 1991 and Beck et al., 2014 (see grey spectrum in Fig. 3.3)). In some spectra of this region, we have also observed a weak shoulder in the large O-H stretching band at 3660 cm^{-1} which corresponds to a narrow band assigned to structural OH of a phyllosilicate phase. Raman analyses confirmed the detection of chrysotile in the same region as shown in Fig. 3.5(c) (using band positions reported by Rinaudo et al., 2003). In another part of the sample, we observed peaks at 1069 cm^{-1}, 960 cm^{-1} and 917 cm^{-1} characteristics of diopside (Omori 1971) in the infrared spectra. The attribution of the diopside was confirmed by Raman analyses of this peculiar region and the detection of a band at 1010 cm^{-1} (Huang et al., 2000) in the Raman spectra of the same region (see Fig. 3.5(c)). Finally, we observed the main band of the olivine in FTIR at 883 cm^{-1}, also detected the typical olivine doublet in the 818-846 cm^{-1} spectral region in the Raman spectrum (see Fig. 3.5(b)). In both cases the positions of the band(s) indicated a ratio Mg/(Mg+Fe) around 54%, according to Hamilton (2010) for the FTIR and Kuebler et al., (2006) for the Raman measurements. The olivine was hard to detect and we could detect it only in a few Raman spectra.

The aliphatic CH stretching bands around 2900 cm^{-1} were also observed with slightly varying intensities throughout the sample. The detection of the bending (1500-1750 cm^{-1}) and the stretching (3000-3750 cm^{-1}) OH modes indicated the presence of water in our sample

Carbonate contribution was also visible around 1400 cm^{-1}. Thanks to the Raman spectra (see Fig. 3.5(a)) exhibiting peaks at 1085 cm^{-1} and 281 cm^{-1}, we identified the calcium carbonate seen in IR as calcite (Rutt and Nicola 1974). The elementary composition pro-

vided by SEM-EDX analyses in the spots identified as calcite indicates that they are indeed enriched in calcium, which supports the calcium carbonate identification. Finally, the IR band at 1165 cm^{-1} was attributed to sulfates (Yesiltas et al., 2014; Salisbury et al., 1991), more precisely to gypsum, an anhydrous calcium sulfate (Lane 2007). This attribution was confirmed by the Raman analyses through the detection of bands at 1015 cm^{-1}, 490 cm^{-1} and 415 cm^{-1} (Buzgar et al., 2009).

Spatial distribution of the components studied by mid-infrared

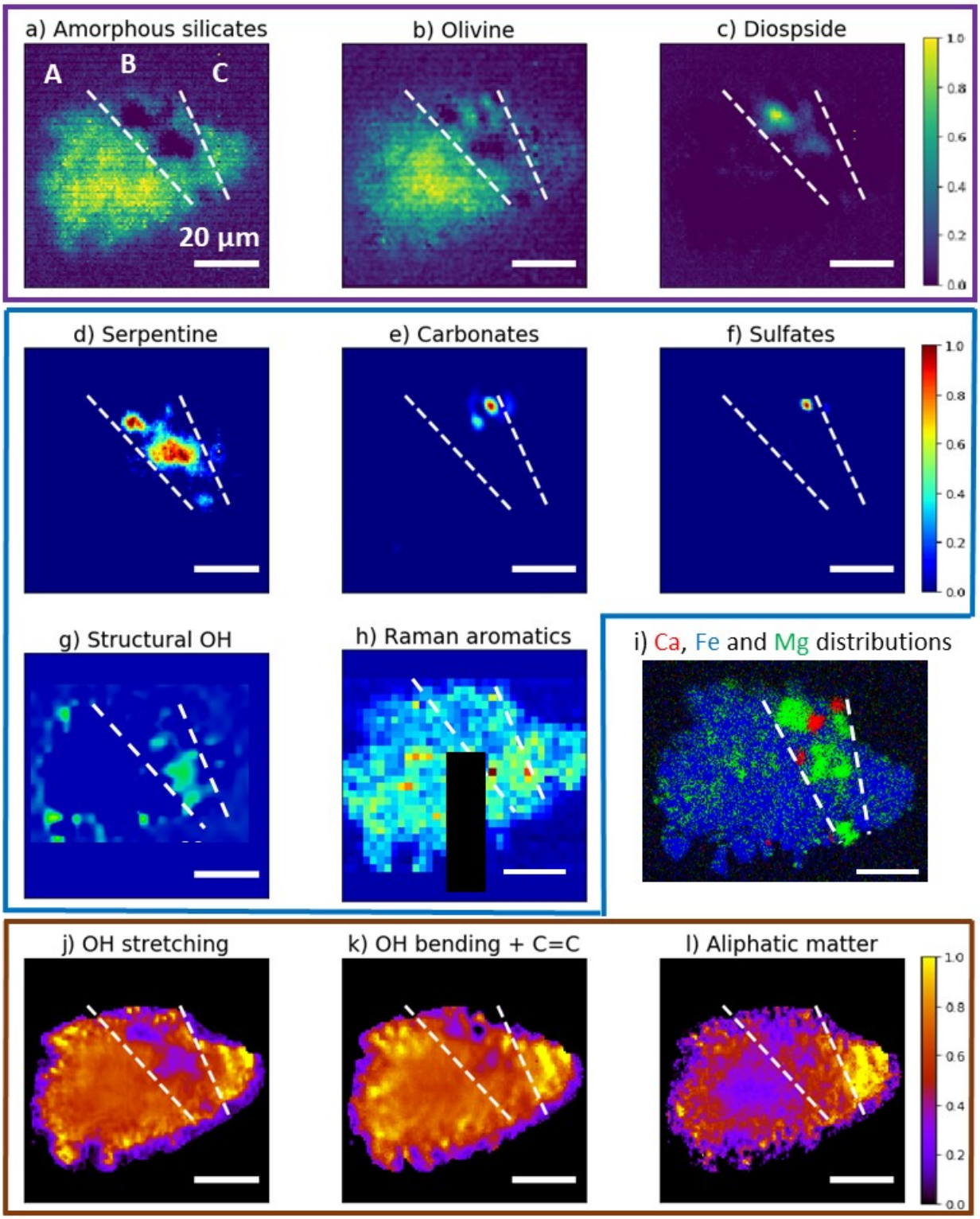

Figure 3.4: Spatial distribution of (a) the amorphous silicates, (b) olivine, (c) pyroxene, (d)

serpentine, (e) carbonate, (f) sulfate, (g) structural OH obtained with synchrotron radiation, (h) the polyaromatic carbons obtained with the Raman spectrometer, (i) distributions of abundance of calcium (red), iron (blue) and magnesium (green) obtained with the SEM, (j) OH stretching vibration, (k) OH bending vibration and (l) the aliphatic CH groups. Except the distributions (g), (h) and (i), all the distributions were obtained with the FPA. The distributions (a), (b) and (c) (purple box) were obtained by the method of the second derivative. Please note that some artifacts are present in map (g) at the border of the meteorite, due to a difficult removal of the spectral continuum. All the distribution presented in the blue box were obtained with raw spectra by integration of the area under the corresponding band. The rings visible in panels (e) and (f) are due to diffraction. The black rectangle in panel (h) represents unavailable data. Finally distributions in the brown box were normalized to the distribution of silicates. The dashed white lines delimit the 3 main regions A, B and C defined in the studied sample.

We mapped the spatial distribution of the different functional groups using the procedure described in paragraph 2.3 by studying the area under the corresponding bands.

First, we studied the silicate distribution. We identified an amorphous or poorly crystalline silicate phase in the majority of the spectra. Using the second derivative, we isolated the corresponding band from the contribution of the other silicates and we obtained the distribution of the amorphous silicate shown in Fig. 3.4(a). In all these spectra, we also observed the broad band of O-H stretching, indicating that the amorphous silicate is hydrated (this fact will be further supported below). Olivine is mainly located at the left of the sample (see Fig. 3.4(b)). We thus observed on the left of the sample a region rich in amorphous silicate and olivine (region A) and on the right of the sample a region (Region C) rich in amorphous silicate but with lower olivine content. SEM analyses (see Fig. 3.4(i)) showed that these two regions are rich in iron compared to the magnesium. Indeed, we measured a Mg/(Mg+Fe) ratio of 0.28 for region A and of 0.25 for region C.

Between these two regions, we observed a region with significantly different spectra (region B). We distinguished a structure inside the silicate band which indicates a crystalline structuration of the mineral phase (see green spectrum in Fig. 3.2). The map of the structural OH was obtained with synchrotron radiation. This suggested the presence of phyllosilicates

in this region. Moreover, this region analyzed with the SEM showed enrichment in Si and Mg and depletion in Fe. A ratio Mg/(Mg+Fe) of 0.66 in this region confirms the depletion in iron in this region The detection of a Mg-rich region confirmed the identification of chrysotile (the magnesium pole of the serpentine). Inside region B, we identified a spot containing pyroxene (diopside) at the top of the sample.

Carbonates (see Fig. 3.4(e)) were also very localized with two very small and concentrated spots (2*3 μm) at the top of region B. Simultaneously, we have detected a spot of calcium sulfate, i.e. gypsum, nearby (see Fig. 3.4(f)).

The OH band was observed in almost every spectrum with different abundances across the sample. The distribution did not seem to be exactly the same for the OH stretching and bending modes. This may be due to the fact that the OH bending spectral region contains contributions from the C=C and C=N absorptions, besides the H_2O signatures. The OH stretching was less present in the crystalline silicate rich region. Indeed, in the serpentine, the OH was present as structural OH.

Figure 3.4(l) shows the heterogeneous distribution of the aliphatic CH bands. Aliphatic CH stretching bands were intense in particular in one area: in a spot at the right of the sample (region C). The concentration in this area was at least three times higher than the average aliphatic C-H concentration in the whole sample. Whereas, we found some spectra around the center of the sample in region A and on top of region B with a much lower content in aliphatic moieties. Olivine (see Fig. 3.4(b)) was co-located with the organic matter poor in aliphatic in the region A, and chrysotile (serpentine) is co-located with the one in region B.

Finally, we also studied the distribution of organic polyaromatic matter with Raman microspectroscopy (see Fig. 3.4(h)) since it provides complementary information to infrared and specific information on the polyaromatic carbons. We easily detected the D and G-bands of polyaromatic carbons, similarly to what was measured by Merouane et al., (2012) in the bulk of the Paris meteorite, and we compared our observed peak intensity with the abundance of aliphatic CH detected with FTIR. It should be noted that absolute intensity values of D band and G bands do not necessarily correlate with actual concentrations of polyaromatic

carbons, since Raman intensities are not quantitative, but it is still gives an indication on the presence or absence of polyaromatic carbons.

We found that the aromatic C=C was present in the entire sample but more presented at the bottom of the sample (Fig. 3.4(h)) (see Fig. 3.5(d)). Moreover, we did not detect significant variations in the position or FWHM of the G and D band inside the sample. We also looked for possible spatial correlations between aliphatic CH and polyaromatic carbons, and found that the distribution of polyaromatic carbons was different from the distribution of aliphatic CH observed in FTIR data. For instance, the aliphatic CH rich spot did not correspond to a region rich in aromatic matter.

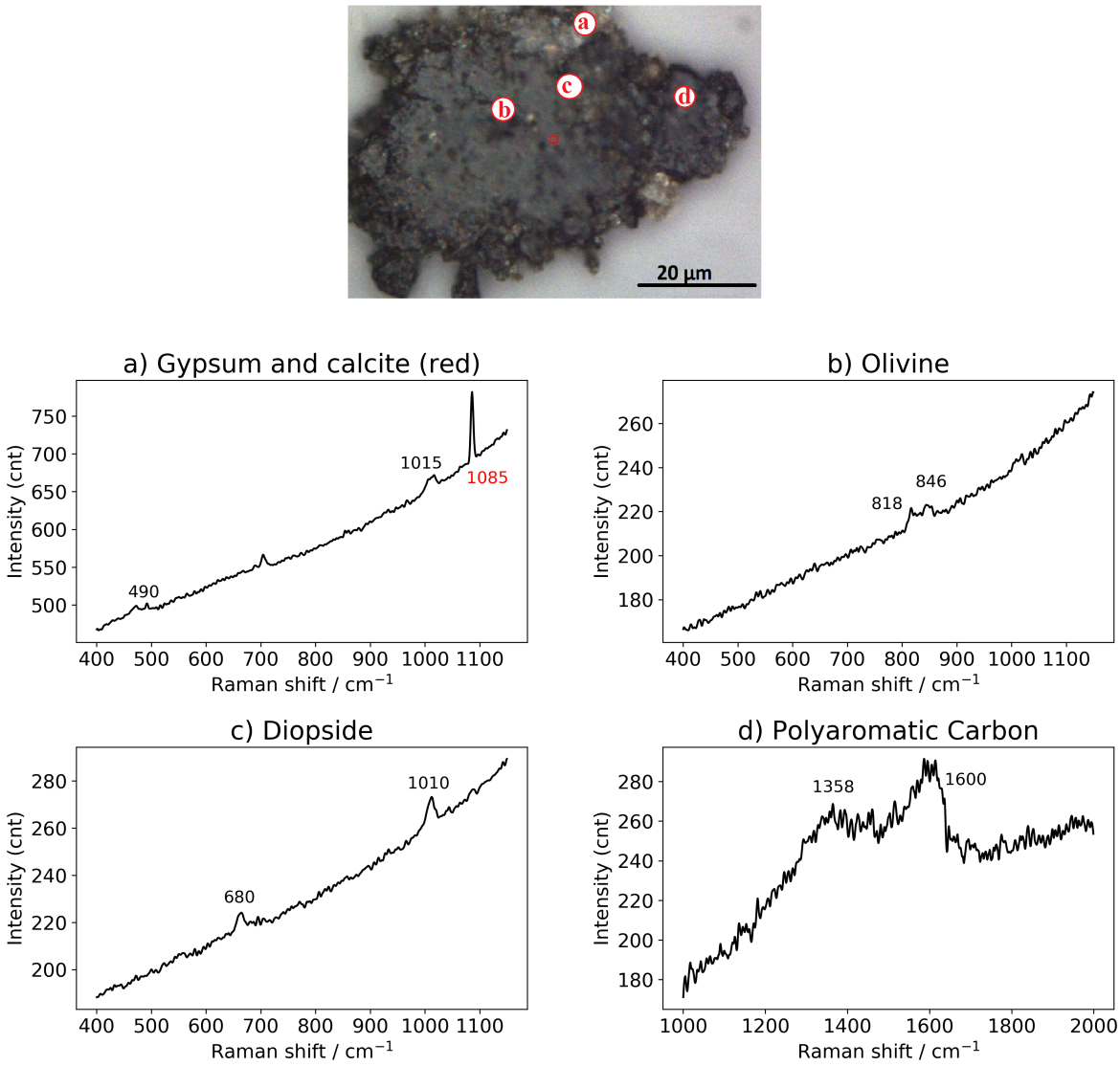

Figure 3.5: Optical image showing in red the spots that have been explored by Raman spectroscopy and micro-Raman spectra showing (a) calcium carbonate and sulfate, (b) olivine, (c) diopside and (d) D and G bands polyaromatics bands.

Analysis of the CH_2/CH_3 ratio

It was particularly interesting to focus on the CH_2/CH_3 ratio in the IR spectra to evaluate aliphatic chain lengths and branching levels (a lower CH_2/CH_3 ratio corresponds to shorter aliphatic chain lengths and/or higher branching levels, especially if we assume chemically similar initial organic compounds or mixtures which would have evolved separately or differently). We first determined this ratio from the average black spectrum shown in Fig.

3.2. For this, we fitted the aliphatic bands with 5 Gaussian profiles to better estimate the contribution of each vibration. The CH_2/CH_3 ratio (calculated after the correction by band strength) was derived from the asymmetrical bands (2926 cm^{-1} for the CH_2 band and 2958 cm^{-1} for the CH_3 band, see Merouane et al., 2012 and references therein). From Fig. 3.6(b) we found a value of 2.6 +/− 0.2 (1.75 +/− 0.1 before correction by band strength).

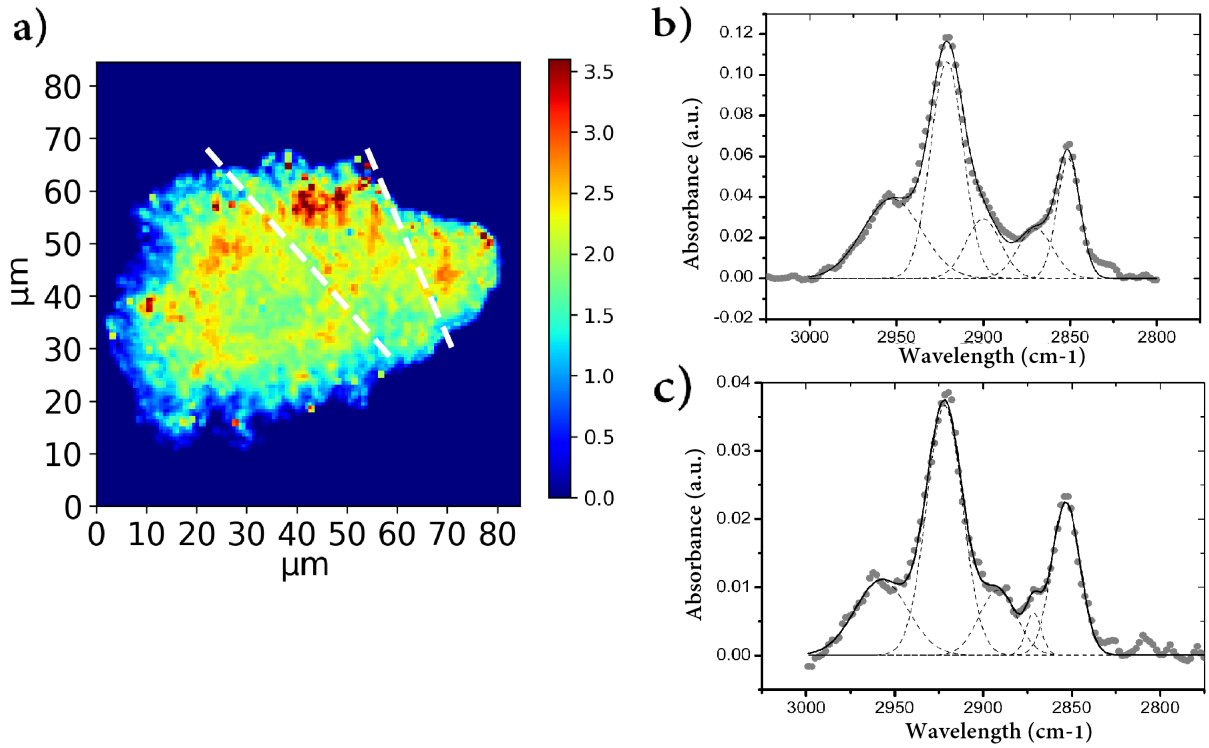

Figure 3.6: (a) Distribution of the CH_2/CH_3 ratio. Points outside the meteorite were forced to zero. The distribution was spatially smoothed by a binning of 4 pixels. (b) Fit of 5 Gaussian profiles obtained for the average spectrum, we obtained a ratio of 2.6 +/− 0.2. (c) Fit of 5 gaussian profiles obtained for a spectrum in the north of the sample, we obtained a ratio of 3.5 +/− 0.2.

We checked for the variation of this ratio in our sample. For this, we used an analytical procedure to estimate the CH_2/CH_3 ratio for each of the 5729 selected spectra. A local baseline was used in the asymmetric-stretching region and a band area ratio was derived from each analyzed spectrum. We thus obtained the distribution shown in Fig. 3.6(a). This figure shows varying values of the CH_2/CH_3 ratio and exhibits some hotspots, located in the top of the region B, close to the carbonates, diopside and serpentine grains. A double-check

of the intensity scale provided in Fig. 3.6(a) was performed on some spectra, including the hotspots. We used the 5 Gaussian fitting procedure for the selected spectra and calculated the CH_2/CH_3 ratio. The maximum value found was 3.5 +/− 0.2 (2.35 +/− 0.1 before correction by band strength) in some spectra of region B, the most altered region in the sample. In the region A we obtained values around 1.75 +/− 0.25 (see Fig. 3.6(c)) (1.18 +/− 0.1 before correction by band strength).

Correlation OH/CH

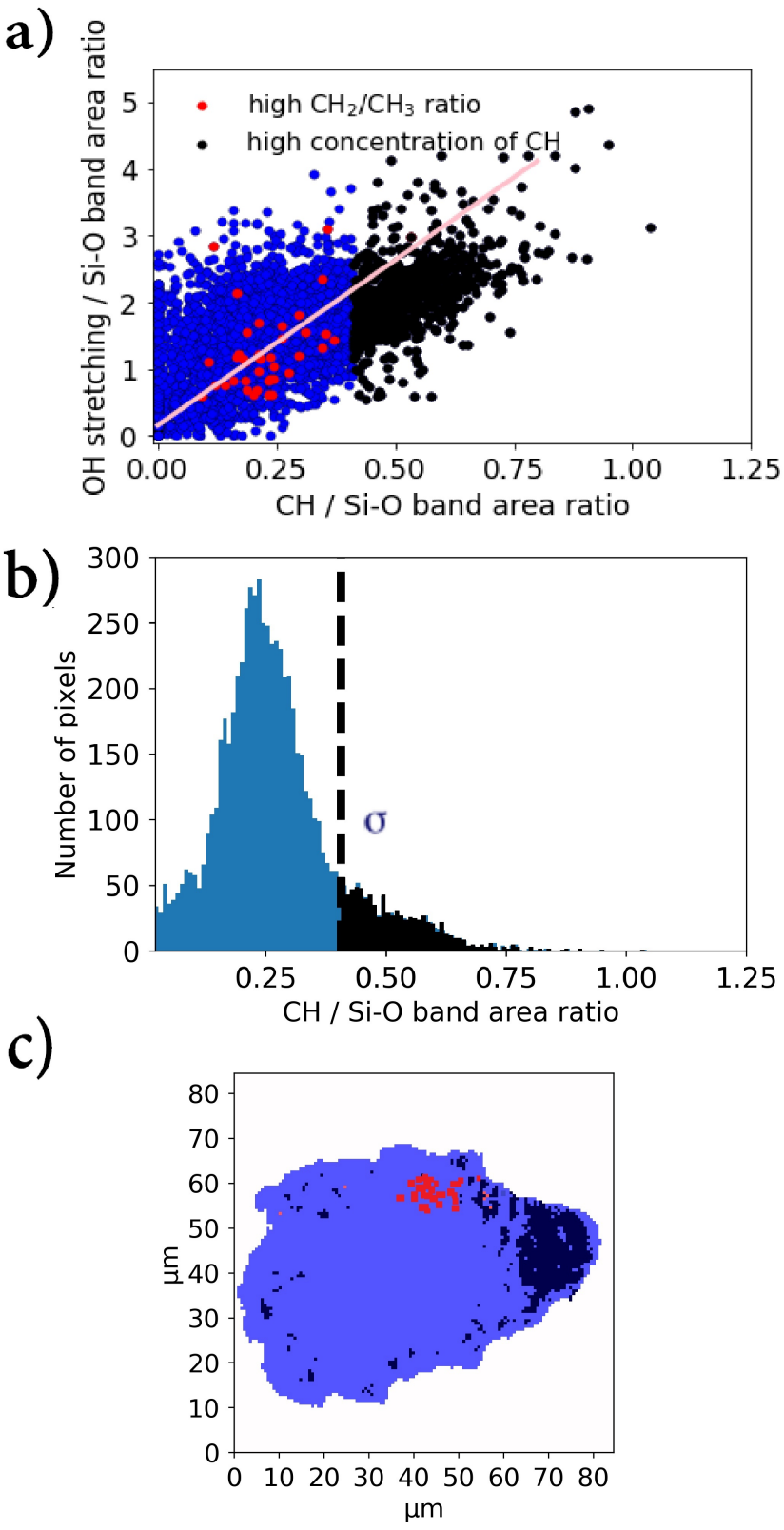

Figure 3.7: (a) Correlation diagram OH-CH: number of OH stretching/SiO oscillators versus number of CH/SiO oscillators with the correlation right; (b) histogram-distribution of the number of CH normalized by the abundance of SiO; (c) insert showing the spatial distribution of the pixels (black points) with CH/SiO band area ratio 1 σ higher than the median value. Red points in all panels correspond to pixels with CH_2/CH_3 values higher than 3.2.

An interesting correlation diagram can be plotted between the abundance of water and aliphatic CH, as shown in Fig. 3.7(a). We observed a distribution along a line, showing a correlation between water and aliphatic moieties signal with correlation coefficient value r = 0.86. The distribution of aliphatic carbon normalized to the quantity of matter was close to an asymmetric Gaussian profile (see Fig. 3.7(b)). From this distribution, we evaluated the median quantity m = 0.27 of CH/SiO oscillators and the standard deviation, σ, calculated after the correction by band strength. We considered spots as particularly rich in CH, when CH/SiO values were 1 σ higher than the median value, i.e. higher than 0.4 CH/SiO oscillators. Then we plotted the spatial distribution of these singular points (see Fig. 3.7(c)), and we found that almost all these spectra were located in region C, an OH-rich region. This confirmed the existence of a co-localization of water and aliphatic rich organic matter in the sample. We also checked for the spatial distribution of spectra with high CH_2/CH_3 ratio (red dots in Fig. 3.7 (c)), and we did not observe any significant correlation with water or the total aliphatic carbon abundance. We stress that the points with high CH_2/CH_3 ratio are relatively poor in aliphatic bonds (see Fig. 3.7) but their spectra still have a signal/noise ratio high enough to evaluate the CH_2/CH_3 ratio correctly (see Fig. 3.6(c)).

The mean value of CH oscillators normalized to the number of SiO oscillators was around 0.25 (see Fig. 3.7(b)). By using the atomic percent of carbon measured in the matrix of the Paris meteorite by Noun et al., (2013), we estimated the total ratio of carbon with respect to silicon. Considering that our sample was large enough compared to the typical size of organic particles (Vinogradoff et al., 2017) to be representative of the matrix, we deduced that between one third and half of the carbon present in the matrix was contained in CH_2 or CH_3 bonds, the rest being included in environments such as C=C, C=O, C=N, C≡C, C≡.

3.1.2 Discussion

Silicates

In our sample we detected regions mainly composed of amorphous silicates (regions A and C). With TEM analyses, Leroux and al., (2015) have also observed amorphous silicates on the Paris meteorite at a small scale (a few hundreds of nm) in the less altered lithology. Our observations confirm the presence of amorphous silicates at a bigger scale (the region rich in amorphous silicate is as large as 40 μm). This part of our fragment probably came from the less altered lithology.

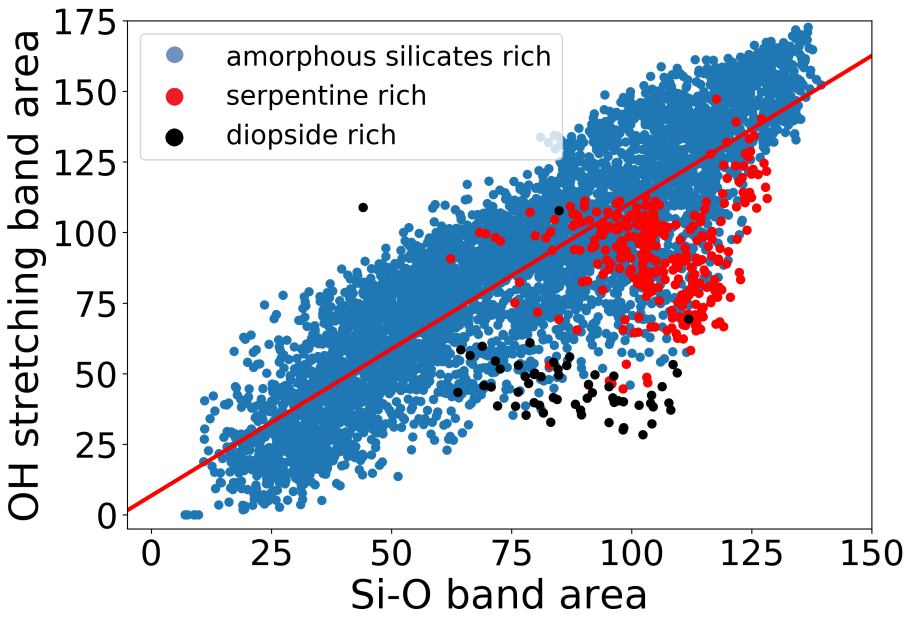

Figure 3.8: Correlation diagrams between the OH stretching and the silicates. The blue distribution represents the amorphous silicate rich pixels, the red one represents the serpentine rich pixels and the dark one represents the diopside rich pixels.

Figure 3.4 shows that the OH stretching and HOH bending modes were co-localized with the amorphous silicates. We plotted in Fig. 3.8 the correlation between the OH and SiO stretching bands in the amorphous silicates (following the example of Yesiltas and Kebukawa 2016). We observed a linear relationship with a small offset, which means that the water and the silicate abundances were correlated (r = 0.89). This suggests that water and/or hydroxyl groups are most probably contained in the amorphous silicate phase. Hydration of amorphous primitive chondrites have already been observed by Le Guillou et al., (2014).

The offset of the linear correlation was 4.25 which represented only 5% of the average area of the OH band. This small offset corresponded to the contribution of water adsorbed on the sample surface as the linear regression presented here was done removing diopside and serpentine rich areas. Indeed, the presence of a diopside rich area could also increase the offset: a second linear regression with all the points gave an offset of 6.75.

We also noticed that the diospide-rich spectra contained less water and were significantly below the correlation curves. Due to the pixel size, we did not observe a pure diopside spectra; the diopside was always mixed with some amorphous silicates. The small OH stretching contribution, seen in the diopside-rich spectra, came from the amorphous silicate phase. Besides, Fig. 3.8 shows that the average OH/SiO ratio in the amorphous silicates spectra was higher than the same ratio in the serpentine-rich spectra. Compared to the serpentine, the amorphous silicate phase contained on average more water and hydroxyl groups.

Finally, the IR spectra indicated that our sample was dominated by hydrated amorphous silicates. This result confirms the suggestion made by Leroux et al., (2015) about the probable hydration of the amorphous silicates they observed in the matrix of the Paris meteorite.

In addition to amorphous silicates, region A contained olivine (Fo_{55}). IR spectra indicated that the mixture between the amorphous phase and the olivine was intimate at a scale smaller than the size of the pixel (0.7 μm). This is in agreement with the TEM analyses performed by Leroux et al., (2015), where they observed small grains of forsterite at a scale of hundreds of nanometers embedded in amorphous structures. However, the ratio Mg/(Mg+Fe) measured in our sample is not in agreement with the one measured by Leroux et al., (2015). Moreover, studies of CM and C2 chondrites with MIR analyses have shown that olivine is progressively replaced by OH-bearing phases through aqueous alteration (Beck et al., 2014). The olivine-poor region had a concentration of OH oscillators twice more significant than the concentration in olivine-rich region (region A). Note, that the iron rich olivines in region A should have easily disappeared under aqueous alteration (Wogelius and Walther 1992). These observations corroborate the idea that regions B and C with a depletion in olivine underwent aqueous alteration. The olivine-rich amorphous region A showed limited signs of alteration compared to region C that appeared depleted in olivine and enriched in water.

Located between these amorphous-rich regions (regions A and C), region B was rich in crystalline minerals, such as serpentine, diopside, carbonate and sulfate. Leroux et al., (2015) detected some serpentine in the part of the Paris meteorite which underwent aqueous alteration. Vinogradoff et al., (2017) also performed TEM studies of sections extracted from the matrix of Paris and confirmed the observations made by Leroux et al., (2015). In particular, both studies showed evidence that amorphous silicates have been progressively replaced by crystalline nano-phyllosilicates in the matrix. Secondary alteration phases included micron-sized carbonates, as those observed in region B (see Fig. 3.4(e)). The detection of crystalline phases in region B shows that this region underwent more hydrothermal alteration comparing to the regions A and C.

In summary, the study of the mineral components in our sample in the context of what was measured by Leroux et al., (2015) and Vinogradoff et al., (2017) indicates that region A was amorphous-rich and olivine-rich with little signs of alteration, region C underwent moderate degrees of aqueous alteration leading to the disparition of olivine and enrichment of OH-bearing phases, and region B included phyllosilicates and carbonates pointing to stronger degrees of aqueous alteration. Such local heterogeneities were probably due to different initial conditions (temperature, porosity, pH, mineralogy and composition) of alteration at a micro-size scale (Brearley 2006).

Organic matter

Paris, as a very primitive meteorite (Zanda et al., 2010; Hewins et al., 2014), has undergone limited thermal metamorphism, thus providing an interesting opportunity to study the link between very early aqueous alteration and meteoritic organic matter. Many studies have already been conducted on the SOM (Soluble Organic Matter, see Martins et al., 2015; Schmitt-Kopplin et al., 2010, and references therein) and the IOM (Insoluble Organic Matter) of carbonaceous chondrites (e.g. Quirico et al., 2014; Kebukawa et al., 2011). However, they often involved the destruction of the sample and aggressive processes to separate the two components (hydrolysis, harsh acid hydrolysis, solvent extraction). In our case, we worked on the bulk organic matter without extracting or separating the SOM or IOM, and our non

destructive analysis provided information on the diversity of the organic matter preserving the mineral context. Here, we discuss detection of spatial and compositional heterogeneities of the organic matter.

4.2.1 The aromatic component

The organic matter of the Paris meteorite has been recently studied by Vinogradoff et al., (2017). By combining different techniques, they detected spatial and compositional heterogeneities of the organics in the matrix of Paris. They observed that organic particles are embedded within the silicate matrix and frequently are in contact with nanosulfides. More specifically, through XANES and STXM studies they were able to detect a spatial and compositional heterogeneity defining two populations: sub-micrometric discrete organic-rich particles and diffuse organics closely embedded within silicates. The discrete particles were richer in C=C and poorer in carboxylic groups than the diffuse organics. Similar evidences of the existence of two populations of organic materials have been reported by Le Guillou et al., (2014) in the matrix of Renazzo (CR2), Murchison (CM2), and Orgueil (CI). The size of the discrete particles observed by Vinogradoff et al., (2017) was a few hundreds of nm, which is unfortunately smaller than the resolution of our microspectroscopic analysis. Thus, it was not possible to clearly separate the two populations in our hyperspectral maps.

However, Vinogradoff et al., (2017) noted that the XANES signatures of the discrete particles within the matrix were closer to the XANES signatures of the extracted IOM of Paris, than the diffuse organics. In addition, Raman spectra of the Paris matrix reported here and by Merouane et al., (2012) are essentially indistinguishable from the Raman spectra of the Paris IOM reported by Vinogradoff et al., (2017). In all these studies, typical Raman G-band parameters were 1585-1590 cm^{-1} for peak position and 90-100 cm^{-1} for the FWHM, both in the IOM and in the bulk fragments of Paris. All measurements agreed within typical error bars of the chosen fitting functions. The Raman G and D band are known to be particularly sensitive to the structure and degree of order of the polyaromatic component in complex carbons of meteorites (see e.g. Quirico et al., 2014). Based on these evidences, we suggest that the kind of discrete particles identified by Vinogradoff et al., (2017) were probably the main carriers of the Raman D and G-bands we observed in the matrix of Paris (see Fig.

3.4(h)).

4.2.2 Spatial heterogeneity of the aliphatics

In Figs. 3.4 and 3.6 we reported evidence of the detection of organic materials rich in aliphatic CH_2 and CH_3 bonds. This component was observed everywhere in the sample but its spatial distribution was not uniform. In particular, in region C we detected a hotspot of aliphatic carbon with a concentration between 3 and 4 times the average concentration in the whole sample. By using the band strength (Brunetto et al., 2011), we estimated that the ratio between aliphatics and silicates was 5% in mass on the average spectra (whole sample) and reached 12% in mass in region C, shown in Fig. 3.4 (panel l). The average value was consistent with the ones measured in other CMs (Anders and Zinner 1993), and with the one measured with macro-PIXE by Noun et al. (2013). The hotspot of aliphatic organic matter observed in region C was also rich in amorphous silicates, in water (about 2 times richer than the average of region A), and in iron (see Fig. 3.4(i)).

4.2.3 Compositional heterogeneities of the aliphatics

In addition to a non-uniform spatial distribution of the aliphatics, one can also study their compositional heterogeneity by evaluating the CH_2/CH_3 ratio. A study of the heterogeneity of the CH_2/CH_3 ratio was presented by Kebukawa et al., (2010) in the meteorite Bell (CM2) using near-field IR spectroscopy. They mapped the distribution of the CH_2 and the CH_3 vibrations at micron scale for a region of about 8 μm in size, then they extracted the ratio CH_2/CH_3, but they did not observe local heterogeneities.

First, we evaluated the average ratio CH_2/CH_3 in our sample, which was found to be 2.6 +/− 0.2, a value in agreement with the one measured by Merouane et al., (2012) on the Paris meteorite. A ratio of 2.5 +/− 0.4 was measured on bulk matrix fragments of Murchison (CM2) by Matrajt et al., (2005). This value is similar to the one measured in grains in the interstellar medium (Sandford et al., 1991). However, it is higher than the one of CM Murchison bulk (R=1.0) and Bell bulk (R=1.4) powders reported by Kebukawa et al., (2010). The estimated value of the CH_2/CH_3 ratio may slightly depend on the chosen fitting

functions: our calculation on data provided by Kebukawa et al., (2010) with our method provided a value of about 1.4 +/− 0.2.

Subsequently, we studied the local variations of the CH_2/CH_3 ratio. In region A of our sample (the least aqueously altered), the ratio CH_2/CH_3 ratio decreased to about 1.75 +/− 0.25 (see Fig. 3.6(a)), while in region B (the most aqueously altered) it increased up to about 3.5 +/− 0.2. Note, that our study presents for the first time a heterogeneous CH_2/CH_3 ratio detected spectroscopically in the matrix of the Paris meteorite.

Some processes, such as the breaking of bonds by energetic particles or the aromatization and/or 'polymerization' of aliphatic molecules by heating can affect the chain length and branching level of aliphatics. For instance, some laboratory experiments on IDPs have shown that ion irradiation can decrease chain lengths and give lower CH_2/CH_3 ratios (see e.g. Munoz-Caro et al., 2006). The effects of hydrothermal alteration on CH_2/CH_3 ratios are less clear. Kebukawa et al., (2011) proposed a classification of meteorites as a function of the ratio CH_2/CH_3 in the extracted IOM. They defined a group, which included the majority of the primitive IOM type 1 and 2 chondrites, characterized by low CH_2/CH_3 and high H/C ratios. Another spectral group, which included type 3.0 chondrites was characterized by a slightly higher CH_2/CH_3 ratio and a lower aliphatic C-H intensity. Moreover, they noticed lower abundance of aliphatic moieties and lower abundance of OH-bearing phase in more altered meteorites. They suggested this could be a signature of partial oxidation of aliphatic moieties during a mild parent body alteration. Orthous-Daunay et al., (2013) studied the variations of the IOM composition in meteorites showing different degrees of hydrothermal alteration. They concluded that the more altered is the meteorite, the higher is the CH_2/CH_3 ratio, and the more the IOM has an aromatization. There does not seem to be a clear similar tendency on bulk (Quirico, personal communication). A low CH_2/CH_3 ratio could be due to a partial oxidation of aliphatic during the mild parent body alteration (Kebukawa et al., (2011)). We do not have evidences to go further.

In our sample, a peculiarly high CH_2/CH_3 ratio of the aliphatic carbon was observed in region B close to phyllosilicates and carbonates. As discussed above, based on the evolution of the silicates proposed by Leroux et al., (2015), we have inferred that this region is the

most hydrothermally altered in our sample. Region B was also relatively poor in carbons with respect to region C. Higher CH_2/CH_3 ratios imply higher elongation of the aliphatic chains or lower degrees of branching and/or cross-linking. We conclude that longer aliphatic chains and/or a lower degree of ramification in region B were a result of the hydrothermal alteration.

3.1.3 Conclusions of the study in transmission

We have used the Paris meteorite to show the possibility to investigate the heterogeneity of primitive extraterrestrial materials via the combination of full field IR imaging, IR microspectroscopy with synchrotron source and Raman microscopy. Taking advantage of the high signal to noise ratio of the synchrotron source, the speed of analysis and high definition of the FPA images as well as the high resolution and specificity of Raman microscopy, we have obtained a more comprehensive description of the composition of organic and inorganic matter in our sample

We have detected several micro-environnements corresponding to different degrees of aqueous alteration. Based on the study of the mineral phases, we have proposed a scenario which describes the effect of variable aqueous alteration inside our sample. The more primitive part of our fragment was mainly composed of small grains of olivine embedded in hydrated amorphous silicates. The aqueous alteration led, in the first stage, to the disappearance of olivine and enrichment of OH-bearing amorphous silicate. Finally, a higher degree of hydrothermal alteration led to the formation of phyllosilicates and carbonates.

Based on this information about the evolution inside the sample, we have characterized the effect of aqueous alteration on the organic matter. We have shown that the advantage of FTIR spectroscopy is the possibility to characterize all organic matter at once without chemical modification due to extraction, thus preserving the mineral context. We have observed an accumulation of aliphatic rich organic matter in the amorphous silicate and water-rich region, that was also rich in iron. The most altered region was characterized by a lower abundance of aliphatics and a higher elongation of the aliphatic chains or lower degrees of branching and/or cross-linking.

3.2 Study in reflectance

To complement the study of Paris shown above, I participated to a multi-analytical study led by D. Baklouti (IAS) and S. Della Negra (IPNO), on a millimetric chip of the same meteorite. These results will be included in a paper submitted for publication in MAPS. This part of the chapter is entirely based on that paper.

Here, we have studied a millimetric fragment of Paris meteorite, cutted by a diamond saw at MNHN (Museum National d'Histoire Naturelle, Paris, France) and comes coming from the meteorite inner side. A 500x500 μm^2 area was analyzed by a multi-techniques approach: visible and IR reflectance spectroscopies, micro-Raman, TOF-SIMS with imaging, and micro-PIXE were used. We have defined specific area inside this zone with the letters A, B, C and D to help for the discussion (Fig. 3.9). The depths of analysis is about a few μm for the IR and Raman spectroscopies depending on materials absorbencies and only the IR part is presented here. For IR measurements, both set ups described in sections 2.2, were used : the MCT was coupled to the synchrotron for a first set of measurements and some complementary measurements were done with the FPA coupled to the globar source.

3.2.1 Results

Contrary to the previous measurement, done on crushed grain, IR reflectance measurements were here performed on the rough surface of the Paris sample to preserve spatial information and for direct comparison with the other techniques used. Despite this experimental constraint, it was possible to measure IR spectra that are good enough to be interpreted.

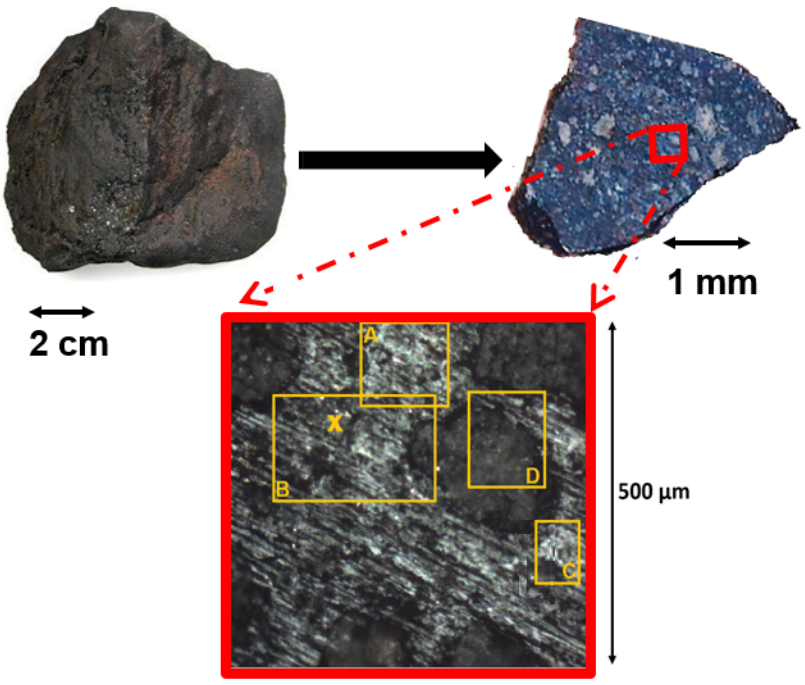

Figure 3.9: the analyzed fragment of Paris meteorite. The principal 500 μm x 500 μm area analyzed is indicated in red with the A, B, C et D regions discussed below.

A first look on Fig. 3.10 and 12 shows that 'reststrahlen' bands (also called 'first surface reflection' or 'surface scattering') dominates the reflectance spectra. This phenomenon is expected and well explained by J. W. Salisbury (Salisbury 1993): we obtain spectra that are similar to reflectance spectra from cleaved surfaces of minerals or from big size powdered particles ($>$ 75 μm of diameter) for which some volume scattering occurs and reduces spectral contrast for reststrahlen peaks, but the backscattered energy remains dominated by surface scattering. Consequently, if we compare our spectra with the one measured on fine grinded powders, we measure spectra with different bands position and shape for the main vibration bands (Si-O, S-O, C-O etc ... stretchings) occurring between 15 and $\approx$ 6 μm. Indeed, our spectra are much similar to IR transmission spectra . Besides, in the 6 - 2 μm range, when some volume scattering occurs, we can detect and identify O-H and C-H stretching vibrations (as troughs instead of peaks, like expected for fine powders reflectance spectra). However, contrary to transmission spectra it remains difficult to detect C-H bands because of their smaller intensity and because of a quite irregular base line.

The first set up (MCT coupled with the synchrotron) gives the spectra presented in Fig. 3.10 and 12. In the matrix area, 6 major components are detected. With this set up, each IR spectrum corresponds to a square area of 20x20 μm^2, therefore most of the measured spectra in the matrix show a variable combination of these 6 major components. We notice the presence of anhydrous and hydrated amorphous silicates (mapped in Fig. 3.11), and some crystalline silicates spread all over the matrix, sulfate and carbonate (precisely mapped in Fig. 3.11 panels a and b), similarly to what we observe in the study in transmission. An iron hydroxide (found in regions A and C in Fig 3.9) was also detected.

3.2.2 Matrix main composition

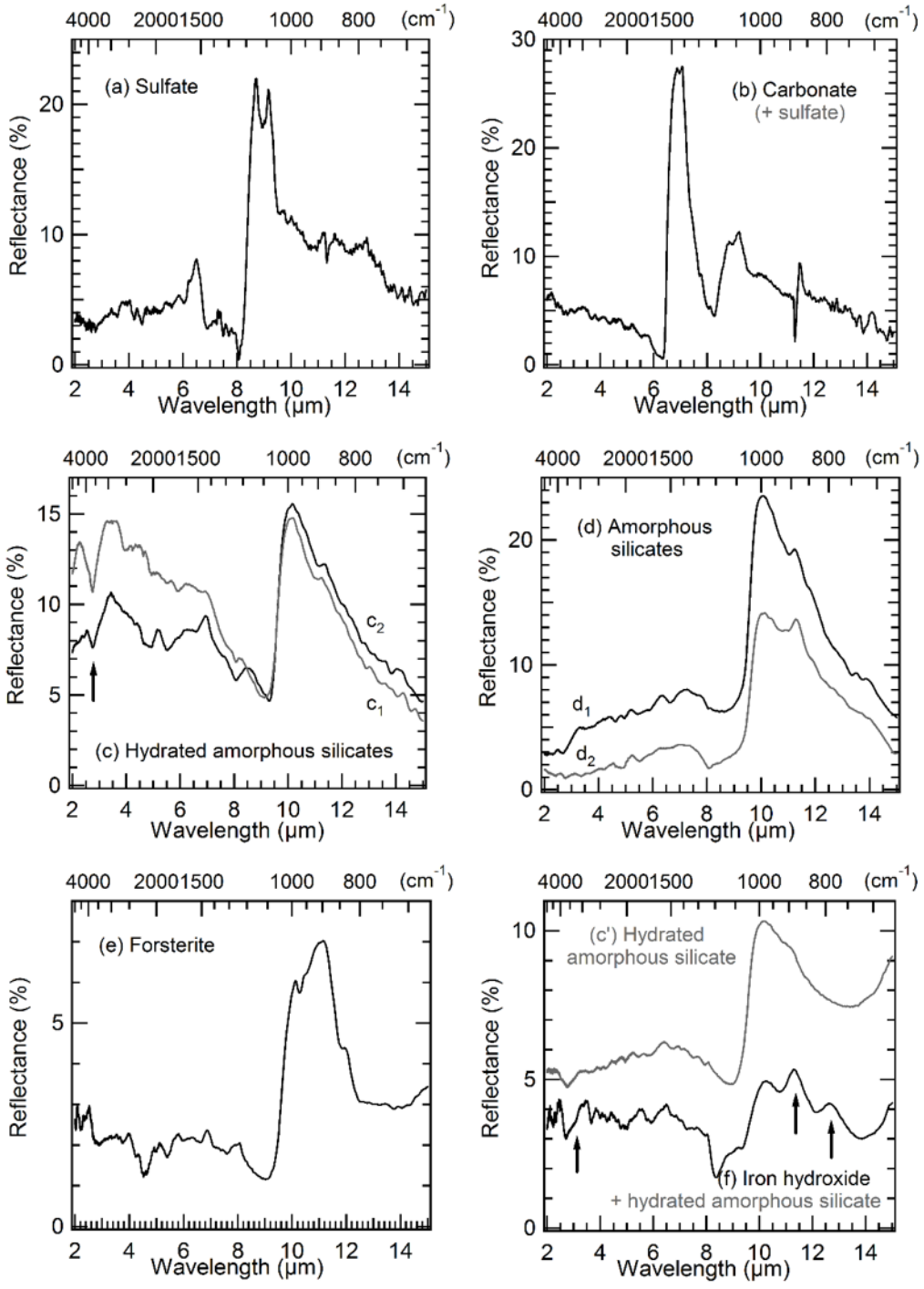

Figure 3.10 : FTIR micro-reflectance spectra showing the major components found in the analyzed regions of the matrix of the 500 x 500 μm^2 chosen surface area. (a) Sulfate spectrum (b) Carbonate (mixed to some sulfate) spectrum. (c) Two hydrated amorphous silicates spectra (the arrow points to the hydroxyl absorption at 2.75 μm). (d) Two

amorphous silicates spectra: d1 is more amorphized than d2 and possibly weakly hydrated. (e) Forsterite found in the matrix at the top right of region B. (f) An iron hydroxide (mixed to a hydrated amorphous silicate) found in regions A and C ((c') is a hydrated amorphous silicate spectrum for comparison). (An offset has been applied on spectra d2 and c' for a better visibility)

The silicates dominating the analyzed area are either anhydrous or hydrated. Most of the identified hydrated silicates spectra (see spectrum c in Fig. 3.10) have a prominent band ranging from 1000 to 975 cm^{-1}, with sometimes a lower band on its shoulder at $\approx$ 880 cm^{-1} (11.3 μm) (the position of these bands is similar to the one observed in transmission), and systematically, the typical OH absorbance band with a relatively sharp feature at $\approx$ 3630 cm^{-1} ($\approx$ 2.75 μm) that is due to the stretching O-H mode of the hydroxyl groups in the octahedral layer of hydrated silicates (Beck et al., 2010; Bishop et al., 2008). A saponite attribution (Beck et al., 2014) is possible according to the position of the prominent band, but it is more probably a partially or totally amorphous phyllosilicate or to be more accurate, a hydrated amorphous silicate. This latter hypothesis is supported by the amorphous silicates spectra dominating the matrix of the analyzed meteorite area. Indeed, the bands position and shape of part of the amorphous silicates spectra found in the matrix are very similar to the hydrated silicates ones, except that the hydroxyl band absorption is absent or comparatively very weak (spectrum d1 in Fig. 3.10). We also detect amorphous silicates (spectrum d2 in Fig. 3.10) showing a stronger 11.35 μm band, indicating a less advanced stage of amorphization (or a more advanced stage of crystallization). The fact that the anhydrous amorphous silicates and the hydrated ones are related is obvious in their IR signatures and indicates that the matrix presents a mixture of different and gradual stages of silicates amorphization/crystallization and hydration.

In the matrix, we also observe sulfates (Fig. 3.10, spectrum a) and carbonates (Fig. 3.10, spectrum b). Very often, their two signatures are spatially correlate (see Fig 3.12 panel a and b). We also note a correlation between the iron hydroxide and the hydrated amorphous silicates signature (Fig. 3.10, spectrum f). This iron hydroxide presents 3 distinguishable and specific bands at 12.7, 11.3 and 3.1 μm (signaled by arrows on the spectrum) that well fits a goethite attribution (O-H deformation vibrations for the firsts bands and O-H stretching for the last one) (Cambier 1986; Ruan et al., 2002). This attribution is supported by Raman

measurements which indicate that it is mixed with a small contribution of hematite.

In region A and C (Fig. 3.9), we observe a small absorption bands around 2850 - 3000 cm^{-1}, generally situated in the shoulder of a more intense OH absorbance band related to a hydrated amorphous silicate contribution (Fig. 3.10). The C-H stretching vibration (attributed to an organic content in the matrix) signs as a small absorption band, not always easy to distinguish from the noisy base line. It is more precisely collocated with part of the hydrated amorphous silicates. The organic content must be quite important to be observed in these reflectance spectra as the spectra are measured in the reflectance mode on the rough meteorite fragment: the C-H stretching vibrations observed are necessarily due to volume scattering. Even though the C-H band intensity is very small compared to the Si-O bands and to what is obtained in transmission measurements (Merouane et al., 2012).

The second set of IR measurements with the globar source and the FPA detector allowed to map part of the previously discussed components over the whole area (see Fig. 3.11). Indeed, as the IR range slightly reduced at high wavelengths, the identified iron hydroxide is not be precisely mapped with this second set of measurements. Moreover, the signal to noise is not good enough to allow an ambiguous mapping of the C-H stretching bands. Fig. 3.11 shows the mappings of the carbonate (panel a), the sulfate (panel b), the silica of the matrix (panel c), the Mg-rich pyroxene ($> En_{80}$, panel d) components, the amorphous silicate (hydrated or anhydrous ones, panel e), the H-O-H bending of water molecules (panel f, with maybe some contribution from a C=C stretching band) and the H-O-H stretching of hydroxyl groups (panel g) of the hydrated amorphous silicates.

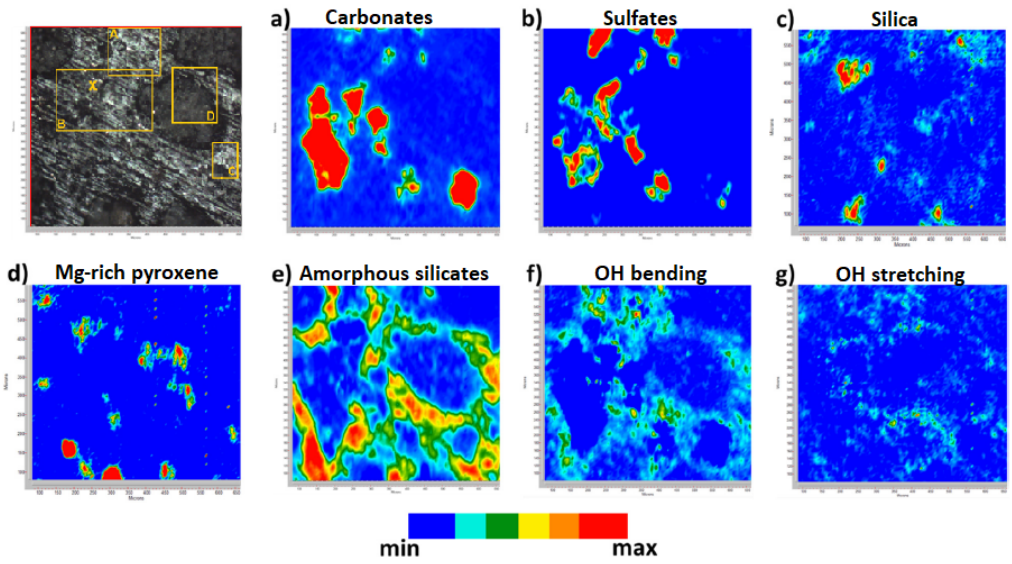

Figure 3.11: Infrared mapping of a) the carbonate component, b) the sulfate component, c) the silica polymorph component at 9.22-9.13 μm, d) the Mg-rich pyroxene (>En_{80}), e) the amorphous silicate Si-O band at 10-10.25 μm, f) the O-H bending band at ≈6.25 μm, and g) the O-H stretching band at 2.75 μm.

We observe a correlation between the distribution of the O-H bending and the amorphous silicate Si-O band (panel e). As a consequence, the H-O-H bending mode doesn't correspond to water adsorbed on the surface, (if it is the case, it would be more homogeneously distributed over area 1) but correspond to the molecular water contained in part of the amorphous silicate structure. This results confirms the one obtained on the study in transmission thanks to correlation diagram (see Fig 3.8). Finally the amorphous silicates are well partially hydrated.

3.2.3 Study of peculiar regions with CAIs and chondrules

In some specific regions, the IR spectra measured are peculiar compared to matrix spectra (g spectra in Fig. 3.12). For instance, in the B region, in the area around the X cross marked on Fig. 3.9, we can observe structures inside the Si-O stretching region that are not found elsewhere in the matrix spectra of the studied area. Even if these features correspond to a mixture of silicates which are difficult to individually identify, we can infer that Mg-rich pyroxene (≈En_{75} (Bowey et al., 2007)) is probably contributing to spectrum g5 (bands at 9.4, 10.4 and 11.4 μm), for example, and a silica polymorph band is clearly present in spectra

g1, g2, g3 and g4 with variable intensities (see arrow on Fig 3.12). Moreover, a broad but weaker band appears at 13.9 μm in part of the spectra measured in that X region (spectra g1, g3, g4, and g5 in Fig. 3.12). This band is possibly due to a spinel. More generally, the IR signature of the X region shares many similarities with the IR spectra measured by Morlok et al., (2008) on different CAI inclusions in various CV ad CO chondrites. This X cross region is then probably a CAI region. The spinel found covers a region that does not exceed an area of 50 x 50 μm^2 around the X cross. The silica polymorph covers a bit larger region around the X cross and overlaps the spinel region. The other silicates are surrounding the spinel, pyroxene unambiguous signature (spectrum g5 in Fig. 3.12) being on the bottom of the X essentially.

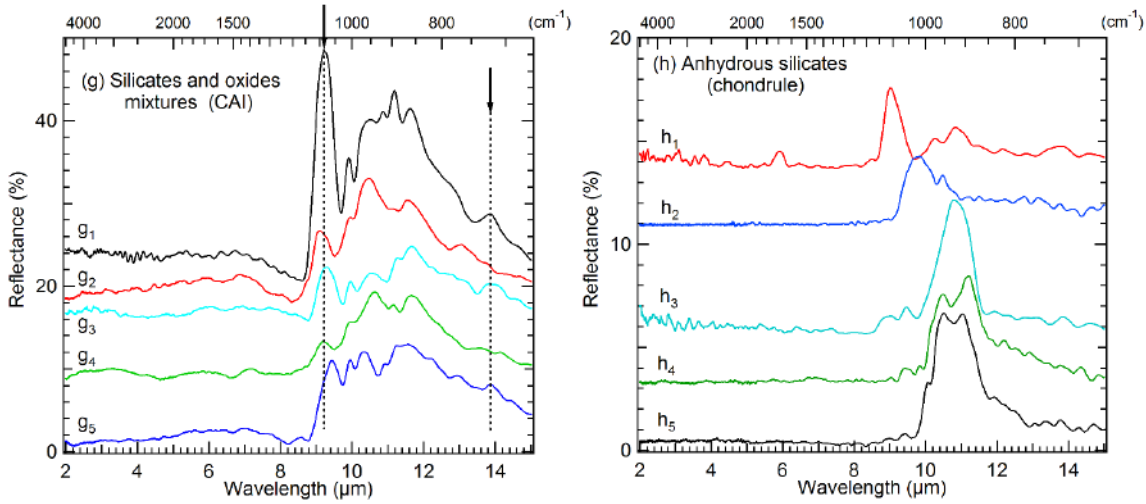

Fig. 3.12: (g) FTIR micro-reflectance spectra of a CAI region (marked by an 'X' cross in Figure 3). (h) FTIR micro-reflectance spectra of a chondrule region. (An offset has been applied on spectra g1, g2, g3, g4, h1, h2, h3 and h4 for a better visibility).

With the first set of IR synchrotron measurements, we have only partly analyzed one chondrule located on the top of region D (see Fig. 3.9). No pure crystalline mineral was measured. The spectra obtained rather correspond to amorphous silicates at different amorphization/crystallization stages and variable compositions: spectrum h2 in Fig. 3.12 probably corresponds to a partially amorphized silicate with an enstatite composition, whereas spectra h3, h4, and h5 would be closer to an olivine composition (Demyk et al., 2004; Morlok

et al., 2010). Another silica polymorph signature is found at 9 μm (spectrum h1 in Fig. 3.12).

3.2.4 Tracing the aqueous alteration

Our IR measurements made directly on the meteorite chunk without grinding it into powder and homogenizing it, let us directly monitor its diversity in silicates structure and water and/or hydroxyl group content, and obviously show a parental/filiation link between these silicates at different hydration and crystallization or amorphization stages.

This millimetric fragment matrix presents a mixture of different and gradual stages of silicates amorphization/crystallization and hydration : the different components go from the hydrated amorphous silicate to the anhydrous crystalline silicate (forsterite is found here in the matrix in the top right of region B). These different stages are also observed in the spectra obtained by Morlok et al., (Morlok et al., 2010) when applying gradual shock experiments on Murchison matrix samples. The samples studied by Morlok et al., are initially dominated by serpentine which progressively turns into an amorphous and anhydrous silicate, and then to olivine under very high shock pressure.

Hydrated amorphous silicates and amorphous silicates (and even some crystalline silicates) are here clearly intermingled in the matrix. Consequently, if either irradiation have transformed crystals into amorphous matter, or shocks have transformed phyllosilicates into amorphous -hydrated or not- silicates, it must have affected the individual grains before they accreted. The only mechanism that could have affected them differently post accretion and could explain the IR observations, would rather be interstitial fluids (water) circulation which could explain the differential 'alteration'. With this conclusion, we confirm the observation done by Leroux et al., (2015) with TEM studies and prove that their hypotheses about the aqueous alteration in Paris matrix and the way its amorphous silicates have been partially turned into hydrated ones and then, eventually into phyllosilicates, is most probably correct. Moreover, the silicates hydration mappings obtained by IR spectroscopy (Fig. 3.11.e and 3.11.g) at a much larger scale (500 x 500 μm^2) than TEM studies (< 1 μm^2), give the fluid circulation path throughout the matrix following the amorphous silicate component.

We have already observed a variability between the distribution of the O-H bending and stretching in transmission (see Fig. 3.4 panels j and k) due to different kind of hydration. Our IR results in reflection also indicate that there are two kinds of hydration signatures on the amorphous silicates: water molecules situated in the interlayer regions of the silicate amorphous structure, and hydroxyl groups covalently bonded to octahedral cations. The mappings of both signatures do not exactly coincide (the brightest spots in Fig. 3.11.f do not all correspond to the brightest ones in Fig. 3.11.e and vice versa) and may indicate two different hydration stages: one would correspond to the penetration of water molecules that progressively become part of the amorphous silicate disordered structure, and the other would consist in forming the hydroxyl group bonds which implies a chemical reaction involving water molecules. The first hydration does not involve the formation of chemical bonds with water and could be favored by the porous structure reported by Leroux et al., The second is a chemical reaction that is probably dependent on pH conditions. However, it would be too speculative to state which process should have occurred first without further evidence from experimental simulation and kinetic studies.

Finally, similarly to what we found in transmission, we do not observe a spatial correlation betwen the hydrated amorphous silicates and the carbonates and sulfates (both are generally associated with aqueous alteration). The carbonate found is a calcium carbonate (according to ToF-SIMS, and more precisely, calcite, according to Raman) with the presence of some potassium (according to TOF-SIMS measurements) . According to previous studies (Lee et al., 2014), this kind of carbonate would indicate a primary stage of aqueous alteration. At least, this would be in tune with the very partial hydration of the silicates present in the matrix.

3.2.5 Conclusions

We studied the distribution of different carbonaceous and mineral phases in Paris both in transmittance and reflectance. With the transmittance study, we can well detect the CH bands and study the heterogeneity of the CH_2/CH_3, but reflectance study allows study at larger scale on a preserve sample. In the meteorite matrix we observed a mixture of different and gradual stages of silicates amorphization/crystallization and hydration, consistent with

the hydrothermal alteration scenario proposed by Leroux et al. (2015). Our IR maps also revealed local heterogeneities in the composition and abundance of the organic matter, that are most probably the result of the hydrothermal alteration.

Chapter 4

Hyperspectral micro-FTIR imaging of irradiated meteorites

Contents

We have previously emphasized compositional heterogeneity as a key to give us information about the history of extraterrestrial samples, but when we study samples coming directly from the surface of an asteroid, the space weathering could also modify the surface properties and thus introduce differences between surfaces. During my thesis, I also had the opportunity to work on the effects of space weathering. With the development of micro-FTIR imaging, we can now quickly analyze large surfaces of irradiated samples, but keeping a micrometric analytical spot. This allows us characterizing the heterogeneity of the meteorites and the irradiation effects at the 20 μm spatial scale. In this chapter, we are going to discuss the effects of space weathering on large heterogeneous surfaces and we are trying to establish spectral criteria on how to distinguish irradiation from compositional heterogeneity effects on asteroid surfaces.

This chapter is entirely based on the following publication:
Brunetto, R., Lantz, C., Dionnet, Z., Borondics, F., Aléon-Toppani, A., Baklouti, D., Barucci, M.A., Binzel, R.P., Djouadi, Z., Kitazato, K., and Pilorget, C., 2018. Hyperspectral FTIR imaging of irradiated carbonaceous meteorites. Planetary and Space Science, Volume 158, Pages 38-45.

4.1 Introduction

Surface alteration processes - also known as space weathering (SpWe), i.e. ion irradiation and micrometeorite impacts - on atmosphereless small bodies induce optical properties changes of the surface detected via spectral variations. Thus, surface alterations imply a physico-chemical difference between the materials composing the uppermost surface and the ones just underneath. Understanding how these modifications act on asteroids and change their spectra will allow a better compositional interpretation of remote observations. Similarly, they will provide valuable support for the planning forthcoming space missions to collect samples of primitive asteroids and bring them back to Earth: Hayabusa2/JAXA at (162173) Ryugu (Takagi et al., 2011) and OSIRIS-REx/NASA at (101955) Bennu (Lauretta et al., 2015). Collecting asteroid materials of likely primitive composition, i.e. unaltered by SpWe, will be of particular interest for studying them in details using state-of-the-art laboratory techniques, with the ultimate goal of obtaining information about the composition of materials that formed in the early Solar System.

Research of unaltered areas on an asteroid surface has been focused on well known possible SpWe effects on spectral properties in the visible and near-infrared ranges (VIS-NIR refers to the range 0.4-2.5 μm in the following): changes of albedo and spectral slope (see the examples of Stype asteroids Eros (Clark et al., 2001) and Itokawa (Hiroi et al., 2006)). SpWe of silicate-rich S-type asteroids are well understood, especially the role of nanophase reduced iron particles (npFe^0) producing darkening and reddening (increasing slope toward longer wavelengths) of their surfaces (Clark et al., 2002). On Itokawa, multicolor SpWe maps have been obtained in the visible spectral range (Ishiguro et al., 2007). Hayabusa spectrometers at Itokawa showed SpWe effects on different regions of the surface (Hiroi et al., 2006).

Returned Itokawa grains, analyzed in the laboratory show multi-layer structures related to SpWe effects, including amorphized silicates and npFe^0, as well as iron sulfide inclusions (Noguchi et al., 2011, 2014). The VIS-NIR spectral slopes of returned Itokawa grains were found to be redder than unirradiated LL chondrites (Bonal et al., 2015), confirming the general trend of reddening and darkening first observed on the Moon (Adams and McCord, 1973) and later on among S-type asteroid families (Binzel et al., 1996). Numerous laboratory experiments on analog materials, terrestrial silicates and ordinary chondrites (OCs), have been able to reproduce SpWe effects and spectral trends using ion (solar wind simulation) or laser (micrometeorite impacts simulation) irradiation (see a review in Brunetto et al. (2015)). However, it is still unclear which spectral changes upon SpWe we should expect on the primitive carbon-rich asteroid classes and more specifically on Bennu's and Ryugu's surface. These C-complex asteroids (DeMeo et al., 2009) are expected to contain organic compounds and small amounts of water. Studies based on asteroids spectroscopic observations showed both reddening (Lazzarin et al., 2006; Fornasier et al., 2016; Kaluna et al., 2016) and blueing (Nesvorny et al., 2005; Lantz et al., 2013) effects of spectral slopes.

Some laser and ion irradiation experiments on primitive meteorites have been performed in the last few years (see Table 1 in Lantz et al. (2017)). Matsuoka et al., (2015) performed laser irradiation of the Murchison CM meteorite and observed spectral darkening and blueing with increasing laser energies. Hiroi et al., (2013) reported laser irradiation experiments of several carbonaceous chondrites (CCs), showing different VIS-NIR spectral variations on different meteorite samples. Lantz et al., (2017) performed a large experimental campaign on ion irradiation of CCs to better understand the SpWe of dark objects. Brightening/blueing or darkening/reddening spectral effects were observed in the visible range depending on the initial albedo/composition, thus demonstrating that composition plays a major role in determining the visible SpWe trend. Overall, the laser experiments by Hiroi et al., (2013) and ion irradiation experiments by Lantz et al., (2017) consistently point towards a blueing trend for hydrous carbonaceous chondrites and a reddening trend for the anhydrous ones. The brightest anhydrous carbonaceous materials like the COs and CVs (albedo, a $>$ 8-10%) mainly composed of chondrules and poor in carbon follow the same trend after irradiation as the S-types and OCs. The dark meteorites like CMs and CIs (a $<$ 4-5%), rich in hydrated minerals and matrix dominated, have the opposite spectral behavior: the carbonaceous phases, to-

gether with metals and sulfides, dominate the optical effects in the visible, producing blueing upon irradiation. The blueing is accompanied by brightness changes: shorter wavelengths becoming brighter, and the longer darker.

This has important consequences for missions visiting dark asteroids, and in particular for Hayabusa2 and OSIRIS-REx: as VIS-NIR spectral changes upon irradiation depend on the original composition, one should have additional spectral evidence to determine the original composition and be able to separate young (pristine) from old (irradiated) terrains at Ryugu and Bennu. From the featureless spectra of the 0.4-2.5 μm range, it is impossible to unambiguously determine the composition of C-complex asteroids. Our experiments bring additional information to bear on solving this issue. Here we report new measurements on the previously studied CV Allende (Brunetto et al., 2014) and CM Murchison (Lantz et al., 2015) using infrared micro-reflectance spectroscopy from 2.5 to 12 μm. We choose these samples as a case for a typical thermally metamorphosed surface (Allende) and a typical aqueously altered surface (Murchison). Using the band position of the 2.7 and 10 μm features and acquiring maps of sample surfaces - which will also be done by spacecrafts -, we provide experimental evidences that SpWe and compositional heterogeneity can be separated at the asteroid surfaces. We also discuss the detectability of SpWe effects by instruments onboard Hayabusa2 and OSIRIS-REx.

4.2 Experimental setup

Four pellets (13mm diameter) of the Allende and Murchison meteorites were irradiated using 40 keV He^+ and Ar^+ ion beams at the SIDONIE implanter of CSNSM-Orsay (France). Four irradiation spots (4mm diameter) were produced on the surface of each pellet, with different ion doses: 5.10^{14}, 2.10^{15}, 1.10^{16}, 3.10^{16} for He^+ ions/cm^2, and 1.10^{14}, 5.10^{14}, 2.10^{15}, 6.10^{15} for Ar^+ ions/cm^2. Details of the irradiation conditions are described by Brunetto et al., (2014) and Lantz et al., (2015).

The FTIR hyperspectral imaging measurements reported in this study were performed with an Agilent Cary 670/620 micro-spectrometer equipped with a 128x128 pixels FPA (Focal

Plane Array) detector, installed at the SMIS beamline of the SOLEIL synchrotron (France). Mid-IR (MIR, 4000 to 850 cm^{-1} or 2.50-11.76 μm) spectra were measured using the internal globar source at 8 cm^{-1} spectral resolution. The infrared maps were acquired in reflectance geometry, with respect to gold references.

The sample was projected on the FPA through a 15x objective (numerical aperture 0.62), providing a field of view of about 700 x 700 μm^2 and a projected pixel size of about 5.5 μm (spatial sampling of the infrared maps). 16384 spectra were collected simultaneously without moving the X-Y stage of the microscope. In one complete acquisition we accumulated 512 or 1024 scans. Larger spectral mosaics were acquired by moving the X-Y stage and acquiring several 700 x 700 μm^2 tiles, to cover mm to cm sized areas of the irradiated pellets. This enabled mapping the MIR features over a large portion of the sample, both on unirradiated and irradiated areas with different doses. In the case of the large mosaics, a 4-pixels bin was applied producing a pixel size of about 22 μm, and in this case we accumulated 16 or 32 scans per tile of the map. Typical acquisitions lasted 1-2 h and produced 50000 to 500000 spectra.

Thanks to the imaging microscope, we obtained visible and MIR images over large portions of the pellets. The visible images allow to quickly visualize the heterogeneity ($\approx$20 μm scale) of the pellet and spot grains with different compositions, colors, and sizes. However, variations due to irradiation effects are very hard to detect by visual inspection. The MIR images we show in the following section are much more descriptive of the irradiation-induced variations and easily highlight the irradiated zones.

Note that the irradiation experiments and the hyperspectral imaging measurements were performed in two different laboratories, and the spectra were thus measured ex situ. The time-span between the two was about two years. During this time the samples have been exposed to different extents to vacuum, controlled N2-atmospheres and laboratory air. During these cycles, potential air-exposure effects such as oxidation cannot be excluded. However, if present, they do not seem to have any significant effect over time on the spectral modifications shown below, as we have verified by comparing the average spectra and the band shifts after irradiation obtained in the hyperspectral micro-imaging with the bulk spectral

measurements reported by Lantz et al., (2015).

4.3 Results

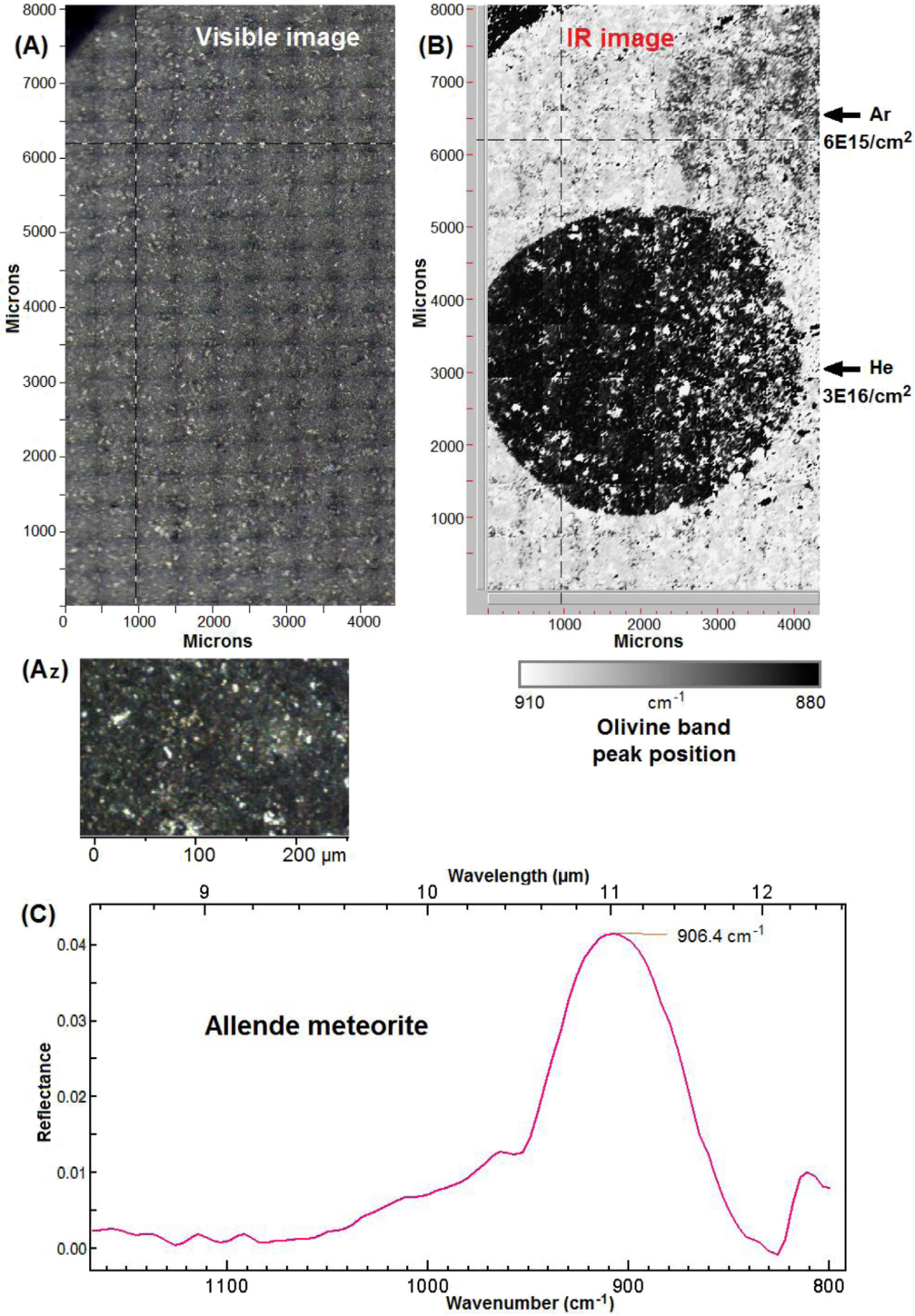

Figure 4.1: Mid-Infrared spectral imaging of the Allende meteorite, with two irradiation areas at different ion dose. Panel (A): visible image showing the typical heterogeneous composition of the meteorite pellet at the tens of microns spatial scale (zoom Az). Panel (B): infrared map showing the peak position of the 11-μm band in gray scales, with white for short and black for long wavelength peak position. Panel (C): a typical matrix spectrum of Allende with the prominent 11-μm anhydrous silicates band collected on one spot of ≈20 μm.

The bottom panel of Fig. 4.1 shows a typical spectrum of the CV Allende meteorite taken on the unirradiated area. The main peak at $\approx$ 11 μm (around 910 cm^{-1}) is due to the olivines (Hamilton 2010), which are the dominant silicate of the matrix of Allende and have a typical composition of Fo_{53} (Peck 1983). The position of this olivine band shifts to longer wavelengths after irradiation (Brunetto et al., 2014). We also present the visible image of the pellet: brighter and dark grains are visible down to a scale of $\approx$ 20 μm but the irradiated areas are not detected. The corresponding IR image shows the map of the maximum reflectance value within a specific range, between 910 and 880 cm^{-1}, thus reporting a gray scale distribution of the olivine band peak position. In this way, it is possible to easily evidence 'dark' areas corresponding to the irradiated areas. Because the He^+ irradiation has more effect than the Ar^+ irradiation (see deails in Brunetto et al., (2014)), the associated areas do not have the same color. One also has to note that even within the irradiated area several grains are very bright/white. These grains have a composition different than Fo_{53} olivine: using the data reported by Hamilton (2010) we determined that they are mainly fragments of chondrules with Mg-rich olivines (Allende chondrules typically have Fo $>$ 90 olivines, e.g. Simon and Haggerty (1980)) and their bands peak far out of the edges of the defined spectral range, i.e. they are out of the gray scale. Similarly, some grains of different composition (such as diopside, nepheline or spinel commonly present in the refractory inclusions, Posch et al., (2007)) in the non-irradiated areas have their peak position below 880 cm^{-1} thus appearing as black spots in the image.

	Parameter	Allende unirradiated	Allende irradiated	Murchison unirradiated	Murchison irradiated
Main Si-O band	Mode (highest probability)	11.08 μm	11.39 μm	9.89 μm	9.98 μm
	Mean	11.046 μm	11.289 μm	9.901 μm	9.967 μm
	Standard deviation	0.05 μm	0.08 μm	0.04 μm	0.05 μm
	Variance	0.01 μm	0.03 μm	0.001 μm	0.002 μm
	Skewness	2.24	2.64	2.18	0.84
-OH band	Mode (highest probability)	-	-	2.73 μm	2.77 μm
	Mean	-	-	2.738 μm	2.762 μm
	Standard deviation	-	-	0.02 μm	0.02 μm
	Variance	-	-	0.003 μm	0.002 μm
	Skewness	-	-	0.33	0.17

Table 4.1: Relevant statistical parameters for the distributions shown in Figs. 4.4 - 4.6, for the main silicate bands (olivine for Allende and hydrated silicates for Murchison) and the -OH band (observed in Murchison). A relatively smaller shift is observed for the -OH band, although it remains statistically significant (about 2σ distance between the modes).

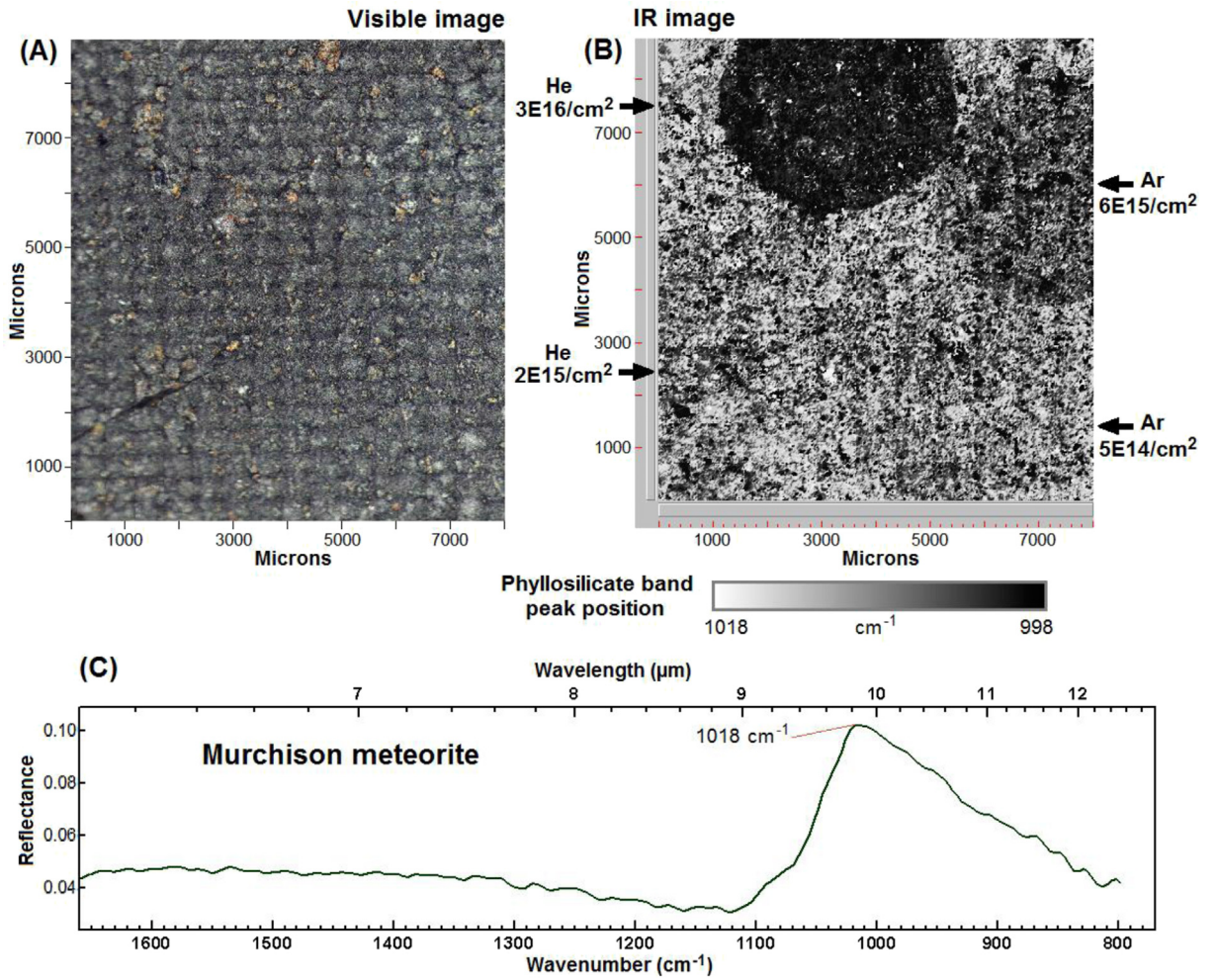

Figure 4.2: Same as Fig. 4.1, for the Murchison meteorite, with the four irradiation areas at different ion doses. Here the typical spectrum (collected on one pixel of about about 20 μm) is dominated by the hydrated silicate band at 10 μm.

The same procedure has been applied to the CM Murchison meteorite to produce Fig. 4.2. The visible image of the pellet shows a higher heterogeneity within the matrix compared to Allende which appeared much more homogeneous. On the Murchison sample, the main band at $\approx$ 10 μm is associated with Si-O stretching of hydrated silicates (Lantz et al., 2015), the dominant matrix mineral of this meteorite and more generally of CM meteorites (see e.g. Beck et al., (2014) for a detailed analysis of the 10-μm feature). Here we present a large area of the pellet with the four irradiation zones. The IR image maps the peak position between 1018 and 998 cm^{-1}. The highest irradiation areas are easily detected, while the two lower doses are not, indicating that irradiation effects are spectrally non-detectable at these two doses. Like on Allende, the He^+ irradiation has more effects than the Ar^+ one. This is

probably related to the combination of a deeper penetration depth of He^+ ions with respect to Ar^+ (about 300 nm vs. 40 nm), and to the highest fluence used for He^+ (Brunetto et al., 2014).

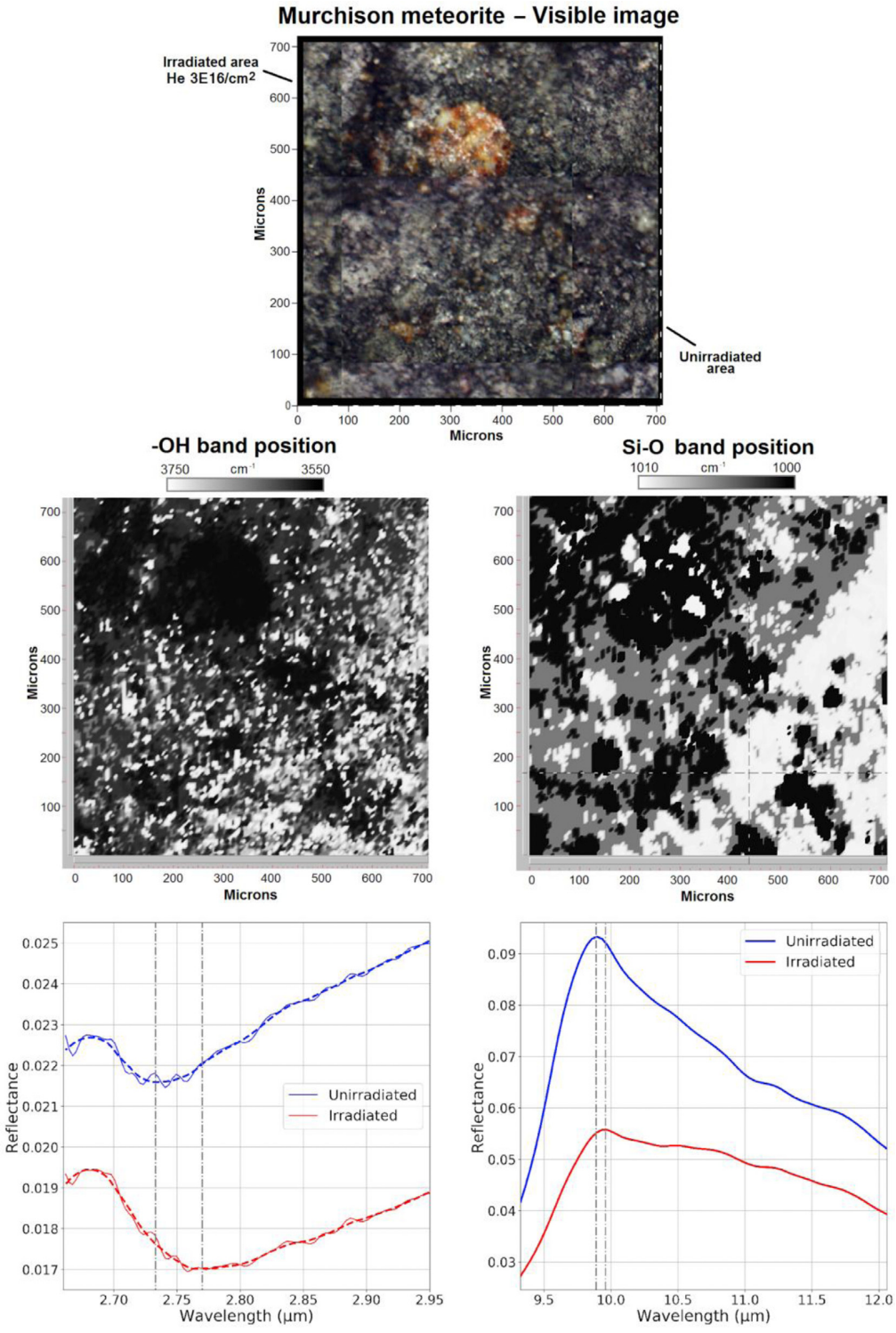

Figure 4.3: Zoom on Murchison meteorite pellet covering an unirradiated area and the irradiated area with 3.10^{16} He^+/cm^2. Top: Visible image. Central panels: IR image of the peak position at ≈2.75 μm (left) and at ≈10 μm (right). Lower panels: typical IR spectra (obtained by averaging about 100 spectra of single positions with similar composition) of the irradiated and unirradiated areas around ≈2.75 μm (left) and at ≈10 μm (right) showing the behavior of the hydrated silicate component dominating the matrix. The vertical dash-dot lines are traced to guide the eye on the peak positions.

Fig. 4.3 compares the effects of irradiation on the band peak positions of Murchison hydrated materials in two key spectral ranges: the above discussed 10 μm peak (right panel) and the band associated to the -OH stretching within hydrated silicates at ≈ 2.7 μm (left panel). Typical spectra of the unirradiated and irradiated areas are shown in the lower panels. We only show a 700 x 700 μm transition zone between the unirradiated area and the one at the highest irradiation dose with 3.10^{16} He^+/cm^2 (upper left part on the image) to illustrate that irradiated and unirradiated areas can be separated also at small scales (the pixel size in this image is 5.5 μm). On the visible image, some orange-colored grains are observed, in particular one large 100 μm diameter grain is located in the upper middle, surrounded by matrix material. These grains are spectroscopically identified as anhydrous silicates (mostly olivine) and thus appear black in both IR images because of their different composition compared to the surrounding matrix. The transition between the unirradiated and irradiated zones is easily seen on the image at 10 μm due to the strong spectral peak shift in the matrix. The transition is less noticeable on the 2.7 μm image, essentially because this band is more difficult to map. This is due to the fact that the intensity of the -OH stretching band with respect to the spectral continuum and its signal to noise ratio are both lower than in the case of the 10 μm band. Note that the irradiation-induced spectral shift of the 2.7 μm band is smaller than the 10 μm band when measured in nm (≈ 40 nm vs. ≈ 100 nm) but higher when measured in wavenumbers (≈ 50 cm^{-1} vs. ≈ 10 cm^{-1}).

In Fig. 4.4 we present the histogram of the distribution of the silicates band peak position on the pellet of Allende. In gray we show the distribution without separating unirradiated from irradiated areas. The maximum is centered at 11.1 μm. We overplot the same kind of distribution for data extracted exclusively from an unirradiated zone and from the irradiated area with the highest dose. The 'irradiated' distribution is centered at 11.4 μm, so

the irradiation effect is seen thanks to a peak shift of about 300 nm. We do observe the same pattern on Murchison in Figs. 4.5 and 4.6, but with smaller shifts: the Si-O band of hydrated silicates centered around 9.9 μm shifts of about 100 nm in the MIR, and their -OH band around 2.73 μm is shifted of about 40 nm. Fig. 4.5 also shows that at the highest doses used in our experiments it is possible to separate compositional heterogeneity from irradiation effects: the positions of anhydrous silicate main bands are clearly separated from the hydrated silicates distribution even considering the irradiation-induced spectral shifts. In the spectra before irradiation, the anhydrous silicate band at about 10.5 μm is essentially due to olivine. This band also shifts towards longer wavelengths, and the spectral shift is larger in this case than in the Si-O band of hydrated silicates observed in the same meteorite sample (about 300 nm vs. 100 nm).

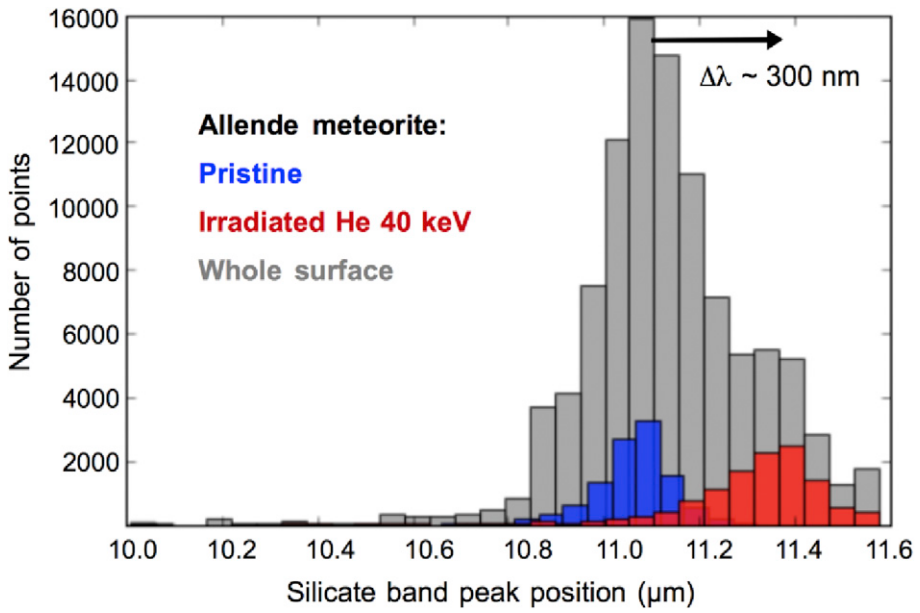

Figure 4.4: Histogram showing the band peak position of all spectra collected on the Allende pellet. The gray data include a large surface of the pellet (with both unirradiated and irradiated areas) while the red data were acquired on the irradiated area with the highest dose of He and the blue data were extracted from a small virgin area.

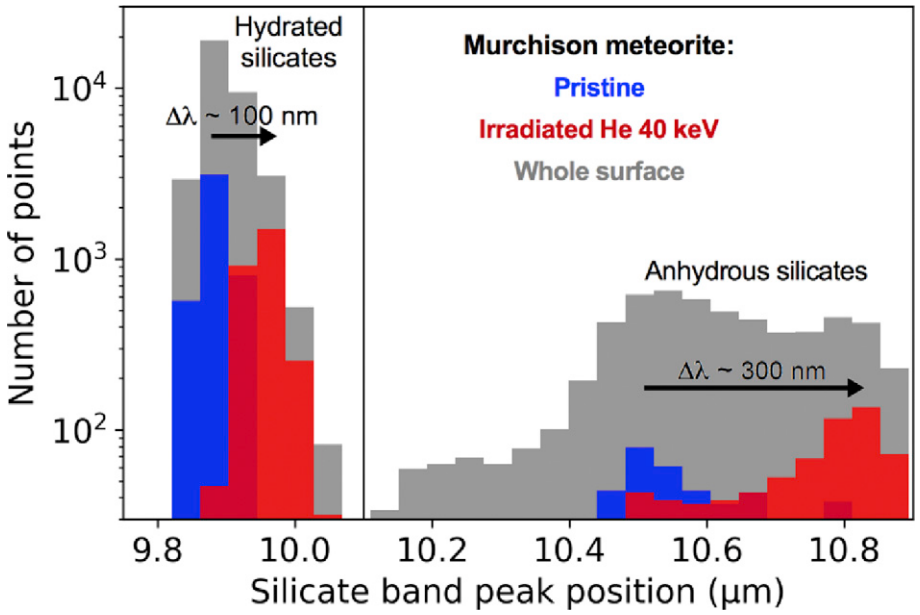

Figure 4.5: Same as Fig. 4.4 for Murchison pellet. Different families of Si-O stretching bands are detected in this sample. The ones above 10.2 μm are due to different anhydrous silicates (mainly olivine around 10.5 μm), those below are due to the hydrated silicates dominating Murchison matrix. A y-log scale is used to better visualize the two families of the main Si-O bands. The spectral shift is larger for anhydrous than hydrated silicates.

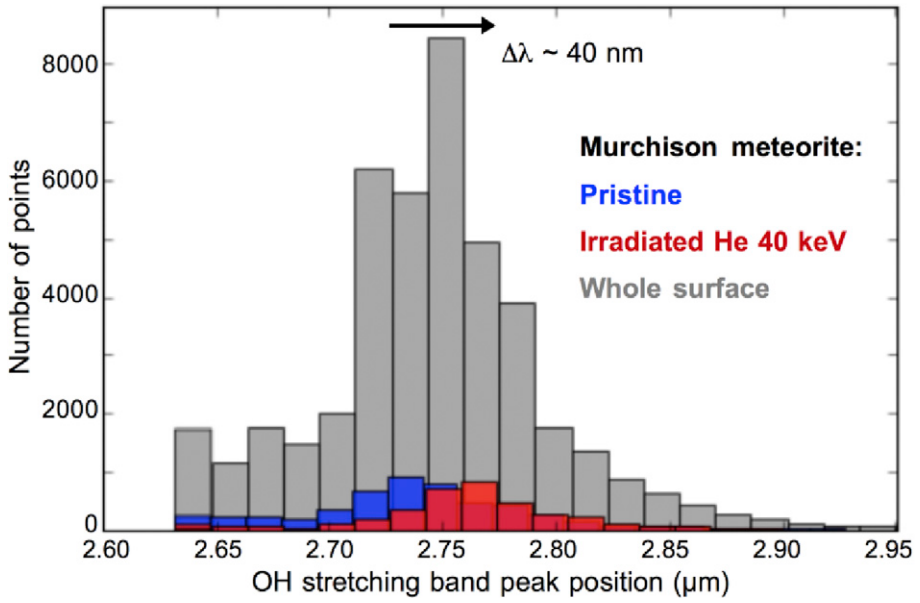

Figure 4.6: Same as Fig. 4.5 at shorter wavelengths, for the -OH stretching band at 2.7 μm of the hydrated silicates dominating the Murchison sample. The spectral shift is smaller than in the mid-infrared.

In Table 4.1 we provide some statistical parameters for the distributions shown in Figs.

4.4-4.6. The distributions are not gaussian nor symmetric, which explains why in most of the cases the mode (most probable value) and the mean are not the same. The skewness provides an estimate of the asymmetry of these distributions. For all the main features (the main Si-O band of olivine for Allende and the hydrated silicates for Murchison, and the -OH band for Murchison) we observe statistically significant shifts after irradiation. However, the shifts are much more significant for the anhydrous Si-O bands (about 4-6 σ) than for the hydrated Si-O bands (only about 2 σ). Due to the asymmetry of the distributions, these shifts are better evidenced when considering the mode rather than the mean values.

4.4 Discussion

Both our previous study of several irradiated CCs and the laser experiments performed by Hiroi et al., (2013) clearly indicate that the initial composition rules the trends on reflectance and slope variations in the VIS-NIR (0.4-2.5 μm) range after irradiation (see Fig. 3, 10, and 13 in Lantz et al. (2017)). The spectral variations for Tagish Lake (initial albedo $< 4\%$) are quite clear and easy to detect. For CM chondrites however, the variations are smaller than for Tagish Lake: e.g. less than 20% visible albedo variations for CMs vs. about 40% for Tagish Lake (Lantz et al., 2017). According to these results, asteroids whose albedo lies in the 4.5-9% range upon irradiation should show VIS-NIR slope and albedo relative variations of the order of 0.1 μm and 10% respectively. This may explain the little color and albedo variations observed on asteroid Mathilde (albedo of 0.041-0.053, Clark et al. (1999)). More specifically, Lantz et al., (2015) reported that the SpWe VIS-NIR slope modifications for Murchison (under the same irradiation conditions reported here) were smaller than effects due to geometry of observations and other surface properties of the grains (roughness, porosity, grain size): with an albedo around 5%, this meteorite is a typical case for those objects whose initial composition/albedo makes SpWe hard to be detected using the VIS-NIR only.

Because Ryugu and Bennu have a geometric visible albedo of 6.3 +/− 0.2% and 4.5+/− 0.5% respectively, we anticipate changes in the visible range due to SpWe effects that are smaller of those produced by other effects such as grain size, geometry of observations and porosity. Moreover, even if slope and albedo variations are observed locally due to possible

compositional heterogeneities, the visible data alone would not be able to remove the ambiguity on which terrain is more pristine: would a given terrain become redder like CO/CV or bluer like CM/CI upon SpWe?

Our experiments indicate that performing spectral imaging of the 3 and 10-11 μm diagnostic features is one key to solve the SpWe ambiguity. In the irradiated areas of the meteorites, we observed spectral modifications of all silicates. In particular, we detected spectral shifts towards longer wavelengths of all diagnostic infrared bands after irradiation. Murchison, a meteorite which underwent aqueous alteration, has the -OH band near 2.7 μm displaced of about 40 nm to longer wavelength after irradiation (see Fig. 4.6). A clearer effect happens farther in the IR with the longward shift of the Si-O bands near 10 μm: both Murchison (hydrated) and Allende (which underwent thermal metamorphism) show this trend (see Figs. 4.4 and 4.5). It is interesting to notice how the irradiation-induced spectral shifts are larger and about 3 times (considering the respective standard deviations) more significant for anhydrous than hydrated silicates.

In the case of anhydrous silicates, the IR bands shift towards the wavelengths range that are typical of a magnesium-poor composition (Hamilton 2010). This may be the result of preferential sputtering (a differential sputtering of atoms near the surface; the lighter Mg being more easily sputtered backwards than the heavier Fe) (Hapke et al., 1975) accompanied by silicate amorphization (seen thanks to the broadening of the bands, and confirmed by Raman) (Brucato et al., 2004; Demyk et al., 2004). The formation of npFe^0 after sputtering and vaporization/condensation process (Hapke et al., 2001) is possible but it cannot be confirmed with the spectroscopic data only and requires complementary analyses, such as high resolution transmission electron microscopy of the uppermost irradiated layers (Noguchi et al., 2014; Keller and Berger, 2014). In the case of hydrated silicates, our experiments show that ion irradiation induces smaller band shifts than on olivine. The reason behind this different behavior is not clear at this stage of our investigation. It may be due to the fact that the hydrated silicates initially present in the meteorite are not entirely crystalline (= phyllosilicates), but possibly much more structurally disordered (= partially amorphous) than the anhydrous components (an olivine signature is clear, for instance). In that case, irradiation will induce a drastic structural change for crystalline components, whereas a more

subtil effect will be seen for already disordered structures. Further analyses including electron microscopy will be necessary to verify this hypothesis and clarify what physico-chemical mechanisms cause the observed spectral modifications on the hydrates silicates.

Thanks to our new micro-spectral imaging data, we have been able to separate the irradiation effects from the compositional heterogeneity typical of chondritic materials. The most remarkable observation is that the band position can be mapped over the shift range and this shift is so sensitive to ion bombardment that irradiated areas on samples of a CM chondrite are clearly distinguishable from unirradiated areas down to the scale of tens of microns. This would be impossible to achieve based on VIS-NIR colors and albedo alone (see Fig. 4.3). Different doses corresponding to different exposure ages at the asteroid can also be detected (see Fig. 4.2). There is a range of irradiation doses where SpWe has effects that are smaller than the spectral variations that are due to the heterogeneous composition of the chondrites; above 5.10^{15} - 1.10^{16} ions/cm^2 there is clear evidence of damages on minerals, and SpWe effects can be easily distinguished from compositional heterogeneity.

The ratio between the irradiation fluences used in the laboratory and the solar wind flux at a given distance from the Sun provides an estimate of the timescale for which the spectral alterations occur in space at that distance. In this way, the effects caused by ion bombardment on S-type asteroids at about 1 AU were estimated to saturate between 10^4 and 10^6 years (Hapke et al., 2001; Strazzulla et al., 2005; Loeffler et al., 2009). However, even though the SpWe induced by ions is a relatively efficient process, there are many S-type asteroids that are not fully weathered, even though they are likely older than the above estimated timescale. This indicates that rejuvenating processes such as small (non-destructive) impacts or planetary encounters (Binzel et al., 2010) are able to partially resurface the asteroid, which effectively lowers the SpWe rate. This has been confirmed by laboratory analysis of Itokawa particles that showed short exposure times (Noguchi et al., 2014). In the case of our experiments on carbonaceous meteorites, the highest doses we use (3.10^{16} He^+/cm^2) correspond to timescales of about 10^2-10^3 years at 1 AU (a detailed calculation can be found in Brunetto et al., (2014)). Thus from Fig. 4.2 we infer that based on IR spectral mapping, SpWe effects would be observable on a region of a C-rich near-Earth asteroid whose surface age is of the order of 10^2-10^3 years. However, Fig. 4.2 also tells us that exposure times about 10 times

smaller (10^1-10^2 years) would not be detectable. This may have interesting implications for the determination of asteroid surface ages in the Hayabusa2 and OSIRIS-REx missions.

We also determined which spectral features are more sensitive to SpWe: the main Reststrahlen Si-O band of the anhydrous silicates (olivine in particular) is the most affected feature by a factor of about 3 with respect to the Si-O feature of hydrated silicates. The -OH band shift seems more difficult to evidence with respect to its variations due to the compositional variety (e.g., degree of aqueous alteration) typical of CM chondrites. Therefore, the distribution of the composite 2.7 μm band alone may not be enough to discriminate the space weathered regions, and other complementary spectral indicators such as spectral slopes may be necessary.

This defines new laboratory-based spectral criteria to describe asteroid surface alteration by SpWe. These criteria can be applied to the spectral observations of instruments onboard the Hayabusa2 and OSIRISREx spacecrafts. OSIRIS-REx carries a Visible and Infrared Spectrometer (OVIRS; Reuter et al., (2018)) and a Thermal Emission Spectrometer (OTES; Christensen et al., (2017)) covering the spectral ranges of 0.4-4.3 μm and 5.7-100 μm respectively. These instruments will provide global spectral maps at 20- and 40-m resolution, and local spectral information of the sampling site at 2- and 4-m resolution, respectively. Hayabusa2 also carries a remote sensing Near-Infrared spectrometer (NIRS3; Iwata et al., (2017)) to observe at wavelength of 1.8-3.2 μm, and to perform a global mapping at 20-m spatial sampling and SCI crater observations at 2-m sampling. The hyperspectral near-infrared microscope MicrOmega (Bibring et al., 2017) implemented within the MASCOT lander (Ho et al., 2017) is designed to characterize in situ the surface materials of the target from 0.99 to 3.65 μm (image size of 3.2x3.2 mm^2 with spatial sampling of 25x25 μm^2).

We find that the band modifications we observe on irradiated meteorites will all be observable by instruments onboard these missions (see Table 4.2). This is extremely promising in view of building reliable SpWe maps of both asteroids Ryugu and Bennu. Note however that the spectral shifts should be easier to detect for anhydrous than hydrated silicates, and in particular the irradiation effects on the hydrated silicates at 10 μm may result at the limit of the spectral resolution for OTES.

Mission	Instrument	Spectral resolution	Band	SpWe expected shift
Hayabusa-2	NIRS3	18 nm		
	MicrOmega	$\approx$ 15 nm	2.7 μm	$\approx$ 40 nm
OSIRIS-REx	OVIRS	$\approx$ 13 nm		
	OTES	$\approx$ 90 - 100 nm	10 - 11 μm	$\approx$ 100 - 300 nm

Table 4.2: Detectability of SpWe effects in the NIR-MIR range for spectrometers onboard theHayabusa-2 and OSIRIS-REx missions. Band shifts after irradiation (SpWe) should be observable by both missions.

4.5 Conclusions

We performed new analyses of ion irradiated samples of carbonaceous chondrites to provide better constraints on the understanding of space weathering effects of primitive asteroids. We show that the band shifts after irradiation detected in the infrared (2-12 μm) spectral maps provide useful tools to interpret the spectral variations that will be observed by Hayabusa2 and OSIRIS-REx on their targets. These sample return missions will cast light on the processes that prevailed in the early Solar System and on the delivery of water and complex organics to the primitive Earth.

Our laboratory-based criteria may provide fundamental support on how to distinguish SpWe from compositional heterogeneity effects at the surface of asteroids. The anhydrous silicates showed spectral shifts about 3 times more significant than the hydrated silicates. Thus in the case of the hydrated surfaces, the MIR data will need to be combined to albedo and slope changes in the VIS-NIR range to clearly detect SpWe. Then, imaging data will be necessary to link SpWe spectral evidence with surface features (cratering, landslope, etc.). Thus, the spectral data will need to be put in context with the geological structures to constrain relative ages of different terrains, and these will provide the necessary information to remove the ambiguity on the albedo and slope variations discussed above. Ultimately, the infrared spectroscopic data may have important implications in view of surface selection for sample return.

Chapter 5

Analytical methods in 3D

Contents

Many IR studies were led on extraterrestrial samples in our group (Merouane et al., Brunetto et al., ...) but most of the time, the sample was crushed, cut or at least partially destroyed. As I showed in Chapter 3, crushing between diamond windows has the advantage of reducing scattering effects but has the drawback of destroying the original 3D structure. Samples cannot then be used for other analysis and study of co-localization of different phases is much more complicated in a crushed sample as grains initially in contact with each other could be separated after the crushing and vice-versa. Finally, physical characterization like estimation of original porosity of the sample is not possible anymore.

During my Ph.D. thesis, I tried to go beyond this limitation and develop a setup which allows a physical-chemical characterization of the structure and detection of organic and mineral phases without destroying the 3D structure of our precious samples. Until recently, 3D characterization of samples has been mainly performed by X-ray Computed Tomography (X-CT). Only one paper has described IR tomography on extraterrestrial sample (see Yesiltas et al., 2016).

X-CT is a very useful technique used to characterize the internal structure and physical properties of samples, including precise shape, internal structure, and porosity, without destroying them and with a high spatial resolution.

This technique has been already used on extra-terrestrial materials, see for instance Ebel et al. (2007), for application on meteorites, or Tsuchiyama et al. (2011), for example on Itokawa particles. It has been used to characterize the mineral phase, and to identify minerals inside samples.

During my Ph.D. thesis, I implemented IR micro-tomography, similar to the setup described in Martin et al., 2013, to obtain chemical information complementary to X-CT. As IR spectroscopy is sensitive to the organics, water and mineral phases, we can map all these

components and gather information about their co-localization in three dimensions. Then, we can analyze X-CT and IR tomography data recorded on the same samples to obtain a complete physical-chemical characterization. As X-CT is a well-known method, we used knowledge and software developed for X-CT as a first step for the development of our experimental method. This will be described in the beginning of this chapter: I will explain the principle of the tomography measurement and reconstruction for a given energy. Then I will describe our setup, the data pre-treatment and software used for IR tomography reconstruction. Finally, I will explain the advantage of IR tomography, compare this technique with X-CT and describe some experimental limits encountered during my Ph.D.

5.1 From 2D to 3D: need for new sample preparation

To preserve the 3D structure, we have implemented a new kind of sample preparation. Our samples were welded to a tungsten needle using a FIB (Focused Ion Beam) SEM microscope. It operates by decomposing a platinum-organic compound to weld the sample to the metallic needle with a 5 keV Ga ion beam. The welding was done by David Troadec from the Institut d'électronique de microélectronique et de nanotechnologie (Lille, France). All the standard and meteoritic samples analyzed in 3D during my Ph.D. were prepared with this technique.

I also participated to a larger experimental effort, led by Alice Aléon-Toppani at IAS, aimed at establishing an optimized multi-analytical sequence ,which goes from the less destructive (e.g. IR tomography) to the more destructive (e.g. TEM, nanoSIMS) techniques, in preparation for upcoming sample return missions. These efforts are not described here, but they will be the subject of a forthcoming publication by A. Aléon et al.

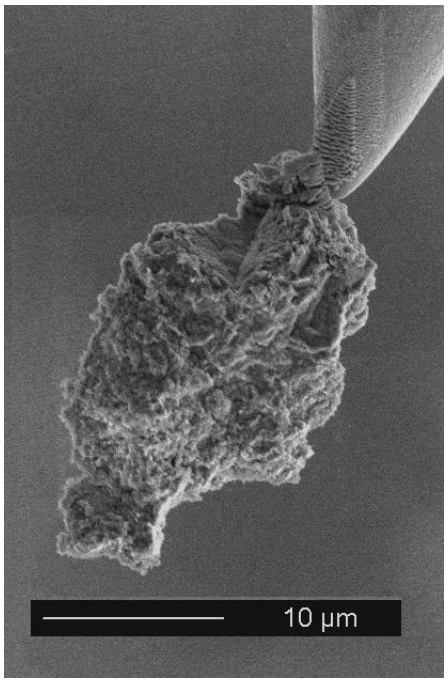

Figure 5.1: Paris sample welded on a tungsten needle

Characterization of the contamination induced by the FIB preparation

For samples prepared with the FIB method we performed Raman analysis to characterize the possible surface contamination by amorphous carbon.

We first studied a small deposit of the Pt-C material (from now on, the pure contaminant) on a clean surface of a ZnSe window (see Fig. 5.2(b)). With this deposit we identified the Raman bands that are characteristic of the pure contaminant: the G band is centered at about 1500 cm^{-1} and has a Full Width at Half Maximum (FWHM) of 210 cm^{-1}.

We then analyzed the carbon G band in the FIB mounted Paris grain. We acquired maps of 4 regions on different areas: on the welding region, its neighborhoods, and the central part of the sample (see Fig. 5.2(a)). For each region we have determined the position and the FWHM of the G band.

We noticed that the characteristics of the D and G band change according to the nature of organics (either originating from the meteorite itself or from the contamination). The position of the G band is between 1580 cm^{-1} and 1610 cm^{-1} in the meteorite (Merouane et

al., 2012) and the contamination has a G band around 1500 cm^{-1}. By studying the position of the G band in different point locations of the sample, we have seen that the carbon due to contamination is localized near the needle (closer than 5 μm) and the intensity of the band due to the contamination is very weak. The absence of CH in the contaminated region (see Fig. 5.3 region 4) indicates that we only detect meteoritic aliphatic matter with FTIR.

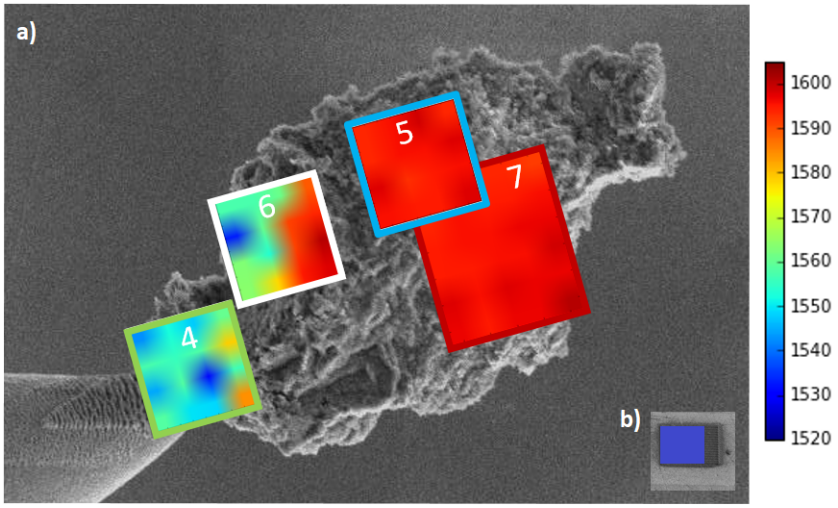

Figure 5.2: Peak position of the G peak in cm^{-1} for (a) different regions of the sample (regions 4-7) and (b) a small deposit of the Pt-C material on a clean surface of a ZnSe window.

The G band of carbon have been studied in literature (Brunetto et al., (2009), Rotundi et al., (2008)) for several carbonaceous meteorites and the typical meteoritic position is between 1580 cm^{-1} and 1610 cm^{-1} with a FWHM around 100 cm^{-1}. This is represented by the square *"Meteorites"* in Fig. 5.3. The position also depends, in a less extent measure, on the degree of metamorphism of the sample. In fig. 5.3, the contamination is also represented and we reported the data obtained in the different regions mapped on the sample.

We observe that the region 5 and 7 are very far from the welding area and we found them in the typical meteoritic region concerning the position of the G peak and its width. On the opposite the regions 4 and 6 show several points which extend from the contamination region to the meteoritic region. This leads to the conclusion that the contamination is very localized ($<$ 5 micrometers to the welding point).

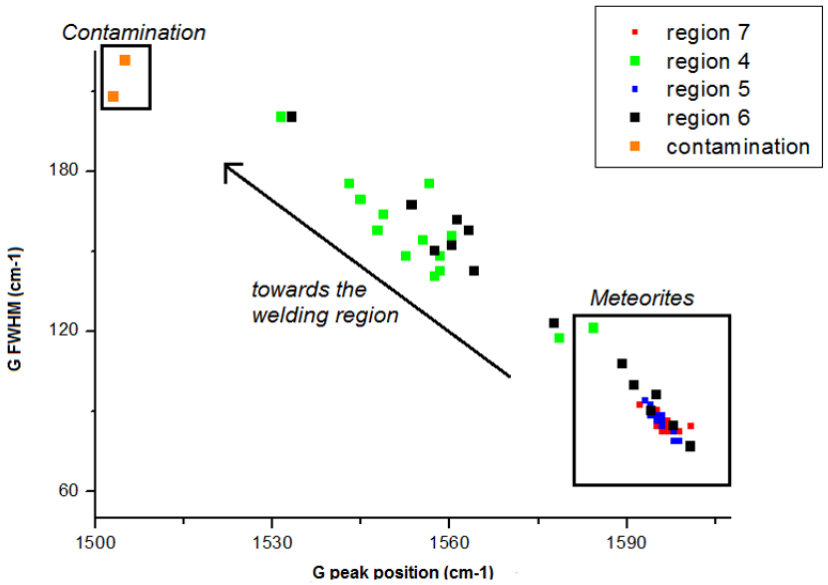

Figure 5.3: G band position according to the FWHM of the G band

Moreover the number of counts per second is also different. Indeed it is very low when we are focused on the contamination (less than 10cps), and much higher when it is a meteoritic carbon. It is a contamination surface, and this contamination is negligible in IR transmission, as it does not appear in our IR spectra.

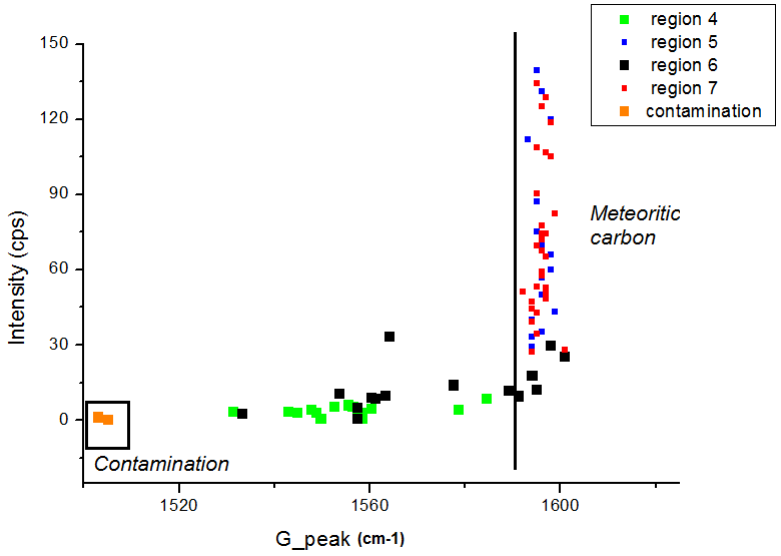

Figure 5.4: Number of counts as a function of the G band position

Then, we can conclude that the contamination is localized but also very weak in intensity and this preparation can be used to prepare properly samples for tomography. Unfortunately,

this preparation is still delicate and most of our samples were lost after several manipulations. In particular, X-ray tomography seems to especially weaken the bond. Some improvements need to be done before working on very precious samples. The possibility to increase the quantity of platinum deposited and a preparation based on e-glue are currently under test.

5.2 Principles of tomography

5.2.1 Single energy tomography: Linear Attenuation Coefficient measurement

For the clarity of explanation, we are going to consider first a monochromatic beam as the source (as in the case of X-CT tomography). We send the beam through the sample, and we collect the light after passing through the sample. We obtain a 2D image as in the previous section, and for each pixel, we record the percent of light which crosses the sample for the column of matter above this pixel. Outside of the sample, no photon is absorbed: the linear attenuation coefficient (LAC) is minimal. If the sample absorbs all the light, the LAC will be maximal. Finally, we obtain 2D pictures, which we will call the projections of the sample.

To reconstruct the 3D information, we have to rotate the sample and collect a set of projections. The connection between the space of projections and the real space: we have an object in real space (x,y,z), with y the axis of rotation of the sample. As the sample turns along the y axis the mark (x,z) is also going to turn. We define a non-moving coordinate system (u,v,w). The relation between this two coordinate systems is given by the projection of angle θ (see Fig 5.5): u is the horizontal projection of the moving axis x, and w is the vertical projection of the moving axis z and the axes v and y are overlapped.

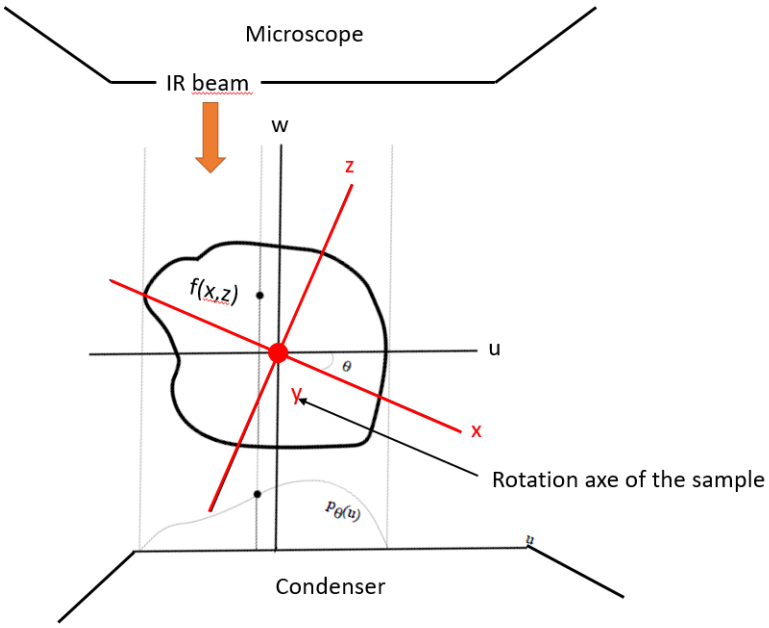

Figure 5.5: Creation of the projection

We turn the sample with steps of $\Delta\theta = 1$ degree, and for each value of θ, we collect a projection p(u,v) (see Fig 5.5). If we plot the projection $p_\theta(u)$ according to θ and with a given v, we obtain a sinogram. To pass from a set of projections to a set of sinograms we just have to rearrange the data as demonstrated on Figure 5.6.

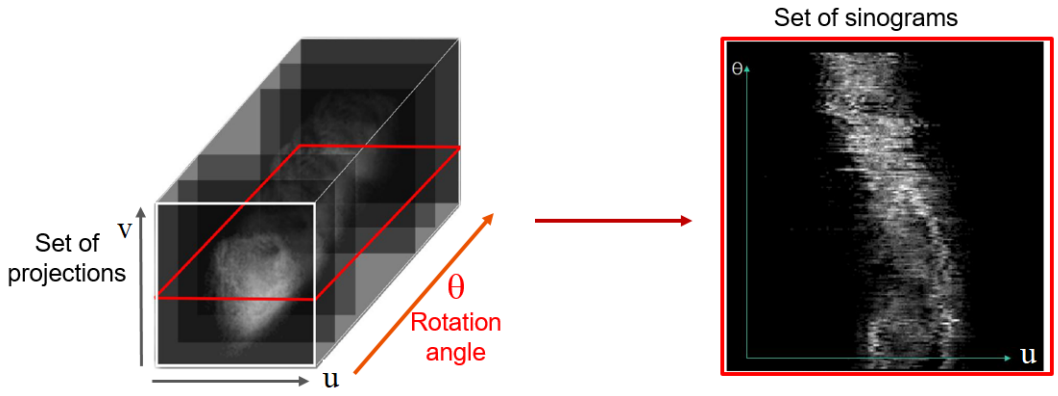

Figure 5.6: Relation between projections and sinograms

The reconstruction algorithm will work with sinograms as starting point. The principle used by reconstruction algorithm is very well described in the Ph.D. of David Laloum and the end of this section is inspired by his thesis manuscript.

5.2.2 Radon transformation and Backprojection

The Radon transformation R, introduced by the mathematician Johann Radon, is the mathematical expression of the projection of an object $f(x, z)$.When we apply the R operator to an object described by f at a specific angle, θ along a direction, u, we obtain the projection $p_\theta(u)$ as described in the equation 5.1. This operator is a linear transformation, defined by the integral of $f(x, z)$ for all x, and z. The equation of the normal is given by $u = xcos\theta + zsin\theta$ and finally, we have:

$$R[f](u, \theta) = p_\theta(u) \tag{5.1}$$

$$R[f](u, \theta) = \int_{-\infty}^{\infty} \int_{-\infty}^{\infty} f(x, z)\delta(xcos\theta + zsin\theta - u)dxdz \tag{5.2}$$

with δ as the Dirac pulse.

The tomography problem consists of finding the real shape of $f(x, z)$ from a set of measured projections $p_\theta(u)$. A simple solution, called backprojection, could be to take all the contribution $p_\theta(u)$ present along the direction of projection and sum them. We name $h_\theta(x, z)$ the backprojection in real space and define as:

$$h_\theta(x, z) = p_\theta(xcos\theta + zsin\theta) \tag{5.3}$$

Then we can define the backprojection operator B as the sum of the contributions given by the previous equation for all angles:

$$B[p](x, z) = \int_0^{\pi} h_\theta(x, z)d\theta \tag{5.4}$$

$$B[p](x, z) = \int_0^{\pi} p_\theta(xcos\theta + zsin\theta)d\theta \tag{5.5}$$

The obtained image a blurred version of $f(x, z)$. Indeed, the backprojection is not precisely equal to the inverse of the Radon transformation (as we will show in section 5.2.4). This direct method is not exact, but it is the first one used in the past to obtain the first historical reconstructions.

5.2.3 Central slice theorem

The central slice theorem is used in every modern reconstruction method. It gives the relation between the Radon transformation of an object and its Fourier transform (Banhart, 2008). If $F(m,n)$ is the 2D Fourier transform of the function $f(x,z)$, then:

$$F(m,n) = \int_{-\infty}^{\infty}\int_{-\infty}^{\infty} f(x,z)e^{-2i\pi(mx+nz)}dxdz \tag{5.6}$$

$R[f](u,\theta)$ the Radon transform of f is defined by equation (5.1). Then the 1D Fourier transform $S(\theta,k)$ of $R[f](u,\theta)$ is given by :

$$S(\theta,k) = \int_{-\infty}^{\infty} R[f](u,\theta)e^{-2i\pi uk}du \tag{5.7}$$

The central slice theorem says that the 1D Fourier transform of a projection along one direction is equal to the cutting along the same angle of the 2D Fourier transformation of the function $f(x,z)$. So we could write :

$$S(\theta,k) = F(kcos\theta, ksin\theta) \tag{5.8}$$

This equation makes a link between the projection space and the real space. With this information we can now do the reconstruction by using the following scheme: calculate a set of 1D Fourier transforms from the set of projections. Then the central slice projection theorem gives $F(kcos\theta, ksin\theta)$ and finally inverse 2D Fourier transformation provides $f(x,z)$ characteristic of the sample in real space (see Fig 5.7). This method is called direct Fourier reconstruction method.

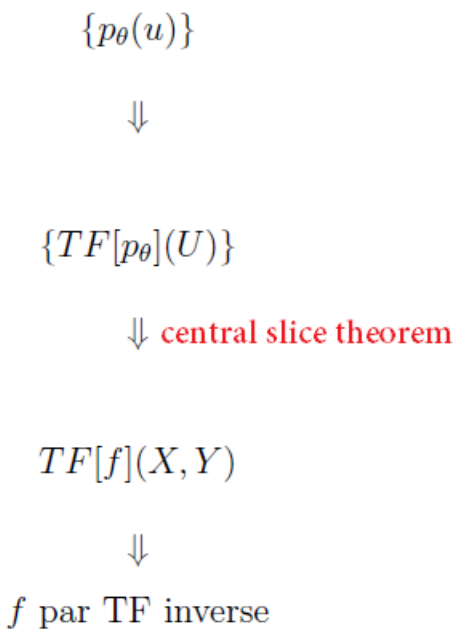

Figure 5.7:Use of the central slice theorem to obtain the reconstruction

In practice this direct method is not often used as it requires an accurate interpolation of data in the Fourier space to convert the data from polar coordinates to Cartesian coordinates (Stark et al., 1981) and therefore requires very high angle resolution measurements.

5.2.4 Filtered backprojection

We have just seen that it is necessary to inverse the Fourier transform obtained from the set of projections. Therefore, we have:

$$f(x,z) = \int_{-\infty}^{\infty}\int_{-\infty}^{\infty} F(m,n)e^{2i\pi(mx+nz)}dmdn \tag{5.9}$$

The data are defined in the polar coordinates so we have to introduce the polar coordinates in the Fourier space:

$$(m,n) = (kcos\theta, ksin\theta) \tag{5.10}$$

So we obtain:

$$f(x,z) = \int_0^{2\pi} \int_0^{\infty} F(kcos\theta, ksin\theta) k e^{2i\pi k(cos\theta x + sin\theta z)} d\theta dk \tag{5.11}$$

and because of the definition of u we have:

$$f(x,z) = \int_0^{2\pi} \int_0^{\infty} F(kcos\theta, ksin\theta) k e^{2i\pi ku} d\theta dk \tag{5.12}$$

$$f(x,z) = \int_0^{\pi} \int_{-\infty}^{\infty} F(kcos\theta, ksin\theta) k e^{2i\pi ku} d\theta dk + \int_{\pi}^{2\pi} \int_{-\infty}^{\infty} F(kcos\theta, ksin\theta) k e^{2i\pi ku} d\theta dk \tag{5.13}$$

Moreover, as we notice that:

$$F(kcos\theta, ksin\theta) = F(-kcos(\theta + \pi), -ksin(\theta + \pi)) \tag{5.14}$$

we can do the variable change (w, θ) by (-w, $\theta + \pi$) and we obtain:

$$f(x,z) = \int_0^{\pi} \int_{-\infty}^{\infty} F(kcos\theta, ksin\theta) |k| e^{2i\pi ku} d\theta dk \tag{5.15}$$

Then thanks to the central slice theorem (eq. (7.8)) we have:

$$f(x,z) = \int_0^{\pi} \int_{-\infty}^{\infty} S(\theta, k) |k| e^{2i\pi ku} d\theta dk \tag{5.16}$$

This equation is the characteristic equation of the filtered backprojection and we can write it:

$$f(x,z) = \int_0^{\pi} Q(\theta, u) d\theta \tag{5.17}$$

with:

$$Q(\theta, u) = \int_{-\infty}^{\infty} S(\theta, k) |k| e^{2i\pi ku} dk \tag{5.18}$$

This last equation represents a filtering operator. And $Q(\theta, u)$ is the filtered projection in the Fourier space filtered by a ramp expressed as $|k|$. With the sampling in the Fourier space, the low frequencies (near the center of the Fourier space) are more represented, so we need to use this filter to ponder all the frequencies. The filter corresponds to the removal of the blurring mentioned in the previous part if we use direct Fourier reconstruction methods.

Indeed we have :

$$f(x,z) = B[p'_\theta(u)] \tag{5.19}$$

with $p'_\theta(u)$ the filtered back projection:

$$p'_\theta(u) = TF^{-1}[TF(p_\theta(u).|u|] \tag{5.20}$$

To conclude we can summarize the principle of the filtered back projection by the following scheme :

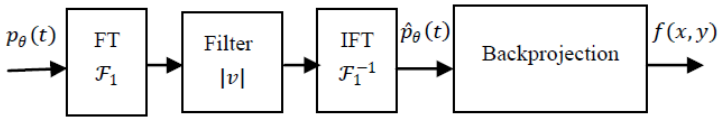

Figure 5.8: Principe of the Filtered back projection reconstruction (modified from Messali et al., 2015)

This method is the faster one and as a consequence the more used in physics, but it requires many projections and also a good quality in the projections (high signal to noise). It is not the case in our data, so we have to use in addition an iterative method to improve our reconstruction.

5.2.5 Iterative method: ART

The Algebraic Reconstruction method (ART) is an iterative method based on the decomposition of the initial images on different pixels, then we can reformulate the problem in a matrix form (see Fig. 5.9).

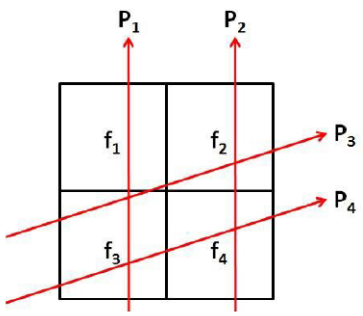

Figure 5.9: Decomposition of the projection

We can describe the problem by the following equation:

$$P_i = \sum_{j=1}^{N} R_{ij} f_j \quad with \quad i = 1, ..., M \tag{5.21}$$

where N is the number of pixels in the projection and M is the number of measured projections. The coefficient R_{ij} corresponds to the contribution of the jth pixel to the ith projection. Because of the high number of pixels and projections, we obtain a huge system of equations ($N = 16384$ and $M = 180$ in our case) so to solve the system, we need to use iterative algorithms for example as described by Kak and Slaney, 1988 and Geyer et al., 2015.

The principle is to find a solution by successive iterations. To implement this algorithm, we first make an initial guess $f^{(0)}$ of the description of the sample in the real space (given by direct backprojection) and then, we take successive intermediate projections $f^{(k)}$. The intermediate projections are compared with the measured projections and the difference δp is used to implement a small correction in the projection space and improve the reconstruction. When the estimated projection and the measured projection are close enough or when the algorithm reaches the number of iterations fixed by the operator, the loop aborts, and the algorithm takes the last estimate projection and applies filtered backprojection. For our reconstructions I noticed that we do not have any significant improvement after the 20 iterations. The scheme in Fig. 5.10 describes the principle of this technique.

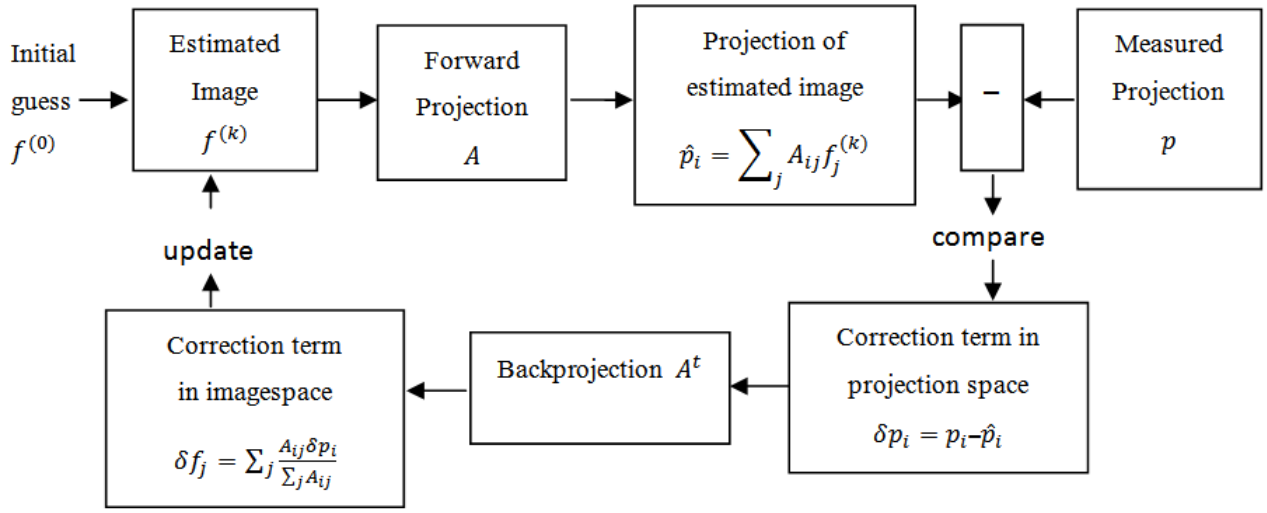

Figure 5.10: Principle of the ART reconstruction (modified from Messali et al., 2015)

Both FBP and ART could be used to reconstruct infrared data and both solutions are proposed in available reconstruction software. In our case, the iterative method gives better results, as it is more efficient in the case of noisy signal and it reduces artifacts (Geyer et al., 2015). This technique has the advantage to work with missing angles and is also efficient when we have noisy projections (Beister et al., 2012).

Fig 5.11 presents a comparison of slices inside the reconstructions of the OH stretching bands for our data both with FBP (panel a) and ART (panel b). We can notice that the ART help us to avoid artefact inside reconstruction. For all our data, we are going to use ART with 20 iterations.

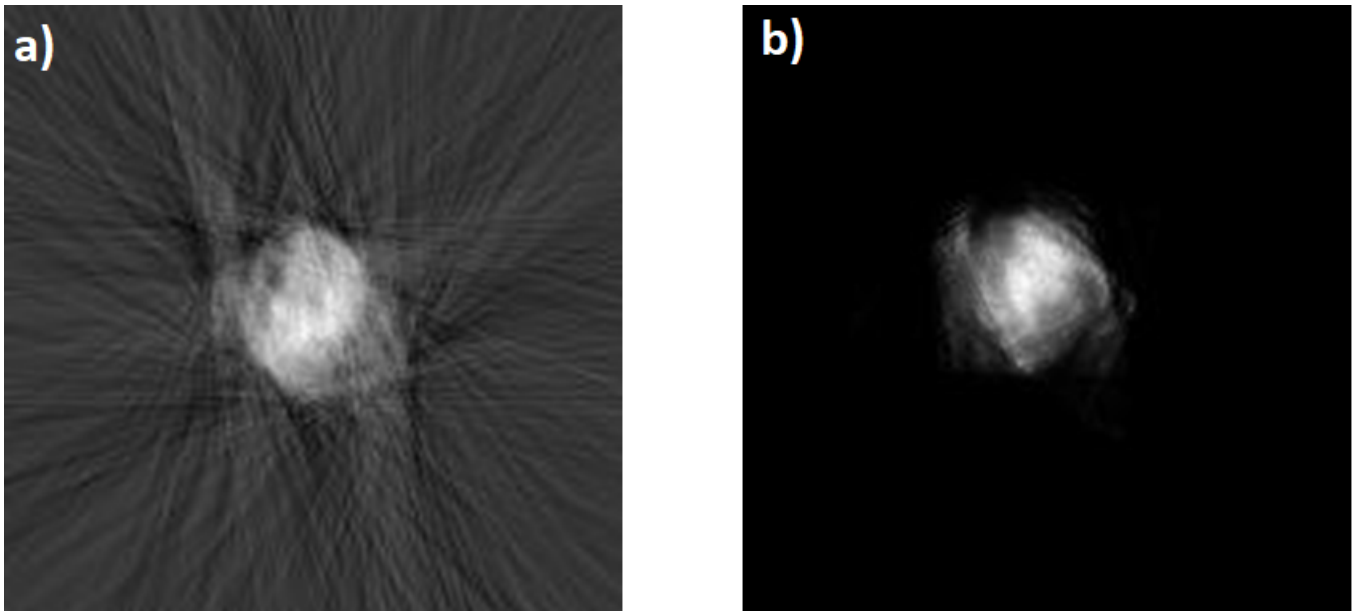

Figure 5.11: Reconstructed slices of the OH bending for one grain of Paris meteorite obtained with 'a) FBP and (b) ART.

5.3 X-ray tomography

As I will show in the following chapters, IR tomography can provide information about the chemical composition but the spatial resolution is limited and physical information as porosity and internal structure at a scale below 1 μm are very hard to get. IR tomography is also limited to samples smaller than 50 μm by saturation and scattering. As a consequence, X-ray tomography is a useful method to provide complementary information, therefore we also performed such measurements on our samples. A part of the data was measured at the PSICHE beamline in SOLEIL and for the Hayabusa grains we have used the measurements kindly provided by A. Tsuchiyama and collaborators, that they performed at beamline BL47XU in SPring-8, Japan.

Moreover, as a robust technique with a very high resolution compared to the IR, we also use the X-ray data to create a shape model for our IR reconstruction and thus validate IR tomography and to mitigate problems arising due to diffraction as described in the last part of this chapter.

5.3.1 Monochromatic measurements at PSICHE

We have mainly done measurements with a monochromatic beam at 17.6 keV. These analyses were conducted at the PSICHE beamline in SOLEIL. We have measured the LAC and reconstructed our data as explained above with *tomopy* (Gürsoy et al., 2014,).

We have measured two kinds of samples. A first set of measurements was done on the same samples used in IR tomography to obtain precise information about the shape and internal structure at the micrometer scale. All these samples were welded at the tip of tungsten needles. The measurements were first done with IR and then with X-rays, as X-rays could have a destructive impact on the organic matter. Then we have also measured a set of bigger samples (about 1-2 mm in size) to characterize the structure and the porosity at a larger scale.

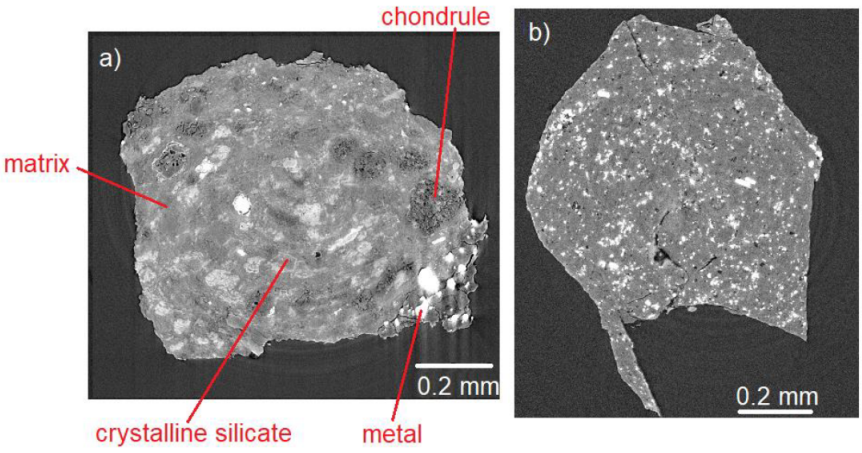

Figure 5.12: X-CT slices of (a) Paris and (b) Orgueil meteorites measured at the PSICHE beamline (SOLEIL).

In Fig. 5.12, we can see two examples of X-CT slices obtained with the PSICHE setup on macroscopic samples. We can see the difference of absorption of the difference phases and well characterize the shape and the structure. We observe some artifacts: first, there is a pattern of bright and dark contrast at the edge of the sample which is due to the refraction of the X-ray beam. We also observe concentric structures, which is an artifact due to the imperfect choice of the center of rotation.

Measurements at a higher energies (18 keV and 25 keV) were also performed to study the evolution of the LAC with the energy and to obtain additional information on the composition of our samples. The processing of these measurements is in progress.

5.3.2 Dual energy X-CT

This technique was already used by Tsuchiyama et al., 2011 on Hayabusa particles. The five Hayabusa particles studied during my Ph.D. work had also been measured with dual energy X-CT and the reconstructions were kindly provided by A. Tsuchiyama. As explained by Tsuchiyama et al., 2011, combining X-CT at two energies can provide information on the chemical composition of samples. They combined tomography at 7 and 8 keV, two energies located below and above the K absorption edge of Fe (7.11 keV). They observed differences in the LAC according to the concentration in iron: minerals with elements heavier than Si but lighter than Fe have relatively large LAC values at 7 keV, while Fe-rich minerals have large LAC values at 8 keV. They have applied this method to several grains of Hayabusa. Fig. 5.13 is an example of the same reconstructed slice with measurements done at 7 and 8 keV. We clearly see the difference in contrast between these two energies. The gray scale represents the value of the linear absorption for each voxel when sending a beam of 7-8 keV on the sample. Just below the slice, we see the histogram of the voxels distribution of the LAC, and we observe several maxima in the distribution corresponding to the different minerals present in the sample.

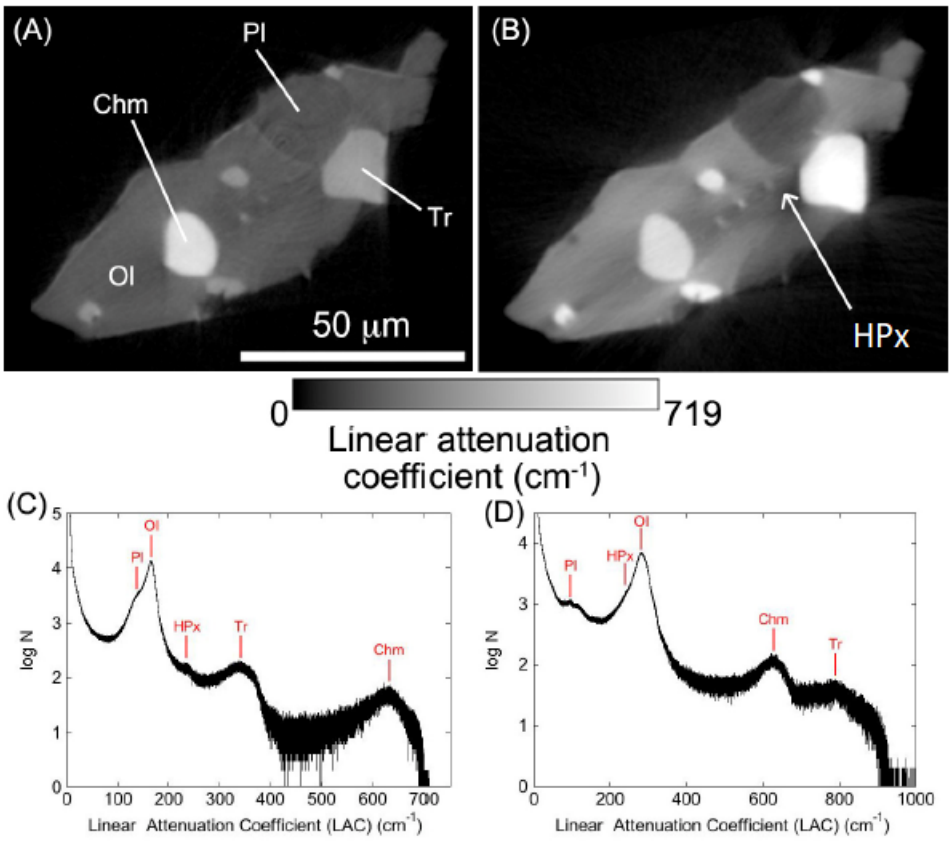

Figure 5.13: Reconstructed X-CT slices of the grain RA-QD02-0031 (a) at 7 keV, (b) at 8 keV and corresponding distribution of the LAC (from Tsuchiyama et al., 2011). Note that cm^{-1} represents linear attenuation and not vibrational frequency on this figure. The abbreviation Ol, Pl, Chm, Tr and HPx are used for olivine, plagioclase, chromite, troilite and high-Ca pyroxene.

To precisely determine the composition and to distinguish between different minerals like enstatite and forsterite, they combined information at 7 and 8 keV. In the Fig. 5.14, the LAC at 7 keV is shown as a function of the LAC at 8 keV for different standards measured in the same conditions. The used of two energies helped them to remove degeneracy between different minerals with similar composition.

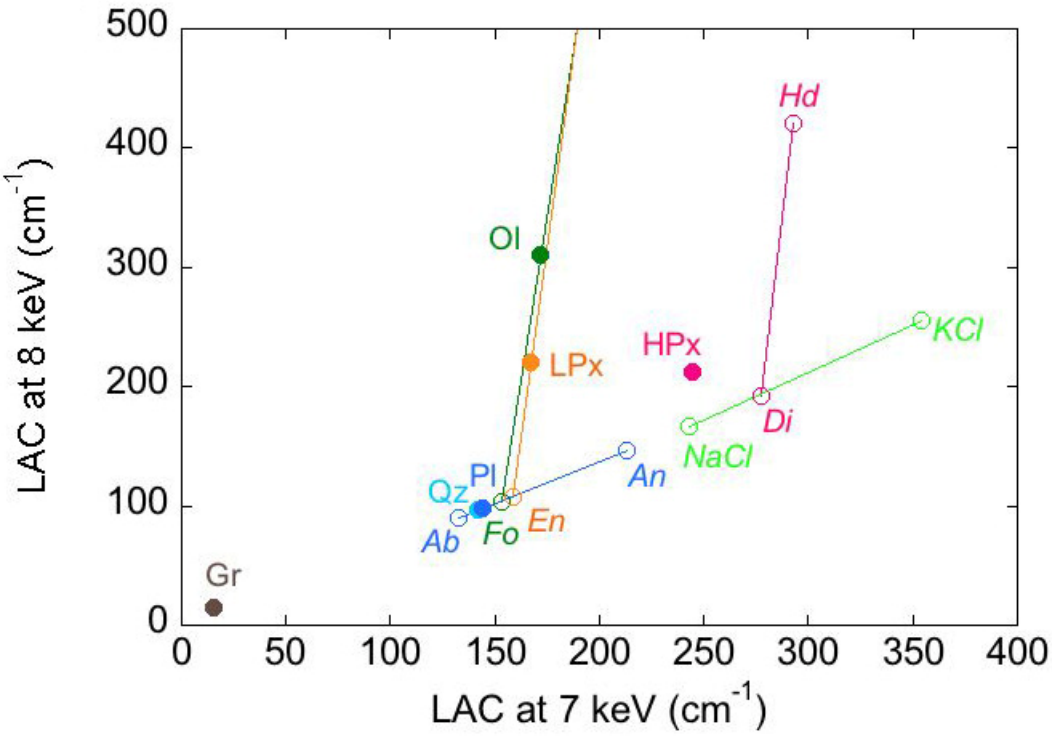

Figure 5.14: LAC at 8 keV according to the one at 7 keV for standard minerals (from Tsuchiyama et al., 2012).

Finally, they identified the minerals and gave indications about the ratio between the different cations, Fe/Mg for ferromagnesian minerals or Na/Ca for plagioclase for instance. This method is very powerful and can precisely characterize minerals. Some of the samples analyzed in this Ph.D. using IR tomography were analyzed before with this method and we have the opportunity to directly compare our results (see Chapter 6).

5.4 Hyperspectral IR tomography

All the methods described above concern the reconstruction at a given energy as it is the case traditionally with X-CT. In the case of FTIR, we measured hyperspectral data, i.e. for each pixel of each projection we collected a whole IR spectrum.

IR micro-tomography was developed on the IRENI beamline (Martin et al., 2013). Mainly biological samples were measured and they succeeded in reconstructing the different com-

ponents in 3D. Quaroni et al., (2015) have also demonstrated the possibility to perform IR tomography with a conventional light source. They performed IR tomography on cells. Moreover, a first application on a meteorite of IR tomography with a synchrotron was performed by Yesiltas et al., 2016. They studied the relation between the organic and the mineral parts of the meteorite and they observed a correlation between the phyllosilicates and the presence of the groups C-O and CH_3 which suggested that organics need hydrated silicates to form.

In this section I will first describe the IR setup for tomography. Then I will present the way to pre-treat our IR data to make them comparable to X-CT data. After that, I will described the reconstruction method, and finally, once we have our reconstruction, we will analyze the data to extract scientific information. All the illustrations given in this part comes from the reconstruction of the grain Itokawa RA-QD02-0214.

5.4.1 Experimental set up

First, we had to build a system which gives us the possibility to put the sample under the microscope and to turn it. To do that we have welded the sample at the end of a tungsten needle with a focused ion beam method (see part 1 of this chapter) and we used a mandrel to hold the needle horizontally. This mandrel was connected to a small kinematic adjustable mount which was itself connected to a motor to rotate the assembly. All this set up was fixed to the stage of the microscope (see Fig. 5.15).

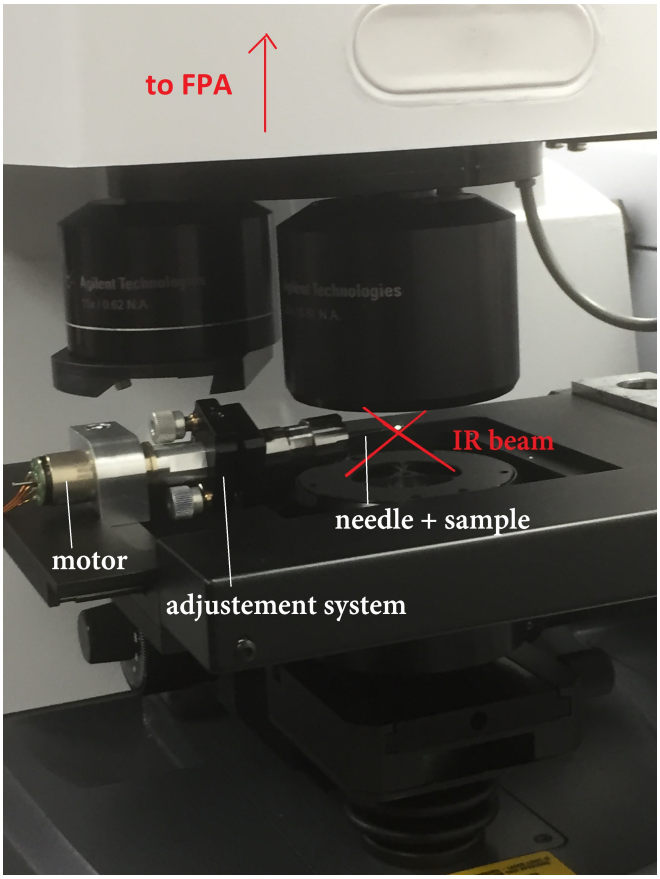

Figure 5.15: Photo of the setup used in IR tomography.

The kinematic mount is used to correct the angle of the needle/sample assembly in the focal plane. Indeed the needle is never perfectly straight, and the sample is neither perfectly aligned with the needle. So when the sample turns, its position necessarily changes of few microns. This problem is common, and this is not an issue in the case of X-CT as it uses a parallel beam and large field of views. In the case of IR tomography, we have a focused beam, so the sample needs to stay right on the focus plane during all the measurements. Thanks to our adjustment system, we can induce an angle between the needle and the motor axis to correct the misalignment due to the preparation as described here.

To address focusing we have carried out numerical simulation of the electric field focused through the objective using PSFLab developed by M. J. Nasse in 2010. It is important to note that PSFLab was developed with regular objectives and therefore the calculation doesn't account for the central obscuration of the Schwarzschild objective, but in our case, at IR wavelengths the error is negligible. Similarly, the simulations are done for perfect illu-

mination, which in case of using a Globar source is far from reality. All these instrumental parameters are in our favor as they increase the depth of focus as well as the illumination homogeneity on the sample plane.

Based on these simulations shown on Fig. 5.21 we can emphasize a few important aspects of IR tomography. The field intensity is concentrated by the focusing objective into an ellipsoid elongated along the z direction of the system (w on Fig. 5.5) with axes about 5.2 μm and 17.3 μm. This is beneficial for both providing insensitivity for the sample alignment and also somewhat mimicing a parallel beam in the vicinity of the geometrical focus. During our measurement, we have tried to put the focal plane at the center of the sample, however, we had to manually correct the z position of the microscope stage between measurements due to slight angle misalignments of the kinematic mount.

5.4.2 Pre-treatment of the data

Once the setup is installed and the sample well aligned, we can proceed to the measurement. We collect projections of 128x128 pixels with 25× and high magnification configuration, with 32 scans and a spectral resolution of 16 cm^{-1} using the Globar source. The background is taken with 128 scans. The speed of the mirror movement inside the interferometer is 2.5 kHz, and the sampling interval is 4. We measured 180 projections with a step of 1 degree between each measurement. In this configuration, the measurement of all angles for one sample takes between 8 and 9 hours. Other configurations were tested but are too long or give worse results, the configuration presented above is the best compromise and almost all the samples were measured with these conditions. One bigger sample was measured with a 15× objective to have a larger field of view in order to cover the whole sample.

On Fig. 5.16, I present a spectrum obtained for a given pixel for a given angle. On this spectrum, we can notice some organic bands and some minerals bands characteristic of our sample. Below the spectra, we can see the map of the area under the band for two examples of bands.

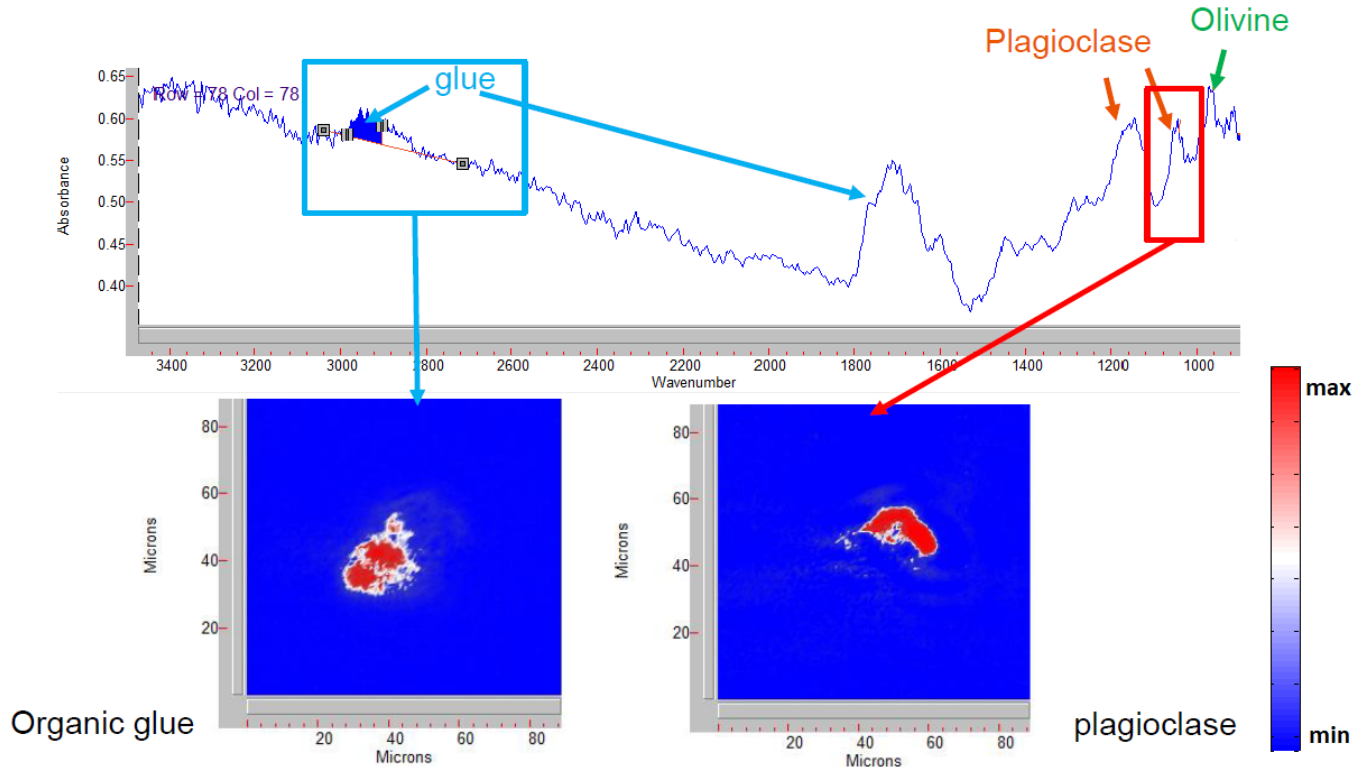

Figure 5.16: Example of treatment on a spectrum of the grain RA-QD02-0214 of Hayabusa to isolate the different components for a projection.

The 2D projections (maps) were generated as follows: for each spectrum of a projection we extracted a map of the concentration of each component, given by the area under the corresponding band. By creating a set of pictures in RGB scale (normalization to 255 for the maximum inside the whole data set), we have data similar to X-CT data and reconstruction of such data with X-CT software gives us the 3D localization of one of the components of the sample. For every component of interest we have repeated this procedure.

We can also identify components using second derivatives of our spectra. We used the raw spectra to determine the major and broad band positions like stretching and bending O-H, or broad bands composed of smaller, structured peals as the whole silicate band at 10 micrometers or organic bands including both CH_2 and CH_3 signatures. To identify and to map fine structures like those for different minerals used second derivatives (see distinction between amorphous and crystalline materials presented in Chapters 2 and 3) as the signal to noise ratio is too small to easily distinguish the structures in the spectra.

At this point, we have the map of one component for all measurement angles. As the position of the sample on the focal plane is still adjusted by hand between each measurement, the reference point is moving in each projection. We need to correct this movement and to give a fixed point to the software to readjust the position of each projection: it is necessary to create a file which contains the position of a fixed point (here we took the transition between the needle and the sample), the map can then be re-sized and re-centered around the reference point.

5.4.3 Reconstruction and 3D data analysis

With this newly generated set of projections, we can reconstruct the spatial distribution in 3D of the different components. We used TXM Wizard, a software developed and described by Liu and al., 2011 and 2016. The algorithm used is the iterative ART with 20 iterations. After execution, TXM Wizard provides a new set of images which represent slices inside the sample for the three planes (x,y), (x,z), (y,z).

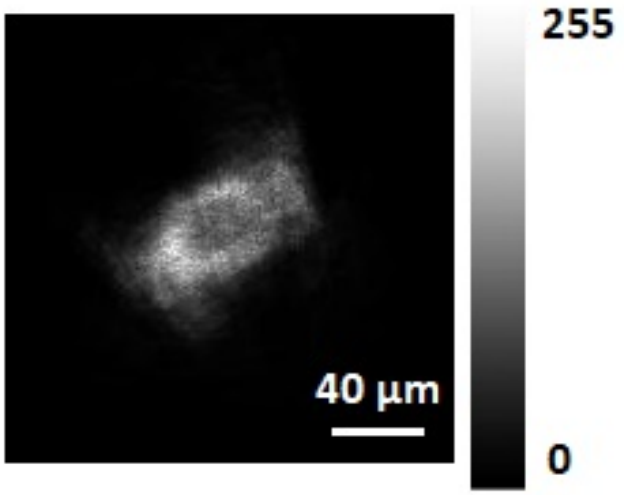

Figure 5.17: Example of reconstructed (x,z) slice of the organic matter.

For instance, we can see in Fig. 5.17 the distribution of the organic matter through reconstructing the CH stretching vibration region of the spectra for a given slice (x,z). We obtain voxels with a size corresponding to the size of pixels in the measured projections.

Once we have the reconstruction, we study the co-localization of the phases. To do this, we can visualize the position of each phase in 3D using the Avizo software. Scientific analysis (calculation of the porosity, etc.) can then be performed with ImageJ or with custom Python scripts.

5.5 Calibration of IR tomography with mineral standards

To calibrate our setup, we have first studied terrestrial homogenous grains. We have chosen to study a grain of saponite as representative of phyllosilicates present in the matrix of some meteorites. A grain of pure carbonate was also analyzed. The saponite and the carbonate were prepared with the FIB preparation described above. Fig. 5.18 shows the two grains used as standards. These tests were also an opportunity to test the preparation with FIB, welding samples with different composition and physical properties (porosity, structure, etc.).

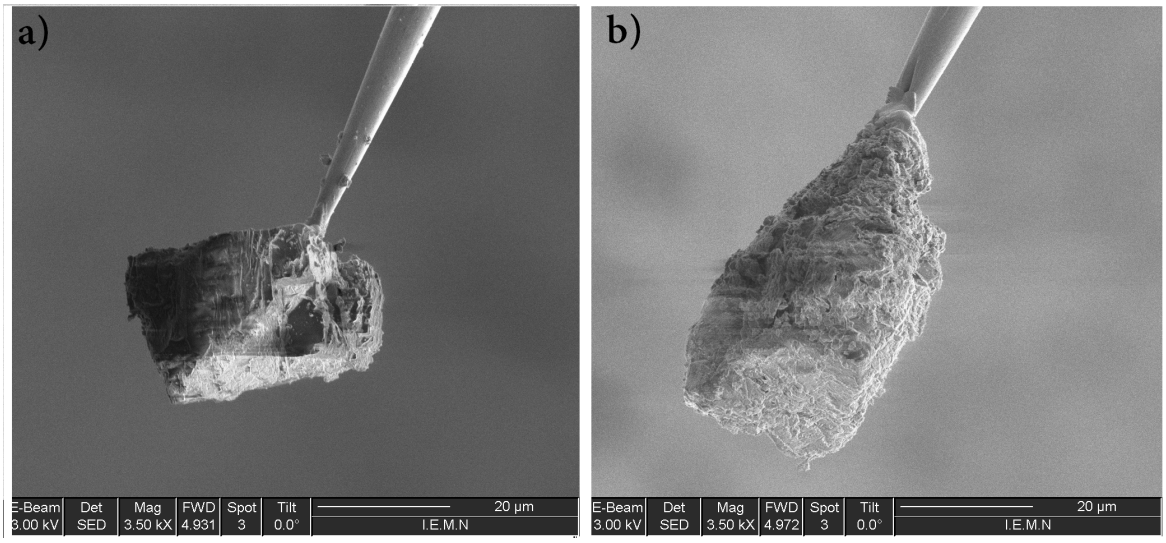

Figure 5.18: Image of the standards prepared with FIB: a) calcite and b) saponite grains.

5.5.1 Reconstruction of pure components

In this part, we are going to test our setup with different standards to see its limits. It is also useful to validate the best protocol to take a measurement (32 scans, 16 cm^{-1} spectral resolution, 180 spectral measurements, steps of 1 degree).

The first step was to compare our spectra with the literature and check that we have sufficient signal to noise to identify the bands, and enough bands to reconstruct the samples in 3D. We have examined the spectra of the measured grain of saponite we have found a band around 1000 cm^{-1} similar to the one described by Beck et al., 2014. Similarly, bands at 1440 cm^{-1}, 1810 cm^{-1} and 2510 cm^{-1} were present in our spectra of calcite as described in Bruckman et al., 2012. After we have checked the presence of the bands, we can reconstruct them to see if we can obtain a shape close to the one of the sample determined from the SEM images.

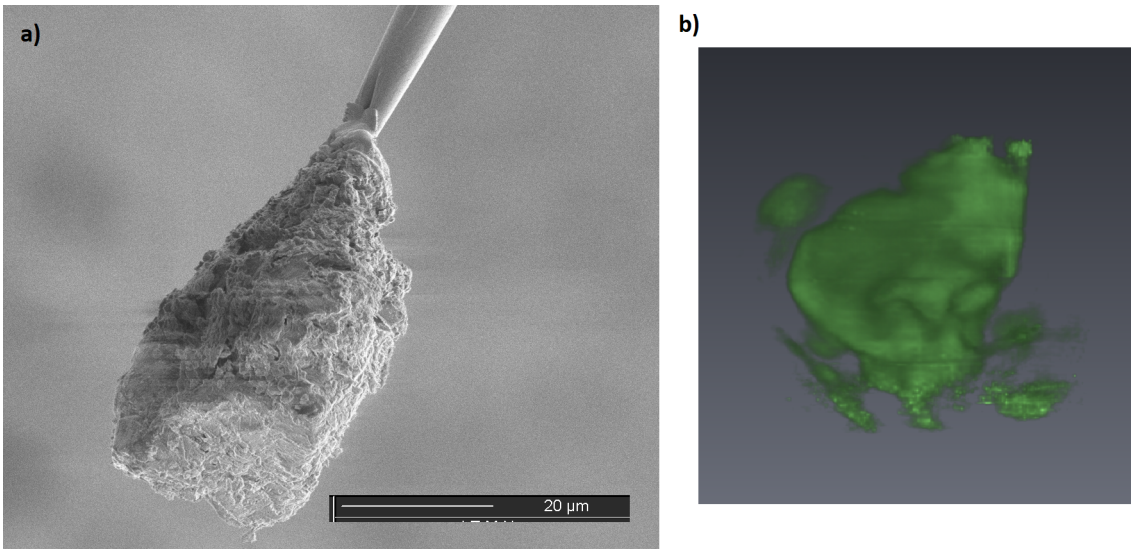

Figure 5.19: (a) SEM analysis and (b) reconstruction after IR tomography of a grain of saponite.

The Fig. 5.19 and 5.20 show a comparison between the image of the sample obtained by SEM and the reconstruction of the sample with our setup. We notice that we reconstruct the sample well and we recognize the sample shape globally.

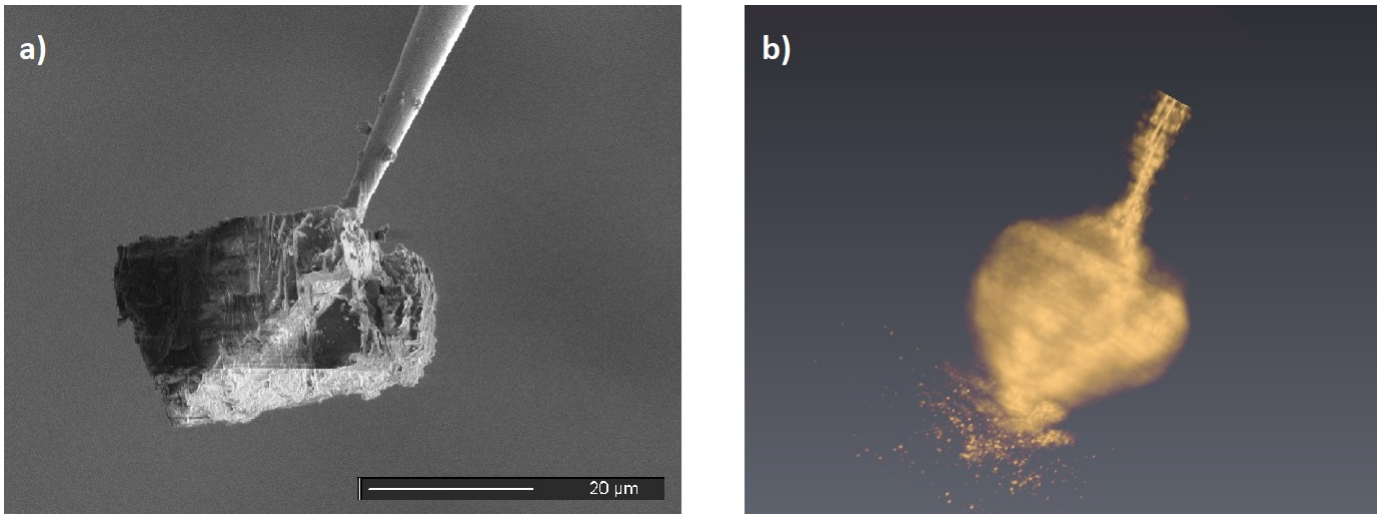

Figure 5.20: (a) SEM analysis and (b) reconstruction after IR tomography of a grain of calcite.

Unfortunately, we do not have X-ray data for these two samples, because the grains were lost during the manipulation between IR and X-rays setup, so we cannot compare precisely the shape obtained in IR with the shape obtained by X-ray analysis.

5.5.2 Study of a symmetrical standards to understand optical effects

We also analyzed a spherical silica sample, with a different preparation: by tapping the needle on a tape, we deposited some glue at the tip and then we collected silica samples. This method is less precise and clean, but it has the advantage of an easier and less expensive preparation that is useful for tests. Moreover, the presence of the glue and the mineral matter allows us to test the possibility to separate different phases with our methods. We have glued three spheres for this sample. As these three spheres cannot stay on the same focal plane at the same time for all angles, we have to choose the one we want to analyze with IR tomography and focus only on that one. In this case, we have focused on the biggest one (size of 45 μm) for IR reconstruction.

Saturation: a constraint on sample size

Our setup is well adapted for few tens of micrometer-sized grains. However, if the samples are too big, the light is fully absorbed and we do not have a signal to reconstruct. Indeed, as soon as the grains are bigger than 20 μm, the most intense bands could be saturated. In the following part, we are going to explain the different solutions used to go beyond this limitation for samples between 20 and 50 μm. In our case, the saturation is easily revealed in the 3D reconstructions as it appears as a difference of density inside the spheres. Thanks to X-ray tomography on this sample, we know that the spheres are homogeneous in density. In our reconstruction however, the big sphere appears empty as if we were underestimating the quantity of silicate inside the sample.

We have tried different solutions for this problem deescribed below.

Reconstruction on overtones

The first idea was to explore the possibility to work with the overtones at shorter wavelengths and not with the main stretching band for a given bond. For instance, for the large band of silicate around 900 cm^{-1} we looked for the overtone at 1800 cm^{-1}. Even if we managed to detect the overtone, the obtained reconstruction was not much better: in fact, even if we avoided the saturation, we had a noisy band hard to detect and this introduced too much degeneracy in our reconstruction. Nonetheless, this solution could be applied in the future for major components with a broad band in the case of not too noisy signal (for instance if the synchrotron IR radiation is used instead of the Globar).

Study of the derivative

Another method could be the study of the spectral derivative. Saturation changes the intensity of the band by creating an edge but there is still a band and the position of the inflection point could be an indication of the abundance of the mineral. We tried to follow the variation of the position of the minimum of the first derivative (corresponding to the inflection point at about 1120 cm^{-1} for this particular sample) and use it as an indicator of the abundance of the silicates. We performed some reconstructions using this method, and although it seemed to somewhat correct the problem of saturation (the false difference of density inside the spheres was reduced), it still produced artifacts.

Left shoulder of the band

Finally, we can do the reconstruction by integrating only the left shoulder of the band and avoid the saturated range. With this method, we obtained a better reconstruction of the sphere without creating a void inside. We have thus chosen to use this method for all the samples treated in this Ph.D. thesis, when we want to reconstruct the whole band of the silicate between 850 and 1150 cm^{-1}. For all the other oscillators (CH bands, OH bands, etc.) we have no problems of saturation.

Focused beam versus parallel beam

Another issue is that as we have adapted methods used for X-rays data, the algorithms have been developed for a parallel beam, and this could be a limitation of our reconstruction. In our case, we have a focused beam: the shape of the beam on the focal plane was simulated by PSFLab on Fig 5.21. The example above illustrates well this limitation. As the whole studied samples is quite large, only one sphere could be focused by our IR beam at once and the other two were out of the focal plane. On Fig. 5.22, we see one sphere well reconstructed and the trace due to the other two samples.

Some tests with other algorithms as *tomopy*, a Python library, have been carried out, but we did not get conclusive results for the moment. However, as explained by Martin et al., 2013, we can use a parallel beam model to do our reconstruction and this approximation is reasonable as the wavelengths are between 3 and 10 times bigger than the pixel size.

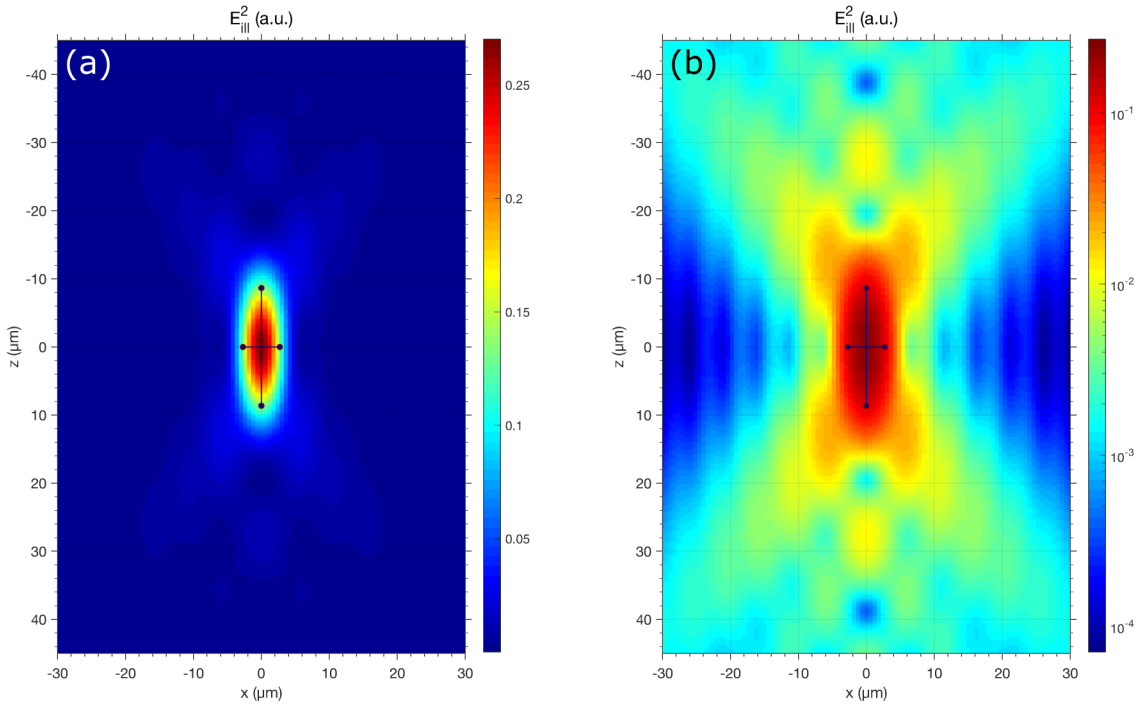

Figure 5.21: Simulation of the point spread function using PSFLab in the (uw) plane as defined on Fig. 5.5 corresponding to (xz) on this fig. (a) linear scale (b) logarithmic scale. The field FWHM dimensions at the focus in u (x) and w (z) directions are 5.4 μm and 17.3 μm, respectively. The simulation was carried out for 8 μm wavelength illumination.

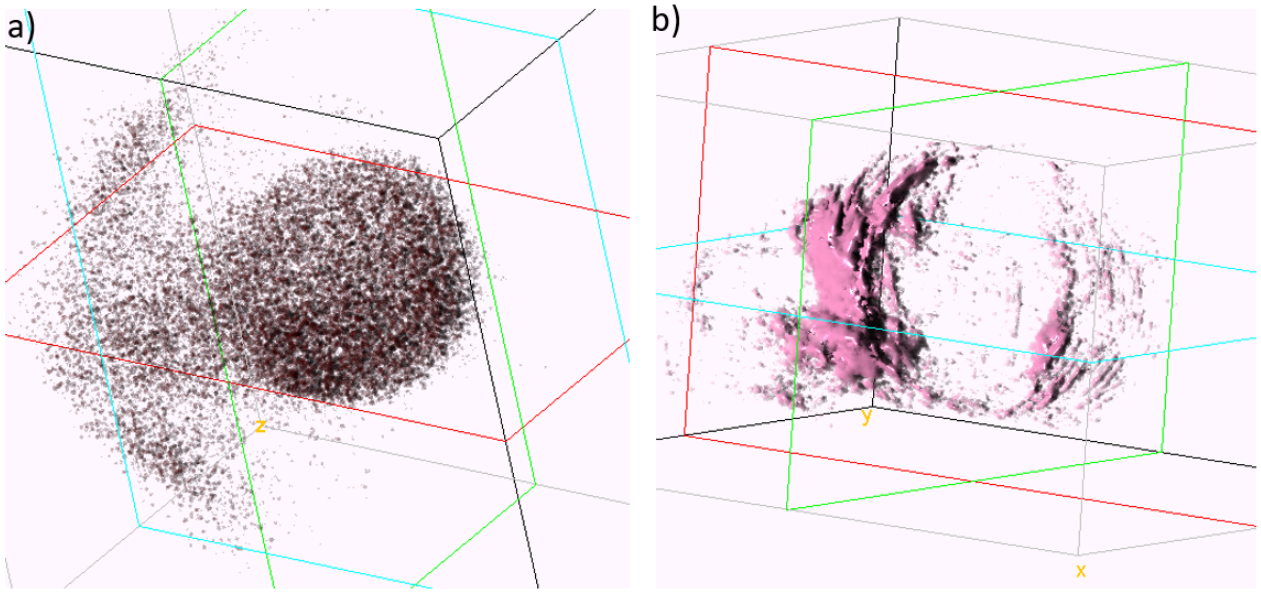

Figure 5.22: Reconstruction of the spherical samples: (a) the silicates band; (b) the organic aliphatic band representative of the glue.

Strengths and limits of IR tomography

With IR tomography, we are able to obtain the spatial distribution of different chemical phases, both the organic and the mineral in three dimensions. Moreover, we can collect all this information without destroying or damaging the sample (the sample can be collected after measurement and used for more destructive analyses, we are developing a whole protocol for precious sample with A. Aléon).

However, our setup has several limitations:

- We have strong constraints about the size of the sample. If the sample is bigger than about 50 μm, the transmitted signal is not enough to do correct measurements. Our set up is well adapted for IDPs, Hayabusa samples and small fragments of meteorites.
- The scattering/diffraction effects are still important and the their treatment needs to be better taken into account.
- The spectral resolution used is not high enough to properly map small bands. We shall improve this point when the FPA will be coupled with the synchrotron as the signal to noise will be much better (see Chapter 8).

5.6 Superposition of X-ray and IR tomography reconstructions

Another set of measurement was also performed on some of our samples with X-rays. X-ray tomography could compensate some drawbacks of the IR tomography and it is useful to couple the two techniques to have a powerful physical-chemical characterization. In this section, we are going to describe the procedure to superimpose the two sets of data. Subsequently, we will show how X-ray tomography was used to define the shape of our grains and give some constraint to filter the matter once the reconstruction is done.

5.6.1 Superposition procedure

The superposition of the IR and X-ray datasets is not obvious: X-ray tomography does not have the same spatial resolution as IR tomography. Indeed the voxel size of X-rays is 0.127 micrometers, while it is 0.66 micrometers in IR. Moreover, the two measurements were taken on different setups and the orientation of reconstructed samples is not related to one another. We have to re-sample one of the two distributions and adjust the spatial position and orientation of the samples.

The first step was to downsample the X-ray data. We used an average of 5 voxels in each direction to define a new voxel distribution. Then we have to superimpose the distribution spatially. We worked on the continuum signal at 2.8 μm in IR to adjust the superposition, as the continuum is very sensitive to the whole quantity of matter and the spatial resolution is better for small wavelengths. A first adjustment was made by hand by matching the needle's position in the two datasets. Then we vary six parameters (3 rotations and 3 translations) and we maximize the correlation between the X-ray data and the continuum at 2.8 μm in the IR. In Fig. 5.23 we can see the reconstruction of the continuum in IR, the one in X-rays and the superposition of the two.

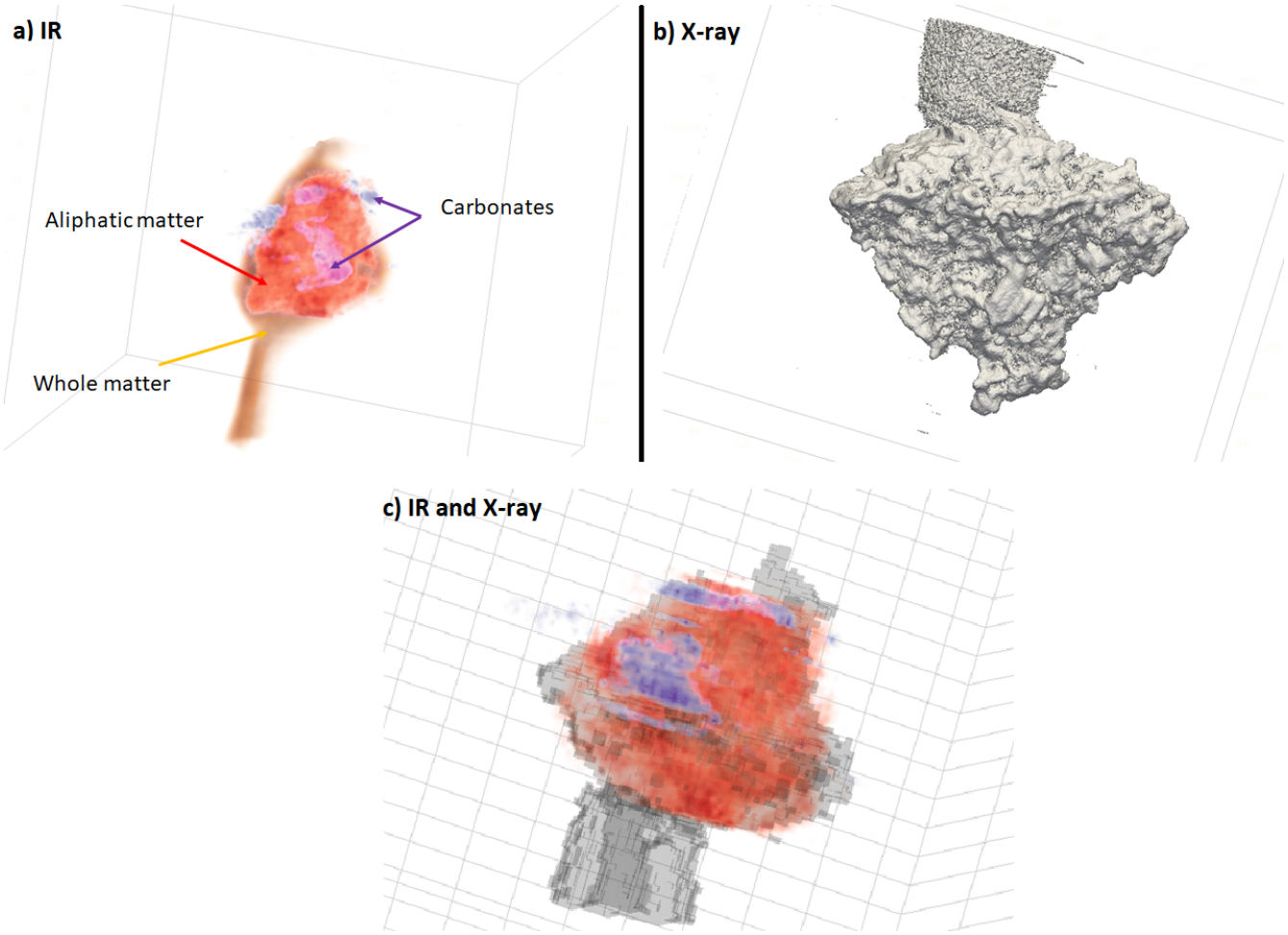

Figure 5.23: 3D distribution of (a) continuum at 2.8 μm of IR, (b) X-ray data and (c) and their superposition for *grain 3* of the Paris meteorite.

5.6.2 Shape model based on X-rays: a way to treat diffraction

We can now use the distribution of the voxels in the X-ray dataset to define criteria to filter the IR data. An example of the X-ray voxel intensity distribution of the sample is given in Fig. 5.24, the points with low value (lower than 5) represent the empty space around the sample and the noise due to the measurement of the absorption as well as due to the reconstruction. Few pixels with very high values correspond to the needle. If we keep only the ones corresponding to the sample, we define a sort of shape-model and we can use it to spatially filter the IR data.

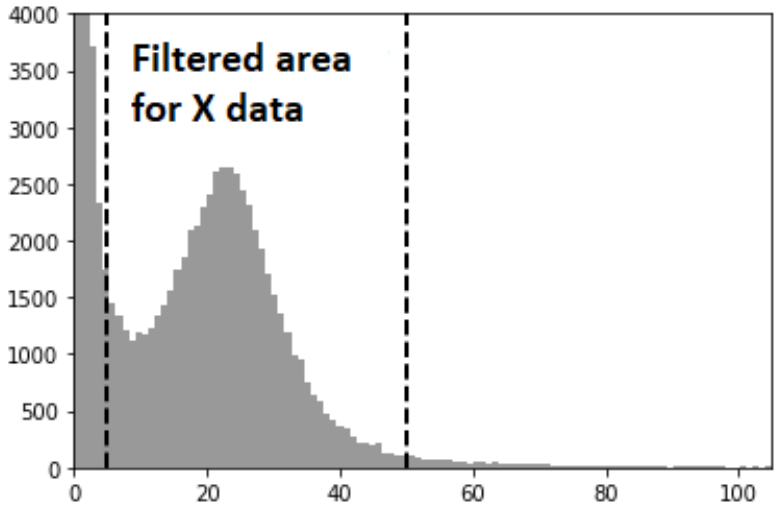

Figure 5.24: Voxel intensity distribution in the X-ray reconstruction.

When we only keep the points inside this 'shape', we emphasize compositional heterogeneity inside the sample. So far, this seems to be the quickest way to filter the effects of scattering on the IR data. The effect of applying such filter is shown in the following figure.

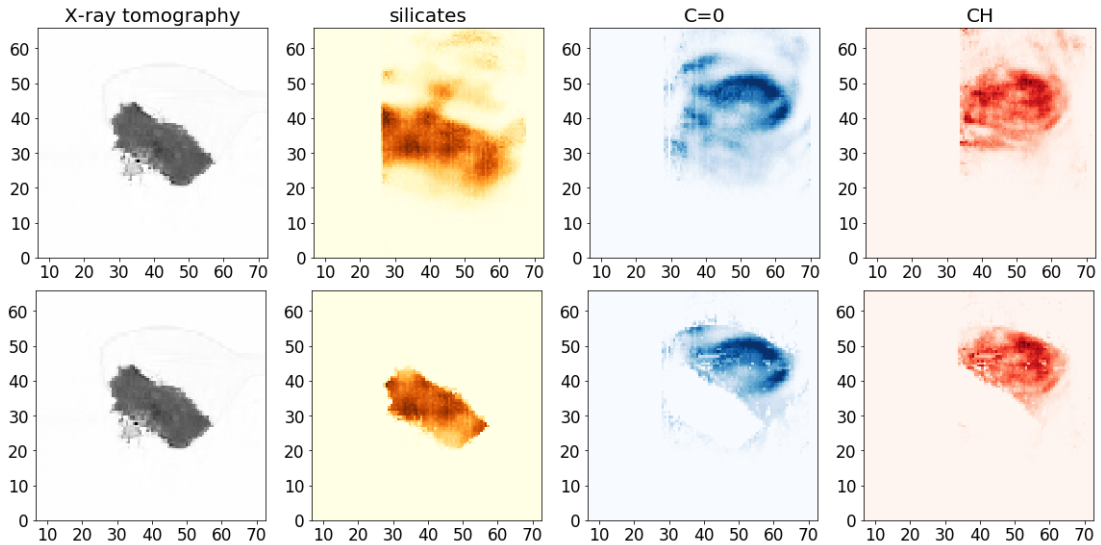

Figure 5.24: Distribution along a slice of different components reconstructed with IR before (first row) and after the application of the X-ray shape filter (second row).

Chapter 6

IR micro-tomography of 5 particles from Itokawa

Contents

After validation of the reconstruction procedure on standards, we can perform IR tomography on extraterrestrial samples. The first set of extraterrestrial samples analyzed during this Ph.D. thesis were particles from asteroid Itokawa. They are composed of pure mineral phases spatially separated at spatial scales quite larger than the pixel size, which makes the tomography easier. We received 5 grains from JAXA: RA-QD02-0214, RA-QD02-0223, RA-QD02-0232, RA-QD02-0156, and RB-QD04-0046. They are already mounted at the extremity of a carbon fiber and they are fixed by epoxy glue (JAXA preparation).

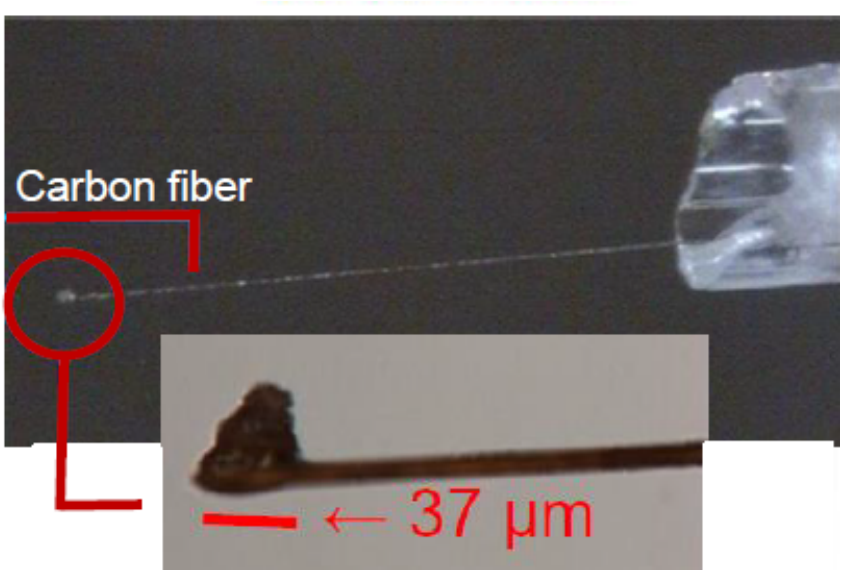

Figure 6.1: Preparation done at JAXA of Hayabusa grains for tomography.

The samples were previously analyzed by X-rays dual tomography by A. Tsuchiyama (as presented in Tsuchiyama et al., 2011) and X-rays diffraction by T. Nakamura (as presented in Nakamura et al., 2011) and they kindly provided X data presented in this thesis.

Measuring precious grains coming from Itokawa is also a useful preparation for samples that will be collected by the next sample return missions. As non-destructive technique bringing complementary information to XCT tomography and XRD, IR tomography could be part of a multi-scale analytical sequence in the preliminary characterization of samples returned by the OSIRIS-REx and Hayabusa2 missions.

6.1 Global composition study

6.1.1 Identification of functional groups

Study of IR spectra

We have first listed the bands present in the different spectra. The attribution was done based on Yesiltas et al., 2014, Beck et al., 2014 for the mineral bands and Dartois et al., 2005 for the organic bands. In the following table, we sum up the bands observed in the different grains embedded in glue and the attribution of each band. Only the three last numbers are

used to refer to the sample.

Frequency	Component	samples				
		214	223	232	156	046
1140-850	Silicate	x	x	x	x	x
971	Olivine	x			x	x
1018-1025	Calcium poor pyroxene		x	x		
1049	Calcium rich pyroxene	x				
1110	C-O stretching	x	x	x	x	x
1180	sulfates	x	x	x	x	x
1249	CC aromatic skeleton	x	x	x	x	x
1373	CH_2 deformation	x	x	x	x	
1450	CH bending	x	x	x	x	
1604	C=C	x	x	x	x	x
1751-1774	C=O (COO ester)	x	x	x	x	x
2864	CH_2 symmetric stretching	x	x	x	x	x
2962	CH_2 asymmetric stretching	x	x	x	x	x
3062	CH aromatic stretching	x	x	x	x	x
3000-3750	OH stretching	x	x	x	x	x

Table 6.1: List and attribution of the main spectral signatures in the 5 Hayabusa grains.

We observed several groups of signatures: a first group is due to the organic glue which surrounds the sample. Indeed all these signatures (in blue in the table below) are spatially correlated. To prepare the sample, the JAXA used glycol phthalate glue to fix the sample to the carbon fiber. This organic wax is responsible for the following vibrations: we detect the C-O stretching at 1110 cm^{-1}, the CH_2 deformation at 1373 cm^{-1} and the CH_2 stretching (symmetrical at 2864 cm^{-1} and asymmetrical at 2962 cm^{-1}). We can also notice the presence of a small band at 3062 cm^{-1} due to CH aromatic stretching. Finally, a large OH stretching band between 3000 and 3750 cm^{-1} is visible. The presence of the ester group COO conjugated to the aromatic cycle of phthalate explains the presence of the band due to the C=O vibration at 1751-1774 cm^{-1} and the C=C vibration at 1604 cm^{-1}. All these bands are visible in Fig. 6.2, in the red spectrum coming from an area mainly composed of glue on

a projection of the grain RA-QD02-0214.

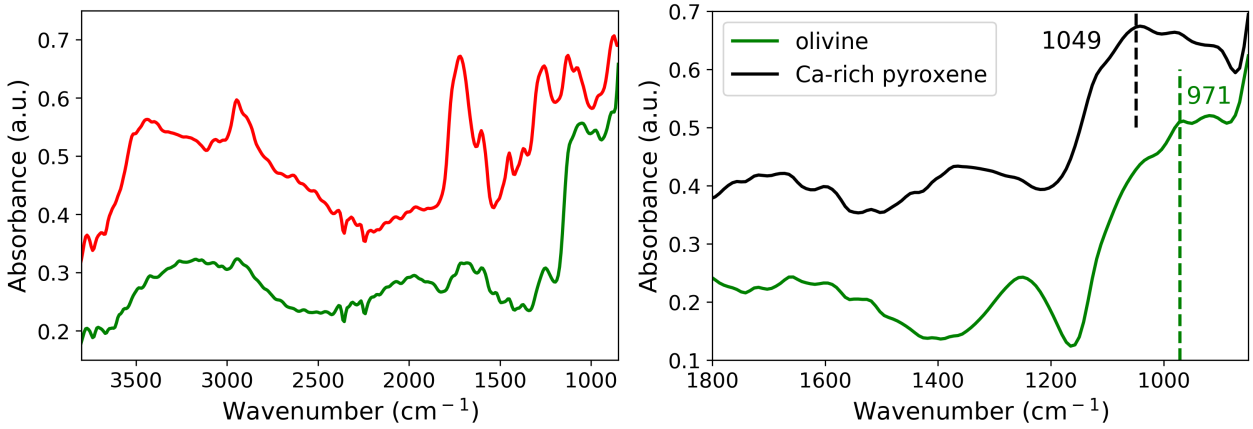

Figure 6.2: (a) Example of spectra typical of the glue (red) and the minerals (green) for one projection of the grain RA-QD02-0214. (b) Zoom in the the mineral region showing two spectra of the grains RA-QD02-0214 with a difference in the mineral composition.

Then we note a broad band around 10 μm due to Si-O stretching. We observe heterogeneity in the structure of this band. Indeed the shape and the position of the maximum varies inside samples. For instance, a maximum around 1050 cm^{-1} signs the presence of Calcium rich pyroxene while a maximum at 971 cm^{-1} is characteristic of the presence of the olivine: forsterite 60-65 (Hamilton et al., 2010 for the identification of the olivine, Omori et al., 1971 for pyroxene identification). We have shown in the panel (b) of the previous figure two spectra extracted during the measurement of the grain RA-QD02-0214. Heterogeneity inside Hayabusa grains is visible even if the signal to noise ratio is low in our spectra.

Finally, for the five grains, we detect a strong band at 1180 cm^{-1} in a very localized spot, the position of the IR band suggest sulfate but this identification need to be confirm as other papers as Noguchi et al., 2014 did not detect any sulfate on Hayabusa samples.

2d projections and spatial coherence

Once the bands were identified, we studied their spatial distribution in the projections. We observed that glue and silicates of the grain are spatially well separated. We also distinguished a third phase which is not co-localized with any other band. This phase has a signature at

1180 cm^{-1} and we identify it as sulfate (Yesiltas et al., 2016). Fig. 6.3 shows the spatial distribution of these three phases for one projection, in panel (a) the glue represented by the area under the CH aliphatic band, in panel (b) the left shoulder of the general band of the silicate and in panel (c) the band of the sulfate. In this example, the spatial anti-correlation of these phases is well visible.

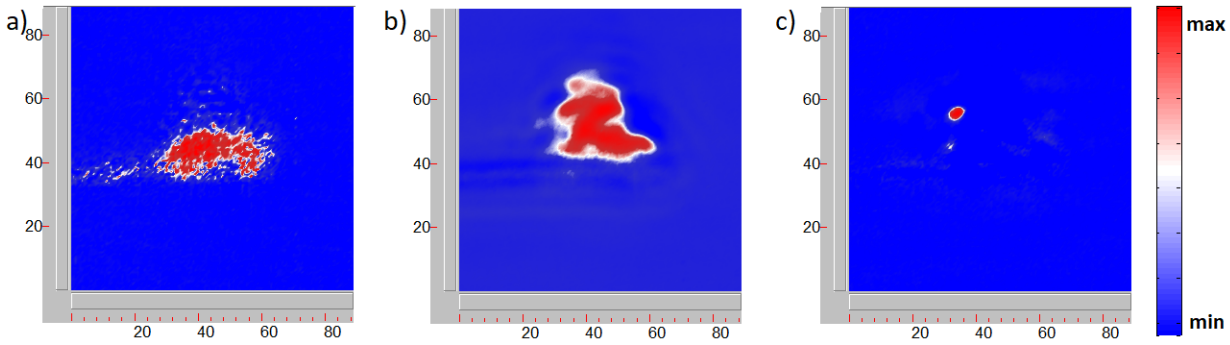

Figure 6.3: Spatial distribution of (a) CH aliphatic stretching of the glue, (b) silicate large band, and (c) a sulfate grain for one projection of the grain RA-QD02-0214.

The next step was to separate different minerals inside the large silicate band. For the polymineralic grain RA-QD02-0214, we separated the olivine and the Ca-rich pyroxene. The following figure shows the spatial distribution of olivine and Ca-rich pyroxene on grain RA-QD02-0214 and we see that they are spatially separated.

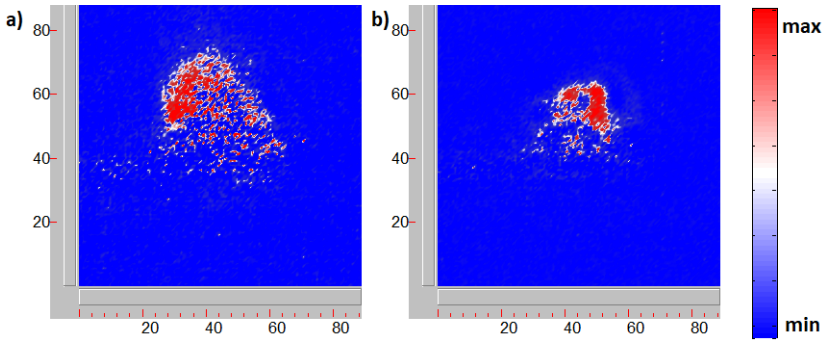

Figure 6.4: Spatial distribution of (a) olivine and (b) Ca-rich pyroxene for one projection of the grain RA-QD02-0214.

6.1.2 Comparison with X-rays analysis

These 5 grains had already been analyzed by dual-energy XCT by A. Tshuchiyama and by S-XRD by T. Nakamura. Explications and examples of results of these techniques applied

on Hayabusa grains are presented in Chapter 1 of this thesis. In the next section, we are comparing the results obtained by these three methods for our five grains and discuss the complementarity of these methods.

In the following table, we compare the composition observed by the three methods. We have listed the major phases in black. Minor phases (occupying small volume in samples) are listed in red and blue: the phases detectable by FTIR are in red and the other ones (phosphate, chromite, troilite and taenite) visible only with X-rays are in blue.

Method	band reconstructed on samples				
	214	223	232	156	046
IR tomography	Ca-rich pyroxene Olivine	Ca-poor pyroxene	Ca-poor pyroxene	Olivine	Olivine
S-XRD	Ca-rich pyroxene Olivine Plagioclase	Ca-poor pyroxene Ca-rich pyroxene Plagioclase	Ca-poor pyroxene Plagioclase Olivine	Olivine	Olivine
dual energy X-CT	Ca-rich pyroxene Olivine Plagioclase	Ca-poor pyroxene Plagioclase Ca-rich pyroxene	Ca-poor pyroxene Plagioclase Ca-rich pyroxene Chromite Troilite Taenite	Olivine	Olivine Plagioclase Troilite

Table 6.2 : Comparison of the component observed by IR tomography, S-XRD and dual energy X-CT.

With the S-XRD analysis, we have a precise global identification about the type of mineral and the dual energy X-CT data confirms identification and brings spatial information and structural information. These two complementary techniques are adapted to study the mineral part of the sample.

For the 5 grains, IR confirms the detection by XCT and S-XRD concerning the major phases, which validates the IR spectral attributions. In the case of the grain RA-DQ02-0214,

the two mineral phases are well separated, and each one of them is around 10x10x10 μm^3 which makes the detection easier and the distinction feasible. However, with the current state of our setup, it is hard to extract more information concerning minerals as the signal to noise ratio is quite low in our data (due to the time constraints). Also, the minor phases (in red) are not detected in our data: minor phases sign as small absorption bands which are hard to distinguish from the noise. Moreover, it is harder to distinguish two phases with quite close spectra as Ca-rich pyroxene and Ca-poor pyroxene. The coupling of the tomography setup with a synchrotron beam will help us to go further (see Chapter 8).

In the next section, we are going to study the 3D structure of grains and compare spatial distribution obtained with X-CT and IR tomography.

6.2 Three-dimensional Study

6.2.1 Dual X-CT analysis

Comparison between the 5 particles

First, we analyzed the results of X-CT data and we noticed differences between grains that allowed us to classify the grains in three categories. A first kind of sample is monomineralic samples (grains RA-QD02-0156 and RB-QD04-0046) or mostly monomineralic particle (grain RA-QD02-0223): we observe mainly one phase on X-CT slices of these grains as shown in panel (a) of Fig. 6.5 and we detect only one component in IR tomography. The grain RA-QD02-0214 is composed of two phases, spatially well separated and each of them occupies about half of the sample. The panel (b) of the next figure shows a slice of this grain (we distinguish the olivine on the left and the Ca-rich pyroxene on the right of the sample). Finally the grain RA-QD02-232 shows a more complex structure with a higher heterogeneity (see Fig. 6.5), we observe some small inclusions of troilite, chromite and taenite inside Ca-rich pyroxene.

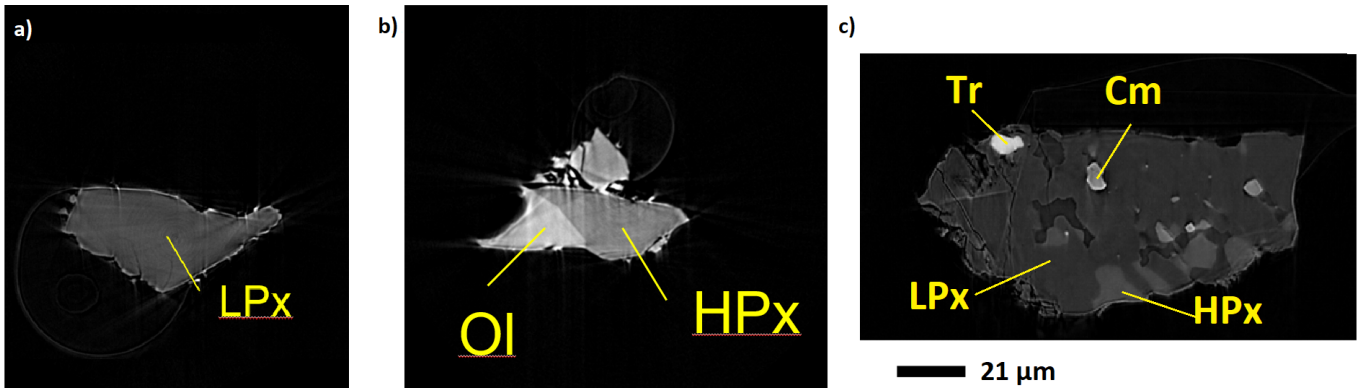

Figure 6.5: X-ray (xy) slices measured at 7 keV for (a) RA-QD02-223, (b) RA-QD02-0214, and (c) RA-QD02-0232 (from measurements made by A. Tsuchiyama).

Shape model obtained from X-data

We also used the X-ray data to constrain the shape of the sample, to create a filter for the IR and reduce scattering effects, as explained in Section 5.6.2. To define this spatial filter, we relied on levels of gray. In the following figure, a slice of a sample and the profile along the yellow line is shown. We have defined one filter for the grain (LAC higher than 50, see Fig. 6.6.a) and one for the glue surrounding the grain (LAC between 2 and 35, see Fig. 6.6.b) based on the LAC profile.

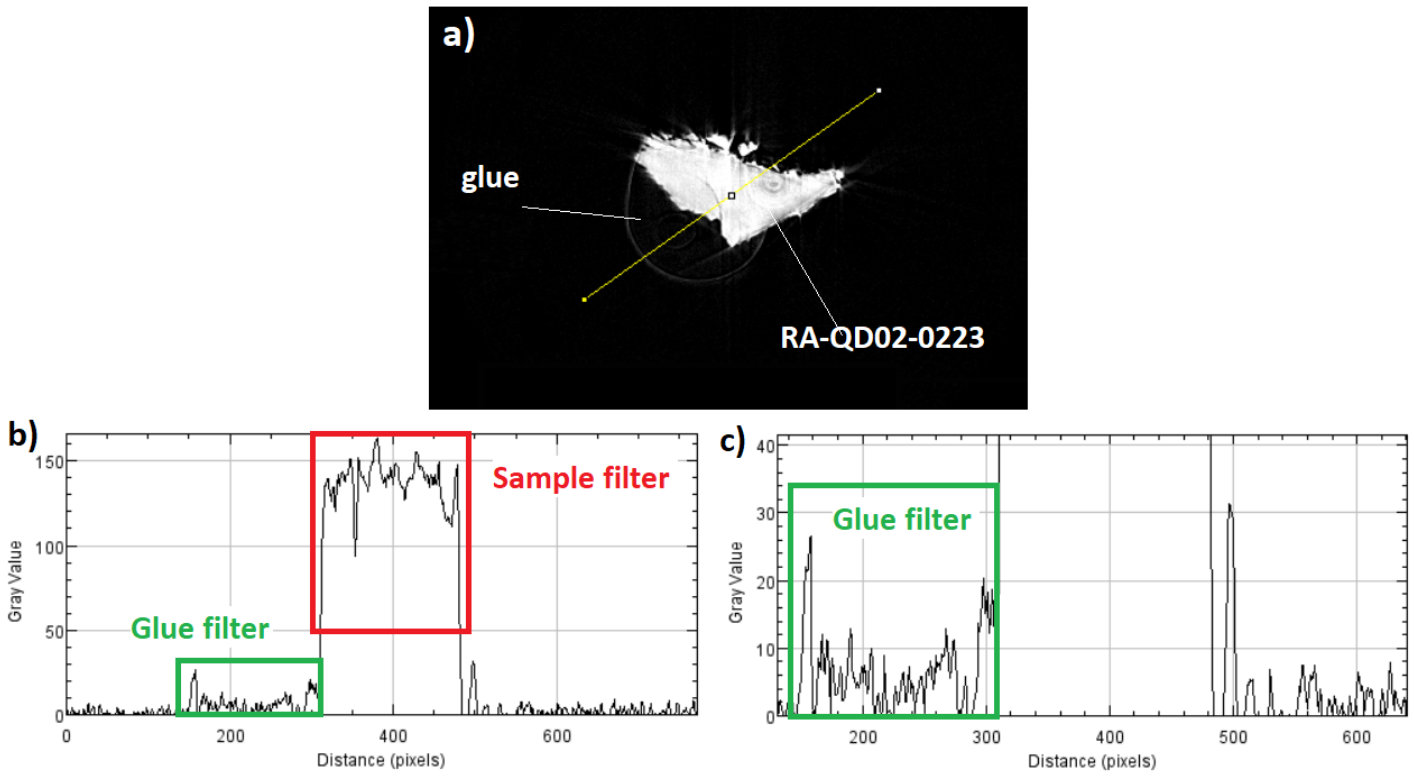

Figure 6.6: (a) slice (xy) of the grain RA-QD02-0214, (b) LAC profile along the yellow line of panel a, (c) zoom of the LAC profile for small values.

6.2.2 IR 3D reconstruction

For each of the five grains, we have reconstructed the following bands: the silicate general band (with the left shoulder as explained in the previous chapter), the CH aliphatic band and the OH bending (or C=O) bands. On the polymineralic particle RA-QD-0214, we also reconstructed the different mineral phases. In the following, we will present the 3D structure reconstructed by IR for one grain of each category defined above: with the grain RA-QD-0223, we will try to reconstruct both organic and mineral part and well separate them. The study of the grain RA-QD-0214 will then help us to check our ability to separate mineral phases in 3D and finally, we will study the more complex grain RA-QD-0232.

Reconstruction on a monomineralic grain: the example of RA-QD02-0223

In the following figure, we see the reconstruction of the CH aliphatic band which is characteristic of the glue (panel a) and the silicate large band reconstruction (panel b) which

fits the X-ray shape of the grain RA-QD02-0232. The X-ray data are represented in a gray scale (the glue and the needle are represented in very light gray and the grain is visible in a brighter gray). We see that the two data-set agree quite well, considering that these are the raw reconstructed data, visualized before applying any filter on IR data. This shows that the IR reconstruction protocol can be used for Hayabusa grains. The video 1, provided as supplementary material, shows the 3D distribution of the different components for this grain.

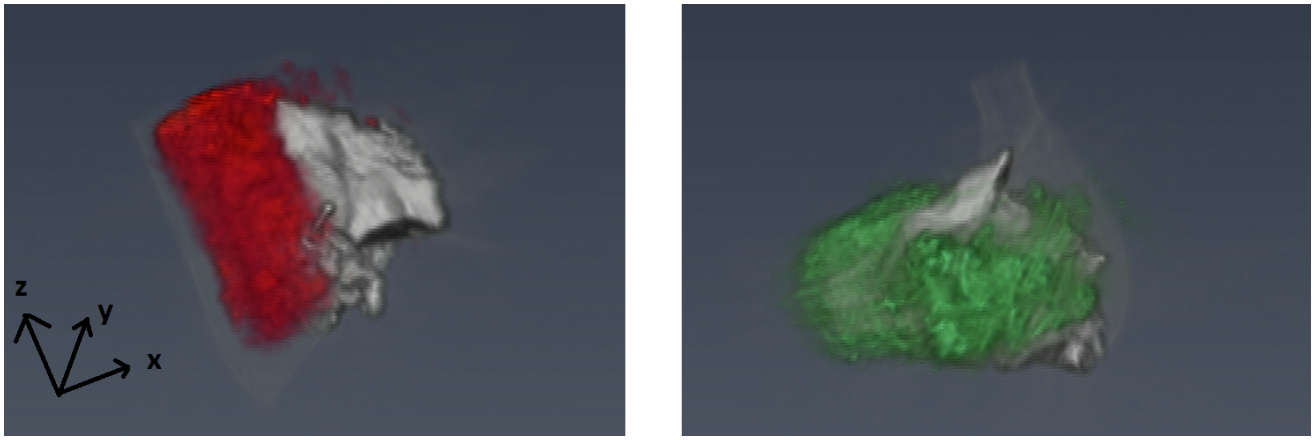

Figure 6.7: separation between glue (in red) and grain in 3D (in green)

Moreover, on reconstructed data, we can check that the grain and the glue surrounding it are well separated. Indeed, even if the glue is in contact with samples and a small part of it has maybe slotted in samples, this two phases must be spatially separated and the correlation between them should be small.

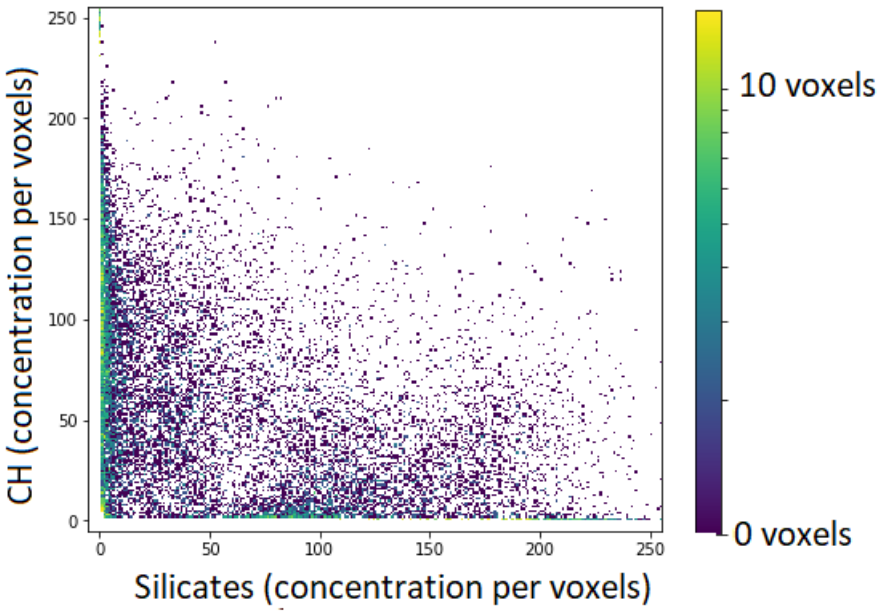

Figure 6.8 : Correlation diagram between the CH aliphatic and the silicate. The scale is given in log scale.

Fig. 6.8 shows the correlation diagram between the abundance of the CH oscillators and the silicates. We can see that the distribution of the CH aliphatic (glue) and the silicate (grains) give two clouds of dots, which confirms that the two populations are well anti-correlated. The calculation of the correlation between the broad band of the silicates and the band of the aliphatic CH, characteristic of the glue, gives a value of 0.13. Such low value proves the absence of correlation of these two phases and our ability to well-separate glue and grains.

After doing these verification, we have used the X-ray data to create a shape model and limit the scattering/diffraction on the IR sample. We can then represent the reconstructed data by filtered slices inside the reconstructed samples. In Fig. 6.9, we see average slices (xy) (plan parallel to the needle axis) for a given z. The four phases reconstructed are represented.

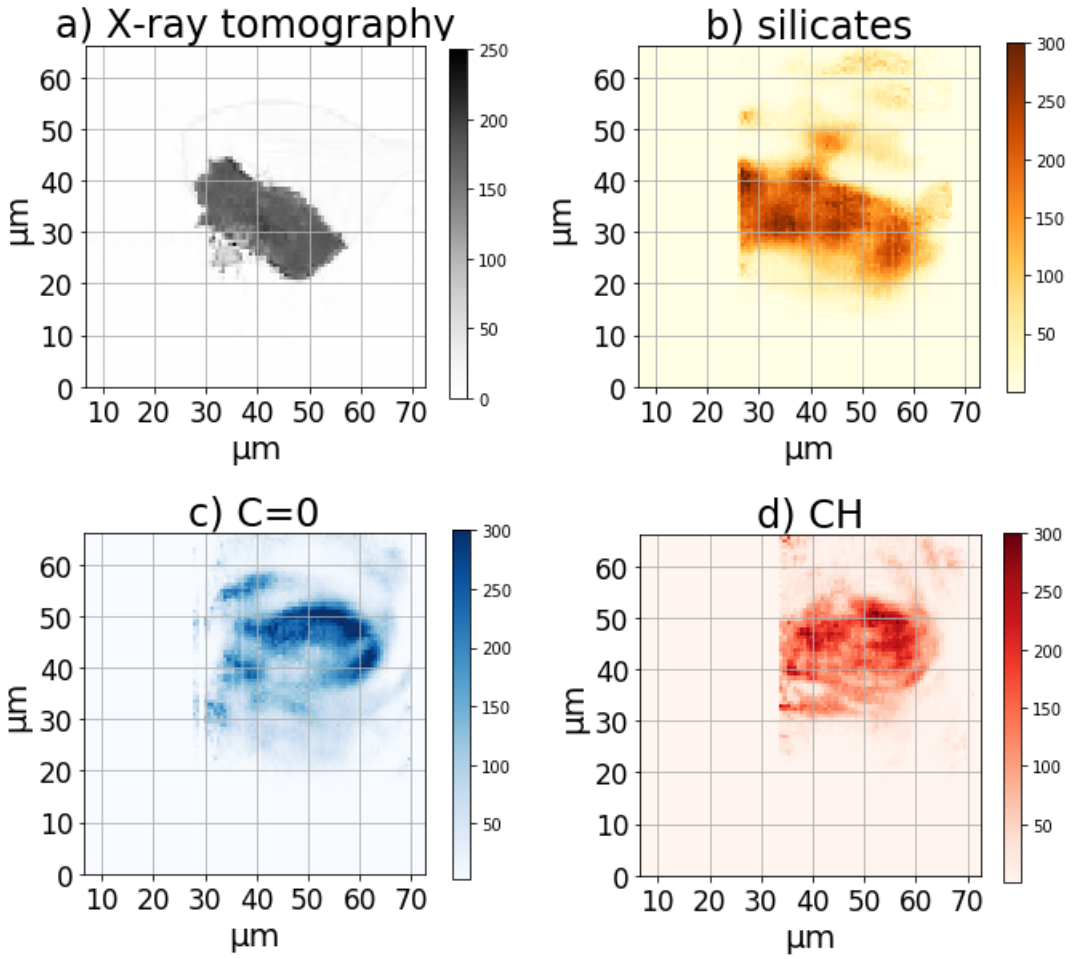

Figure 6.9: Slices (xy) of grain RA-QD02-0223, reconstruction of (b) silicate, (c) C=O and (d) C-H aliphatic bands. The corresponding X-ray slice is reported in the (a) panel.

We confirm the presence of the silicate band inside the points corresponding to the sample. We see some small heterogeneity inside the distribution of silicates, a part of this heterogeneity could be real in the sample, but it is hard to complete spread the possibility of heterogeneity due to reconstruction artifact. The heterogeneity visible in the organic reconstruction seems more real as its distribution is probably heterogeneous in density.

Reconstruction on a bi-mineralic grain: the example of RA-QD02-0214

For polymineralic grains, in addition to the reconstruction mentioned above, we have also performed separated reconstructions for different minerals based on the intensity of the second derivative (see Chapter 2). Fig. 6.10 shows in panel (a) the X-ray data for grain RA-QD02-

0214. Only the grain (and not the glue) is represented and the two levels of grays, significant of the different linear attenuation coefficient at 8 keV, represent the olivine distribution (in light gray) and the Ca-rich pyroxene distribution (in dark gray). In panel (b), we can see the distribution of the IR reconstruction of the olivine in green and Ca-rich pyroxene in brown. We see that IR tomography based on the second derivative agrees well with the distribution of different minerals predicted by the X-data. The video 2 in appendix shows the distribution of the different components for this grain.

Figure 6.10: separation between minerals in 3D for RA-QD02-0214.

Then we can represent the reconstructed data by slices inside the reconstructed sample. In Fig. 6.11 we see slices (xy) (plan parallel to the needle axis) for a given z. The two mineral phases and the organic phases reconstructed are represented. Once again, we clearly see the separation between the olivine and the pyroxene in the slices.

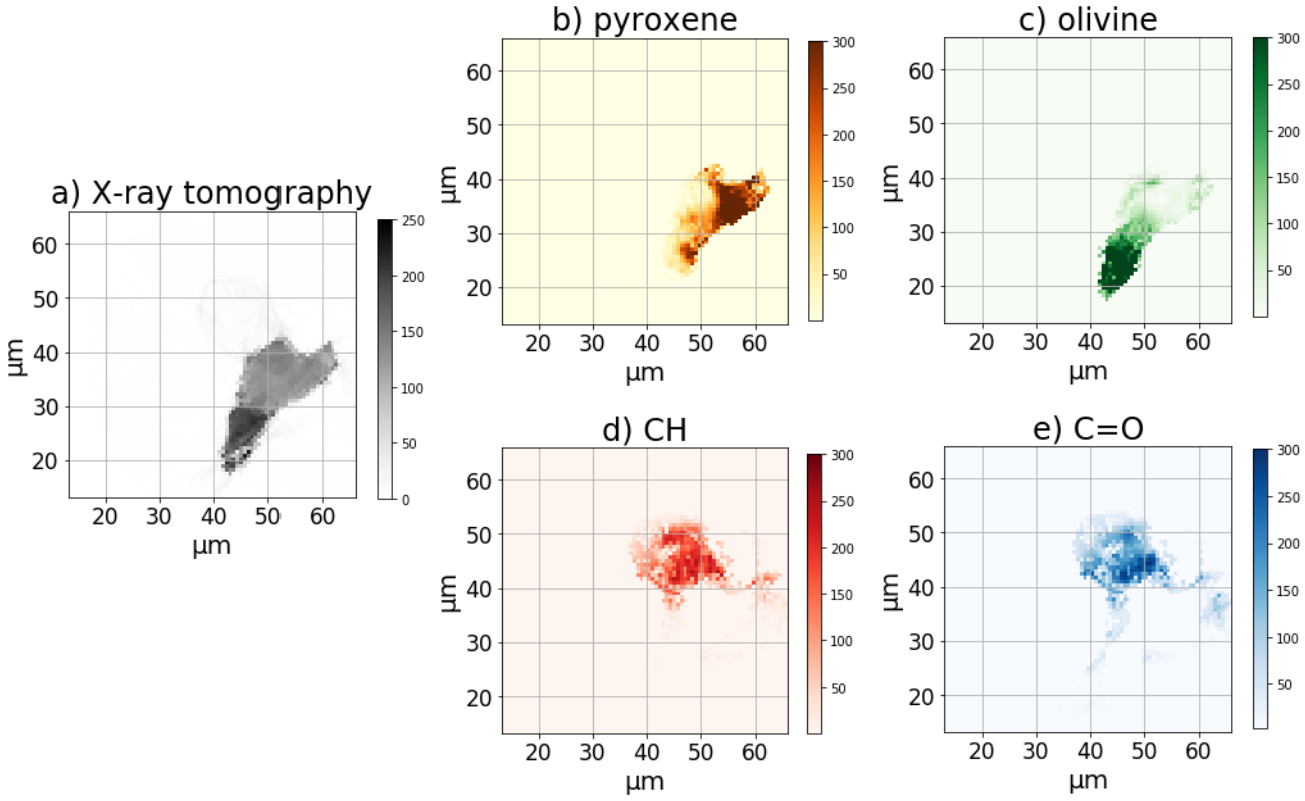

Figure 6.11: slices (xy) of grain RA-QD02-0214, reconstruction of (a) X-rays data (b) pyroxene, (c) olivine, (d) C=O band, and (e) C-H aliphatic band.

Reconstruction on a polymineralic grain: example of RA-QD02-0232

Finally, we studied the more complex grain RA-QD02-0232 to understand how much we are sensitive to the heterogeneity inside mineral phases when we reconstruct data in the infrared. In Fig. 6.12 we see slices yz for a given x (three different slices spaced by 3.3 micrometers from each other). This grain is mainly composed of Ca-poor pyroxene with different smaller phases of about 10x5x10 μm^3 embedded in the Ca-poor pyroxene, so we can well see the heterogeneity on this grain in the X-ray data. In addition to X-ray data, the silicate reconstruction is represented.

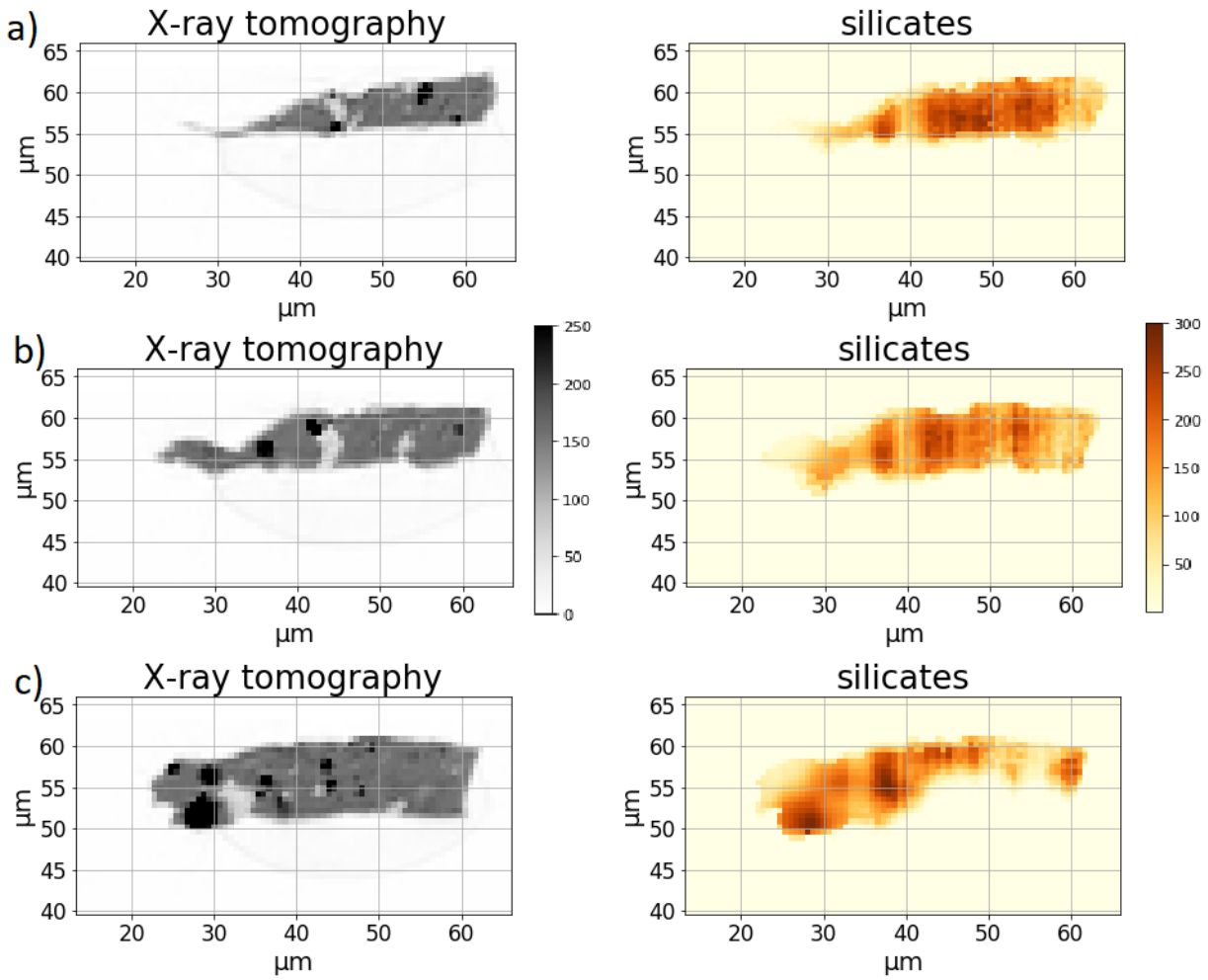

Figure 6.12: grain RA-QD02-0232 reconstruction from X-rays data (left), and from the IR silicate band (right) for (a) slice (yz) 55, (b) slices (yz) 58 and (c) slice (yz) 61.

We detect well the differences in composition in the X-ray data with some black points (trolite or chromite) and some bright spots (plagioclase), but unfortunately, we do not clearly see these points in the silicate distribution. This shows the limit of our setup to detect small phases, as we are not yet able to detect empty spaces or space occupied by phases not detectable in the MIR range. With this example, we stress the necessity of coupling X-ray data to IR data.

Strength of the IR tomography for precious astrophysical grains

We have proven in this chapter our ability to perform coupled IR and X-rays analysis on precious grains. In a sequence of analysis, micro-FTIR 3D spectral imaging coupled with X-rays

tomography can provide a first non-destructive characterization of whole grains, to identify areas of interest, to identify and spatially separate organics and minerals, and thus provide useful information before subsequent destructive analysis. Moreover, laboratory infrared spectroscopy allows comparison with astronomical observations of primitive Solar System small bodies (asteroids, comets, TNOs). In the next chapter I will show the results of IR tomography on a sample rich in extraterrestrial organic matter, the Paris meteorite.

Chapter 7

3D study of the Paris meteorite

Contents

The sample return missions Hayabusa2 (JAXA) and OSIRIS-REx (NASA) are currently visiting and will soon collect samples from carbon-rich (and possibly hydrated) asteroids 162173 Ryugu and 101955 Bennu. Hayabusa2 has reached Ryugu in June 2018, and it will return material from the asteroid to Earth by December 2020. Similarly, the OSIRIS-REx mission of NASA's New Frontiers Program was launched towards Bennu on September 8, 2016. It is reaching the asteroid in August 2018 and it will return samples from this C-type asteroid to Earth in 2023.

The returned samples may cast light on the processes that took place in the early Solar System and on the delivery of water and complex organics to the primitive Earth. In the analysis of returned samples, FTIR spectroscopy will be a valuable non-destructive tool to

detect and characterize the extraterrestrial organics. In particular, FTIR microtomography can provide spatially resolved chemical composition and spatial correlations between organics, minerals and water.

The first exemple of the use of this technique on a meteorite was provided by Yesiltas et al., (2016), who analysed a fragment (45 μm in size) of the CM Murchison by synchrotron-based FTIR microtomography. They illustrated the highly heterogeneous chemical composition of Murchison. Looking at the spatial distribution relative to water, they were able to identify hydrous and anhydrous silicates. They also evidenced a proximity of phyllosilicates to CH_3 and CO, suggesting that hydrated silicates possibly played a role in the formation of certain organics.

In this chapter, we will show the preliminary results of the microtomography analysis of three fragments of the matrix of the CM Paris meteorite. On these samples, we have performed both X-rays and FTIR microtomography at the PSICHE and SMIS beamlines of SOLEIL. Differently from the case of Itokawa samples discussed in the previous chapter, the Paris meteorite samples show the presence of an extraterrestrial organic matter component that is intimately mixed with the mineral components at the micron- and sub-micron scale. We will show the detection of this organic matter in 3D and we will illustrate the limits of detection in our current setup. We will also discuss how the tools developed in this chapter may be used for the future analysis of samples returned from space.

7.1 Studied samples and experimental details

We studied three small fragments from the matrix of the Paris meteorite (about 30x35x30 μm^2 for Paris 2, 30x60x30 μm^2 for Paris 3 and 50x40x20 μm^2 for Paris 5). The samples were provided by B. Zanda (MNHN, Museum d'Histoire Naturelle de Paris). These three fragments were extracted from the least altered lithologies of Paris (Hewins et al., 2014 and Marrochi et al., 2014). The samples were mounted at the extremity of tungsten needles (see Fig. 7.1) thanks to the FIB preparation described in chapter 5.

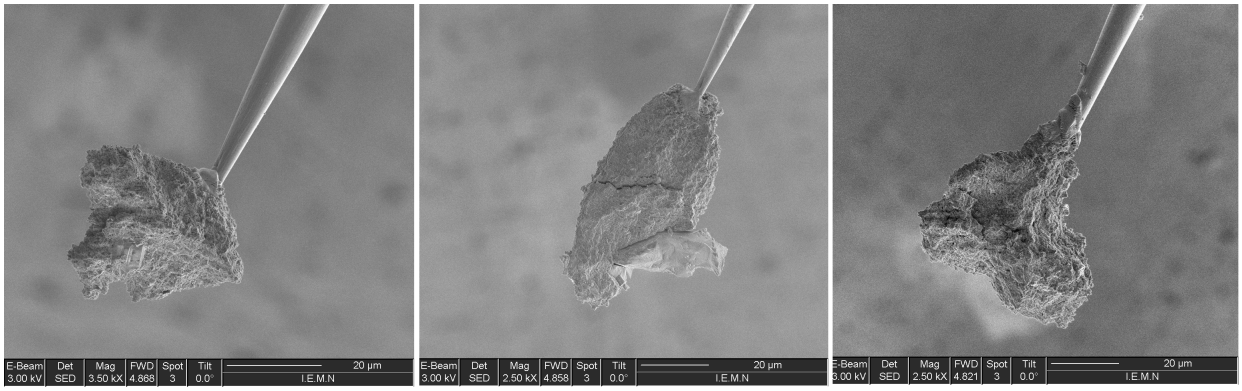

paris 2 **paris 3** **paris 5**

Figure 7.1: SEM images of the three Paris samples welded on tungsten needles (preparation by D. Troadec, IEMN-Lille).

We performed FTIR microtomography of these samples at the SMIS beamline with a globar source, using a 128x128 FPA detector, a 25x objective (numerical aperture 0.81), a 25x condenser, and an optical system providing additional 2.5x magnification. The spectral range was 850-4000 cm^{-1} and the spectral resolution was 16 cm^{-1}. For the background measurements we averaged 128 scans, while we used only 32 scans for the meteorite projections to limit the whole tomographic acquisition to less than 6 hours. The spatial resolution for every 2D projection was between 3.3 μm (for a wavelength of 2.7 μm) and 12 μm (for a wavelength of 10 μm). The field of view was 84x84 μm^2 and the pixels size projected on the focal place was about 0.66 μm. Such dense spatial sampling produced more than 2 millions voxels (0.66x0.66x0.66 μm^3 in size) in the reconstructed 3D images, and allowed the detection of structures smaller than the wavelength (although the system remained diffraction-limited in terms of spatial resolution, see section 2.6).

The meteorite samples were rotated by steps of 1 degree and we measured the 2D IR projections for 180 angles per sample. All IR projections were ratioed to reference measurements obtained on an empty field of view. All spectra were treated with a PCA-denoise procedure, similarly to what discussed in section 2.3. For each 2D IR projection, we calculated the spatial distribution of specific functional groups by integrating the areas under the corresponding IR bands (aliphatic CH_2 and CH_3 stretching, -OH stretching, SiO bands, etc.). Tridimensional reconstructions of the abundance of these functional groups were then obtained with the TXM Wizard software according to the procedure described in chapter 5.

After FTIR microtomography, we have performed X-rays microtomography on the same samples. Measurements were led at 17.6 and 20 keV at PSICHE, with a 50x objective. We used 400 projections, overall scanning 180 degrees and an exposure time of 10s per projection. We obtained a pixel size of 0.127 μm and a field of view of 130x130 μm^2. All the X-ray measurements were performed after micro-FTIR measurements to ensure that the organics were well preserved for IR tomography. The 3D reconstruction was calculated using Tomopy on Python coding.

All the post-treatment of the data was done with Python and the 3D visualization was performed with the Avizo software. Superposition of the X- and IR-images was obtained following the procedure described in chapter 5.

7.2 Results

In this section we will first describe the components observed by FTIR in the three samples and then we will study the spatial distribution of each component.

7.2.1 Average spectra and global composition of the fragments

The average IR spectrum of each sample was obtained before reconstruction. We averaged all the IR spectra containing a significant amount of meteoritic material., This was obtained by introducing a filter on the silicate band area: for each 2D projection, we only kept spectra with a silicate band area higher than 20% of the maximum value of this band. This filter allowed to reduce the diffraction and scattering effects, especially at the edges of the grains. We obtained a filtered dataset of 360 365 spectra for sample Paris 5, 455 030 spectra for sample Paris 3, and 156 654 spectra for sample Paris 2. Fig. 7.2 presents the obtained average spectra for the three samples. The assignment of the IR bands in the average spectra is given in table 7.1 (based on Matrajt et al., 2004, Dartois et al., 2005, Merouane et al., 2012, Yesiltas et al., 2016).

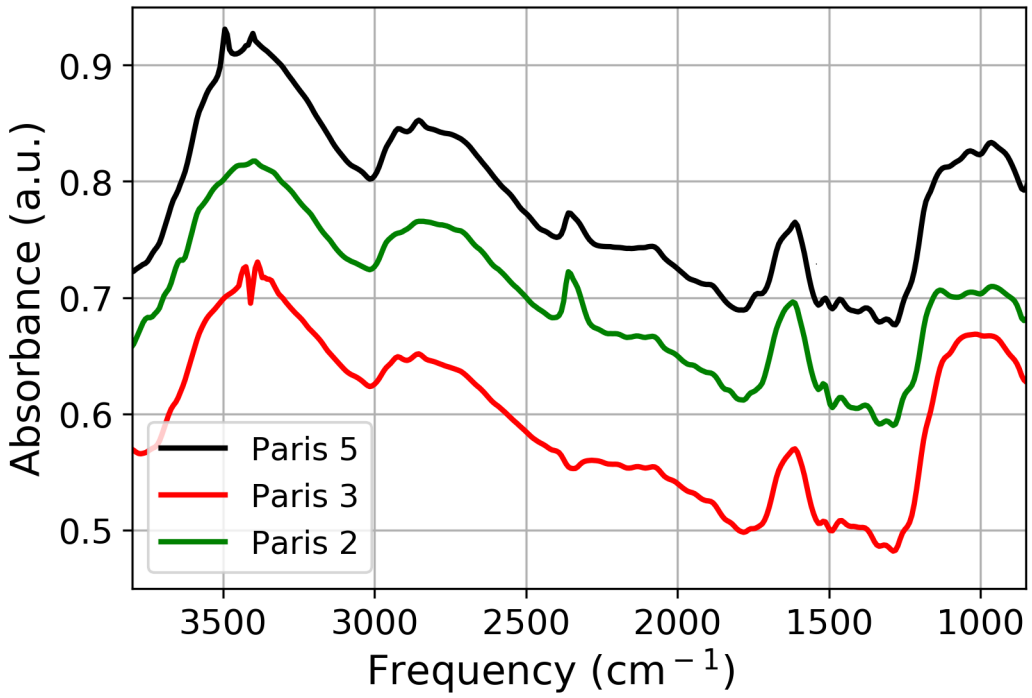

Figure 7.2: Average spectra of the three fragments of the Paris meteorite : in green Paris 2, in red Paris 3, and in black Paris 5.

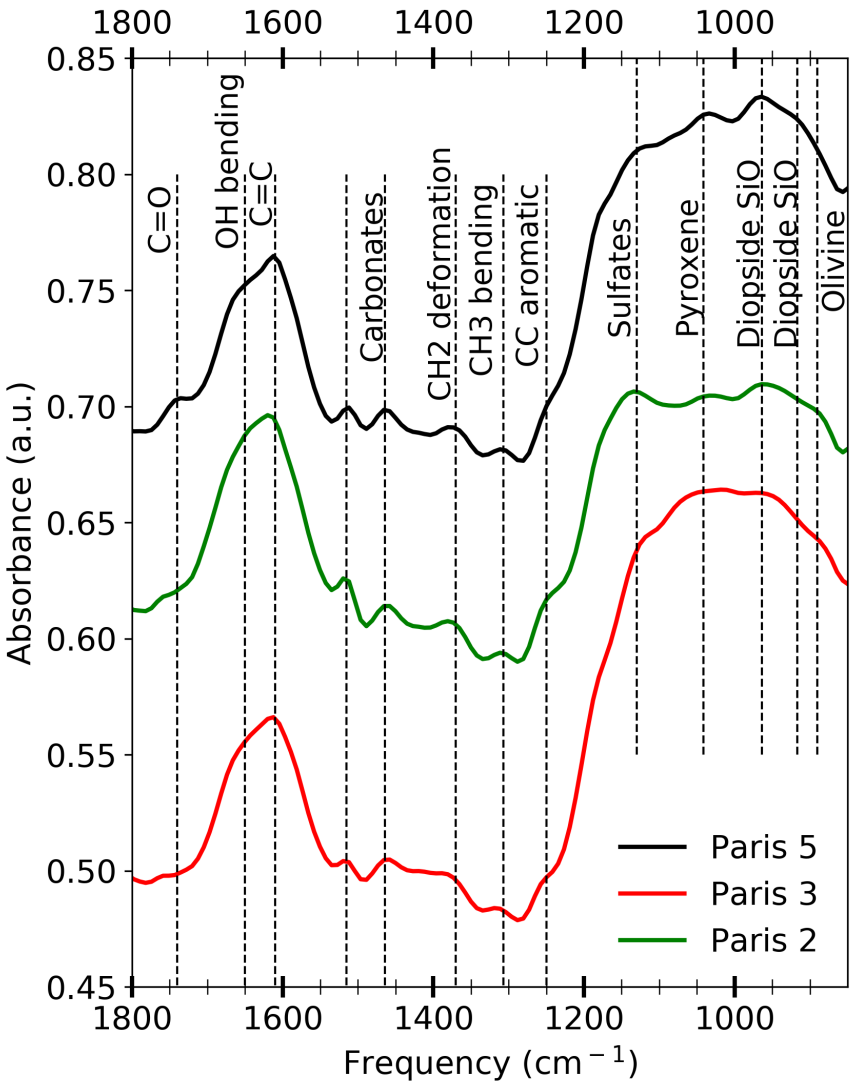

Figure 7.3: Zoom on a spectral regions to evidence the positions of the organic and silicate bands for the three fragments of the Paris meteorite.

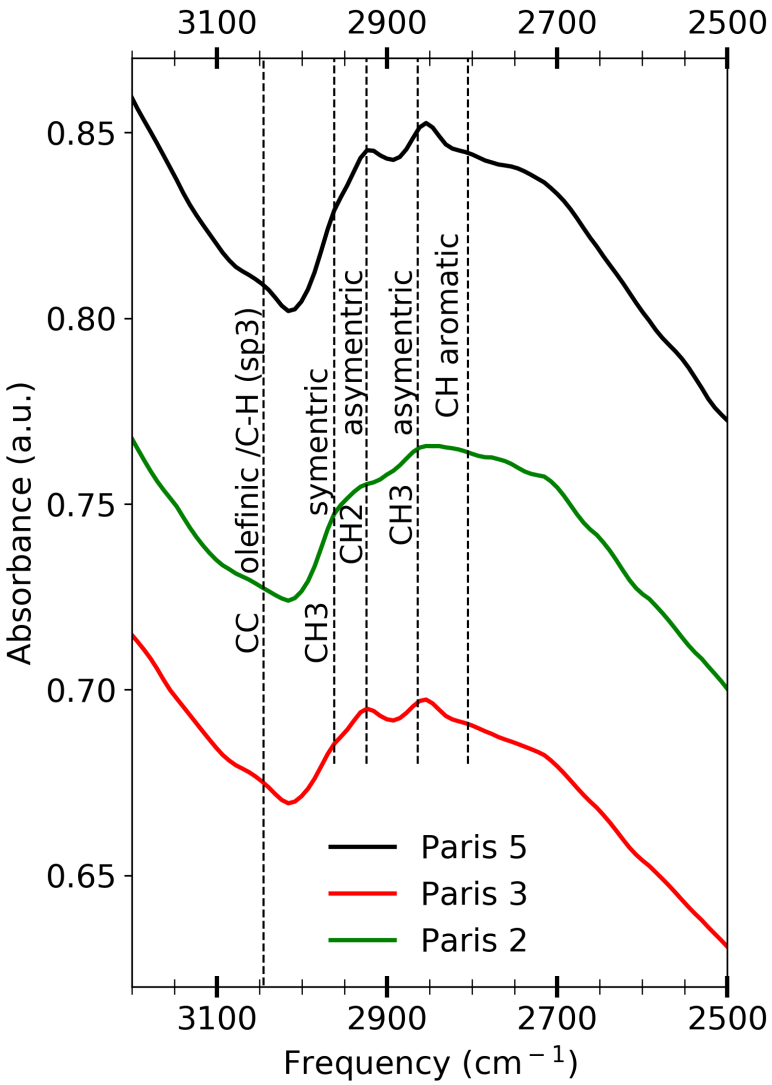

Figure 7.4: Zoom on the aliphatic region to evidence the positions of the organic and silicate bands for the three fragments of the Paris meteorite.

The main band in all samples was the silicates SiO band around 1000 cm^{-1}. We observed a broad band with several small sub-features, essentially due to pyroxenes, olivines, amorphous and hydrated silicates (see Fig 7.3). In particular two prominent features were observed at 964 cm^{-1} and 1041 cm^{-1}, possibly due to serpentine and Ca-rich pyroxene. A small carbonate contribution was also present around 1400 cm^{-1}. A band tentatively attributed to sulfates was observed at about 1120-1130 cm^{-1}. Water bending and stretching modes around 1633 cm^{-1} and 3000-3700 cm^{-1} were very strong in all samples. Some spectra also suggested the presence of a very weak band at about 3660-3670 cm^{-1} due to structural -OH, although the presence of other spectral artifacts (see below) in that spectral region

hampered a clear identification.

Organic signatures were easily detected in all samples (see Fig. 7.4). Aromatic carbons were responsible for the aromatic C-H stretching at 3045 cm^{-1}, and aromatic C=C modes at about 1600 cm^{-1} and 1250 cm^{-1}. Aliphatic CH_2 and CH_3 groups were identified thanks to the stretching modes between 2854 cm^{-1} and 2958 cm^{-1} and to the bending and deformation modes in the region 1300-1400 cm^{-1}. Unfortunately, we also observed a large band in the spectral region around 2700-3000 cm^{-1} which complicated the detection of aliphatic CH stretching bands. This band was probably due to volume effects as scattering inside the sample. Additional spectral artifacts possibly due to volume scattering seemed to be present at 1800-2200 cm^{-1}, with a potential contribution of the overtones of the silicate bands. Some residual atmospheric water and carbon dioxide bands were observed due to variations of their abundances over the day of measurements with respect to the background acquisitions. The residual atmospheric water in particular impeded an unambiguous identification of the structural -OH in the samples. Finally, some interference fringes were recognized in the spectra of Paris 2 and Paris 3.

Frequency (cm^{-1})	Component	band reconstructed on samples		
		Paris 5	Paris 3	Paris 2
1140-850	Silicate	x	x	x
890	olivine	x	x	x
915-920	diospide SiO	x		
964	diospide SiO	x	x	x
1015			x	
1041	pyroxene (calcium-rich)	x		x
1082		x		
1120-1130	sulfates	x	x	x
1250	CC aromatic skeleton	x	x	x
1305-1310	CH_3 bending	x	x	x
1370-1380	CH_2 deformation	x	x	x
1460-1465	Carbonate or CH bending	x	x	x
1510-1515		x	x	x
1605-1615	C=C	x	x	x
1650	OH bending	x	x	x
1740-1750	C=O	x	x	x
1884	overtone silicate	x	x	x
2078	overtone silicate	x	x	x
2805	-C≡C-H or CH (sp3)	x		
2854	CH_2 symetric stretching	x	x	x
2864	CH_3 symetric stretching			
2924	CH_2 asymetric stretching	x	x	x
2962	CH_3 asymetric stretching	x	x	
3045	CH aromatic	x	x	x
3000-3700	OH stretching	x	x	x

Table 7.1: Identification of the bands present in the three samples.

7.2.2 Spatial distribution of the components

We mapped the spatial distribution of the different functional groups in each IR projections by using the area under the IR band, and then we reconstructed each component following

the procedure described in chapter 5. To reconstruct the silicate distribution in 3D, we used the left shoulder of the silicate band to avoid a possible saturation bias. Unfortunately some edge effects remained on the silicate band, evidenced locally by the appearance of a pseudo-Christiansen feature, and implied that the silicate band area is underestimated at the edge of all samples.

Examples of 3D reconstructions and superposition of IR and X data are given in Fig. 7.5. We well distinguish hot spots inside the distribution of aliphatic moieties and carbonates, but the distribution of the OH stretching seems to present a smaller heterogeneity. The video 3 provided as supporting material shows the distribution of the different components for this grain.

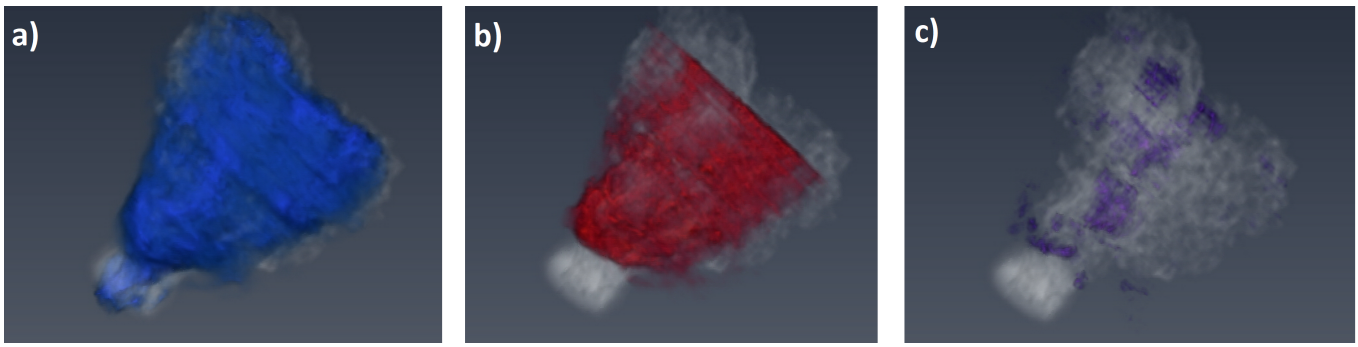

Figure 7.5: Superimposed X-ray and FTIR 3D reconstructions of (a) OH stretching, (b) CH aliphatic vibrations and (c) carbonates for the Paris 5 fragment.

To better illustrate the spatial distributions of the components, we present in Fig. 7.6 a 2-μm thick slice of Paris 5, extracted from the 3D FTIR dataset, along with the corresponding X-ray slice extracted from the 3D X-microtomography dataset. The distribution of the chemical component in each slice was normalized to its maximum value to display a 255-levels intensity scale. The distributions were spatially filtered using the superposition with the X-ray slice, but differently from Yesiltas et al., (2016) no additional saturation on the intensity values was included in this representation. Fig. 7.5 shows only the aliphatic CH stretching, the carbonates and the water, but we managed to reconstruct also the OH bending band, the sulfates, the whole silicate bands and some small bands characteristic of the crystalline structure as the bands of the diospside at 964 cm^{-1}. For the other components

(sulfates and diospide bands) the relatively low signal to noise and the low spectral resolution used here did not allow to obtain a reliable 3D reconstruction. Several reconstruction are presented in video 3 provided as complementary material.

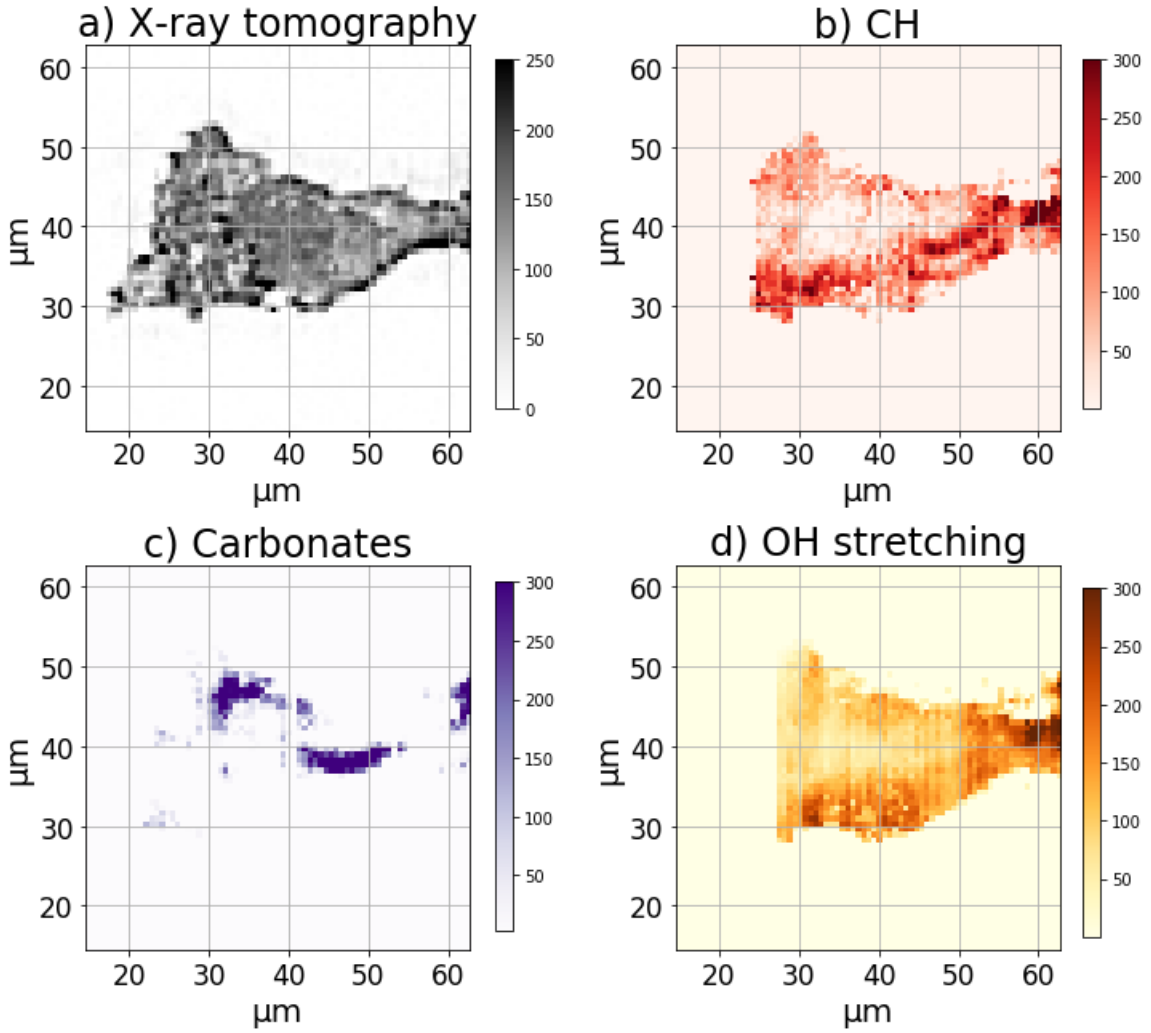

Figure 7.6: A slice of Paris 5 obtained by averaging 3 voxels along one axis (3 x 0.66 μm = 2 μm thick) showing the distribution of aliphatic matter (b), carbonates (c), and water (d). The corresponding high resolution X-ray slice is reported in the (a) panel.

7.3 Discussion

7.3.1 Comparison between the three samples

Even if the three fragments presented globally the same signatures, we can notice some significant differences between them: the mineral bands in the 10-μm region are clearly different in the three samples. Paris 3 seems to have an especially broad and structure-less band of silicates, that could be a sign of a significant abundance of amorphous silicates, similarly to the Paris fragment analysed in transmission in the Chapter 3. On the contrary, Paris 2 shows specific signatures in the 10-μm region and the presence of additional sulfate bands. Paris 5 has somewhat intermediate spectral features. Thus, the 10-μm region suggests that Paris 3 is the least hydrothermal altered among the three (see discussion of Chapter 3).

Much smaller variations among samples are observed on the organics: the aliphatic CH bands are slightly stronger in Paris 5 and Paris 3 than Paris 2, and the C=O band is also stronger in Paris 5, while for the aromatic bands the differences seem to be too small to be clearly evidenced. This implies that the heterogeneity of the mineral components among different meteorite fragments is already detectable at the scale of few tens of microns, while the heterogeneity of the carbonaceous materials must reveal at smaller scales, as it has been evidenced for instance by Vinogradoff et al., (2017) on Paris meteorite using XANES. In the following we will focus on the Paris 5 fragment, as it is the one showing an intermediate spectral behavior and also less interference fringes along the spectrum.

7.3.2 Comparison with extracted IOM of carbonaceous chondrites

In the three fragments, we have emphasized many small bands characteristic of the organic moieties. All the bands observed in previous studies of the IOM of carbonaceous chondrites led by Kebukawa et al. (2011) and Orthous-Daunay et al. (2013) were also present in our sample and the structure of the bands is similar to the one described by Orthous-Daunay et al. (2013). Based on the IR spectrum, the organics of Paris resemble those of others CM2 (bells and Murchison) and CR2 (EET92042) measured by Kebukawa et al., 2011.

Kebukawa et al. (2011) and Orthous-Daunay et al. (2013) reported spectra of IOM once it is extracted from the original meteorites. The sample has undergone an aggressive extraction to isolate the IOM, this process may have modified the structure of the organic matter. It is interesting to observe that, thanks to the big volume of our data, we are able to detect the same signatures on bulk rocks, without any chemical (e.g. extractions) or physical (e.g. crushing) processes. Moreover the possibility to improve our setup by coupling it to the synchrotron radiation seems very promising (see perspectives in Chapter 8), and in the future, we should be able to observe for each projection all the small bands of the organics on preserved samples, and thus to reconstruct them in 3D.

7.3.3 Heterogeneity inside a single fragment

In Paris 5 we observed heterogeneity of the mineral components by looking at the form of the 10-μm band: some spectra show a predominance of the band at 1041 cm^{-1}, while other regions of the sample have their maximum shifted toward smaller wavenumbers at around 964 cm^{-1}. This trend resembles what observed in Chapter 3 on the crushed 2D sample, as a sign of different degrees of amorphisation and aqueous alteration inside the fragment. Unfortunately, due to the current limitations of our setup (low signal to noise essentially due to the use of the globar source, see Chapter 8 for details) it is hard to reconstruct in 3D the two distributions separately.

We managed to reconstruct the distribution of aliphatic CH, water and carbonates in Paris 5. The carbonates distribution is very localized, as shown in Fig. 7.6. This result confirms what discussed in Chapter 3. Water and organics show a less localized distribution. However, some zones of high-abundance are observed both for water and organics, quite close to each other but not exactly co-localized. The spatial heterogeneity of the organics can be also visualized by looking at the histogram of their abundance in all the voxels that is reported in Fig. 7.7. We can notice that the hot spots rich in aliphatic moieties presents an abundance around three time higher than the average concentration. This result is in agreement with our result on the 2D samples. We give particular emphasis to a zone rich in organics that appears in the lower-left area of the fragments shown in Fig. 7.6: this structure is few microns large and it shows an abundance of aliphatics that is about three times higher than the average value

of the whole fragment. This zone is also rich in water. This co-localization suggests that aliphatic matter formation could be promoted or related to the presence of hydrated silicates.

It is interesting to note that the distribution of the OH bending and stretching modes is not the same. A part of the water could come from the contribution of the adsorbed terrestrial water. Also, the bending mode at about 6-μm is very close to the C=C and C=O modes, and it is hard to separate the three components with the low spectral resolution used in this study.

Similarly to Yesiltas et al. (2016), we observe localized hot spots of carbonates and aliphatic moieties. But the distribution of silicates in our grains seems more homogeneous than in Yesiltas et al. (2016), and we even detect some silicate structures characteristic of a higher degree of crystallinity. The heterogeneity of the OH bands could give indications about the degree of hydration of the silicates and similarly to what is described by Yesilstas et al., (2016), we can make a distinction between more or less hydrated silicates.

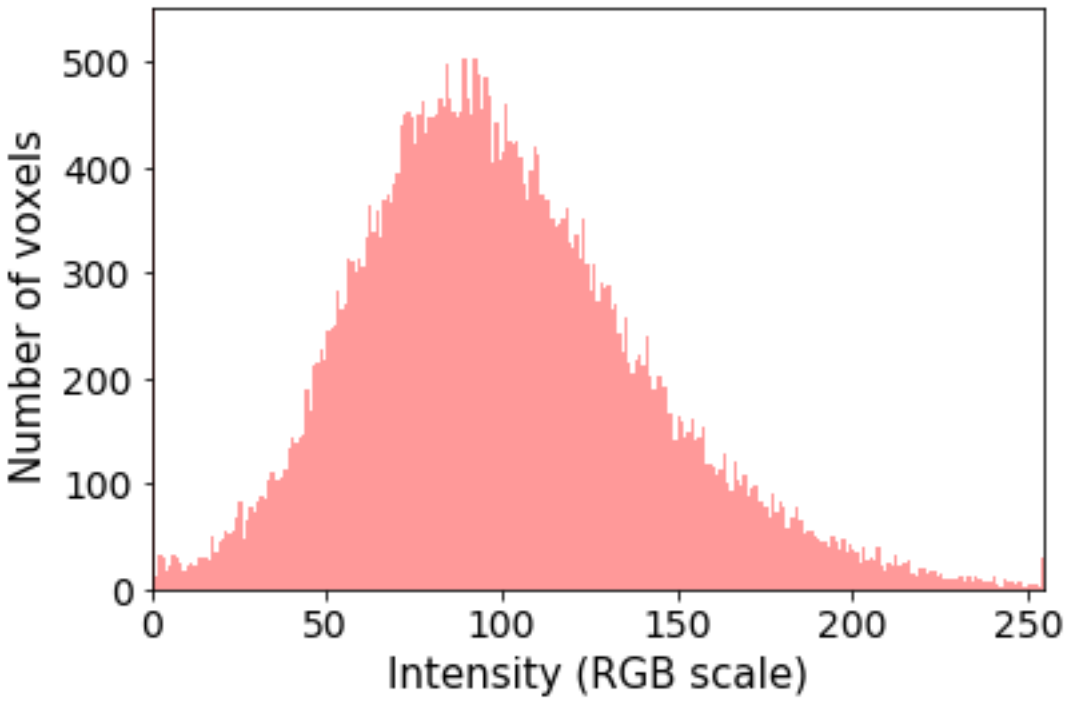

Figure 7.7: Distribution of the aliphatic CH band intensity in all voxels of the reconstructed Paris 5 fragment. The voxels are filtered based on the calculated X-ray tomography.

We also studied the spatial auto-correlation of each chemical function to evaluate the

heterogeneity of their spatial distribution inside the fragment Paris 5. Larger values imply more homogeneous distributions. We obtained the following values:

Component	auto-correlation (+/− 0.05)
Silicates	0.179
Aliphatic organics	0.148
OH bending	0.315

Table 7.2: Auto-correlation for the main component of the Paris 5 fragment.

We observe that the value is smaller for the CH band, and we interpret this as an indication of the heterogeneity of the aliphatic distribution. When comparing these values with the ones obtained for Hayabusa grains, we can see significant differences: calculation on the auto-correlation of the silicate gives values between 0.48 and 0.87 for mineral Hayabusa samples, with the more porous grains giving the lower values. Moreover, Hayabusa particles and Paris particles have very different physical properties such as the porosity (at least five times bigger in the Paris meteorite) and the diversity of the phases inside the sample (Hayabusa samples are mostly made of large minerals). In the future, auto-correlation could be an interesting parameter to quantify the distribution of each functional groups, once a significant number of samples will be studied by tomography.

Chapter 8

Conclusion and perspectives

8.1 Main results

The spatial distribution of chemical components in primitive extraterrestrial materials and especially the spatial link between the mineral and the organic phases was the central question of this work. To address this issue in an non-destructive way, we have studied both 2D and 3D samples using FTIR imaging. With the development of imaging, we have access to a large quantity of a data and we can study large heterogeneity inside samples. This heterogeneity is the result of complex processes undergone by small bodies before and after the accretion into planetesimals.

During this thesis, the first set of IR analysis was done in 2D on a primitive sample. Thanks to the study of the mineral context, I have studied the evolution of the organic matter through aqueous alteration. I presented a selection of results based on FTIR micro-spectroscopy and hyperspectral imaging of two different samples of the Paris meteorite, the least altered known CM2 chondrite. The first one was a wide area (500x500 μm^2) of a millimetric fragment directly measured in reflectance without any preliminary preparation of its surface. The region included matrix and chondrules and was chosen for its mineralogical and chemical diversity. The second one was a micrometric particle pressed between two diamond windows and measured in transmittance using an imaging system with of 0.66 μm pixel resolution.

I studied the distribution of the different phases (amorphous silicates hydrated and non-hydrated, crystalline silicates, phyllosilicates, aliphatic organic moieties, calcium carbonate and calcium sulfate) on both samples. Based on IR analysis, the Paris fragment matrix presents a mixture of different and gradual stages of silicates amorphization/crystallization and hydration, consistent with the hydrothermal alteration scenario proposed by Leroux et al., 2015. Furthermore, the small particle analyzed shows several micro-environments corresponding to different degrees of aqueous alteration and suggests the following scenario: the more primitive part is mainly composed of small grains of olivine particles embedded in hydrated amorphous silicates. The aqueous alteration led, in the first stage, to the disappearance of olivine and enrichment of OH-bearing amorphous silicate. Finally, a higher degree of hydrothermal alteration led to the formation of phyllosilicates and carbonates. Besides, at a larger scale, infrared mapping gives an interesting glimpse on the way the fluid circulated into the matrix and partially altered it.

For the micrometric particle, IR measurements also reveal local heterogeneity in the organic matter. Compared to the other parts of the grain, its most altered region is poorer in organics and characterized by a distinctly higher CH_2/CH_3 ratio. This implies longer aliphatic chains or a low degree of branching and/or cross-linking. I conclude that longer aliphatic chains and/or a low degree of ramification in this region are the result of the hydrothermal alteration.

Thanks to my spectral imaging analyses, I was also able to study the evolution of this small-scale heterogeneity in meteorites under the effects of energetic processing. I acquired IR micro-reflectance spectra scanning large portions of laboratory-irradiated meteorites. Spectral maps provided a characterization of the heterogeneity of the meteorites at the 20 μm spatial scale. In the irradiated areas, we observed spectral modifications of both anhydrous and hydrated silicates. After irradiation, we detected spectral shifts of the IR bands, larger for anhydrous than hydrated minerals. By comparing the compositional heterogeneity of the pristine materials with the irradiation effects as a function of the dose, we determined which spectral features are more sensitive to ion irradiation.

The new results suggested an original spectroscopic method to detect irradiated areas

that may be used by missions visiting carbon-rich asteroids. We showed that a distinction between primitive and altered samples is possible through the study of the 3 and 10 μm bands, and we compared the laboratory results with the IR spectral capabilities of instruments onboard Hayabusa2 and OSIRIS-REx, to provide these missions with spectral criteria on how to distinguish irradiation from compositional heterogeneity effects at the asteroid. We found that the band modifications of irradiated meteorites should be observable by instruments onboard these missions.

In all these studies, the spatial distribution has a central place and the next step to better understand the assembly of the different phases is to work on samples in 3D to preserve the spatial distribution. To do this, I have implemented a new setup to measure IR tomography. This technique allows studying the spatial distribution in 3D of the chemical components on intact samples. Moreover, with X-ray tomography we can obtain complementary physical information such as porosity, shape and distribution of metallic inclusion. Finally, the combination of IR and X-ray tomography gives a complete physico-chemical characterization of grains. With this method, we can emphasize areas of interest inside the sample and plan subsequent destructive analyses.

First, I tested the combination of IR and X-ray tomography on grains coming from the asteroid Itokawa. I have thus proven the possibility to study precious grains and to extract spatial information as the spatial distribution of the different minerals. Another study was led on three fragments of the Paris meteorite to answer questions about the organic matter and also to prepare the analysis of the samples that will be collected on carbonaceous asteroids by Hayabusa2 and OSIRIS-REx. IR tomography also reveals a spatial heterogeneity inside the organic matter and different degrees of amorphization in the different fragments. The detection of this heterogeneity seems very promising and with a better signal we should be able to extract more information, as described in the next section.

8.2 Perspectives

Experimental improvement

In the short term, some technical improvements can be implemented in our setup. As the measurement is quite long and needs human manipulation at each angle for the moment, the next step is to automatize the measurements.

Another priority is to improve the quality of the data. The first thing to do is to better take into account the diffraction of the light induced by the setup itself. A correction of the response of the instrument with its own PSF (Point Spread Function) will be important to correct diffraction effects. The other crucial point will be the use of the synchrotron beam to increase the signal to noise ratio. By using synchrotron radiation, we can significantly improve the quality of the signal (see Fig. 2.3). Some preliminary tests were conducted to quantify this improvement.

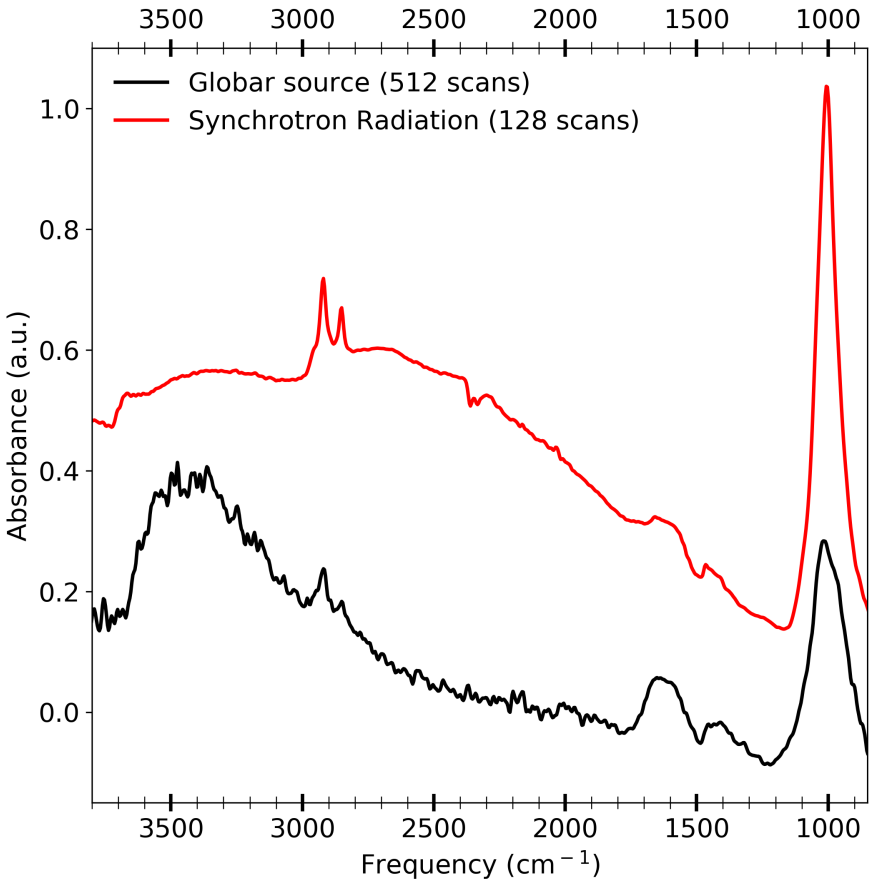

Figure 8.1: Meteorite spectra taken with a globar source (black) and with the synchrotron radiation (red).

In Fig. 8.1, we can see two spectra of meteoritic samples. The black one comes from the Paris meteorite and the red from the Tagish Lake meteorite. Obviously, the two meteorites have different composition. Both spectra were taken at 4 cm $^{-1}$, but the black one was measured with a Globar source while the second one was measured by using the synchrotron radiation. Moreover, the number of scans was 4 times higher in the case of the Globar source. Despite this, we can see that the signal to noise ratio is much higher when we use a synchrotron (by about a factor 5). Therefore, we can estimate that if we performed tomography measurements in the same conditions, we would multiply the signal to noise ratio by about ten thanks to the synchrotron radiation. The detection of small bands and their mapping will be much easier, and their 3D reconstruction will be possible.

Data treatment

Currently, we reconstruct chemical components one after the other, but the next step is to reconstruct the whole IR spectrum in 3D. Then, we will be able to directly study the spectra of a voxel of interest in the reconstructed data. For instance, this may bring some answer about the issues discussed in our 2D analysis of the quantification of amorphization/crystallization of the silicates or the ratio CH_2/CH_3. We have already started to implement this, thanks to XANES tomography software and a collaboration with Y. Liu (SSRL, SLAC).

Once the set up is automatized and improved, we can enlarge the study to a wider set of extraterrestrial samples. Our setup is well adapted for samples with a size between 10 and 40 μm, so it is well suited to study IDPs (Interplanetary Dust Planetary). As potential fragments of comets and very primitive objects, they may provide important keys to a better understanding of our early Solar System. At longer term, this setup, hosted by the SOLEIL synchrotron, could also be used by other communities such as biologists or material physicist to characterize the spatial structure of their samples. The study of hydration and the organic matter in details seems very promising for biological samples.

Porosity

During this Ph.D., I have also collected many data with X-ray tomography on both micrometric and millimetric samples. X-ray tomography reveals the presence as expected of chondrules, metal inclusions and matrix. The goal of this study is to characterize the porosity at different scales for samples of different origins. Information about the porosity on primitive materials can be a critical input for the models of grains either in the interstellar medium or in protoplanetary disks or at the surface of small bodies. Moreover, with macroscopic meteorites samples, we wanted to study the effects of aqueous alteration.

Meteoritic samples were chosen to cover a large degree of aqueous alteration from not altered meteorites (Pavlovka) to very altered ones (Orgueil). I have already evaluated the porosity of these samples. Indeed, the literature predicts a decreasing of porosity with aqueous alterations. The following table presents the estimated porosity of few samples.

Sample	Average Porosity +/- 0.2%	Class of the sample
Paris	1.6 %	CM
Murchison	0.6 %	CM
LMAB	0.3 %	Unclassified
Orgueil	1.6 %	CI

Table 8.1: Calculation of the Porosity according to the class of different samples.

This preliminary study shows important differences in the structure and the porosity among meteorites with different degrees of alteration. However, the porosity obtained with this study seems very low comparing to other studies conducted using volume measurements (around 35% for CM and 23% for CI). Our set of data gives access to the porosity at a scale above 0.8 μm and thus, nanometric pores inside the sample cannot be detected. Not taking into account such porosity could explain the discrepancy between the literature and our data. The estimate of the porosity for the micrometric samples could consolidate this explanation. Porosity at different scales is relevant to different phenomena. In our scale, we are more sensitive to cracks and fractures inside the sample, that could witness the history of agglomeration and shocks undergone by macroscopic fragments. In the future, further analysis of the shape, the layout, and the assembly of these structures could lead to better understanding of

the aqueous alteration process. Future measurements are also planned on the ANATOMIX beamline in SOLEIL at lower energy and with better spatial resolution to reach smaller scales.

List of videos provided as supporting material:

Video 1: different components of the grain RA-QD02-0223. We successively see the IR reconstruction of the continuum in yellow, the CH aliphatic band in red (characteristic of the glue), the silicate large band green (characteristic of the whole sample), the OH stretching in dark blue and the OH bending with some aromatic CC in light blue (both characteristic of the glue). The video can be seen at: `https://youtu.be/Tw-Tb-xspxM`

Video 2: different components of the grain RA-QD02-0214. We can see first the X-ray tomography reconstruction with two level of grey for the two component of the grain RA-QD02-0214. Then, we see the reconstruction of the olivine obtained by IR tomography in green and finally, the reconstruction of the pyroxene appears in brown. The video can be seen at: `https://youtu.be/mAeREeYvyIk`

Video 3: different components of the grain 5 of the Paris meteorite. First, we observe the reconstruction obtained by X-ray tomography in grey. Then we successively see the IR reconstruction of the OH bending with some aromatic CC in light blue, OH stretching in dark blue, silicate large band in green, CH aliphatic in red and carbonate in purple. The video can be seen at: `https://youtu.be/rpzi-Hu-y2A`

List of publications connected to this work

Articles:

- 'Organic and mineralogic heterogeneity of the Paris meteorite followed by FTIR hyperspectral imaging', Dionnet et al., 2018, Meteorit Planet Sci. . doi:10.1111/maps.13178

- 'FTIR Micro-tomography of Five Itokawa Particles and one Primitive Carbonaceous Chondrite' Dionnet et al., 2018, Microscopy and Microanalysis, vol. 24, issue S1, pp. 2100-2101

- 'Hyperspectral FTIR imaging of irradiated carbonaceous meteorites', Brunetto et al., 2017 Planetary Space Science, special issue VSI: ACM

- 'Different origins or different evolutions? Decoding the spectral diversity among C-type asteroids' P. Vernazza et al., 2017, The Astronomical Journal, 153:72

- 'Ion irradiation of Allende meteorite probed by visible, IR, and Raman spectroscopies' R. Brunetto et al., Icarus 237, 278-292

- 'Visible-IR and Raman micro-spectroscopic investigation of three Itokawa particles collected by Hayabusa: mineralogy and degree of space weathering based on non- destructive analyses ' Bonal L. et al. , MAPS, V.50, Issue 9, September 2015, 1562-1576

Conferences:

- '2D and 3D FTIR hyperspectral imaging of the Paris meteorite', European Planetary Science Congress, 2018 (poster)

- 'FTIR Micro-tomography of Five Itokawa Particles and one Primitive Carbonaceous Chondrite', Microscopy & Microanalysis 2018 (oral)

- 'FTIR micro-tomography of five Hayabusa particles' Hayabusa Symposium 2017 (oral)

- 'Hyperspectral FTIR immaging of meteorites' WIRMS 2017 (poster)

- 'IR Imaging of the Paris Meteorite with an FPA Detector for Micro-tomography' SUM17 (oral)

- 'Non-destructive IR micro-imaging of the Paris meteorite' LPSC 2017 (poster)

- 'Non-destructive IR micro-imaging of two grains of the Paris meteorite' Metsoc 2016, Berlin (oral)

Bibliography

Abe, M., Takagi, Y., Kitazato, K., et al., 2006, Science 312(5778): 1334.

Adams, J.B., & McCord, T.B., 1973, Proceedings of the Lunar Science Conference 4: 163.

Aleon, J., 2008, ArXiv e-prints.

Alexander, C.M.O.D., Cody, G.D., De Gregorio, B.T., Nittler, L.R., & Stroud, R.M., 2017, Chemie der Erde - Geochemistry 77(2): 227.

Alexander, C.M.O.D., Fogel, M., Yabuta, H., & Cody, G.D., 2007, Geochimica et Cosmochimica Acta 71(17): 4380.

Aminghafari, M., Cheze, N., & Poggi, J.-M., 2006, Computational Statistics & Data Analysis 50(9): 2381.

Anders, E., & Zinner, E., 1993, Meteoritics & Planetary Science 28: 490.

Balan, E., Saitta, A.M., Mauri, F., & Calas, G., 2001, American Mineralogist 86(11-12): 1321.

Banhart, J., 2008, Advanced tomographic methods in materials research and engineering.

Basri, G., & Bertout, C., 1993, Protostars and planets III: 543.

Beck, P., Garenne, A., Quirico, E., et al., 2014, Icarus 229: 263.

Beck, P., Quirico, E., Montes-Hernandez, G., et al., 2010, Geochimica et Cosmochimica Acta 74(16): 4881.

Beister, M., Kolditz, D., & Kalender, W.A., 2012, Physica Medica 28: 94.

Bibring, J.P., Hamm, V., Langevin, Y., et al., 2017, Space Sci Rev 208(1-4): 401.

Binzel, R.P., Bus, S.J., Burbine, T.H., & Sunshine, J.M., 1996, Science 273(5277): 946.

Binzel, R.P., Morbidelli, A., Merouane, S., et al., 2010, Nature 463(7279): 331.

Binzel, R.P., Rivikin, A.S., Bus, S.J., Sunshine, J.M., & Burbine, T.H., 2001, Meteoritics & Planetary Science 36: 1167.

Bishop, J.L., Lane, M.D., Dyar, M.D., & Brown, A.J., 2008, Clay Minerals 43(1): 35.

Bonal, L., Bourot-Denise, M., Quirico, E., Montagnac, G., & Lewin, E., 2007, Geochimica et Cosmochimica Acta 71(6): 1605.

Bonal, L., Brunetto, R., Beck, P., et al., 2015, Meteoritics & Planetary Science 50(9): 1562.

Bonal, L., Quirico, E., Bourot-Denise, M., & Montagnac, G., 2006, Geochimica et Cosmochimica Acta 70(7): 1849.

Boss, A.P., 1995, The Astrophysical Journal 439: 224.

Bottke, W.F., Morbidelli, A., & Jedicke, R., 2002, Icarus 156: 399.

Boulet, N., Mutschke, H., & Navral, C., 2005, The Astrophysical Journal 633: 272.

Bourot-Denise, M., Zanda, B., Marrocchi, Y., et al., 2010, Lunar and Planetary Science Conference 41: 1683.

Bowey, J.E., Morlok, A., & Grady, M., 2007, Monthly Notices of the Royal Astronomical Society: 1367.

Bradley, J.P., 1999, Science 285(5435): 1852.

Bradley, J.P., 2003, Treatise of Geochemistry Volume 1: 689.

Bradley, J.P., Keller, L.P., Snow, T.P., et al., 1999, Science 285(5434): 1716.

Brearley, A., & Jones, R., 1998, Planetary Materials, chapter 3 : Chondritic meteorites.

Brearley, A.J., 2006, Meteorites and the early Solar system II (livre): 567.

Brucato, J.R., Strazzulla, G., Baratta, G., & Colangeli, L., 2004, Astronomy & Astrophysics 413(2): 395.

Bruckman, V.J., & Wriessnig, K., 2012, Environmental Chemistry Letters 11(1): 65.

Brunetto, R., 2007, Space weathering in the solar system: from laboratory to observations, through spectral models, (Universita del Salento).

Brunetto, R., Borg, J., Dartois, E., et al., 2011, Icarus 212(2): 896.

Brunetto, R., Lantz, C., Ledu, D., et al., 2014, Icarus 237: 278.

Brunetto, R., Loeffler, M.J., Nesvorny, D., Sasaki, S., & Strazzulla, G., 2015.

Brunetto, R., Pino, T., Dartois, E., et al., 2009, Icarus 200(1): 323.

Brunetto, R., Vernazza, P., Marchi, S., et al., 2006, Icarus 184(2): 327.

Busemann, H., Alexander, C., & Nittler, L.R., 2007, Meteoritics & Planetary Science 42(7/8): 1387.

Buzgar, N., Buzato, A., & Sanislav, I.V., 2009, Geologie. Tomul LV(1).

Cambier, P., 1986, Clay Minerals 21: 191.

Caussinus, H., 1986, DWSO Press: 149.

Chaisson, E., & McMillan, S., 1993, Astronomy Today.

Chaumard, N., Charon, E., Rouzaud, N.Z., & Devouard, B., 2013, Lunar and Planetary Science Conference 44.

Choi, K., Wang, J., Zhu, L., et al., 2010, Medical Physics 37(9): 5113.

Clark, B.E., Lucey, P., Helfenstein, P., et al., 2001, Meteoritics & Planetary Science 36(12): 1617.

Clark, B.E., Veverka, J., Helfenstein, P., et al., 1999, Icarus 140: 53.

Clark, e.a., . 2002, Asteroid space weathering and regolith evolution, Asteroids III. (University of Arizona Press).

Clark, R.N., King, T.V.V., Klejwa, M., Swayze, G.A., & Vergo, N., 1990, Journal of Geophysical Research 95(B8): 12653.

Cody, G.D., & Alexander, C.M.O., 2005, Geochimica et Cosmochimica Acta 69(4): 1085.

Connelly, J.N., Bizzarro, M., Krot, A.N., et al., 2012, Science 338(6107): 651.

Consolmagno, G.J., Britt, D.T., & Macke, R.J., 2008, Chemie der Erde - Geochemistry 68(1): 1.

Corrigan, C.M., Zolensky, M.E., Dahl, J., et al., 1997, Meteoritics & Planetary Science 32: 509.

Coupeaud, A., Demyk, K., Meny, C., et al., 2011, Astronomy & Astrophysics 535: A124.

Dartois, E., Engrand, C., Duprat, J., et al., 2017, Astronomy & Astrophysics 609: A65.

Dartois, E., Marco, O., Munoz-Caro, G.M., et al., 2004, Astronomy & Astrophysics 423(2): 549.

Dartois, E., Munoz Caro, G.M., Deboffle, D., Montagnac, G., & d'Hendecourt, L., 2005, Astronomy & Astrophysics 432(3): 895.

de Leuw, S., Rubin, A.E., & Wasson, J.T., 2010, Meteoritics & Planetary Science 45(4): 513.

de Marcellus, P., Fresneau, A., Brunetto, R., et al., 2017, Monthly Notices of the Royal Astronomical Society 464(1): 114.

de Sanctis, D., Ammannito, E., McSween, H.Y., et al., 2017, Science 355: 719.

de Sanctis, M.C., Ammannito, E., Raponi, A., et al., 2015, Nature 528(7581): 241.

Demeo, F.E., Binzel, R.P., Slivan, S.M., & Bus, S.J., 2009, Icarus 202(1): 160.

Demyk, K., d'Hendecourt, L., Leroux, H., Jones, A.P., & Borg, J., 2004, Astronomy & Astrophysics 420(1): 233.

Demyk, K., Meny, C., Leroux, H., et al., 2017, Astronomy & Astrophysics 606: A50.

d'Hendecourt, L., & Allamandola, L.J., 1986, Astronomy & Astrophysics 64: 453.

Djouadi, Z., d'Hendecourt, L., Leroux, H., et al., 2005, Astronomy & Astrophysics 440(1): 179.

Dominguez, G., Mcleod, A.S., Gainsforth, Z., et al., 2014, Nature Communications 5(5445).

Dumas, P., Jamin, N., Teillaud, J.L., Miller, L.M., & Beccard, B., 2004, Faraday Discussions 126: 289.

Ebel, D.S., & Grossman, L., 2000, Geochimica et Cosmochimica Acta 64(2): 339.

Ebel, D.S., & Rivers, M.L., 2007, Meteoritics & Planetary Science 42(9): 1627.

Floss, C., Le Guillou, C., & Brearley, A., 2014, Geochimica et Cosmochimica Acta 139: 1.

Fornasier, S., Lantz, C., Perna, D., et al., 2016, Icarus 269: 1.

Garvie, L.A.J., & R., B.P., 2007, Meteoritics & Planetary Science 42: 2111.

Geyer, L.M., Schoepf, J.U., Meneil, F.G., et al., 2015, Radiology 276(2): 339.

Gilmour, I., 2003, Treatise on Geochemistry, 1.

Godard, M., Féraud, G., Chabot, M., et al., 2011, Astronomy & Astrophysics 529: A146.

Gradie, J., & Tedesco, E., 1982, Science 216: 1405.

Gürsoy, D., De Carlo, F., Xiao, X., & Jacobsen, C., 2014, Journal of Synchrotron Radiation 21(5): 1188.

Hackett, M.J., Caine, S., Liu, X., May, T.E., & Borondics, F., 2015, Vibrational Spectroscopy 77: 51.

Hamilton, J.P., Brantley, S.L., Pantano, C.G., Criscenti, L.J., & Kubicki, J.D., 2001, Geochimica et Cosmochimica Acta 65(21): 3683.

Hamilton, V.E., 2010, Chemie der Erde - Geochemistry 70(1): 7.

Hanesch, M., 2009, Geophysical Journal International 177(3): 941.

Hapke, B., 2001, J Geophys Res-Planet 106(E5): 10039.

Hapke, B., Cassidy, W., & Wells, E., 1975, Moon Planets 13(1-3): 339.

Hewins, R.H., Bourot-Denise, M., Zanda, B., et al., 2014, Geochimica et Cosmochimica Acta 124: 190.

Hewins, R.H., Connolly, H.C., Lofgren, G.E.J., & Libourel, G., 2005, Chondrites and the Protoplanetary Disk, ASP Conference Series, 341: 286.

Hiroi, H., Sasaki, K., Misu, T., & Nakamura, T., 2013, 44th LPSC, LPI contribution 1719: 1276.

Hiroi, T., Abe, M., Kitazato, K., et al., 2006, Nature 443(7107): 56.

Ho, T.M., Baturkin, V., Grimm, C., et al., 2017, Space Sci Rev 208(1-4): 339.

Hoi-Ying N. Holman, Bechtel, H.A., Hoa, Z., & Martin, M.C., 2010, Analytical chemistry feature 82: 8757.

Hu, Z.W., & Winarski, R.P., 2016, Meteoritics & Planetary Science 51(9): 1632.

Huang, E., Chen, C.H., Huang, T., Lin, E.H., & Xu, J.-a., 2000, American Mineralogist 85: 473.

Huss, G., Rubin, A., & Grossman, J., 2006, Meteorites and the early solar system II, chapter Thermal metamorphism in chondrites.

Huss, G.R., Rubin, A.E., & Grossman, J.N., 2006, Thermal Metamorphism in Chondrites. Meteorites and the Early Solar System II.

Ishiguro, M., Hiroi, T., Tholen, D.J., et al., 2007, Meteoritics & Planetary Science 42(10): 1791.

Iwata, T., Kitazato, K., Abe, M., et al., 2017, Space Sci Rev 208(1-4): 317.

Jäger, C., Molster, F.J., Dorschner, J., et al., 1998, Astronomy & Astrophysics 339: 904.

Jones, A.P., 2004, ASP Conference Series 309.

Kak, A.C., & Slaney, M., 1988, Principles of Computerized Tomographic Imaging.

Kaluna, H.M., Masiero, J.R., & Meech, K., 2016, Icarus 264: 62.

Kebukawa, Y., Alexander, C.M.O., & Cody, G.D., 2011, Geochimica et Cosmochimica Acta 75(12): 3530.

Kebukawa, Y., Nakashima, S., Ishikawa, M., et al., 2010, Meteoritics & Planetary Science 45(3): 394.

Keil, K., Stöffler, D., Love, S., & Scott, E., 1997, Meteoritics & Planetary Science 32: 349.

Keller, G., & Berger, S.L., 2014, Earth, Planets, Space 66: 71.

Kerridge, J., & Bunch, T., 1979, Asteroids, chapter Aqueous activity on asteroids : evidence from carbonaceous chondrites.

Kitajima, F., 2011, Lunar and Planetary Science Conference 42: 1855.

Kuebler, K.E., Jolliff, B.L., Wang, A., & Haskin, L.A., 2006, Geochimica et Cosmochimica Acta 70(24): 6201.

Laloum, D., 2016, Tomographie par rayons X haute rÃľsolution : application à lâĂŹintégration 3D pour la microélectronique. in Université de Grenoble.

Lancet, H.S., & Anders, E., 1970, Science 170: 980.

Lane, M.D., 2007, American Mineralogist 92(1): 1.

Lantz, C., Brunetto, R., Barucci, M.A., et al., 2015, Astronomy & Astrophysics 577.

Lantz, C., Brunetto, R., Barucci, M.A., et al., 2017, Icarus 285: 43.

Lantz, C., Clark, B.E., Barucci, M.A., & Lauretta, D.S., 2013, Astronomy & Astrophysics 554.

Lasch, P., & Naumann, D., 2006, Biochimica et Biophysica Acta (BBA) - Biomembranes 1758(7): 814.

Lauretta, D., Nagahara, H., & Alexander, C.M.O.D., 2006, Petrology and Origin of Ferromagnesian Silicate Chondrules.

Lauretta, D.S., Bartels, A.E., Barucci, M.A., et al., 2015, Meteoritics & Planetary Science 50(4): 834.

Lazzarin, M., Marchi, S., Moroz, L.V., et al., 2006, Astrophys J 647(2): L179.

Le Guillou, C., Bernard, S., Brearley, A.J., & Remusat, L., 2014, Geochimica et Cosmochimica Acta 131: 368.

Lee, M.R., Lindgren, P., & Sofe, M.R., 2014, Geochimica et Cosmochimica Acta 144: 126.

Leroux, H., Cuvillier, P., Zanda, B., & Hewins, R.H., 2015, Geochimica et Cosmochimica Acta 170: 247.

Liu, Y., Kiss, A.M., Larsson, D.H., Yang, F., & Pianetta, P., 2016, Spectrochimica Acta Part B: Atomic Spectroscopy 117: 29.

Liu, Y., Meirer, F., Williams, P.A., et al., 2012, Journal of Synchrotron Radiation 19(2):

281.

Lodders, K., 2003, The Astrophysical Journal 591(2): 1220.

Loeffler, M.J., Dukes, C.A., & Baragiola, R.A., 2009, J Geophys Res-Planet 114.

Marrocchi, Y., Gounelle, M., Blanchard, I., Caste, F., & Kearsley, A.T., 2014, Meteoritics & Planetary Science 49(7): 1232.

Martin, M.C., Dabat-Blondeau, C., Unger, M., et al., 2013, Nature Methods 10(9): 861.

Martins, Z., Modica, P., Zanda, B., & d'Hendecourt, L.L.S., 2015, Meteoritics & Planetary Science 50(5): 926.

Matrajt, G., Borg, J., Raynal, P.I., et al., 2004, Astronomy & Astrophysics 416(3): 983.

Matrajt, G., Munoz Caro, G.M., Dartois, E., et al., 2005, Astronomy & Astrophysics 433(3): 979.

Matsumoto, T., Tsuchiyama, A., Miyake, A., et al., 2015, Icarus 257: 230.

Matsuoka, M., Nakamura, T., Kimura, Y., et al., 2015, Icarus 254: 135.

McAdam, M.M., Sunshine, J.M., Howard, K.T., et al., 2018, Icarus 306: 32.

McAdam, M.M., Sunshine, J.M., Howard, K.T., & McCoy, T.M., 2015, Icarus 245: 320.

McSween, H., Sears, D., & Dodd, R., 1988, Meteorites and the early solar system, chapter 3.

Merouane, S., Djouadi, Z., d'Hendecourt, L.L.S., Zanda, B., & Borg, J., 2012, The Astrophysical Journal 756(2): 154.

Merouane, S., Djouadi, Z., & Le Sergeant d'Hendecourt, L., 2013, The Astrophysical Journal 780(2): 174.

Merouane, S., Zaprudin, B., Stenzel, O., et al., 2016, Astronomy & Astrophysics 596: A87.

Messali, Z., Chetih, N., Serir, A., & Boudjelal, A., 2015, International Journal of Probability and Statistics 4(1): 12.

Miller, L.M., & Smith, R.J., 2005, Vibrational Spectroscopy 38(1-2): 237.

Miller, S.L., Urey, H.C., & OrÃş, J., 1976, J Mol Evol. 9: 59.

Morbidelli, A., Levison, H., Tsiganis, K., & Gomes, R., 2005, Nature 435: 462.

Morbidelli, A., Tsiganis, K., Crida, A., Levsion, H.F., & Gomes, R., 2007, The Astrophysical Journal 134: 1790.

Morlok, A., Kohler, M., & Grady, M.M., 2008, meteoritics & Planetary Science 160: 79.

Morlok, A., Koike, C., Tomioka, N., Mann, I., & Tomeoka, K., 2010, Icarus 207: 45.

Moss, D., Gasharova, B., & Mathis, Y.-L., 2006, Infrared Physics & Technology 49(1-2): 53.

Munoz Caro, G.M., Matrajt, G., Dartois, E., et al., 2006, Astronomy & Astrophysics 459(1): 147.

Nagao, K., Okazaki, R., Nakamura, T., et al., 2011, Science 333(6046): 1128.

Nakamura, E., Makishima, A., Moriguti, T., et al., 2012, PNAS 109(11): 624.

Nakamura, T., Nakato, A., Ishida, H., et al., 2014, Meteoritics & Planetary Science 49(2): 215.

Nakamura, T., Noguchi, T., Tanaka, M., et al., 2011, Science 333(6046): 1113.

Naraoka, H., Mita, H., Hamase, K., et al., 2012, Geochem J 46: 61.

Nasse, M.J., & Woehl, J.C., 2010, Journal of the Optical Society of America A 27: 295.

Nasse, M.J., Mattson, E.C., Reininger, R., et al., 2011, Nuclear Instruments and Methods in Physics Research Section A: Accelerators, Spectrometers, Detectors and Associated Equipment 649(1): 172.

Nasse, M.J., Reininger, R., Kubala, T., Janowski, S., & Hirschmugl, C., 2007, Nuclear Instruments and Methods in Physics Research Section A: Accelerators, Spectrometers, Detectors and Associated Equipment 582(1): 107.

Nasse, M.J., Walsh, M.J., Mattson, E.C., et al., 2011, Nature Methods 8(5): 413.

Nasse, M.J., Woehl, J.C., & Huant, S., 2007, Applied Physics Letters 90(3): 031106.

Nesvorny, D., Jedicke, R., Whiteley, R.J., & Ivezic, Z., 2005, Icarus 173(1): 132.

Noguchi, T., Kimura, M., Hashimoto, T., et al., 2014, Meteoritics & Planetary Science 49(2): 188.

Noguchi, T., Nakamura, T., Kimura, M., et al., 2011, Science 333(6046): 1121.

Noguchi, T., Kimura, M., Hashimoto, T., et al., 2014, Meteoritics & Planetary Science 49(7): 1305.

Noun, M., Roumie, M., Calligaro, T., et al., 2013, Nuclear Instruments and Methods in Physics Research Section B: Beam Interactions with Materials and Atoms 306: 261.

Omori, K., 1971, The American Mineralogist 56.

Orthous-Daunay, F.R., 2011, Empreinte moléculaire des processus post-accrétionnels dans la matière organique des chondrites carbonées., (Université de Grenole).

Orthous-Daunay, F.R., Quirico, E., Beck, P., et al., 2013, Icarus 223(1): 534.

Peck, J.A., 1983, Meteoritics 18(4): 373.

Pedregosa, F., Varoquaux, G., Gramfort, A., et al., 2011, Journal of Machine Learning Research 12: 2825.

Pilorget, C., & Bibring, J.P., 2013, Planetary and Space Science 76: 42.

Pizzarello, S., Cooper, G.W., & Flynn, G.J., 2006, Meteorites and the Early Solar System II. (D. S. Lauretta & H. Y. McSween).

Pizzarello, S., & Shock, E., 2010, Cold Spring Harbor Perspectives in Biology 2(3): a002105.

Posch, T., Mutschke, H., Trieloff, M., & Henning, T., 2007, The Astrophysical Journal 656: 615.

Quaroni, L., Obst, M., Nowak, M., & Zobi, F., 2015, Angewandte Chemie International

Edition 54(1): 318.

Quaroni, L., Zlateva, T., Sarafimov, B., et al., 2014, Biophysical Chemistry 189: 40.

Quirico, E., Moroz, L.V., Schmitt, B., et al., 2016, Icarus 272: 32.

Quirico, E., Orthous-Daunay, F.R., Beck, P., et al., 2014, Geochimica et Cosmochimica Acta 136: 80.

Reddy, R.K., Walsh, M.J., Schulmerich, M.V., Carney, P.S., & Bhargava, R., 2013, Applied Spectroscopy 67(1): 93.

Remusat, L., Palhol, F., Robert, F., Derenne, S., & France-Lanord, C., 2005, Earth Planet Sc Lett 243: 15.

Reuter, D.C., Simon, A.A., Hair, J., et al., 2018, Space Sci Rev 214(2).

Rietmeijer, F.J.M., 1998, Mineralogical Society of America, Washington 36: 95.

Rinaudo, C., Gastaldi, A., & Bellusco, E., 2003, The Canadian Mineralogist 41: 883.

Rotundi, A., Barrata, G.A., Borg, J., et al., 2008, Meteoritics & Planetary Science 43(1/2): 367.

Rotundi, A., Rietmeijer, F.J.M., Ferrari, M., et al., 2014, Meteoritics & Planetary Science 49(4): 550.

Ruan, H., Frost, R., Kloprogge, J., & Duong, L., 2002, Spectrochimica Acta Part A: Molecular and Biomolecular Spectroscopy 58: 967.

Rubin, A.E., & Brearley, A.J., 1996, Icarus 124(1): 86.

Rubin, A.E., Trigo-Rodriguez, J.M., Huber, H., & Wasson, J.T., 2007, Geochimica et Cosmochimica Acta 71(9): 2361.

Russell, S., Hartmann, L., Cuzzi, J., et al., 2006, Meteorites and the Early Solar System II.

Rutt, H.N., & Nicola, J.H., 1974, Journal of Physic C: Solid State Physics 7: 4522.

Sadezky, A., Muckenhuber, H., Grothe, H., Niessner, R., & PÃűschl, U., 2005, Carbon 43(8): 1731.

Salisbury, J.W., 1993, Mid-infrared spectroscopy laboratory data: Chapter 4 in Remote Geochemical Analysis.

Salisbury, J.W., d'Aria, D.M., & Jarosewich, E., 1991, Icarus 92: 280.

Sasaki, S., Nakamura, K., Hamabe, Y., Kurahashi, E., & Hiroi, T., 2001, Nature 410(6828): 555.

Schmitt-Kopplin, P., Gabelica, Z., Gougeon, R.D., et al., 2010, Proceedings of the National Academy of Sciences 107(7): 2763.

Scott, E., & Krot, A., 2005, "Meteorites, Comets and Planets" Treatise on Geochemistry, chapter 7 : Chondrites and their components.

Sears, D., Batchelor, J., Lu, J., & Keck, B., 1991, Proc. NIPR Symp. Antarc. Meteorites 4: 319.

Sears, D.W.G., & Dodd, R.T., 1988, Meteorites and the Early Solar System.

Sears, D.W.G., Sears, H., Ebel, D.S., Wallace, S., & Friedrich, J.M., 2016, Meteoritics & Planetary Science 51(4): 833.

Sephton, M.A., 2002, Natural Product Reports 19(3): 292.

Simon, S.B., & Haggerty, S.E., 1980, P Lunar Planet Sci 11: 901.

Srámek, O., Milelli, L., Ricard, Y., & Labrosse, S., 2012, Icarus 217(1): 339.

Sandford, S. A., Allamandola, L. J., Tielens, A. G. G. M., et al. 1991, ApJ 371:, 607

Stark, H., Woods, J.W., Paul, I., & Hingorani, R., 1981, IEE transactions on Acoustics, Speech and Signal Processing 29: 237.

Strazzulla, G., Dotto, E., Binzel, R., et al., 2005, Icarus 174(1): 31.

Suto, H., Sogawa, H., Tachibana, S., et al., 2006, Monthly Notices of the Royal Astronomical Society 370(4): 1599.

Takagi, Y., Yoshikawa, M., Abe, M., et al., 2011, AGU fall meeting.

Tamanai, A., Mutschke, H., & Blum, J., 2009, ASP Conference Series 414.

Tsiganis, K., Gomes, R., Morbidelli, A., & Levison, H., 2005, Nature 434: 459.

Tsuchiyama, A., 2014, Elements 10(1): 45.

Tsuchiyama, A., Nakano, T., Uesugi, K., et al., 2013, Geochimica et Cosmochimica Acta 116: 5.

Tsuchiyama, A., Uesugi, M., Matsushima, T., et al., 2011, Science 333(6046): 1125.

Tsuchiyama, A., Uesugi, M., Uesugi, K., et al., 2014, Meteoritics & Planetary Science 49(2): 172.

Vernazza, P., Marsset, M., Beck, P., et al., 2015, The Astrophysical Journal 806(2): 204.

Vernazza, P., Marsset, M., Beck, P., et al., 2016, The Astronomical Journal 152(3): 54.

Vinogradoff, V., Bernard, S., Le Guillou, C., & Remusat, L., 2018, Icarus 305: 358.

Vinogradoff, V., Le Guillou, C., Bernard, S., et al., 2017, Geochimica et Cosmochimica Acta 212: 234.

Walsh, K.J., Richardson, D.C., & Michel, P., 2008, Nature 454: 188.

Wartewig, S., 2003, IR and Raman spectroscopy: Fundamental Processing.

Weidenschilling, S., 1980, Icarus 44: 172.

Weidenschilling, S., 1995, Icarus 116: 433.

Westphal, A., Herzig, G.P., & Flynn, G., 2016, Elements 12: 197.

Wogelius, R.A., & J.V., W., 1992, Chemical Geology 97: 101.

Yesiltas, M., & Kebukawa, Y., 2016, Meteoritics & Planetary Science 51(3): 584.

Yesiltas, M., Kebukawa, Y., Peale, R.E., et al., 2014, Meteoritics & Planetary Science 49(11):

2027.

Yesiltas, M., Sedlmair, J., Peale, R.E., & Hirschmugl, C.J., 2016, Applied Spectroscopy 71(6): 1198.

Youdin, A.N., 2008, Physics and Astrophysics of Planetary Systems (arXiv).

Yurimoto, H., Abe, K., Abe, M., et al., 2011, Science 333: 1116.

Zanda, B., Bourot-Denise, M., Hewins, R.H., Barrat, J.-A., & Gattacceca, J., 2010, Meteoritics & Planetary Science (Suppl.) 73: 5312.

Zolensky, M., & McSween, H., 1988, Metorites and the early solar system, chapter 3.

Résumé en Français

L'étude des petits corps du Système Solaire nous donne des indications sur les conditions qui ont régi les premières phases de sa formation. En effet, certains corps trop petits pour s'être différenciés, ont peu évolué depuis la formation du Système Solaire. Bien qu'ils aient été altérés par des processus locaux (rayons cosmiques et solaires et processus d'impact en surface, métamorphisme thermique et altération aqueuse au sein du corps parent), ces corps peuvent avoir conservé une structure et une composition proche de celles qu'ils avaient lors de la formation des premiers planétésimaux. Ils nous permettent donc d'avoir des indices sur les transformations physico-chimiques subit par les corps primitifs du Système Solaire. Durant cette thèse, des fragments de l'astéroïde Itokawa ramenés sur Terre par la mission Hayabusa seront analysés.

Les météorites sont aussi une source clé d'informations. En particulier les météorites carbonées peuvent nous apporter beaucoup de renseignements sur la formation et l'évolution de la matière organique dans notre Système Solaire. Beaucoup de questions telles que ses liens avec la matière minérale sont encore en suspens. Durant cette thèse j'ai étudié des fragments bruts de la météorites de Paris, une météorites carbonée très primitive.

La spectroscopie infrarouge est une technique non invasive qui nous permet de collecter une information chimique à la fois sur la partie minérale et sur les composés organiques. Bien que l'on sache que ces deux phases ont évolué ensemble au sein des différents constituants du Système Solaire, le lien entre ces deux phases est encore mal connu. Durant cette thèse, leur étude simultanée sera un point crucial : le contexte minéralogique servira notamment à poser des contraintes sur l'évolution de la matière organique au sein des corps parents.

Grâce au progrès de l'imagerie infrarouge à transormée de Fourier, et notamment grâce au développement technique des détecteurs matriciels, il est maintenant possible d'accéder à une large quantité de données pour étudier l'hétérogénéité à grande échelle.

Analyse bi-dimensionnelle de la météorite de Paris

Dans un premier temps, deux fragments de la météorite de Paris ont été étudiés. Cette météorite est une des chondrites carbonées les plus primitives connues à l'heure actuelle.

Une première étude a été réalisée en transmission sur la ligne SMIS du synchrotron SOLEIL, avec une taille de pixel de 0.66 micromètre. Notre fragment a été écrasé entre deux cellules diamant. J'ai étudié la distribution spatiale des différentes phases chimiques : silicates amorphes hydratés ou anhydres, silicates cristallins, phyllosilicates, matière organique aliphatique, carbonates et sulfates de calcium. L'étude de l'hétérogénéité spatiale des différentes phases minerales m'a permit de détecter des zones ayant subit un degré plus ou moins fort d'altération acqueuse, et de suivre les effets de cette altération sur la matière organique. J'ai aussi eu l'occasion de contribuer à une étude multi analyses sur un deuxième échantillon plus large de cette météorite. Cette fois, j'ai pu participer à une étude en réflexion à une échelle millimétrique. Des analyses complémentaires en RAMAN et en EDX ont aussi été ménées et ont conforté nos observations : ces deux fragments sont composés d'un mélange de différents stades d'hydratation et d'amorphisation/cristallisation des silicates. Notre observation est cohérente avec les différentes étapes de l'effet de l'altération aqueuse décrite par Leroux et al., (2015). Ce résultat nous a permis d'identifier différents micro-environnements au sein de l'échantillon ayant subi un degré plus ou moins marqué d'altération aqueuse : la partie la plus primitive est principalement composée de petits grains d'olivine intégrés dans des silicates amorphes hydratés, puis l'altération aqueuse a dans un premier temps mené à une disparition progressive de l'olivine et à un enrichissement en silicates amorphes porteurs de molécules OH. Finalement, une altération aqueuse plus marquée va conduire à la production de phyllosilicates et de carbonates. A une échelle un peu plus large, l'étude infrarouge a permis de suivre la circulation de l'eau au sein de notre échantillon et comment celle-ci l'a altéré.

Pour le fragment microscopique, l'étude des spectres a aussi révélé une hétérogénéité de la matière organique. La région la plus altérée est plus pauvre en aliphatique comparée au reste du grain et le rapport CH_2/CH_3 est significativement plus élevé. Ainsi, l'altération aqueuse aurait provoqué un allongement des chaines aliphatiques ou aurait induit un dégré de ramification plus faible.

Etude de l'effet de l'altération spatiale sur des mététorites irradiées

L'infrarouge est aussi une technique très appréciée en astrophysique car elle permet une comparaison directe avec les observations des astéroïdes. Comme pour les météorites, une grande diversité est observée au sein des astéroïdes. En plus d'une hétérogénéité compositionnelle originelle, un ensemble de processus regroupés sous l'appellation altération spatiale peut modifier la surface des astéroïdes et biaiser les observations. Durant cette thèse, j'ai pu contribuer à une étude de météorites irradiées par des faisceaux d'hélium et d'argon pour simuler le vent solaire. Nous avons cherché à mieux discerner l'hétérogénéité liée à une différence compositionnelle primaire et celle introduite par l'altération spatiale. Dans les zones iradiées, nous avons pu oberver une modification spectrale des composés silicatés hydratés ou anhydres, nous avons pu ensuite quantifier le déplacement spectral des différentes bandes du spectre IR.

Création d'un nouveau protocole d'étude 3D

L'information spatiale est cruciale et étudier la co-localisation des phases est une aide précieuse pour mieux comprendre les processus pré et post accrétionnels. J'ai pu au cours de cette thèse développer une expérience de tomographie 3D IR. Ce dispositif permet d'étudier la localisation des phases chimiques en 3D et de travailler sur un grain préservé. Cette technique d'analyse non destructive donnera de précieuses informations sur les points les plus riches en organique ou présentant une structure particulière sans pour autant altérer l'échantillon. Elle pourra être envisagée comme première étape d'un processus d'analyses plus destructives, en effet une fois les régions d'intérêt détectées, des analyses sur des coupes FIB pourront être effectuées.

Tomographie IR

Pour réaliser cette expérience, la première étape a été de mettre au point une nouvelle technique de préparation d'échantillons permettant de préserver sa structure et de le maintenir horizontal dans le plan focal du microscope tout en permettant sa rotation. Nous avons ici utilisé une pointe en tungstène pour tenir l'échantillon. L'échantillon est attaché à la pointe grâce ùne soudure au platine faite au FIB.

Une série de mesures 2D (180 rotations de 1 degré) en transmission a ensuite été collectée sur plusieurs échantillons sur la ligne SMIS de SOLEIL, en tournant entre chaque mesure l'échantillon. Une fois toutes ces mesures prises, j'ai obtenu une série de projections, matrice 2D de spectres, pour chaque angle. La suite de mon travail a consisté à adaptée des méthodes de reconstruction basées sur les protocoles en tomographie X. Pour les principales bandes d'absorption du spectre IR : l'etirement des liasons CH_2 etCH_3 aliphatiques, l'étirement de la liaison OH et son pliage (cette bande contenant aussi une petite contribution du CC aromatique), la bande large des silicates et enfin les petites structures caractéristiques des régions plus structurées (olivine, pyroxène), j'ai extrait la distribution spatiale de leur abondance pour chacune des 180 mesures. Puis j'ai appliqué une méthode itérative basée sur la rétro-projection pour obtenir la distribution spatiale de tous ces composent en 3D.

Tomographie en rayons X

Une partie des échantillons étudiés pendant cette thèse a aussi fait l'objet de mesures en tomographie X sur la ligne PSICHE du synchrotron SOLEIL ou ils avait été au préalable mesurés par A. Tsuchiyama. Grâce à cette technique des paramètres physiques tels que la porosité mais surtout une forme plus précise du grain peuvent être extrait. En effet la résolution spatiale des données X étant beaucoup plus faible, nous pouvons produire des contraintes plus fortes sur la forme des échantillons et des sous structures internes.

Couplage des deux méthodes pour une caractérisation physico-chimique

La dernière étape du développement expérimental a finalement été de coupler ces deux méthodes d'analyse. Une fois les deux jeux de reconstruction superposés (remise à l'echelle, rotation et translation des données X pour minimiser la distance entre les deux distribution), nous pouvons pour un pixel donné calculer l'abondance relative des principales phases chimiques grâce aux données IR et avoir une idée des caractéristiques physiques grâce au données X. De plus, les données X ont permit de créer un modèle de forme sur laquelle filtrer les données IR ce qui nous a permit de diminuer les effets de diffraction/diffusion et de vérifier nos reconstructions IR.

Application à des grains asteroïdaux

Une première étude 3D a été menée sur 5 grains ramenés de l'astéroïde Itokawa. Ces grains avaient été au préalable collés à une fibre de carbone grâce à une résine organique et ils avaient déjá été analysés par T. Nakamura par étude de diffraction des rayons X et par A. Tsuchiyama grâce à la tomographie X. Le résultat des mesures de ces deux études nous a généreusement été fourni et nous avons pu le comparer à la composition chimique détectée par tomographie IR. De plus l'utilisation des données de tomographie X nous a permis de contraindre la forme de l'échantillon reconstruit en IR.

Après avoir reconstruit et séparé les composantes de la colle de la large bande des silicates, nous avons pu grâce à l'étude de la dérivée seconde des spectres, reconstruire séparément les différents minéraux (olivine, pyroxène riche/pauvre en Ca). Cependant, vu le fort bruit présent dans nos données, seules les phases majoritaires ont pu être reconstruites. Nous avons bien retrouvé la composition et la localisation des phases décrites par l'équipe de la JAXA.

Cette étude a aussi été l'occasion de tester la faisabilité d'analyses en tomographie IR sur des grains précieux ramenés par une mission de retour d'échantillon.

Etude 3D de la météorite de Paris

Finalement, nous avons aussi étudié 3 grains de la météorite de Paris d'abord grâce à notre système de tomographie IR puis sur la ligne PSICHE avec de la tomographie X (ce qui nous a permis la aussi de créer un modèle de forme pour nos échantillons mesurés en IR). Nous avons observé des hétérogénéités entre et à l'intérieur de ces trois fragments.

Concernant la matière organique, la signature moyenne des trois fragments est similaire par contre, une hétérogénéité dans les grains a été observée avec des pôles environ 3 fois plus riche que la moyenne en CH. Nous avons aussi suivi la distribution des phases hydratées : celle-ci est plus homogène. L'hétérogénéité des minéraux a lieu à une échelle plus large et

on peut distinguer un fragment plus amorphe et un autre qui présente une structure plus cristalline (le troisième ayant une signature intermédiaire).

Titre: Micro-tomographie infrarouge pour la caractérisation de matériaux extra-terrestres

Mots clés: Spectroscopie infrarouge, matière extra-terrestre, micro-tomographie, astéroids, irradiation ionique

Résumé: L'étude en laboratoire d'échantillons extraterrestres, issus d'objets primitifs, est fondamentale aussi bien pour améliorer notre connaisance de la formation et de l'évolution de notre Système Solaire que pour interpréter les observations faites par les missions spatiales. Des analyses précises en laboratoire de ces échantillons sont essentielles pour comprendre les conditions physico-chimiques qui ont mené à la formation des petits corps et des planètes. Le but de cette thèse interdisciplinaire à été d'exploiter l'imagerie infrarouge et de développer un dispositif de microtomographie en spectroscopie infrarouge à transformée de Fourrier. Nous étudierons des fragments de météorites et de pousières astéroïdales. De plus, la tomographie en rayons X à été utilisée pour contraindre précisement la forme de l'échantillon. Avec ces analyses, nous avons caractérisé la composition de matériaux extraterrestres à très petite échelle sans les détruire. Nous avons étudié l'effet des processus post-accrétionels, comme l'altération spatiale, à l'intérieur du corps parent, ou l'altération spatiale, à la surface de l'astéroïde, à la fois sur les parties minérale et organique. En particulier, nous avons pu grâce à cette expérience, étudier la corrélation spatiale de la matière minérale et organique, ce qui est fondamental pour comprendre l'origine et l'évolution de la matière organique.

Title: Infrared Micro-tomography for the characterization of extra-terrestrial materials

Keywords: Infrared spectroscopy, extra-terrestrial material, micro-tomography, asteroids, ionic irradiation

Laboratory based studies of extraterrestrial materials derived from primitive objects is fundamental to improve our knowledge about the formation and the evolution of the Solar System as well as for interpreting observations collected by spacecraft and landers. Precise laboratory analyses of samples obtained from sample return missions are essential to understand the conditions and the physico-chemical processes, which lead to the formation of the small bodies and planets. The aim of this interdisciplinary thesis was to exploit the infrared imaging and to implement three-dimensional Fourier transform infrared microtomography to study different extraterrestrial materials (meteorites and asteroidal dust). Moreover, X-ray tomography was used to determine the precise shape of the samples. With these analytical methods, we have characterized the composition of extraterrestrial materials without destroying them at very high resolution. We have studied the post-accretional effects, such as aqueous alteration inside the parent's bodies or space weathering at the surface of asteroids, on both the mineral and the organic components. In particular, we studied the correlations between the organic materials and the minerals observed in the sample, which is fundamental to understand the origin and the evolution of the organic matter.

Université Paris-Saclay
Espace Technologique / Immeuble Discovery
Route de l'Orme aux Merisiers RD 128 / 91190 Saint-Aubin, France